THÈSE

En vue de l'obtention du

DOCTORAT DE L'UNIVERSITÉ DE TOULOUSE

Délivré par : *l'Institut National Polytechnique de Toulouse (INP Toulouse)*

Présentée et soutenue le *11/09/2018* **par :**

Martin Pauthenet

Macroscopic model and numerical simulation of elastic canopy flows

---

JURY

SARA PUIJALON	Chargée de Recherche, CNRS	Membre du Jury
FLORIAN FICHOT	Ingénieur (HDR), IRSN	Membre du Jury
DIDIER LASSEUX	Directeur de Recherche, CNRS	Rapporteur
BENOÎT GOYEAU	Professeur des Universités (HDR)	Rapporteur
YOHAN DAVIT	Chargé de Recherche, CNRS	Membre du Jury
MICHEL QUINTARD	Directeur de Recherche, CNRS	Président du Jury
ALESSANDRO BOTTARO	Professeur des Universités (HDR)	Membre du Jury

---

École doctorale et spécialité :
MEGEP : Dynamique des fluides
Unité de Recherche :
Institut de Mécanique des Fluides de Toulouse (IMFT)
Directeur(s) de Thèse :
Alessandro Bottaro, *Yohan Davit* et *Michel Quintard*
Rapporteurs :
Didier Lasseux et *Benoît Goyeau*

Résumé

On étudie l'écoulement turbulent d'un fluide sur une canopée, que l'on modélise comme un milieu poreux déformable. Ce milieu poreux est en fait composé d'un tapis de fibres susceptibles de se courber sous la charge hydrodynamique du fluide, et ainsi de créer un couplage fluide-structure à l'échelle d'une hauteur de fibre (honami). L'objectif de la thèse est de développer un modèle macroscopique de cette interaction fluide-structure, afin d'en réaliser des simulations numériques. Une approche numérique de simulation aux grandes échelles est donc mise en place pour capturer les grandes structures de l'écoulement et leur couplage avec les déformations du milieu poreux. Pour cela nous dérivons les équations régissant la grande échelle, au point de vue du fluide ainsi que de la phase solide. À cause du caractère non-local de la phase solide, une approche hybride est proposée. La phase fluide est décrite d'un point de vue Eulerien, tandis que la description de la dynamique de la phase solide nécessite une représentation Lagrangienne. L'interface entre le fluide et le milieu poreux est traitée de manière continue. Cette approche de l'interface fluide/poreux est justifiée par un développement théorique sous forme de bilan de masse et de quantité de mouvement à l'interface. Ce modèle hybride est implémenté dans un solveur écrit en C++, à partir d'un solveur fluide disponible dans la librairie CFD Open∇FOAM®. Un préalable nécessaire à la réalisation d'un tel modèle macroscopique est la connaissance des phénomènes de la petite échelle en vue de les modéliser. Deux axes sont explorés concernant cet aspect. Le premier consiste à étudier les effets de l'inertie sur la perte de charge en milieu poreux. Un paramètre géométrique est proposé pour caractériser la sensibilité d'une microstructure poreuse à l'inertie de l'écoulement du fluide dans ses pores. L'efficacité de ce paramètre géométrique est validée sur une diversité de microstructures et le caractère général du paramètre est démontré. Une loi asymptotique est ensuite proposée pour modéliser les effets de l'inertie sur la perte de charge, et comprendre comment celle-ci évolue en fonction de la nature de la microstructure du milieu poreux. Le deuxième axe d'étude de la petite échelle consiste à étudier l'effet de l'interaction fluide-structure à l'échelle du pore sur la perte de charge au niveau macroscopique. Comme les cas présentent de grands déplacements de la phase solide, une approche par frontières immergées est proposée. Ainsi deux méthodes numériques sont employées pour appliquer la condition de non-glissement à l'interface fluid/solide: l'une par interface diffuse, l'autre par reconstitution de l'interface. Cela permet une validation croisée des résultats et d'atteindre des temps de calcul acceptables tout en maîtrisant la précision des résultats numériques. Cette étude permet de montrer que l'interaction fluide-structure à l'échelle du pore a un effet considérable sur la perte de charge effective au niveau macroscopique. Des questions fondamentales sont ensuite abordées, telles que la taille d'un élément représentatif ou la forme des équations de transport dans un milieu poreux souple.

Abstract

We study the turbulent flow of a fluid over a canopy, that we model as a deformable porous medium. This porous medium is more precisely a carpet of fibres that bend under the hydrodynamic load, hence initiating a fluid-structure coupling at the scale of a fibre's height (honami). The objective of the thesis is to develop a macroscopic model of this fluid-structure interaction in order to perform numerical simulations of this process. The volume averaging method is implemented to describe the large scales of the flow and their interaction with the deformable porous medium. An hybrid approach is followed due to the non-local nature of the solid phase; While the large scales of the flow are described within an Eulerian frame by applying the method of volume averaging, a Lagrangian approach is proposed to describe the ensemble of fibres. The interface between the free-flow and the porous medium is handle with a One-Domain-Approach, which we justify with the theoretical development of a mass- and momentum- balance at the fluid/porous interface. This hybrid model is then implemented in a parallel code written in C++, based on a fluid- solver available from the Open∇FOAM® CFD toolbox. Some preliminary results show the ability of this approach to simulate a honami within a reasonable computational cost. Prior to implementing a macroscopic model, insight into the small-scale is required. Two specific aspects of the small-scale are therefore studied in details; The first development deals with the inertial deviation from Darcy's law. A geometrical parameter is proposed to describe the effect of inertia on Darcy's law, depending on the shape of the microstructure of the porous medium. This topological parameter is shown to efficiently characterize inertia effects on a diversity of tested microstructures. An asymptotic filtration law is then derived from the closure problem arising from the volume averaging method, proposing a new framework to understand the relationship between the effect of inertia on the macroscopic fluid-solid force and the topology of the microstructure of the porous medium. A second research axis is then investigated. As we deal with a deformable porous medium, we study the effect of the pore-scale fluid-structure interaction on the filtration law as the flow within the pores is unsteady, inducing time-dependent fluid- stresses on the solid- phase. For that purpose, we implement pore-scale numerical simulations of unsteady flows within deformable pores, focusing for this preliminary study on a model porous medium. Owing to the large displacements of the solid phase, an immersed boundary approach is implemented. Two different numerical methods are compared to apply the no-slip condition at the fluid-solid interface: a diffuse interface approach and a sharp interface approach. The objective is to find the proper method to afford acceptable computational time and a good reliability of the results. The comparison allows a cross-validation of the numerical results, as the two methods compare well for our cases. This numerical campaign shows that the pore-scale deformation has a significant impact on the pressure drop at the macroscopic scale. Some fundamental issues are then discussed, such as the size of a representative computational domain or the form of macroscopic equations to describe the momentum transport within a soft deformable porous medium.

Remerciements

Ma thèse s'est déroulée au sein du Groupe d'Étude des Milieux Poreux (GEMP) de l'Institut de Mécanique des Fluides de Toulouse (IMFT). Elle a été financée par la chaire d'attractivité IDEX du Pr. Alessandro Bottaro. Je tiens donc à remercier l'IDEX et l'IMFT de m'avoir permis de travailler dans un cadre propice à la Recherche.

Je remercie l'équipe du centre de calcul CalMiP pour son soutien logistique et sa grande disponibilité. La majorité des calculs de cette thèse a pu être réalisée sur Eos sous le projet p1540.

Je suis reconnaissant du soutien apporté par le service Codes et Simulations Numériques (CoSiNus) de l'IMFT, ainsi que des languages de programmation et différentes librairies et codes développés et mis à disposition par la communauté scientifique.

Je remercie les services de l'IMFT, efficaces et disponibles au quotidien, qui ont été un atout certain durant ce projet, tant sur le plan administratif qu'au niveau de la maintenance informatique.

Je remercie les doctorants et permanents du groupe GEMP. Les échanges que j'ai pu avoir avec vous (scientifiques ou non), ainsi que votre bienveillance, ont été des éléments importants de la vie au laboratoire.

C'est ici l'occasion de remercier mes professeurs qui tout au long de ma formation ont su me transmettre leur passion, leur rigueur et le goût du travail.

Je tiens à exprimer toute ma gratitude aux membres de mon jury de thèse, qui se sont déplacés jusqu'à Toulouse pour assister à ma soutenance. Leur lecture assidue de mon manuscrit avec un regard extérieur a permis d'en améliorer grandement la lisibilité et de l'enrichir.

Un très grand merci à mes trois encadrants Alessandro Bottaro, Yohan Davit et Michel Quintard pour la confiance qu'il m'ont accordée, et pour leur désir de transmettre leur expérience et leur passion.

Enfin et surtout, ce projet n'aurait pu aboutir sans le concours de ma famille et de mes proches.

Contents

Appendices

Nomenclature

$\bullet_{\beta}$	item related to the fluid phase (β- phase)
C_{λ}	inertial sensitivity of the microstructure, [1]
ϵ_{β}	porosity, [1]
ℓ	length scale used in Re_C, $[L]$
ℓ_{β}	pore length scale, $[L]$
$F_{\parallel}, F_{\perp}$	parallel and orthogonal Forchheimer terms, [1]
F_{λ}	Forchheimer number, [1]
γ_{β}	β- phase indicator, [1]
$\mathbf{g}_{\beta}$	macroscopic pressure gradient, $\left[ML^{-2}T^{-2}\right]$
K_{λ}	scalar permeability, $\left[L^{2}\right]$
$\boldsymbol{\lambda}$	direction of the intrinsic average velocity, [1]
$\mathscr{A}_{\beta\sigma}$	domain of the fluid-solid interface
$\mathscr{V}$	domain of the REV
$\mathscr{V}_{\beta}$	domain of the β- phase
μ_{β}	dynamic viscosity of the fluid, $\left[ML^{-1}T^{-1}\right]$
ν_{β}	kinematic viscosity of the fluid, $\left[L^{2}T^{-1}\right]$
p_{β}	pressure- field, $\left[ML^{-2}T^{-2}\right]$
ψ	generic field
$\mathbb{R}$	real space

Re_C, Re_k	critical- and permeability based- Reynolds number, [1]
ρ_β	density of the fluid, $\left[ML^{-3}\right]$
ℓ_0	dimension of the REV, $[L]$
$\mathbf{v}_\beta$	flow velocity- field, $\left[LT^{-1}\right]$
$\mathbf{f}$	extension of Darcy's law, $\left[L^{-2}\right]$
$\mathbf{K}_D$	Darcy permeability, $\left[L^{2}\right]$
$\mathbf{r}$	general position vector, $[L]$
$\mathbf{s}_\beta$	constant source term, $\left[LT^{-2}\right]$
$\mathbf{y}_\beta = \mathbf{r} - \mathbf{x}$	position vector relative to the centroid of the REV, $[L]$
$\langle \mathbf{v}_\beta \rangle^\beta, \langle p_\beta \rangle^\beta$	intrinsic averages
$\tilde{\mathbf{v}}_\beta, \tilde{p}_\beta$	spatial deviations
$\mathbf{v}^*, p^*$	dimensionless spatial deviations, [1]
b	non-linear part of Ergun's equation, $\left[L^{-1}T\right]$
L_v	macroscopic length scale, $[L]$
Re_D, Re_g	diameter based- and pressure gradient based- Reynolds number, [1]
V	measure of the REV, $\left[L^{3}\right]$
v	magnitude of the intrinsic average velocity, $\left[LT^{-1}\right]$
V_β	measure of the β- phase inside the REV, $\left[L^{3}\right]$

Part I

Introduction

Chapter 1

Introduction to elastic canopy flows

Turbulent fluid flows over rigid impermeable walls covered with elastic filamentous fibres is a challenging process to understand, model and simulate. Many such fluid- poro-elastic systems (referred to as *canopy flows*, Fig. 1.1a) can be observed in nature, and there have been a lot of efforts to understand how canopy flows function and the influence they have on the transport of nutrients, gas and pollutants in ecosystems. This has led to great breakthroughs in physical understanding, but the numerical simulation of canopy flows remains a tough issue [1, 2, 3, 4].

1.1 System of interest

A canopy flow can be either an immersed vegetation on a river bed, a wheat field under windy conditions or a carpet of cilia transporting mucus within the respiratory tract. The physics involved can be much different depending on the type of canopy that we focus on. For example whilst buoyancy dominates in vegetated river beds [5], it can be neglected in the study of the roughness layer over a forest [6]. Most of the knowledge that we have on canopy flows was motivated by the need to understand canopy flows in nature [7, 8, 9]. Canopy flows are at the heart of a lot of transport processes in nature. For example, [10] shows that the relationships between the vegetation covering a river bed, the water flow and the sediment transport is crucial. Typically a river bed covered by a canopy is less likely to erode, as the presence of the canopy helps keep the sediments at the bottom of the river, instead of being advected downstream. In [11], it is shown by experiments that gas transfer at the air/water surface of an immersed canopy is enhanced by the mixing generated by the movement of emergent stems due to the plant waving. Canopies in rivers also play a role in the transport of nutrient and are directly involved in the feeding of living organism, as well as in the improvement of water quality. The enhancement of vertical mixing due to the canopy allows for the removal of nutrients from the

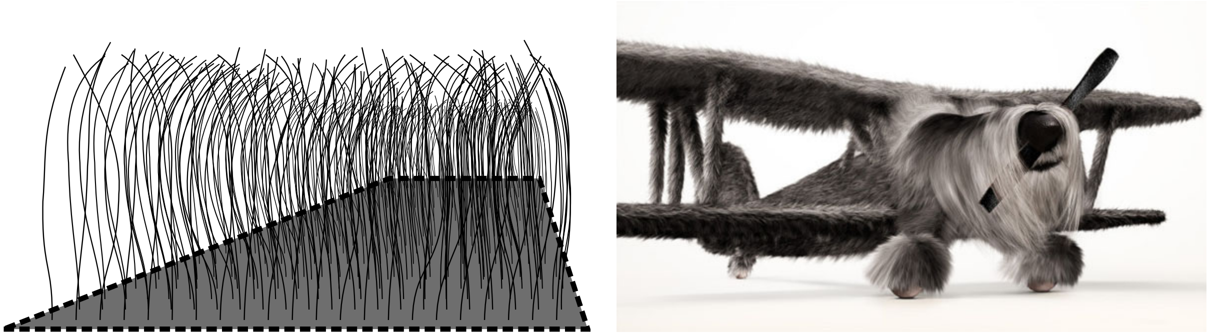

(a) (b)

Figure 1.1: Fig. 1.1a, perspective view of a passive canopy. A passive canopy is in fact a passive poro-elastic layer, made of an ensemble of fibres fixed onto a solid, impermeable wall (delimited by the dashed line). Each fibre is identical to another, and the canopy is homogeneous. Fig. 1.1b, following the biomimetic statement that a hairy surface provides better aerodynamic performances, this picture illustrates what planes might look like in the future. The picture was taken from a series of digital illustrations by INK.

free-flow, so that they remain trapped in the submerged vegetation [12]. The turbulent structures developing over a passive canopy may also cause serious damages to this canopy. For example [13] shows by experiments how a wind gust can damage a forest, and [14] is a study motivated by the need to understand how a wheat field can be damaged by a storm. Eventually, the understanding of canopy flows allows to design flow-control devices or arrange the trees in a forest in such a way that the potential damages due to strong winds are reduced.

1.1.1 Key parameters of a passive canopy flow

Canopies have numerous characteristic features. They can be either active or passive, dense or sparse, stiff or soft, etc. For example, active canopies can be found in lungs, where hairs interact with the mucus to move it forward [15]. In this case the fibres have an active role, as they provide their own mechanical power. This kind of active system might be of interest for flow control devices we can conceive. However canopies made of active fibres are a particular kind of fluid- poro-elastic systems and are beyond the scope of our context. The physics involved are specific. Here we consider only passive fibres, such that the fibres' motion is only due to the fluid-structure coupling. Animal furs, wheat fields, vegetated river beds and forests are a few examples of such passive processes (Fig. 1.1a). This processes have in common that the fibre motion is driven by the hydrodynamic loads, and in turn the fibre opposes a restoring force due to its elastic properties. Each hair can then act as an individual on the flow by restituting its elastic energy. The solid impermeable surface is passive as well, which means that it is rigid and impermeable, and there are no suction nor blowing devices. To be explicit, this means that from a numerical simulation point of view, the solid impermeable wall is

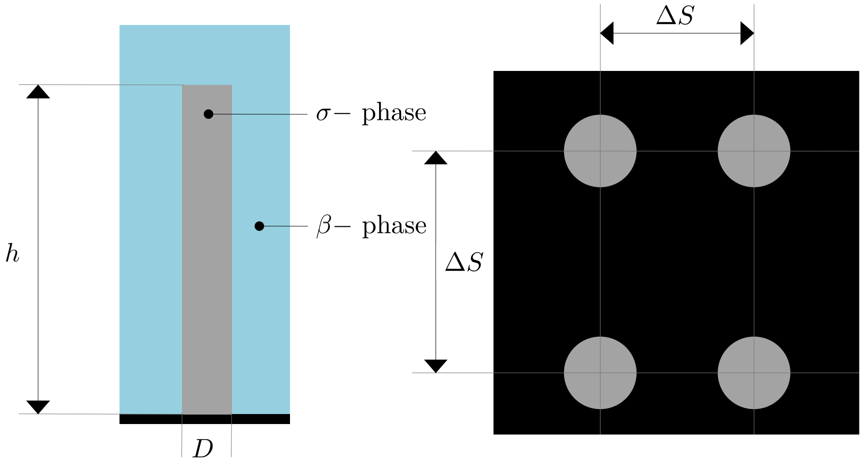

Figure 1.2: Geometrical parameters that define our model system (height and diameter of the fibres, space between fibres). We focus on the simplest canopy, that consists in a homogeneous arrangement of identical fibres attached to a planar rigid surface.

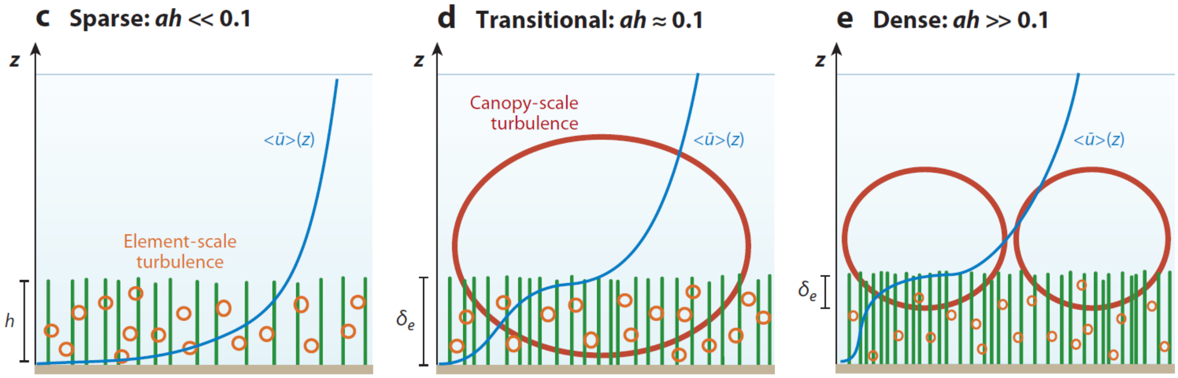

Figure 1.3: Different scales of turbulence that develop in a canopy flow are illustrated in this picture. The smallest scale mostly generates viscous dissipation and occurs at the stem scale. The largest scale consists in canopy scale vortices on top of the canopy. We see that the mean velocity profile, as well as the large coherent structure developing, depends on the frontal area per bed area of the canopy (see Eq. 1.1.2), *i.e.* the canopy sparsity influences the nature of the large scale coherent flow structure developing on top of it (image taken from [9]).

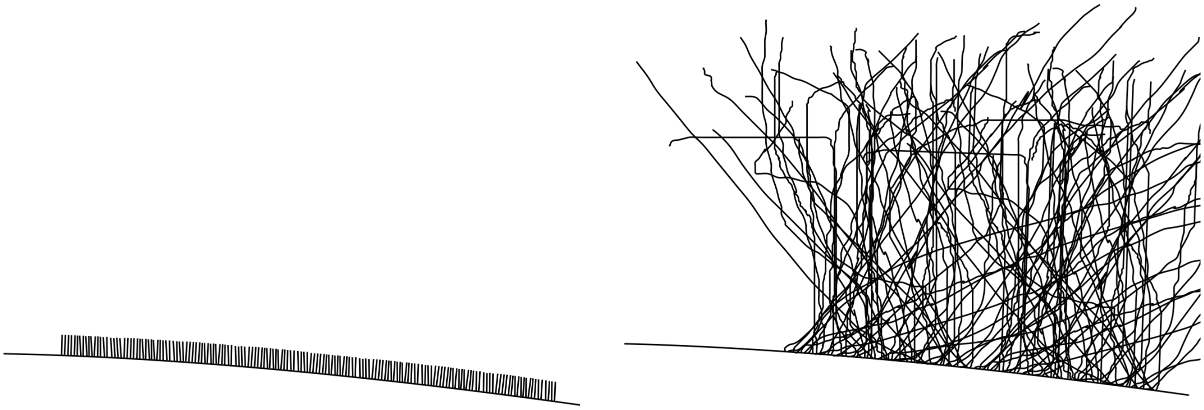

(a) (b)

Figure 1.4: Two different canopy flows that fit in our simple definition of a passive canopy. Fig. 1.4a, the fibres look rather stiff compared to the hydrodynamic load they encounter. Fig. 1.4b, the fibres look rather soft but the hydrodynamic load is small too, and buoyancy forces seem to dominate in this case. This shows that additional dimensionless numbers are required in order to have a better idea of the system we deal with.

modeled via a homogeneous Dirichlet condition for the velocity. A surface made of a combination of blowing devices and covered with an active canopy with heterogeneities is an interesting process to study and might afford ground-breaking applications. First of all, each separate phenomenon should be understood well, and here we focus on passive canopies.

The *passive canopy* term is still vague and can refer to very different processes (*e.g.* Fig. 1.4). Here we define more precisely the type of system that we are interested in and identify the set of parameters that characterizes it. First of all, we should state that each fibre is solidly anchored at its root to the impermeable rigid wall (Fig. 1.1a). This way, the rigid wall and the deformable fibres constitute the solid phase ($\sigma-$ phase), and the region under the tip of the fibres lies entirely in the fluid ($\beta-$ phase), such that any part of space above the impermeable rigid wall is an ensemble of fluid- and solid-regions. A minimal definition of the fibres geometry requires only a few parameters (Fig. 1.2). Let ΔS be the space between two neighbouring fibres, h and D be, respectively, the height and diameter of the fibres. For simplicity, fibres are taken identical and of constant cross section. For a complete description of the geometry, we should determine the way fibres are arranged on the impermeable rigid wall. This introduces notions of disorder and sparsity. In addition to the geometry of the $\sigma-$ phase, the process has several degrees of freedom concerning physical properties such as the density and rigidity of the material composing the $\sigma-$ phase, the fluid physical properties and the velocity distribution, that condition the flow regime at the stem scale and the Reynolds number at the scale of the canopy. Finally, we focus on canopy flows dominated by hydrodynamic load and fibres stiffness (buoyancy effects and fibre-fibre interactions are neglected). This gives us a complete view of the process of interest here.

From the point of view of the large scale flow physics, we distinguish between limit cases of canopy flows by mean of dimensionless numbers that compare the physics involved. As previously stated, observation of natural canopy flows already provides a useful background. As shown in [9], much information can be deduced on the large scale flow physics knowing only a few parameters (see Fig. 1.3). Obviously the Reynolds number is relevant, which we define as

$$Re = \frac{Uh}{\nu_\beta}, \tag{1.1.1}$$

where U is a characteristic velocity of the flow, and ν_β is the fluid kinematic viscosity. Re should be large enough so that the Kelvin-Helmholtz (KH) instability is triggered (we will focus on the KH instability more deeply in the next section). As observed by experiments [9], the frontal area per bed area is a crucial parameter too. This geometrical parameter is defined as

$$ah = \frac{Dh}{\Delta S^2}. \tag{1.1.2}$$

This parameter, associated with the Reynolds number Re, conditions the shape of the velocity profile and the characteristics of the coherent structures that develop in a canopy flow (Fig. 1.3). Let C_D the drag coefficient of a fibre. A third important parameter is the Cauchy number, defined as

$$C_Y = \frac{\frac{1}{2}\rho_\beta C_D D h^3 U^2}{EI}, \tag{1.1.3}$$

where ρ_β is the fluid density, E is the Young modulus of the solid- phase, I is the area moment of inertia of the fibres and h is the height of the fibres. C_Y compares the intensity of the hydrodynamic to the restoring force of the fibre. C_Y allows for an a priori estimate of the response of the solid phase to the flow and allows to assess whether fibres will bend, or if they should be considered as rigid bodies, as their stiffness is very large ($C_Y \ll 1$, *e.g.* an arrangement of skyscrapers). These three parameters Re, ah and C_Y allow for instance to respect similarities in the set-up of a numerical simulation, with the objective to reproduce an experiment or field- conditions. Regarding an application, we can already determine which class of canopy is suitable for the objective we have in mind. Let us say we are willing to use the large-scale fluid-solid coupling occurring over a canopy flow to provide energy to a boundary

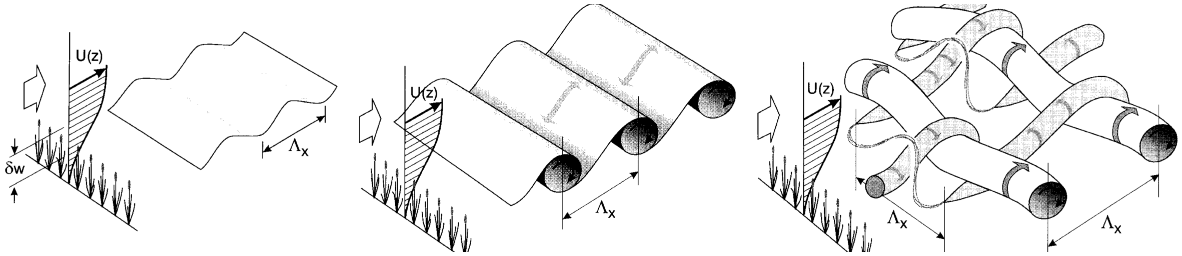

(a) Stage 1 (b) Stage 2 (c) Stage 3

Figure 1.5: The mean flow profile over a canopy can be unstable. A perturbation of the flow generates a large scale complicated structure following three stages of development. Fig. 1.5a The KH instability starts developing. Fig. 1.5b Canopy scale regular parallel rollers travel on top of the canopy. Fig. 1.5c The parallel vortices degenerate into a sophisticated pattern, displaying a complex, 3D shape as a secondary instability develops and takes over (image reproduced from [8]). This illustration underlines the relevance of simulating the large-scale in a numerical study of canopy flows.

layer. We should set Re, ah and C_Y for example to

$$\begin{aligned} Re &\simeq 10^{+4}, \text{(to trigger the KH instability)}, \\ C_Y &\simeq 1, \text{(to take advantage of the honami phenomenon)}, \\ ah &\simeq 10^{-1}, \text{(so that the mixing layer reaches the wall)}. \end{aligned} \tag{1.1.4}$$

This helps design the canopy on purpose. Until now we have mentioned that there was a KH instability developing on top of the canopy in a canopy flow, as well as a honami phenomenon, and we have suggested that there was an interest in the improvement of the vertical momentum transfer. We have not given many details yet on this large-scale fluid-structure coupling (*honami*), and neither have we on the flow structure arising from this instability. The following section aims at providing more details on the honami phenomenon and the applications that could arise from the numerical simulations of the large-scales of a honami.

1.1.2 Physics of a honami

1.1.2.1 Honami

A honami (or monami for aquatic vegetation), refers to the canopy-scale fluid-structure interaction that develops when a turbulent flow occurs over a deformable canopy. This canopy-scale fluid-structure interaction develops under specific conditions and can be seen by the eye on, *e.g.* , wheat fields under windy conditions [16]. The arising of these coherent structures is rather simple to picture. The profile of mean flow velocity over a canopy has an inflection point, due to the blocking effect of the canopy under the free-flow region. This specific feature is keen on developing a canopy-scale, coherent flow structure on top of the canopy, that consists in canopy-scale vortices [17, 18], see Fig. 1.3 and 1.5.

This flow instability is related to the shape of the mean flow (Kelvin-Helmholtz (KH) instability, [19]), and eventually evolves toward complicated turbulent structures that display 3D features. Such flow structures were described as similar to structures that develop in a mixing layer (*e.g.* [8]) observed at the boundary between two fluids at two different velocities. The development of these flow-structures can be described in three main stages (Fig. 1.5). The first stage is due to the the KH instability. As the mean flow is unstable by nature (inflection point), a single perturbation triggers this instability (Fig. 1.5a) and generates canopy-scale vortices on top of the canopy [9]. At the beginning, these vortices are very small, but they keep growing until their dimension reaches the height of the canopy. This is the second stage of the mixing-layer analogy (Fig. 1.5b). These rollers (each of them are of similar size) travel along the top of the canopy with a regular spacing. The region between two rollers is highly strained and generates high viscous dissipation areas. This rather simple pattern then evolves into a more complicated structure sketched on Fig. 1.5c. 3D features and secondary vortices develop in the streamwise direction. This gives an idea of the canopy-scale flow structure occurring over a canopy. Note that at this point, the physics involved is only fluid mechanics.

A honami arises from the coupling of these canopy-scale coherent vortices with the deformation of the canopy, *i.e.* when the fluid dynamics described above couples with the elastic deformation of the fibres that compose the canopy. Indeed if the canopy is flexible, these vortices may interact with the fibres in an unsteady way, so that the elastic properties of the fibres take part in the sweep and ejection events [9] characteristic of the flow over a canopy. This is a fluid-structure interaction, between the flow and the ensemble of elastic fibres. This canopy-scale fluid-structure interaction develops over the canopy under specific conditions [9, 20, 21]. At low values of Re, the Kelvin-Helmholtz instability does not develop, there is no flow unsteadiness, and no flow-canopy interaction is observed (except that the canopy bends under the hydrodynamic load, but it is a steady equilibrium. This phenomenon called *reconfiguration* was studied in [22, 23]). At higher Reynolds number, the Kelvin-Helmholtz instability arises, and canopy scale vortices are likely to be triggered [19]. The resulting canopy-scale coherent flow structures couple with the deformable canopy only if the natural frequency of the fibres corresponds to the time-scale of the rollers. Locally, the elastic fibres bend under the hydrodynamic load and momentarily store elastic energy (sweep event). This elastic energy is then released in a restoring motion of the fibres, which in turn act on the flow as a moving obstacle and accelerate some fluid out to the free-flow (ejection event). The resulting fluid-structure coupling is called a honami, and displays an ensemble motion of the fibres. Typically, the length-scale of a vortex L is much larger than ΔS the space between fibres, so that roughly, the canopy deforms as bundles of $\sim \frac{L}{\Delta S}$ fibres.

1.1.2.2 Motivations of this study

By studying canopy flows, we initially have in mind mimetic approaches to the development of innovative skins. The starting point of this approach is a simple observation. Contrary to most of man-made aerodynamic surfaces, natural surfaces are rarely smooth and rigid, and are often covered with heterogeneities, whether they are elastic or rigid. The study of canopy flows could lead to discover a feasible way of performing passive flow control (*e.g.* with a poro-elastic coating), in order to obtain improved aerodynamic performances. The idea behind this is to use the fluid-elastic coupling between the flow and the poro-elastic layer, so as to manipulate the flow surrounding the surface, in order to achieve goals that cannot be achieved with a simple rigid impermeable wall. A poro-elastic coating could overcome several issues. For example in [24], the presence of elastic filamentous structures at the trailing edge of a cylinder is shown to allow a damping of the wake dynamics, that reduces the amount of energy dissipated in the wake region. Also, postponement of the onset of transition to turbulence could be obtained through taking advantage of the stabilizing effect of a compliant porous surface ([25, 26]), with the advantage that a laminar flow is less dissipative than a turbulent flow, which implies potential drag reduction. On the opposite, the objective of a canopy could be to destabilize the flow in order to improve the vertical momentum transfer and overcome flow separation.

A separated flow (Fig. 1.6a) induces an increase in energy losses by viscous dissipation, an excessive pressure drag applied to the body in motion in the surrounding fluid, and may result in catastrophic deterioration of lift (stall phenomenon) in the case of a lifting device, such as a wing or a compressor blade. For an aircraft, the stall velocity characterizes the velocity under which the plane can not fly, which constitutes the major limitation in reducing the landing distance. Physically, flow separation occurs when a boundary layer is submitted to an adverse pressure gradient. At a certain point, the fluid lacks momentum and can not overcome the adverse pressure gradient, causing the fluid to locally flow back (this is called a *backflow*) compared to the direction of the mean flow. The fluid viscosity plays two opposite roles in the flow separation phenomenon. On the one hand, the viscosity of the flow causes energy losses near the wall. By viscous dissipation, the flow loses momentum, hence favouring backflow under adverse pressure gradient. On the other hand, molecular diffusion (*i.e.* momentum diffusion by viscosity) helps transfer energy from the high-momentum free flow region to the near wall flow, which helps avoid flow separation. Indeed as stated in [27], ”the kernel problem in separation postponement is to add momentum to the very near-wall region of the flow by transferring momentum from flow regions farther from the wall, which are still momentum rich”. In the same way, turbulent boundary layers are known to better resist adverse pressure gradient than laminar boundary layers, as the turbulent mixing is known to enhance the vertical momentum transfer from the high momentum free-flow to the near-wall flow.

The permeability of a porous wall has been observed to play an important role in vertical momentum transfer, compared to a simple impermeable wall. Breugem in [28] implements an immersed boundary method to perform direct numerical simulations of the Navier-Stokes equations over a porous wall. This work based on a simple model porous medium allows for a direct access to the velocity field, and suggests an increase in vertical momentum transfer due to the wall permeability. Indeed this numerical simulation of a turbulent flow over a porous medium shows an increase in the total shear stress compared to an impermeable wall. By looking at the flow in details, Breugem concludes that this improved transfer is caused by a strong increase in the Reynolds-stresses, which in turn is caused by the weakening of the wall-blocking effect compared to an impermeable wall. This allows the turbulent flow to penetrate the permeable wall ($v' < 0$), thereby transporting fluid with relatively high streamwise momentum ($u' > 0$) into the permeable wall. By virtue of mass conservation, fluid with relatively low streamwise momentum ($u' < 0$) is transported from the permeable wall into the channel ($v' > 0$)". The resulting effect is a net increase of momentum transfer from top to bottom, *i.e.* from the free-flow to the near-wall flow. Moreover in [29] it is suggested through experiments that "the efficiency of momentum transfer within the mixing layer remains considerably larger than that in unobstructed flow because of the coherent structures that develop." The author suggests that "the coherent waving of a canopy strongly enhances vertical transport therein", hence the deformation of the canopy may play an important role in the momentum transfer process [30, 6, 9]. This suggests that in the future, planes might be "hairy" (Fig. 1.1b), allowing to manipulate the flow surrounding the canopy by tuning the fur (density, stiffness) on purpose. However we would like to point out that destabilizing the flow is not an insurance of net vertical momentum transfer improvement.

Flow destabilization to a turbulent regime, in addition to the presence of a porous medium, increases viscous dissipation, and the gain in vertical transfer due to the presence of the canopy must be greater than the associated additional energy losses. In particular [6], the canopy should not be too deep and/or dense, otherwise "turbulence cannot mix high-momentum fluid from above the canopy down to the ground" (see also Fig. 1.3). Clearly, there is an optimization problem here. Moreover, the hope for aerodynamic applications follows a biomimetic pattern, based on the observation that aerodynamic surfaces in nature are often not smooth nor rigid. However this assumes that the non-smooth and non-rigid characteristics of these coatings are made for the purpose of achieving better aerodynamic performances. Whilst this was shown for example for the shark skin, that led to the development of super-fast shark-skin-inspired swimsuits, the furs on animals are a priori not designed for aerodynamic purposes. Leopard seals for example are amazing hunters, and we can think that they are extremely capable swimmers, but their fur is also subject to severe constraints, such as bearing extremely low water temperature and undergoing camouflage. As another example, duck feathers [31] are covered

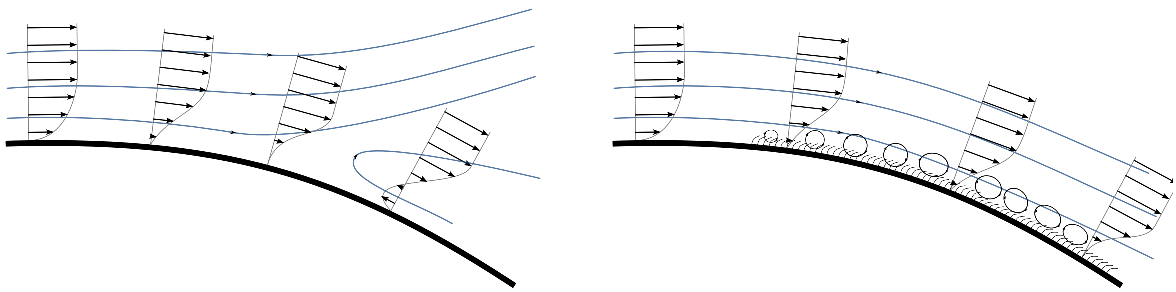

(a) rigid impermeable wall

(b) hairy wall

Figure 1.6: Expected effect of an innovative coating on a near-wall flow detaching. Under adverse pressure gradient, flow separation is keen on occurring in a boundary layer that lacks momentum. Flow separation is in general to be avoided, and this could be achieved by a poro-elastic coating (canopy). The mixing structures that develop on top of the canopy contribute to enhance the vertical mixing, thereby improving the vertical momentum transfer and delaying flow separation.

with a multi-scale microstructure that is responsible for their super-hydrophobic behaviour, helping the duck to keep its body dry. The aerodynamic purpose appears to be secondary in these cases. Clearly, the question of obtaining aerodynamic improvements by covering a surface with hairs remains open. Canopies in ecosystems are subject to multiple constraints, including their own vital needs, and their purpose is not dedicated to momentum transport. We are willing to understand how a canopy can maximize the vertical mixing and improve the vertical momentum transfer. As canopies in nature are subject to multiple constraints other than improving the vertical momentum transfer, they are not optimized for our aerodynamic purpose.

Experiments and field-observation give some evidences that suggest that elastic canopies (as defined in details in Section 1.1) somehow influence the vertical transport in the flow they are immersed in. Numerical tools that we develop here appear relevant to move forward on the issue of understanding canopy flows. The numerical approach is a reasonable way of proposing a model, implementing it and comparing it with experiment or field-data. Also, such a numerical tool is interesting during a design process. When it comes to finding out how a canopy can be optimized in terms of sparsity or stiffness of the fibres, so as to maximize the vertical momentum transfer for instance, it is interesting to have a rough idea of the physical properties of the fibres before starting to build an expensive experiment. For a process as complex as a canopy flow, the numerical tool is complementary to experiments.

1.2 The multiple-scale aspect

Canopy flows are multi-scale (Fig. 1.3). Inside the canopy, the number of heterogeneities is typically very large. Hence simulating the complete system at a microscopic level (*i.e.* each hair dynamics, and the smallest flow structure) can be achieved only at a huge computational cost. To reduce this computational cost we develop a macroscopic model to simulate canopy flows. This is made possible because the microscopic features are redundant. Hence we are not interested in describing these microscopic features in full detail each time they appear. We only need to model them once, and incorporate these models in a macroscopic model.

1.2.1 The relevant scale

The broad range of scales that characterize a canopy flow is roughly made of

- the stem-scale for the smallest scales, and
- the canopy-scale for the largest scales.

We only want to catch the macroscopic (*i.e.* large-scale) fluid-structure coupling of the canopy with the flow, *i.e.* the previously described honami phenomenon. In other words, the information of interest in canopy flows is most of the time contained in the canopy-scale features. For the fluid phase, this amounts to consider a volume-average velocity $\langle \mathbf{v}_\beta \rangle^\beta$ (see Section 2.1 for a detailed definition), and then to build a model for it, referred to as *macroscopic model.* However we emphasize the fact that both the solid- and the fluid- phase are concerned with this variety of scales. For example while the canopy scale vortices constitute the large scale flow, the vortex shedding at the stem scale generates small scale flow features. As well, whilst the deformation of the whole fibre creates a large scale solid deformation, the beating of stems due to vortex shedding can be considered as a small scale feature of the solid phase. Let τ_{macro}, L be the time- and length- scale characteristic of the large scale, respectively. The momentum transport and mass conservation equations for the macroscale L read

$$
\begin{aligned}
\rho_\beta \frac{\partial \langle \mathbf{v}_\beta \rangle^\beta}{\partial t} + \nabla \cdot \left(\rho_\beta \langle \mathbf{v}_\beta \rangle^\beta \langle \mathbf{v}_\beta \rangle^\beta \right) = &- \nabla \langle p_\beta \rangle^\beta + \nu_\beta \nabla \cdot \left[\nabla \langle \mathbf{v}_\beta \rangle^\beta + ^T \nabla \langle \mathbf{v}_\beta \rangle^\beta \right] \\
&+ \underbrace{\mathbf{D}_{\beta\sigma}}_{\text{fluid-solid force}} - \nabla \cdot \underbrace{\left(\rho_\beta \langle \tilde{\mathbf{v}}_\beta \tilde{\mathbf{v}}_\beta \rangle^\beta \right)}_{\text{subgrid scale stresses}} , \qquad (1.2.1) \\
\nabla \cdot \langle \mathbf{v}_\beta \rangle^\beta = 0. &
\end{aligned}
$$

Eqs. 1.2.1 are the Volume Averaged Navier-Stokes equations (VANS), that will be used to model the large scale of the fluid- phase in the macroscopic model we develop for canopy flows. A solid theoretical basis, with assumptions clearly emphasized, is essential to the development of a numerical tool that the user can trust and understand easily. The full details of the development of the VANS are given in Section 2, where the interaction among different scales is discussed in details. This development is conducted so that the $\langle \mathbf{v}_\beta \rangle^\beta -$ field is free of small length-scales. However, it still contains small time-scales.

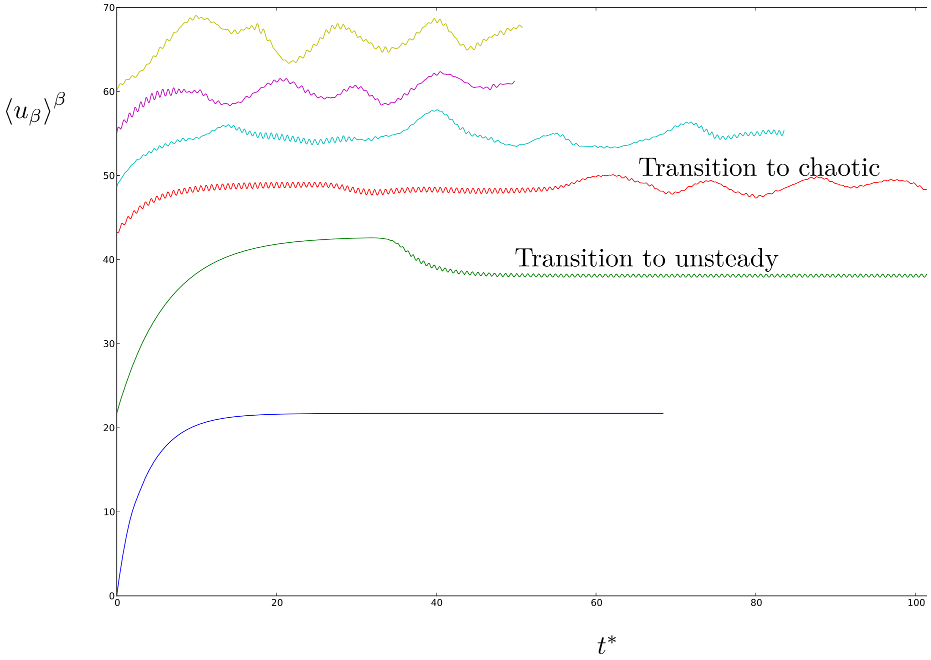

Figure 1.7: Evolution over time of the volume-averaged velocity $\langle \mathbf{v}_\beta \rangle^\beta$ component in the time-average direction of $\langle \mathbf{v}_\beta \rangle^\beta$ in the unit cell, starting from zero initial conditions. Each curve corresponds to a constant-uniform source term in the Navier-Stokes equations. The resulting average velocity is in arbitrary units. We observe different flow regimes, depending on the Reynolds number characteristic for the flow. The study of these different regimes is interesting from a physical point of view, but the details of these regimes is not relevant to the description of the large-scales, and we are willing to filter these small-scale features out.

1.2.2 Time filtering

The fact that the $\langle \mathbf{v}_\beta \rangle^\beta -$ field still contains small time-scales can be figured out by observing the value of the mean velocity $\langle \mathbf{v}_\beta \rangle^\beta$ over time (Fig. 1.7). These results are obtained with Open∇FOAM®, by simulating the 2D incompressible Navier-Stokes equations in a model porous medium with a constant-uniform forcing term. The geometry is made of an arrangement of cylinders and is periodic to mimic an infinitely large porous medium. Periodic conditions are imposed to $\mathbf{v}_\beta$ and p_β at the boundary of the computational domain. The constant-uniform forcing term mimics a constant pressure gradient, and its magnitude was varied so as to obtain different flow rates. Different regimes are displayed [32]. Under a certain Reynolds number, the permanent regime is steady (lower blue curve). Then as the Reynolds number increases, the microscopic streamline patterns begin to destabilize. The microscopic fields start to vary in time, and this reflects on the volume-averaged velocity $\langle \mathbf{v}_\beta \rangle^\beta$. An increase in pressure drop (decrease in flow rate at constant forcing term) is induced as the flow regime changes from steady to unsteady (green curve). As the forcing term further increases, the mass flow rate increases and the Reynolds number reaches a certain value above which the time-periodic feature is lost and

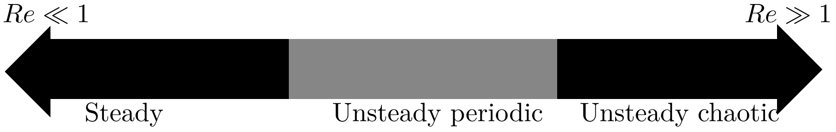

Figure 1.8: Schematic summary of the statistically steady regimes occurring at the pore scale, depending on the pore-scale Reynolds number. In the present simulations, the fluid flows under a constant pressure gradient, and one could wonder what would happen if a different condition were imposed. For example, we could impose a constant flow rate instead of a constant pressure gradient to study the pore-scale. The reason why we choose to impose a constant pressure gradient instead is related to the convenience of the computational setups, and has no clear physical justification.

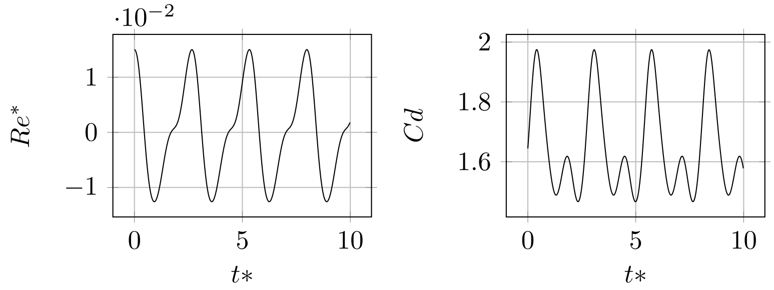

Figure 1.9: Unsteady flow in a periodic elementary cell of an array of cylinders of porosity 0.8. The time-averaged diameter-based Reynolds number Re_D is around 110. t^* is the time adimensionalized with the cylinder diameter and the mean velocity, basically corresponds to the number of passages of a flow particle through the domain. This clearly shows, on a simple case, that small time-scales remain in the volume-averaged velocity. Strictly speaking, the development of a macroscopic model for unsteady flows in porous media requires a double-average (both space and time).

the evolution over time of the volume-averaged velocity becomes chaotic (red curve and above). The three different statistically steady regimes (the regimes that establish after a certain amount of time, see Section. 5.1.2 for a more complete definition) at the scale of the representative cell are summarized on Fig. 1.8. The question of evaluating a priori the transition Reynolds number for a given porous medium is a tough one [33] and is not addressed here.

Details of the periodic regime are given on Fig. 1.9. Re_D is the time-averaged, diameter-based Reynolds number. Re^* is defined as

$$Re^* = \frac{\frac{D\langle u_\beta \rangle^\beta}{\nu_\beta} - Re_D}{Re_D}, \tag{1.2.2}$$

and C_d is the instantaneous drag coefficient. Let τ_μ be the characteristic time scale that we observe. It is clear that this small time scale τ_μ is not simulated in our macroscopic model

$$\tau_\mu \ll \tau_{\text{macro}}, \tag{1.2.3}$$

and we should filter Eq. 1.2.1 in time. We define the time-filtered quantity $\overline{x}$ of any function of time

x as

$$\overline{x} = x * m_\tau, \tag{1.2.4}$$

where m_τ is the kernel of the time filter. m_τ is such that filtered quantities are free of microscopic time variations of characteristic scale τ_μ. We can introduce the time-deviation x' as

$$x = \overline{x} + x'. \tag{1.2.5}$$

The time-filtering of Eq. 1.2.1 yields

$$\begin{aligned}
\frac{\partial \overline{\langle \mathbf{v}_\beta \rangle^\beta}}{\partial t} + \overline{\langle \mathbf{v}_\beta \rangle^\beta} \cdot \nabla \overline{\langle \mathbf{v}_\beta \rangle^\beta} = &- \frac{1}{\rho_\beta} \nabla \overline{\langle p_\beta \rangle^\beta} + \nabla \cdot \frac{\mu_\beta}{\rho_\beta} \left[\nabla \overline{\langle \mathbf{v}_\beta \rangle^\beta} +^T \nabla \overline{\langle \mathbf{v}_\beta \rangle^\beta} \right] \\
&+ \frac{1}{\rho_\beta} \underbrace{\overline{\mathbf{D}_{\beta\sigma}}}_{\text{fluid-solid force}} - \nabla \cdot \left(\underbrace{\overline{\langle \tilde{\mathbf{v}}_\beta \tilde{\mathbf{v}}_\beta \rangle^\beta}}_{\text{subgrid scale stresses}} + \underbrace{\overline{\langle \mathbf{v}_\beta \rangle^{\beta'} \langle \mathbf{v}_\beta \rangle^{\beta'}}}_{\text{Reynolds stresses}} \right), \qquad (1.2.6) \\
\nabla \cdot \overline{\langle \mathbf{v}_\beta \rangle^\beta} = 0.&
\end{aligned}$$

Due to the non-linear advective term, an additional term, that we call here the *Reynolds stresses*, appears in the time filtered VANS. Fig. 1.7 shows that for a rigid medium the values of $\langle \mathbf{v}_\beta \rangle^{\beta'}$ remain small against the values of $\langle \mathbf{v}_\beta \rangle^\beta$. In the context of deformable porous media however, we will see that there might be a fluid-structure coupling between neighbouring fibres and the flow at the pore-scale, that lead to rather large values of $\langle \mathbf{v}_\beta \rangle^{\beta'}$. Proposing a proper closure for the Reynolds shear stresses is a rather difficult task, as it depends on the flow conditions the parametrization is really not obvious. In practice we shall assume that Reynolds shear stresses are rather negligible against the fluid-solid force.

The stem-scale flow structures are involved in the macroscopic momentum transport mainly via energy dissipation (this is hidden in the fluid-solid force), and the subgrid-scale stresses. A direct approach is implemented in [34] to determine the nature of stem-scale turbulence in a homogeneous porous medium. When the flow is macroscopically homogeneous, it is suggested in [34] that stem-scale turbulent structures are localized, *i.e.* restricted to the pore scale. This is an important information, as when we try to evaluate the filtration law through a porous medium, we need to know how large the domain should be in order to capture fairly well the dissipative structures. When the flow is macroscopically heterogeneous, stem-scale turbulence plays a role in the transport of momentum via the subgrid-scale stresses. At the fluid-porous medium interface for example, the large values in gradient of average velocity $\langle \mathbf{v}_\beta \rangle^\beta$ induce large transfers due to these subgrid-scale stresses. An attempt to clarify their impact is proposed in this thesis.

The determination of τ_μ is not straightforward. As can be seen on Fig. 1.10 that illustrates the

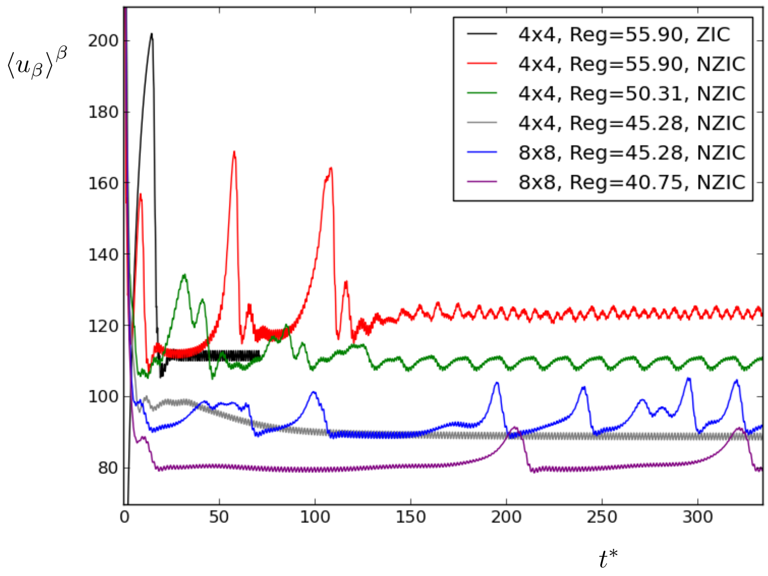

Figure 1.10: Flow through REVs of different sizes (4×4, 8×8) shows the sensitivity of the pressure drop to the size of the REV and to initial conditions. The "ZIC" acronym stands for Zero Initial Conditions, the "NZIC" acronym stands for Non Zero Initial Conditions, which corresponds to simulations started from a destabilized initial state. This indicates with which type of initial conditions the numerical simulations were started. *Reg* characterizes the source term set in the Navier-Stokes equations. The resulting average velocity is in arbitrary units.

results obtained from the numerical simulation of the Navier-Stokes equations, the frequencies involved in- , and the nature of-, the statistically steady regime for the rigid case depends on the size of the physical domain (made of several unit cells of size L_u) considered for the simulation (which we call REV for "Representative Elementary Volume"), and on initial conditions for the $\mathbf{v}_\beta$- and p_β- fields. This can lead to some errors, and one should be aware about the fact that the statistically steady regime is not uniquely defined by the value of the constant pressure gradient g characterized by Reg

$$Reg = \frac{L\sqrt{Lg}}{\nu_\beta}, \tag{1.2.7}$$

in this experiment. In addition to τ_μ the small time scale remaining in statistically steady regimes, there is a second time scale that appears on Fig 1.7, related to transient regimes. Let us call τ_p this time-scale, that characterizes the amount of time before the flow relaxes to the permanent regime in the elementary cell. τ_p is mostly due to the fluid inertia, *i.e.* the time it takes for the fluid to accelerate to a different regime. In our model we implicitly assume that

$$\tau_p \ll \tau_{\text{macro}}. \tag{1.2.8}$$

If this assumption is not satisfied, these transient regimes may have an impact on the fluid-solid coupling occurring in a honami. We could think of incorporating τ_p as a phase lag in a more sophisticated model [35], in order to take its impact into account in the coupling between the flow and the canopy.

1.3 Toward a porous medium approach

We are willing to develop a numerical model of the large scales in canopy flows. Prior to modeling a complex physical system, experiments and observations are essential as

- observation is at the starting point of any scientific approach, and
- validation of numerical simulations requires field data, and
- numerical simulations are subject to severe limitations.

The size of the mesh and the computational time often drastically limit the capability of simulations, even if a macroscopic model is used. Because of this, the study of a physical process can not be strictly numerical, and experiments are useful to reduce the space of parameters to explore previous to running a numerical campaign.

1.3.1 From field observation to the modeling of canopy flows

Real case observations of canopy flows are complementary to numerical simulations. Studies to predict near-surface wind field over canopies are available in the literature [36, 7, 6, 37, 38]. Although valuable, obtaining a detailed measurement of plant displacements and flow structures occurring in canopy flows is a challenge. The method of measurements should be non-intrusive [36], both from a flow point of view, and from a structure point of view. Indeed a sensor standing in a canopy is an undesired obstacle, and a light fibre can not wear a too heavy sensor as it would modify its natural frequency. Therefore implementation of distant measurements techniques, such as ground-based cameras or aerial LiDAR scanning is often required. Moreover the area to measure is often wide (from several hundreds of meters to a few kilometres). In [37, 38] such measurement techniques are reported to be able to provide a fine recording of the frontal area per bed area within the canopy. These field data allow to reproduce by numerical simulations the flow structures occurring over forested area. These turbulent structures are reported to be sensitive to heterogeneities occurring in complex arrangements of plant of trees.

Field observations have led to the development of the mixing layer analogy [7], as well as linear stability analysis to explain the origins of the honami phenomenon [1, 29, 39]. Numerical simulations are a powerful tool in addition to analytical tools and experiments. Indeed a numerical approach to canopy flows allows to numerically implement a model and to challenge it. This helps understand the underlying physics, by making simplifying assumptions, building a model and testing it to reproduce a real case. Due to the aforementioned difficulties, field data of a simple validation case are rather rare and there is a lack of validation cases for numerical simulations. Nevertheless once the numerical model is validated, it can be used to perform a parametric study in an optimization process. For example, heuristic models were proposed in [1, 2] and compared to field-observations. The authors were capable to reproduce the main features of the field data. Attempts to numerically simulate canopy flows in a more direct way have been made, with a much finer description of the canopies' mechanics [3, 4]. Our approach lies in-between these two approaches. The solid- phase mechanics is described but the description remains rough so as to reduce the number of degrees of freedom and keep the simulations tractable.

Many difficult points remain un-resolved in the numerical modeling of canopy flows. For example the need for scale separation between the microscopic- and the macroscopic- level is an important issue in the development of macroscopic equations, as it leads to neglecting some terms. The fluid-solid interface lacks a clear understanding. This region between the free flow and the porous domain is hard to apprehend, as the scale separation is not relevant, and a specific approach is required. The mathematical development of macroscopic transport equations (up-scaling) in general requires care and a detailed derivation to understand each step of the development, depending on the case study that we deal with. In addition, turbulent flows through porous media remains a challenging problem. For example, the interaction between the small-scale solid deformation with the small-scale turbulence affects the level of viscous dissipation. This issue requires direct numerical simulations and experiments to be more deeply understood. Without taking the solid deformation into account, there are only a few data available to evaluate the fluid-solid force acting on the flow in the porous medium depending on the flow orientation, porosity and Reynolds number. This way the coupling between the flow and the deformable porous medium can be more improved. Coupling the flow with the medium deformation requires transport equations for the solid, and volume averaging the solid phase does not always leads to Eulerian equations (non-local aspect). Fortunately the volume averaging technique provides a framework to tackle the aforementioned issues.

1.3.2 Outline of the thesis

The method of volume averaging [40] allows to develop transport equations for macroscopic equations, and to highlight every hurdle that arises. It is based on a clear separation of scales into large and small scales, and the connection and interaction between the two appear explicitly. In practice, the development of the macroscopic numerical model has led us to develop distinct codes, namely

- a *microscopic* code, designed to simulate in detail the flow at the small-scale, and provide data to model the effect of small scales on large scales in the macroscopic model, and

- a *structure* code, dedicated to the mechanics of the $\sigma-$ phase, and
- a *macroscopic* code, that simulates the large scales of the process and incorporates every feature of the finished macroscopic model.

Each code needs to be competitive in its own domain, *i.e.* the efficiency in terms of CPU time spent on a simulation should not be neglected. This has a huge impact on the research project it is related to, and it is crucial to find compromise between the time spent parallelizing and the time spent to run the numerical simulations. The variety of codes and complexity of finding a compromise, as well as the required level of programming skills to obtain a manageable code, illustrates how rich a numerical approach to canopy flows is.

The outline of this thesis is as follows. In Section 2, we derive step-by-step the macroscopic equations (VANS) of the flow that will be implemented in the code. We do so by taking the volume-average of the canopy, under a few assumptions adapted to our case. We recall these assumptions here.

- At the scale of the averaging volume (AV), the porous microstructure is disordered in the two directions orthogonal to the fibres, and invariant in the direction of the fibres (see Fig. 2.2 in Section 2).
- Away from its boundaries, the porous medium can be treated as homogeneous. A specific treatment is then proposed for regions that sustains heterogeneities, such as the free-flow/porous medium interface.
- The porosity ϵ_β (defined by Eq. 2.1.11) of the porous medium is high [2], *i.e.* $1-\epsilon_\beta \ll 1$.
- At the scale of the AV, the bundle of fibres is an ensemble of N rigid bodies. Basically the AV is small enough so that it does not see the curvature of the fibre.
- Finally, the macroscopic solid length- scale L_σ is much larger than the macroscopic fluid scale L (see Section 2.2.2.2).

The validity and the reason of these assumptions appear clearly in the development, which leads to a macroscopic transport equation for the fluid (Eq. 1.2.1). The interaction between the small-scale and the large-scale is then highlighted. A discussion on subgrid-scale stresses (SGS) is provided. An order of magnitude evaluation is proposed and shows that the subgrid-scale stresses should be negligible against the fluid-solid force and the macroscopic momentum advection term in the homogeneous porous region. In the homogeneous free-flow region the situation is different and the effect of the SGS on the large

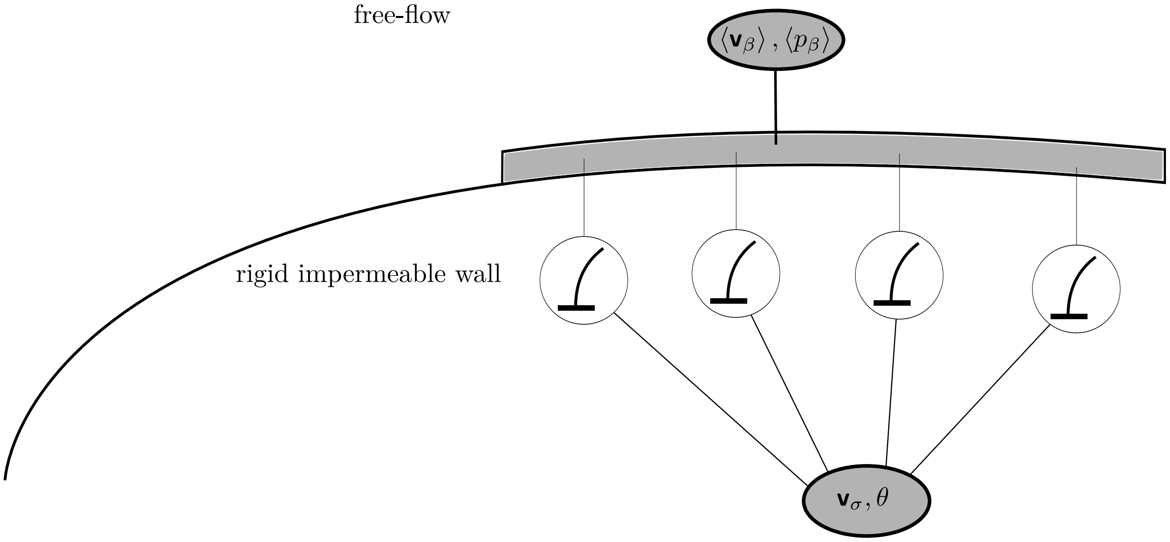

Figure 1.11: Schematic view of the hybrid model. The fluid phase is described in a Eulerian frame with the $\langle \mathbf{v}_\beta \rangle$- and $\langle p_\beta \rangle$- fields, whereas we adopt a Lagrangian description for the solid phase, where only a few fibres' mechanics are computed, which then spread into the whole porous medium to have a complete description of the solid kinematics.

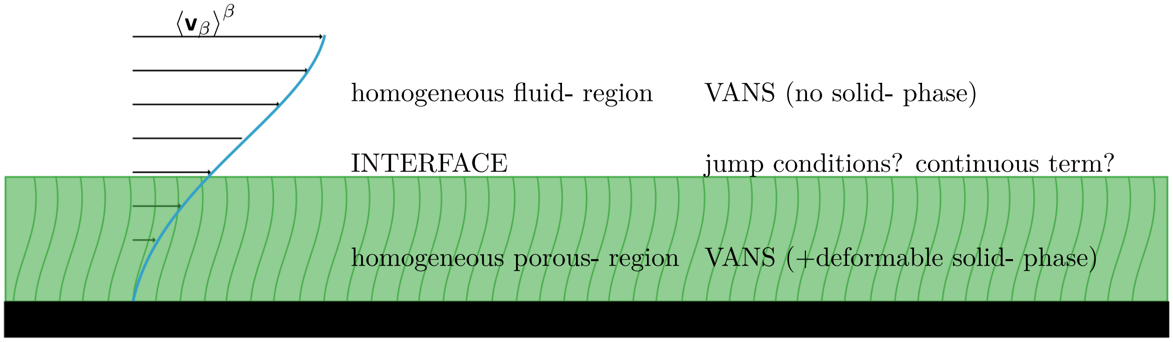

scale should be modeled. An approach to model the free-flow/porous medium interface is proposed (Fig. 2.4) to clarify the numerous issues that arise in this particular region (*e.g.* , [41]). A theoretical justification of the use of a continuous term to model the free-flow/porous medium interface is given, with again constitutive assumptions clearly stated.

In Section 3, we deal with the mechanics of the $\sigma-$ phase. The $\sigma-$ phase is composed of a large number of fibres, that are not rigid and might be subject to large elastic deformations and displacements under the hydrodynamic load. Our model describes the interaction of this fibrous porous medium with the surrounding fluid flow. The level of description is at a length-scale L_σ much larger than the space between two fibres. We are more interested in describing in details the fluid- than the solid- phase. This basic description of the solid-phase that we propose should fairly describe the interaction with the flow. Indeed according to existing observations of canopy flows, the large-scale phenomenon is of the size of the canopy. The non-local nature of the solid phase leads us to consider a hybrid model (Fig. 1.11).

This consists in mapping the canopy with N_f fibres and to resolve these N_f fibres only, in order to reduce the number of degrees of freedom of the canopy. We propose an unsteady solver, that integrates the inclination of the beam over time under an arbitrary, unsteady loading (*i.e.* the hydrodynamic load). The mechanics of the N_f fibres only is resolved, and we extend the obtained kinematics to the whole medium by linear interpolation. This method allows the user to increase arbitrarily the level of description of the $\sigma-$ phase, in order to assess the dependence of results on N_f the number of fibres that we resolve. The structure solver is integrated in a fluid solver of Open∇FOAM®. A reconstruction of the porosity field, depending on the position and inclination of the fibres, allows for the coupling between the solid- phase and the fluid- flow. The issue of parallelization is discussed. Open∇FOAM® appears to be a good solution for distributing the tasks related to the simulation of canopy flows, along with the **pStream** library. The implementation of the hybrid model is tested with an illustrative case that involves an unsteady flow interacting with an arrangement of deformable elastic fibres. An experiment is then numerically reproduced in order to have a quantitative comparison between our numerical approach and a real case experiment. The hybrid model seems a promising tool for the purpose of studying the vertical transport in canopy flows, and the effect of different parameters of the canopy flow.

The two last parts deal with the study of the microscopic scale. The objective is to get insight into the micro-scale, in order to model its impact on the macroscale (the resolved scale).

Section 4 addresses the relation between the macroscopic pressure gradient and the flow rate through the porous medium. In this section, we basically study the first deviation from Darcy's law, when inertia effects become sizeable. We try to define a Reynolds number, Re_C, such that the inertial deviation occurs when $Re_C \sim 1$ for any microstructure. The difficulty in doing so is to reduce the multiple length scales characterizing the geometry of the porous structure to a single length scale, ℓ. We analyse the problem using the method of volume averaging and identify a length scale in the form $\ell = C_\lambda \sqrt{K_\lambda/\epsilon_\beta}$, with C_λ a parameter that indicates the sensitivity of the microstructure to inertia. C_λ is computed from a creeping flow simulation in the porous medium and Re_C can be used to predict the transition to a non-Darcian regime more accurately than by using Reynolds numbers based on alternative length scales. The theory is validated numerically with data from flow simulations for a variety of microstructures, ranging from simple 2D geometries to more realistic samples of sandrock. A good agreement is found. A framework is proposed to study the deviation in terms of direction and magnitude. Theoretical results about the characteristic of the deviation from Darcy's law are obtained, and some results that were obtained with a different method are recovered.

The final section, Section 5, proposes to explore the unsteady flow regime in a deformable-elastic porous medium. We use an Immersed Boundary Method (IBM) with a simplified treatment of solid-

solid collisions and a diffuse fluid-solid interface to simulate unsteady flow regimes in a model porous medium. We show on this model porous medium that the deformation of elastic pores has a significant impact on the fluid-solid force in Eq. 1.2.1 (or the macroscopic pressure gradient as this is equivalent). Details on the code development are given, leading to the questioning of the choice of immersed boundary method, and we conduct a comparison of the diffuse interface method against a sharp interface method. The main difference between the two method relies in the way mass conservation is ensured for the fluid- phase for a flow with moving boundaries. Results show that the two methods give the equivalent same results, and the small differences are interpreted and related to the boundary condition at the solid surface. The conclusion of this section is that the effect of pore-scale displacement of the solid phase has a considerable effect on viscous losses through the porous medium and should be accounted for in the modeling of canopy flows. A detailed discussion shows that different physical phenomena are involved, and we observe a large variety of regimes related to the pore-scale fluid-structure interaction. More effort should be spent to develop a proper code to study this aspect of the microscopic scale. Indeed the results are only preliminaries and show a large impact of the pore-scale deformation on the fluid-solid force. This issue should be studied more deeply, which involves larger simulations, more cases, and at relatively high Reynolds number. This requires an efficient parallelized code, and a large part of this work was about programming physical solvers.

Part II

The macroscopic model

Chapter 2

Macroscopic equations for the fluid phase

As illustrated in Section 1.1.1, canopy flows are multiscale processes characterized by a broad range of scales, yielding a large number of degrees of freedom. In order to render numerical simulations of such processes feasible, one requires an up-scaling process that models the small-scales and resolves the large-scales (the macroscopic scale). In this work, we use the volume averaging method to derive a set of equations that describe our multiscale process from a macroscopic point of view. The volume averaging method is a well known approach to the development of a macroscopic model. We refer the interested reader to [40, 42, 43] for fundamental theoretical developments in the context of porous media.

2.1 Toward a local macroscopic model

We introduce the theoretical basis upon which the macroscopic model that we propose for canopy flows is based. We apply the volume averaging technique to canopy flows, after highlighting a set of assumptions that ensure the macroscopic model is valid.

2.1.1 Principle of up-scaling

First of all, we make the distinction between

- the actual volume averaged fields (which we call the volume-average fields), directly computed by volume averaging the microscopic fields, and
- the macroscopic fields obtained by resolving the macroscopic model, here the Volume Averaged

Navier-Stokes Equations (VANS).

The volume-average- and macroscopic- fields are both large-scale fields. The principle of up-scaling is to build a macroscopic model that produces macroscopic fields that match the volume-average fields.

In a Eulerian frame, mass conservation and momentum transport for a continuum read

$$\begin{aligned} \frac{\partial(\rho \mathbf{v})}{\partial t} + \nabla \cdot (\rho \mathbf{v}\mathbf{v}) &= \nabla \cdot \boldsymbol{\tau} + \mathbf{s}, \\ \frac{\partial \rho}{\partial t} + \nabla \cdot (\rho \mathbf{v}) &= 0, \end{aligned} \tag{2.1.1}$$

with ρ the mass density, $\mathbf{v}$ the velocity vector, $\boldsymbol{\tau}$ the stress tensor and $\mathbf{s}$ an external source term. Inside the fluid phase (β- phase, see Fig 2.1), these momentum- and mass- conservation laws translate into the Navier-Stokes equations, which can be written as

$$\begin{aligned} \frac{\partial \mathbf{v}_\beta}{\partial t} + \nabla \cdot (\mathbf{v}_\beta \mathbf{v}_\beta) &= \frac{1}{\rho_\beta} \nabla \cdot \boldsymbol{\tau}_\beta + \mathbf{s}_\beta, \\ \nabla \cdot \mathbf{v}_\beta &= 0, \end{aligned} \tag{2.1.2}$$

as the flow is incompressible, and we have

$$\boldsymbol{\tau}_\beta = -\mathbf{I} p_\beta + \mu_\beta \left[\nabla \mathbf{v}_\beta +^T (\nabla \mathbf{v}_\beta) \right], \tag{2.1.3}$$

as the fluid is assumed to be Newtonian. $\mathbf{s}_\beta$ represents a uniform source term in the Navier-Stokes equations (*e.g.* , a gravity force). We impose no-slip conditions and continuity of the normal stress on the fluid-solid interface $\mathscr{A}_{\beta\sigma}$, which translates into

$$\begin{aligned} \mathbf{v}_\beta &= \mathbf{v}_\sigma, \\ \boldsymbol{n}_{\beta\sigma} \cdot \boldsymbol{\tau}_\beta &= \boldsymbol{n}_{\beta\sigma} \cdot \boldsymbol{\tau}_\sigma \text{ at } \mathscr{A}_{\beta\sigma}. \end{aligned} \tag{2.1.4}$$

$\mathbf{v}_\sigma$ and $\boldsymbol{\tau}_\sigma$ are the solutions of the boundary value problem driving the dynamics of the solid phase, assumed known here for the sake of simplicity.

2.1.2 Volume averaging

Let ψ_β be a field inside the β- phase. The method of volume averaging starts with the definition of an averaging volume. Let us define the averaging volume (AV) as the sphere V whose centroid is located at x (can be anywhere in R^3) and of radius r_0. For the purpose of up-scaling, r_0 should be large enough to eliminate pore scale variations (characterized by the l_β- length scale), but small enough to preserve the macroscopic length scale (L, corresponding to the $\nabla \langle p_\beta \rangle^\beta$- and $\langle \mathbf{v}_\beta \rangle^\beta$- fields). Indeed the interest of the macroscopic model is to describe phenomena of characteristic length-scale L. This length-scale

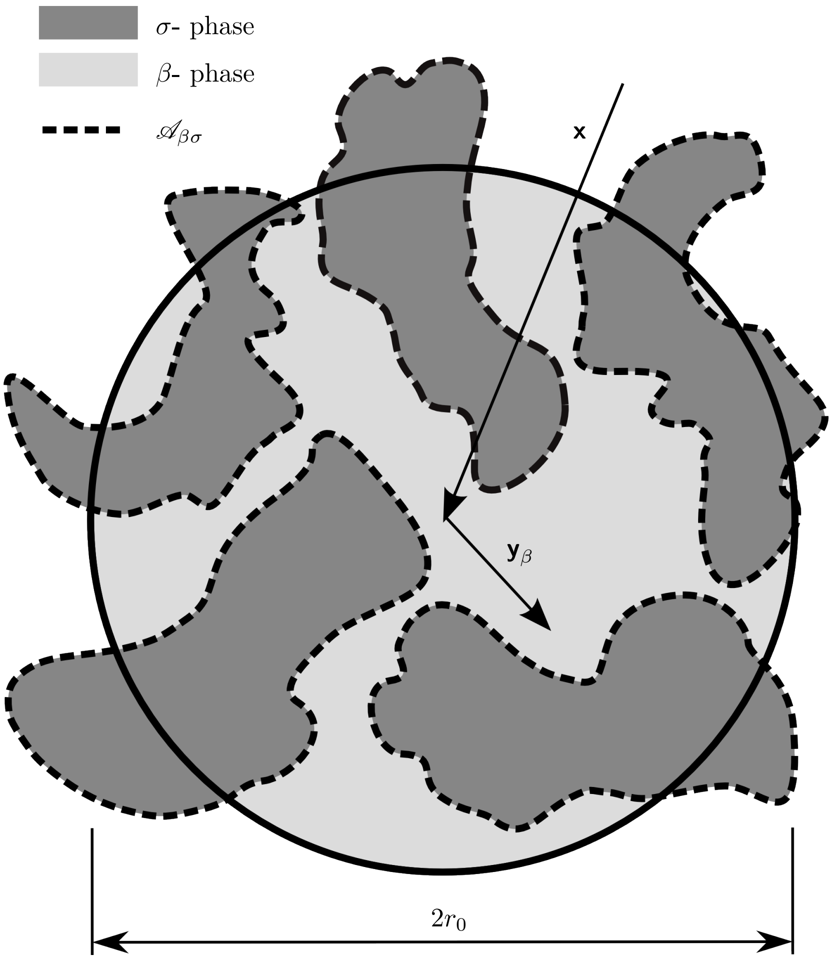

Figure 2.1: Averaging volume operating on a porous medium.

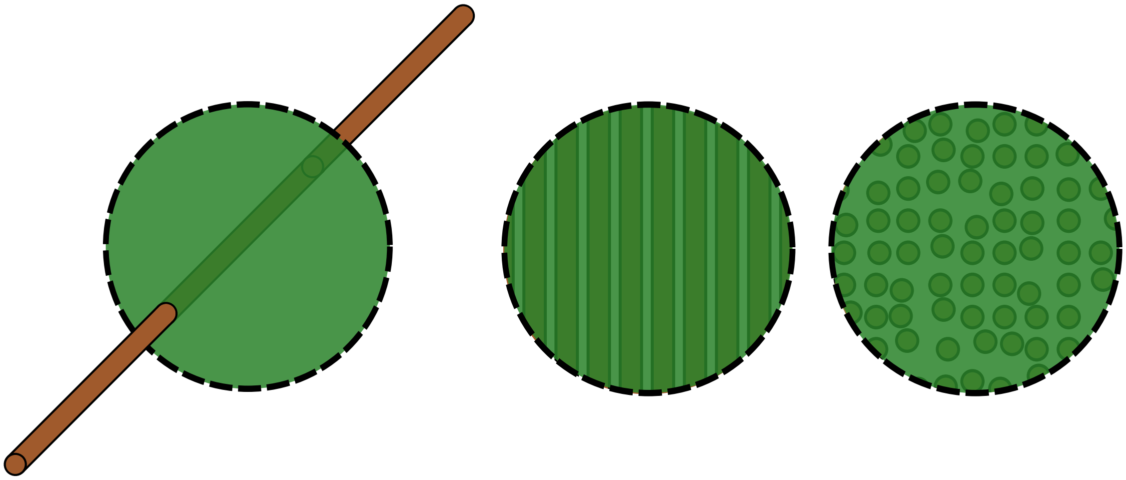

(a) 3D view, only one fibre represented (b) side view, invariant geometry (c) top view, disordered geometry

Figure 2.2

condition is summarized as

$$l_\beta \ll r_0 \ll L. \tag{2.1.5}$$

Condition 2.1.5 is the length scale separation assumption (LSA), an essential condition in every upscaling processes.

A general form of the volume average of ψ_β is

$$\langle \psi_\beta \rangle |_x = \int_{R^3} \gamma_\beta(y)\psi_\beta(y) m\left(y - x\right) \, dV(y), \tag{2.1.6}$$

with γ_β the phase indicator and m the kernel of the volume averaging operator. As pinpointed in [44, 45], the kernel m should be chosen so that

$$\nabla \left\langle \mathbf{y}_\beta \right\rangle \ll 1, \tag{2.1.7}$$

where the definition of $\mathbf{y}_\beta$ is illustrated in Fig 2.1. The choice of kernel m depends on the case that we wish to volume average.

In order to choose a proper kernel m and to allow further developments, we make a few assumptions on the porous medium that we presently volume average.

Assumption 1 *At the scale of the averaging volume (AV), our porous microstructure is disordered in the two directions orthogonal to the fibres, and invariant in the direction of the fibres (Fig. 2.2).*

Assumption 2 *The porous medium can be treated as homogeneous, i.e.*

$$\frac{1}{\epsilon_\beta} \nabla \epsilon_\beta \left\langle \psi_\beta \right\rangle^\beta \ll \nabla \left\langle \psi_\beta \right\rangle^\beta . \tag{2.1.8}$$

As we shall see later, these assumptions play a significant role in the development of the macroscopic equations. In particular, the rectangular function is a good choice for the kernel m in Eq. 2.1.6, and this leads us to define the superficial average of ψ_β as

$$\langle \psi_\beta \rangle |_x = \frac{1}{V} \int_{\mathscr{V}_\beta} \psi_\beta \, dV. \tag{2.1.9}$$

The corresponding intrinsic average is

$$\langle \psi_\beta \rangle^\beta |_x = \frac{1}{V_\beta} \int_{\mathscr{V}_\beta} \psi_\beta \, dV, \tag{2.1.10}$$

and the corresponding porosity (or void fraction) is

$$\epsilon_\beta = \frac{V_\beta}{V}. \tag{2.1.11}$$

In this development, we shall assume that

Assumption 3 *The porosity of the porous medium is high, i.e.* $1 - \epsilon_\beta \ll 1$.

We have the simple relation between the intrinsic- and superficial- averages

$$\langle \psi_\beta \rangle = \epsilon_\beta \langle \psi_\beta \rangle^\beta. \tag{2.1.12}$$

The reason why the rectangular function is a good choice for the kernel m in Eq. 2.1.6 is that it makes sure that condition 2.1.7 is satisfied. Another interesting feature would be that

$$\langle \mathbf{y}_\beta \rangle = 0. \tag{2.1.13}$$

Indeed with a Taylor expansion we can show that

$$\begin{aligned} \left\langle \langle \psi_\beta \rangle^\beta \right\rangle |_x &= \left\langle \langle \psi_\beta \rangle^\beta |_x + \mathbf{y}_\beta \cdot \left(\nabla \langle \psi_\beta \rangle^\beta \right) |_x \right\rangle |_x + O\left(\frac{r_0}{L}\right)^2, \\ &= \epsilon_\beta \langle \psi_\beta \rangle^\beta |_x + \langle \mathbf{y}_\beta \rangle |_x \cdot \left(\nabla \langle \psi_\beta \rangle^\beta \right) |_x + O\left(\frac{r_0}{L}\right)^2, \\ &= \langle \psi_\beta \rangle |_x + \langle \mathbf{y}_\beta \rangle |_x \cdot \left(\nabla \langle \psi_\beta \rangle^\beta \right) |_x + O\left(\frac{r_0}{L}\right)^2, \end{aligned} \tag{2.1.14}$$

so that if condition 2.1.13 is verified, then Eq. 2.1.14 is second order in $\frac{r_0}{L}$. As will be seen in Section 2.2.3, the order of Eq. 2.1.14 drives the convergence rate of the macroscopic model to the volume-average field as $\frac{r_0}{L} \to 0$. This plays a significant role in reducing area where the macroscopic fields does not match the volume-average fields. This is of particular interest at the free-flow/porous medium interface, and this clearly appears in Section 2.4.

2.1.3 Useful relations

We introduce the connection between the space- and time- derivative of the volume average of ψ_β and the volume average of the space- and time- derivative of ψ_β. The proofs of these connections can be found in [40]. For simplicity, we assume that the AV is of constant size, although it could be interesting to have a variable size AV that adapts to the space- heterogeneities of the process.

Theorem 1 *Spatial averaging theorem.*

$$\langle \nabla \psi_\beta \rangle = \nabla \langle \psi_\beta \rangle + \frac{1}{V} \int_{\mathscr{A}_{\beta\sigma}} \boldsymbol{n}_{\beta\sigma} \psi_\beta \, dA. \tag{2.1.15}$$

We obtain from Theorem 1 that

$$\frac{1}{V_\beta} \int_{\mathscr{A}_{\beta\sigma}} \mathbf{n}_{\beta\sigma} \, dA = -\frac{1}{\epsilon_\beta} \nabla \epsilon_\beta. \tag{2.1.16}$$

In particular Assumption 1 yields

Corollary 1

$$\frac{1}{V_\beta} \int_{\mathscr{A}_{\beta\sigma}} \boldsymbol{n}_{\beta\sigma} \langle \psi_\beta \rangle^\beta \, dA = -\frac{1}{\epsilon_\beta} \nabla \epsilon_\beta \langle \psi_\beta \rangle^\beta + O\left(\frac{r_0}{L}\right)^2, \tag{2.1.17}$$

(see [44] for a detailed explanation). A direct consequence is that in homogeneous porous regions, we have

Corollary 2

$$\frac{1}{V_\beta} \int_{\mathscr{A}_{\beta\sigma}} \boldsymbol{n}_{\beta\sigma} \langle \psi_\beta \rangle^\beta \, dA \ll \nabla \langle \psi_\beta \rangle^\beta. \tag{2.1.18}$$

Theorem 2 *General transport theorem (see proof in [40]).*

$$\frac{\partial}{\partial t} \int_{\mathscr{V}_\beta} \psi_\beta \, dV = \int_{\mathscr{V}_\beta} \frac{\partial \psi_\beta}{\partial t} \, dV + \int_{\mathscr{A}_{\beta\sigma}} \psi_\beta \left(\boldsymbol{n}_{\beta\sigma} \cdot \boldsymbol{w} \right) dA, \tag{2.1.19}$$

where $\boldsymbol{w}$ *stands for the local velocity of the* $\mathscr{A}_{\beta\sigma}$ *surface.*

For the purpose of obtaining macroscopic equations that will be used in the hybrid model, we volume average Eqs. 2.1.2 step by step and discuss different issues that arise during the development.

2.2 Macroscopic conservation equations

We derive large-scale transport equations by volume averaging the pore-scale equations for the fluid (β- phase).

2.2.1 Mass conservation

We recall the continuity equation for the β- phase

$$\nabla \cdot \mathbf{v}_\beta = 0. \tag{2.2.1}$$

Theorem 1 provides

$$\langle \nabla \cdot \mathbf{v}_\beta \rangle = \nabla \cdot \langle \mathbf{v}_\beta \rangle + \frac{1}{V} \int_{\mathscr{A}_{\beta\sigma}} \mathbf{n}_{\beta\sigma} \cdot \mathbf{v}_\beta \, dA. \tag{2.2.2}$$

Applying Theorem 2 to the phase indicator γ_β gives

$$\frac{\partial}{\partial t} \int_{\mathscr{V}_\beta(t)} \gamma_\beta \, dV = \int_{\mathscr{V}_\beta(t)} \frac{\partial \gamma_\beta}{\partial t} \, dV + \int_{\mathscr{A}_{\beta\sigma}(t)} \gamma_\beta \mathbf{n}_{\beta\sigma} \cdot \mathbf{w} \, dA, \tag{2.2.3}$$

hence

$$\frac{\partial \epsilon_\beta}{\partial t} = \frac{1}{V} \int_{\mathscr{A}_{\beta\sigma}} \mathbf{n}_{\beta\sigma} \cdot \mathbf{w} \, dA. \tag{2.2.4}$$

As $\mathbf{w}$ is the velocity of the surface $\mathscr{A}_{\beta\sigma}$, boundary condition 2.1.4 implies that the surface integrals in Eq. 2.2.2 and 2.2.4 are the same, and

$$\langle \nabla \cdot \mathbf{v}_\beta \rangle = \nabla \cdot \langle \mathbf{v}_\beta \rangle + \frac{\partial \epsilon_\beta}{\partial t}. \tag{2.2.5}$$

Therefore the superficial average of the continuity equation reads

$$\nabla \cdot \langle \mathbf{v}_\beta \rangle + \frac{\partial \epsilon_\beta}{\partial t} = 0. \tag{2.2.6}$$

It can equivalently be written

$$\nabla \cdot \langle \mathbf{v}_\beta \rangle^\beta = -\frac{1}{\epsilon_\beta} \nabla \epsilon_\beta \cdot \langle \mathbf{v}_\beta \rangle^\beta - \frac{1}{\epsilon_\beta} \frac{\partial \epsilon_\beta}{\partial t}, \tag{2.2.7}$$

by referring to identity 2.1.12. As shown in [15], this equation can be used in a projection step to ensure mass conservation in a porous system where porosity variations have a significant impact on the flow. In the development of our hybrid model however, we consider that $1 - \epsilon_\beta \ll 1$. Moreover the transport process is dominated by the drag force applied by the porous medium to the fluid. Hence the intrinsic average of the velocity is assumed divergence-free

$$\nabla \cdot \langle \mathbf{v}_\beta \rangle^\beta = 0, \tag{2.2.8}$$

i.e. porosity variations in space and time have only a low impact on the flow by comparison to the fluid-solid force.

2.2.2 Macroscopic momentum transport

Let LHS and RHS be respectively the left and right hand sides of the momentum transport part of Eq. 2.1.2

$$LHS = \frac{\partial \mathbf{v}_\beta}{\partial t} + \nabla \cdot (\mathbf{v}_\beta \mathbf{v}_\beta), \tag{2.2.9}$$

$$RHS = -\frac{1}{\rho_\beta} \nabla p_\beta + \frac{\mu_\beta}{\rho_\beta} \nabla \cdot \left[\nabla \mathbf{v}_\beta +^T (\nabla \mathbf{v}_\beta) \right] + \mathbf{s}_\beta. \tag{2.2.10}$$

2.2.2.1 Partial average of the momentum transport equations

Using Theorem 1

$$\langle \nabla \cdot (\mathbf{v}_\beta \mathbf{v}_\beta) \rangle = \nabla \cdot \langle \mathbf{v}_\beta \mathbf{v}_\beta \rangle + \frac{1}{V} \int_{\mathscr{A}_{\beta\sigma}} \mathbf{n}_{\beta\sigma} \cdot (\mathbf{v}_\beta \mathbf{v}_\beta) \, dA. \tag{2.2.11}$$

Using Theorem 2

$$\left\langle \frac{\partial \mathbf{v}_\beta}{\partial t} \right\rangle = \frac{\partial \langle \mathbf{v}_\beta \rangle}{\partial t} - \frac{1}{V} \int_{\mathscr{A}_{\beta\sigma}(t)} (\mathbf{n}_{\beta\sigma} \cdot \mathbf{w}) \mathbf{v}_\beta \, dA. \tag{2.2.12}$$

Due to the boundary condition on $\mathscr{A}_{\beta\sigma}$ surface integrals in Eqs. 2.2.11 and 2.2.12 cancel each other and the superficial average of LHS is

$$\langle LHS \rangle = \frac{\partial \langle \mathbf{v}_\beta \rangle}{\partial t} + \nabla \cdot \langle \mathbf{v}_\beta \mathbf{v}_\beta \rangle. \tag{2.2.13}$$

Theorem 1 yields

$$-\frac{1}{\rho_\beta} \langle \nabla p_\beta \rangle = -\frac{1}{\rho_\beta} \nabla \langle p_\beta \rangle - \frac{1}{\rho_\beta V} \int_{\mathscr{A}_{\beta\sigma}} \mathbf{n}_{\beta\sigma} p_\beta \, dA, \tag{2.2.14}$$

and

$$\langle \nabla \cdot \mu_\beta \nabla \mathbf{v}_\beta \rangle = \nabla \cdot \langle \mu_\beta \nabla \mathbf{v}_\beta \rangle + \frac{1}{V} \int_{\mathscr{A}_{\beta\sigma}} \mathbf{n}_{\beta\sigma} \cdot \mu_\beta \nabla \mathbf{v}_\beta \, dA. \tag{2.2.15}$$

This yields the superficial average of the Navier-Stokes equations

$$\begin{aligned} \frac{\partial \langle \mathbf{v}_\beta \rangle}{\partial t} + \nabla \cdot \langle \mathbf{v}_\beta \mathbf{v}_\beta \rangle = &- \frac{1}{\rho_\beta} \nabla \langle p_\beta \rangle + \frac{1}{\rho_\beta} \nabla \cdot \left\langle \mu_\beta \left[\nabla \mathbf{v}_\beta +^T (\nabla \mathbf{v}_\beta) \right] \right\rangle + \epsilon_\beta \mathbf{s}_\beta \\ &+ \frac{1}{\rho_\beta} \epsilon_\beta \mathbf{D}_{\beta\sigma}, \\ \nabla \cdot \langle \mathbf{v}_\beta \rangle = &- \frac{\partial \epsilon_\beta}{\partial t}, \end{aligned} \tag{2.2.16}$$

where the fluid-solid force $\mathbf{D}_{\beta\sigma}$

$$\mathbf{D}_{\beta\sigma} = +\frac{1}{V_\beta}\int_{\mathscr{A}_{\beta\sigma}} \mathbf{n}_{\beta\sigma} \cdot \left(-\mathbf{I}p_\beta + \mu_\beta \left[\nabla \mathbf{v}_\beta +^T (\nabla \mathbf{v}_\beta)\right]\right) dA, \tag{2.2.17}$$

is the volume force applied to the fluid by the solid.

At this stage, the macroscopic equations are free of length-scale assumptions, and porosity gradients do not intervene in it. This features are important to derive a macroscopic approach to the free-flow/porous medium interface, as explained in Section 2.4.3.

2.2.2.2 Intrinsic average of the momentum transport equations

As we wish to manipulate intrinsic averages in the hybrid model, we use identity 2.1.12 to obtain an expression in terms of intrinsic average quantities $\langle \mathbf{v}_\beta \rangle^\beta$ and $\langle p_\beta \rangle^\beta$

$$\begin{aligned}\rho_\beta \langle RHS \rangle^\beta = &- \left(\frac{1}{\epsilon_\beta}\nabla\epsilon_\beta + \nabla\right)\langle p_\beta\rangle^\beta \\ &+ \left(\frac{1}{\epsilon_\beta}\nabla\epsilon_\beta + \nabla\right)\cdot\left\langle \mu_\beta \left[\nabla \mathbf{v}_\beta +^T (\nabla \mathbf{v}_\beta)\right]\right\rangle^\beta + \mathbf{s}_\beta \\ &+ \mathbf{D}_{\beta\sigma}.\end{aligned} \tag{2.2.18}$$

The pressure part is already in a macroscopic form. Only the viscous term needs to be further developed in order to obtain a macroscopic form. As we consider $\mu_\beta = cste$, we have

$$\begin{aligned}\nabla \cdot \left\langle \mu_\beta \left[\nabla \mathbf{v}_\beta +^T (\nabla \mathbf{v}_\beta)\right]\right\rangle^\beta &= \nabla \cdot \left(\mu_\beta \left\langle \nabla \mathbf{v}_\beta +^T (\nabla \mathbf{v}_\beta)\right\rangle^\beta\right) \\ &= \mu_\beta \nabla \cdot \left\langle \nabla \mathbf{v}_\beta +^T (\nabla \mathbf{v}_\beta)\right\rangle^\beta.\end{aligned} \tag{2.2.19}$$

This step is not as obvious as it seems, since we could imagine modeling directly the average of the viscous stresses, *i.e.* keep the $\left\langle \mu_\beta \left[\nabla \mathbf{v}_\beta +^T (\nabla \mathbf{v}_\beta)\right]\right\rangle^\beta$ term as such. In [46] for example, Soulaine proposed to use a space varying viscosity to model turbulence effects in a porous medium. Here, we choose to continue the development further because this allows to obtain macroscopic equations that resemble very much the Navier-Stokes equations. Using Theorem 1 and identity 2.1.12 we can rewrite the viscous term as

$$\langle \nabla \mathbf{v}_\beta \rangle^\beta = \left(\frac{1}{\epsilon_\beta}\nabla\epsilon_\beta + \nabla\right)\langle \mathbf{v}_\beta\rangle^\beta + \frac{1}{V_\beta}\int_{\mathscr{A}_{\beta\sigma}} \mathbf{n}_{\beta\sigma}\mathbf{v}_\beta \, dA, \tag{2.2.20}$$

and use the no-slip condition at $\mathscr{A}_{\beta\sigma}$ to obtain

$$\langle \nabla \mathbf{v}_\beta \rangle^\beta = \left(\frac{1}{\epsilon_\beta}\nabla\epsilon_\beta + \nabla\right)\langle \mathbf{v}_\beta\rangle^\beta + \frac{1}{V_\beta}\int_{\mathscr{A}_{\beta\sigma}} \mathbf{n}_{\beta\sigma}\mathbf{v}_\sigma \, dA. \tag{2.2.21}$$

We apply the Green-Ostrogradski theorem and obtain

$$\int_{\mathscr{A}_{\beta\sigma}} \mathbf{n}_{\beta\sigma}\mathbf{v}_\sigma \, dA = -\int_{\mathscr{V}_\sigma} \nabla \mathbf{v}_\sigma \, dV + \int_{\mathscr{A}_{\sigma e}} \mathbf{n}_{\sigma e}\mathbf{v}_\sigma \, dA. \tag{2.2.22}$$

We further assume that the length-scale characteristic for the solid- phase deformation is much larger than the size of the AV, *i.e.* $L_\sigma \gg r_0$.

Assumption 4 *At the scale of the AV, the bundle of fibres is an ensemble of N rigid bodies ($L_\sigma \gg r_0$).*

Let $\mathbf{x}_{Gi}$ and $\mathbf{v}_{Gi}$ be the position and velocity of the center of mass of the i^{th} rigid body. Due to Assumption 4 we have an expression for the solid velocity $\mathbf{v}_\sigma$ within this rigid body as

$$\mathbf{v}_\sigma|_{\mathbf{x}_{Gi}+\mathbf{y}_\sigma} = \left(\mathbf{v}_{Gi} + \mathbf{\Omega}_i \wedge \mathbf{y}_\sigma\right), \tag{2.2.23}$$

where $\mathbf{\Omega}_i$ is the rotation vector- of the i^{th} body. Note that

$$\nabla\left(\mathbf{v}_{Gi} + \mathbf{\Omega}_i \wedge \mathbf{y}_\sigma\right) = \begin{bmatrix} 0 & +\omega_z^i & -\omega_y^i \\ -\omega_z^i & 0 & +\omega_x^i \\ +\omega_y^i & -\omega_x^i & 0 \end{bmatrix}, \text{ where } \mathbf{\Omega}_i = \begin{bmatrix} \omega_x^i \\ \omega_y^i \\ \omega_z^i \end{bmatrix}, \tag{2.2.24}$$

i.e. $\int_{\mathscr{V}_\sigma} \nabla \mathbf{v}_\sigma \, dV$ is an antisymmetric tensor. By definition of an antisymmetric tensor, this integral term vanishes in the expression for $\langle \nabla \mathbf{v}_\beta \rangle^\beta +^T \langle \nabla \mathbf{v}_\beta \rangle^\beta$. In addition, we can rewrite

$$\frac{1}{V}\int_{\mathscr{A}_{\sigma e}} \mathbf{n}_{\sigma e}\mathbf{v}_\sigma \, dA = \nabla\left(\epsilon_\sigma \langle \mathbf{v}_\sigma \rangle^\sigma\right). \tag{2.2.25}$$

To handle this term in this development, we assume that

Assumption 5 *The macroscopic solid scale L_σ is much larger than the macroscopic fluid scale L, i.e.*

$$\nabla\left(\epsilon_\sigma \langle \mathbf{v}_\sigma \rangle^\sigma\right) \ll \nabla \langle \mathbf{v}_\beta \rangle. \tag{2.2.26}$$

The validity of the later assumptions is not obvious and should be verified in practice. However it makes sense if we understand that in a generic canopy flow, the solid- phase gently waves in a coordinated way. Hence the fluid- phase is subject to strong shear layers in comparison to the solid phase. This allows to state that the macroscopic viscous term strictly reads

$$\langle \nabla \mathbf{v}_\beta \rangle^\beta +^T \langle \nabla \mathbf{v}_\beta \rangle^\beta = \left(\frac{1}{\epsilon_\beta}\nabla\epsilon_\beta + \nabla\right)\langle \mathbf{v}_\beta \rangle^\beta +^T \left[\left(\frac{1}{\epsilon_\beta}\nabla\epsilon_\beta + \nabla\right)\langle \mathbf{v}_\beta \rangle^\beta\right] + O\left(\frac{L}{L_\sigma}\right). \tag{2.2.27}$$

2.2.3 Spatial deviations

In order to separate the effects of the small and large scales, we decompose the ψ_β-field as

$$\psi_\beta = \tilde{\psi_\beta} + \langle \psi_\beta \rangle^\beta , \tag{2.2.28}$$

where $\tilde{\psi_\beta}$ is the traditional spatial deviation that we find for example in [47].

Applying decomposition 2.2.28 to the volume force $\mathbf{D}_{\beta\sigma}$ yields

$$\begin{aligned}\mathbf{D}_{\beta\sigma} =& + \frac{1}{V_\beta}\int_{\mathscr{A}_{\beta\sigma}} \mathbf{n}_{\beta\sigma}\cdot\left(-\mathbf{I}\tilde{p}_\beta + \mu_\beta\left[\nabla\tilde{\mathbf{v}}_\beta +^T (\nabla\tilde{\mathbf{v}}_\beta)\right]\right)\, dA \\ &+ \frac{1}{V_\beta}\int_{\mathscr{A}_{\beta\sigma}} \mathbf{n}_{\beta\sigma}\cdot\left(-\mathbf{I}\langle p_\beta\rangle^\beta + \mu_\beta\left[\nabla\langle\mathbf{v}_\beta\rangle^\beta +^T \left(\nabla\langle\mathbf{v}_\beta\rangle^\beta\right)\right]\right)\, dA,\end{aligned} \tag{2.2.29}$$

and we use Corollary 1 to get

$$\begin{aligned}\mathbf{D}_{\beta\sigma} =& \frac{1}{V_\beta}\int_{\mathscr{A}_{\beta\sigma}} \mathbf{n}_{\beta\sigma}\cdot\left(-\mathbf{I}\tilde{p}_\beta + \mu_\beta\left[\nabla\tilde{\mathbf{v}}_\beta +^T (\nabla\tilde{\mathbf{v}}_\beta)\right]\right)\, dA \\ &- \frac{1}{\epsilon_\beta}\nabla\epsilon_\beta\cdot\left(-\mathbf{I}\langle p_\beta\rangle^\beta + \mu_\beta\left[\nabla\langle\mathbf{v}_\beta\rangle^\beta +^T \left(\nabla\langle\mathbf{v}_\beta\rangle^\beta\right)\right]\right) + O\left(\frac{r_0}{L}\right)^2 .\end{aligned} \tag{2.2.30}$$

We develop the inertial term as

$$\langle\mathbf{v}_\beta\mathbf{v}_\beta\rangle = \left\langle\langle\mathbf{v}_\beta\rangle^\beta\langle\mathbf{v}_\beta\rangle^\beta\right\rangle + \left\langle\langle\mathbf{v}_\beta\rangle^\beta\tilde{\mathbf{v}}_\beta\right\rangle + \left\langle\tilde{\mathbf{v}}_\beta\langle\mathbf{v}_\beta\rangle^\beta\right\rangle + \langle\tilde{\mathbf{v}}_\beta\tilde{\mathbf{v}}_\beta\rangle . \tag{2.2.31}$$

Due to condition 2.1.13, the convective term reduces to

$$\nabla\cdot\langle\mathbf{v}_\beta\mathbf{v}_\beta\rangle = \nabla\cdot\left(\epsilon_\beta\langle\mathbf{v}_\beta\rangle^\beta\langle\mathbf{v}_\beta\rangle^\beta\right) + \nabla\cdot\langle\tilde{\mathbf{v}}_\beta\tilde{\mathbf{v}}_\beta\rangle + O\left(\frac{r_0}{L}\right)^2 . \tag{2.2.32}$$

Let us rewrite the first term on the right hand side of Eq. 2.2.32

$$\begin{aligned}\nabla\cdot\left(\epsilon_\beta\langle\mathbf{v}_\beta\rangle^\beta\langle\mathbf{v}_\beta\rangle^\beta\right) &= \nabla\cdot\left(\langle\mathbf{v}_\beta\rangle\langle\mathbf{v}_\beta\rangle^\beta\right) \\ &= \langle\mathbf{v}_\beta\rangle^\beta\left(\nabla\cdot\langle\mathbf{v}_\beta\rangle\right) + \langle\mathbf{v}_\beta\rangle\cdot\left(\nabla\langle\mathbf{v}_\beta\rangle^\beta\right).\end{aligned} \tag{2.2.33}$$

Now we develop the first term on the left hand side of Eq. 2.2.16

$$\begin{aligned}\frac{\partial\langle\mathbf{v}_\beta\rangle}{\partial t} &= \frac{\partial}{\partial t}\left(\epsilon_\beta\langle\mathbf{v}_\beta\rangle^\beta\right) \\ &= \frac{\partial\epsilon_\beta}{\partial t}\langle\mathbf{v}_\beta\rangle^\beta + \epsilon_\beta\frac{\partial\langle\mathbf{v}_\beta\rangle^\beta}{\partial t}.\end{aligned} \tag{2.2.34}$$

With the help of Eq. 2.2.6, the sum of Eq. 2.2.33 and 2.2.34 gives

$$\frac{\partial \langle \mathbf{v}_\beta \rangle}{\partial t} + \nabla \cdot \left(\epsilon_\beta \langle \mathbf{v}_\beta \rangle^\beta \langle \mathbf{v}_\beta \rangle^\beta \right) = \epsilon_\beta \frac{\partial \langle \mathbf{v}_\beta \rangle^\beta}{\partial t} + \langle \mathbf{v}_\beta \rangle \cdot \left(\nabla \langle \mathbf{v}_\beta \rangle^\beta \right). \tag{2.2.35}$$

With Eq. 2.2.32, we obtain that

$$\langle LHS \rangle^\beta = \frac{\partial \langle \mathbf{v}_\beta \rangle^\beta}{\partial t} + \langle \mathbf{v}_\beta \rangle^\beta \cdot \nabla \langle \mathbf{v}_\beta \rangle^\beta + \frac{1}{\epsilon_\beta} \nabla \cdot \langle \tilde{\mathbf{v}}_\beta \tilde{\mathbf{v}}_\beta \rangle + O\left(\frac{r_0}{L}\right)^2. \tag{2.2.36}$$

Note that the order of the remaining term depends on the order of Eq. 2.1.14. This shows that choosing the right kernel m directly drives the order at which the macroscopic fields converge to the volume-average fields as $\frac{r_0}{L} \to 0$. The better the order of the macroscopic equations, the faster the macroscopic fields match the volume-average fields as $\frac{r_0}{L} \to 0$, and this is helpful near the free-flow/porous medium interface (as pinpointed in Section 2.4).

We now consider three main regions

- the homogeneous porous medium,
- the free-flow,
- the interface between the two.

2.3 Homogeneous regions

In the homogeneous porous region, Corollary 2 induces that

$$\begin{aligned}
\frac{\partial \langle \mathbf{v}_\beta \rangle^\beta}{\partial t} + \langle \mathbf{v}_\beta \rangle^\beta \cdot \nabla \langle \mathbf{v}_\beta \rangle^\beta = &- \frac{1}{\rho_\beta} \nabla \langle p_\beta \rangle^\beta + \nabla \cdot \left(\frac{\mu_\beta}{\rho_\beta} \left[\nabla \langle \mathbf{v}_\beta \rangle^\beta +^T \left(\nabla \langle \mathbf{v}_\beta \rangle^\beta \right) \right] - \langle \tilde{\mathbf{v}}_\beta \tilde{\mathbf{v}}_\beta \rangle^\beta \right) \\
&+ \frac{1}{\rho_\beta} \frac{1}{V_\beta} \int_{\mathscr{A}_{\beta\sigma}} \mathbf{n}_{\beta\sigma} \cdot \left(-\mathbf{I} \tilde{p}_\beta + \mu_\beta \left[\nabla \tilde{\mathbf{v}}_\beta +^T \left(\nabla \tilde{\mathbf{v}}_\beta \right) \right] \right) dA + \mathbf{s}_\beta, \\
\nabla \cdot \langle \mathbf{v}_\beta \rangle^\beta = 0.&
\end{aligned} \tag{2.3.1}$$

2.3.1 Fluid-solid force in the homogeneous porous medium

2.3.1.1 Representative Elementary Volume

We use a Representative Elementary Volume (REV) to evaluate the fluid-solid force. Here we emphasize the fact that the role of the REV in general is to evaluate macroscopic effective properties of the porous medium.

- The REV can be either a sample of the real porous medium, or a model porous medium that mimics the real porous medium.

- The REV does not have to be as large as the AV. Indeed the AV is constrained by the LSA assumption, whereas the REV is not.

- The REV should be able to give information on the effective properties of the porous medium at the macroscopic scale. For this reason in practice the REV is often chosen cubic, while the AV is spherical for the ease of theoretical developments.

Hence we distinguish between the REV and the AV. They are two different volumes with different objectives.

2.3.1.2 Effect of the fibres confinement

It would be great if the fluid-solid force could be obtained from the sum of hydrodynamic forces applied to each fibre as if it were isolated. To evaluate this approach, we consider an array of spheres in Stokes regime. The Kozeny-Carman permeability was determined by assuming Poiseuille flow in a bundle of capillaries and introducing a correction coefficient to fit experimental data

$$K_{KC} = 180 \frac{\mu_\beta}{D^2} \frac{(1-\epsilon_\beta)^2}{\epsilon_\beta^3}, \tag{2.3.2}$$

where D is the particle diameter. The Kozeny-Carman permeability is widely used and can be considered as a reference permeability.

The Stokes drag of an isolated sphere of mass m_S is often written as

$$\mathbf{f}_{\text{Stokes}} = \gamma m_s \langle \mathbf{v}_\beta \rangle^\beta , \tag{2.3.3}$$

where γ is a constant that depends on the fluid viscosity and the sphere diameter

$$\gamma = 3\pi\mu_\beta D. \tag{2.3.4}$$

Let us assume that the fluid-solid force $\mathbf{D}_{\beta\sigma}$ in our array of spheres is due to the contribution of the Stokes drag of the N_x spheres inside the REV, as if they were isolated. This would yield

$$\frac{1}{\rho_\beta}\mathbf{D}_{\beta\sigma} = \gamma \frac{m_s N_x}{\rho_\beta V_\beta} \langle \mathbf{v}_\beta \rangle^\beta . \tag{2.3.5}$$

We rewrite

$$\frac{m_s N_x}{\rho_\beta V_\beta} = \frac{\rho_\sigma \epsilon_\sigma}{\rho_\beta \epsilon_\beta}, \tag{2.3.6}$$

where ϵ_σ is the solid volume-fraction (by definition $\epsilon_\beta + \epsilon_\sigma = 1$). We obtain a permeability K_S

$$K_S = \mu_\beta \frac{18}{D^2} \frac{1-\epsilon_\beta}{\epsilon_\beta^2} \neq K_{KC}, \tag{2.3.7}$$

by using the expression of the Stokes drag on an isolated sphere. The difference between this permeability and the Kozeny-Carman permeability shows that the spheres in our array of spheres can not be considered isolated. This is the effect of confinement. The same applies for a bundle of fibres, and we must develop a strategy to obtain the fluid-solid force depending on the spacing between fibres.

2.3.1.3 Deviation problem

We must develop a system of equations to determine the fluid-solid force. To do so, we subtract Eq. 2.3.1 from Eq. 2.1.2 and obtain

$$\begin{aligned}
\frac{\partial \tilde{\mathbf{v}}_\beta}{\partial t} + \mathbf{v}_\beta \cdot \nabla \tilde{\mathbf{v}}_\beta &= -\frac{1}{\rho_\beta} \nabla \tilde{p}_\beta + \frac{\mu_\beta}{\rho_\beta} \nabla^2 \tilde{\mathbf{v}}_\beta \\
&\quad - \frac{1}{\rho_\beta} \frac{1}{V_\beta} \int_{\mathscr{A}_{\beta\sigma}} \mathbf{n}_{\beta\sigma} \cdot \left(-\mathbf{I} \tilde{p}_\beta + \mu_\beta \left[\nabla \tilde{\mathbf{v}}_\beta + ^T \left(\nabla \tilde{\mathbf{v}}_\beta \right) \right] \right) dA \\
\nabla \cdot \tilde{\mathbf{v}}_\beta &= 0, \\
\tilde{\mathbf{v}}_\beta &= - \left\langle \mathbf{v}_\beta \right\rangle^\beta \ \ at\ \mathscr{A}_{\beta\sigma},
\end{aligned} \tag{2.3.8}$$

under the following assumptions

$$\left(\tilde{\mathbf{v}}_\beta \cdot \nabla \left\langle \mathbf{v}_\beta \right\rangle^\beta, \nabla \cdot \left\langle \tilde{\mathbf{v}}_\beta \tilde{\mathbf{v}}_\beta \right\rangle^\beta \right) \ll \mathbf{v}_\beta \cdot \nabla \tilde{\mathbf{v}}_\beta, \tag{2.3.9}$$

which is a consequence of the LSA assumption.

In Section 4, a number of studies of System 2.3.8 are reported, and we propose an investigation of this system in the steady inertial regime. To cover the range of Reynolds numbers and porosities encountered in the hybrid model, we combine data from direct numerical simulations, experiments and heuristic expressions in limit regimes to provide a metamodel of $\mathbf{D}_{\beta\sigma}$. This is developed in Section 3.3.2.3.

2.3.2 The effect of subgrid-scale stresses at the macrosocpic level

2.3.2.1 Homogeneous porous region

We focus on the term

$$\nabla \cdot \left\langle \tilde{\mathbf{v}}_\beta \tilde{\mathbf{v}}_\beta \right\rangle^\beta, \tag{2.3.10}$$

in Eq. 2.3.1. The $\langle \tilde{\mathbf{v}}_\beta \tilde{\mathbf{v}}_\beta \rangle^\beta$ term is called the subgrid-scale stresses (SGS) in the Large Eddy Simulation (LES) community. We adopt the SGS term here. Written as such, the SGS are a bit difficult to understand. For an easier interpretation, we can rewrite

$$\nabla \cdot \langle \tilde{\mathbf{v}}_\beta \tilde{\mathbf{v}}_\beta \rangle^\beta = \frac{1}{V_\beta} \int_{\mathscr{A}_{\beta e}} \left(\mathbf{n}_{\beta e} \cdot \tilde{\mathbf{v}}_\beta \right) \tilde{\mathbf{v}}_\beta \, dA, \tag{2.3.11}$$

which shows that the divergence of SGS is in fact the net flux of momentum advected inside the AV by the $\tilde{\mathbf{v}}_\beta$- field, which represents the unresolved flow field. The *grid* size is determined by the dimension r_0 of the AV in the porous medium, and by dx the computational mesh cell size in the free-flow. Here we try to give an estimate of the flux of momentum through the AV due to the SGS in turbulent regime, inspired by the discussion in [28]. Of course this development deserves further justification and some assumptions might be sometimes questionable. We parametrize the time-average flux of momentum due to the SGS as

$$\nabla \cdot \overline{\langle \tilde{\mathbf{v}}_\beta \tilde{\mathbf{v}}_\beta \rangle^\beta} \sim \frac{1}{V_\beta} \tilde{q} \Delta_{\mathrm{AV}}(\tilde{v}), \tag{2.3.12}$$

where $\Delta_{\mathrm{AV}}(\tilde{v})$ characterizes the variation of $\tilde{\mathbf{v}}_\beta$ over the AV, and $\tilde{q}$ is the flow rate due to $\tilde{\mathbf{v}}_\beta$ through the AV in the direction orthogonal to the macroscopic flow. With this parametrization, we state that there are two necessary conditions for the flux of momentum due to the SGS to be non-zero [48]. The first condition is that an intermittent flow rate in the direction orthogonal to the mean flow occur, *i.e.* we lie in the turbulent regime. The second condition is that the macroscopic flow field is sheared. A sheared macroscopic flow field in turbulent regime may be obtained either by forcing the flow near a wall or an interface, or from macroscopic eddies (coherent structures) in a homogeneous region. We can estimate the flux of momentum due to the SGS through the AV in a homogeneous region. We recall the boundary condition

$$\tilde{\mathbf{v}}_\beta = - \langle \mathbf{v}_\beta \rangle^\beta \text{ at } \mathscr{A}_{\beta\sigma}, \tag{2.3.13}$$

and this suggests that

$$\Delta_{\mathrm{AV}}(\tilde{v}) \sim r_0 \nabla v, \tag{2.3.14}$$

where v is the magnitude of $\langle \mathbf{v}_\beta \rangle^\beta$. To estimate $\tilde{q}$, we need to pinpoint the mechanism that generates a net small-scale flow rate in the direction transverse to the macroscopic flow. For that kind of issue, direct numerical simulations in porous media is essential. Direct numerical simulations were conducted in [34, 49] to investigate the nature of turbulence in model porous media made of tube arrays. It suggest that the largest eddies in a homogeneous porous medium are constrained by l_β the characteristic pore space, and that the cylinder diameter is the main length-scale of turbulence in a homogeneous tube array.

Assumption 6 *The net time-average flow rate $\tilde{q}$ through the AV in turbulent regime is due the largest eddies, that are produced in the wake of each cylinders.*

The Strouhal number

$$S_t = \frac{f_w D}{v}, \tag{2.3.15}$$

compares the main wake frequency f_w to the advection time. For a circular cylinder, S_t lies around 0.2 on a wide range of Reynolds number (until $Re_D < 10^{+5}$, [50]). One could wonder if the value of S_t is the same in an array of fibres. This was not deeply investigated here, so we simply assume that the value of the Strouhal number in our bundle of fibres lies around 0.2, hence that $\tilde{q}$ can be estimated as

$$\tilde{q} \sim 0.2 A_{\beta e} v. \tag{2.3.16}$$

This yields

$$\nabla \cdot \langle \tilde{\mathbf{v}}_\beta \tilde{\mathbf{v}}_\beta \rangle^\beta \sim \underbrace{\frac{A_{\beta e}}{V_\beta} r_0}_{\sim 1 \text{ if } 1-\epsilon_\beta \ll 1} \frac{0.2 v}{v} \frac{v^2}{L}. \tag{2.3.17}$$

Finally we have that

$$\nabla \cdot \overline{\langle \tilde{\mathbf{v}}_\beta \tilde{\mathbf{v}}_\beta \rangle^\beta} \sim 0.2 \frac{v^2}{L}. \tag{2.3.18}$$

In quadratic regime, we approximate the fluid-solid force as

$$\frac{1}{\rho_\beta} D_{\beta\sigma} \sim \frac{\nu_\beta}{l_\beta^2} v Re_l, \tag{2.3.19}$$

where

$$Re_l = \frac{l_\beta v}{\nu_\beta}. \tag{2.3.20}$$

We therefore compare

$$\frac{\nabla \cdot \langle \tilde{\mathbf{v}}_\beta \tilde{\mathbf{v}}_\beta \rangle^\beta}{\frac{1}{\rho_\beta} D_{\beta\sigma}} \sim 0.2 \frac{l_\beta}{L}, \tag{2.3.21}$$

i.e. in the homogeneous porous region where the LSA assumption is valid, the net flux of momentum through the AV due to the subgrid-scale stresses (SGS) is small compared to the fluid-solid force.

2.3.2.2 Free flow region

In a free flow there is no solid phase ($\mathscr{A}_{\beta\sigma} = \emptyset$) and we recover the equations used in large-eddy simulations (LES) equations. The only remaining unclosed terms are the subgrid-scale stresses (SGS), corresponding to a space filter of cutting length dx (implicit filtering, [51]). In [28], Breugem studies the influence of wall permeability in turbulent channel flow. He neglects the influence of the SGS in the VANS in the free flow region, and the results compare well with direct numerical simulations, but this is obtained at a large computational cost (due to a fine mesh). To understand this, a development to estimate the SGS can be conducted. In the free flow region, the net flow rate $\tilde{q}$ is due to the largest eddies of size dx the size of the cell, and of orbital velocity $\tilde{v}$. Studies of canopies in nature [6, 9] emphasize the large scale coherent structures appearing in a canopy flow. This suggests that in the turbulent regime, the free-flow over a canopy consists of eddies of different sizes, namely

- macroscopic eddies, coherent structures of size L that extract energy from the free flow, and
- pore-scale eddies, of size l_β typically produced in the fibres' wakes, and
- dissipation eddies, of size δ the Kolmogorov scale, related to the viscous dissipation.

As proposed by Richardson in [52], in steady state the kinetic energy of the flow is transferred from the largest eddies to the smallest one where it is dissipated. This energy cascade can be illustrated by

$$L \to dx \to \delta. \tag{2.3.22}$$

We can rewrite Eq. 2.3.17 in the free-flow region as

$$\nabla \cdot \langle \tilde{\mathbf{v}}_\beta \tilde{\mathbf{v}}_\beta \rangle^\beta \sim \frac{\tilde{v}}{v} \frac{v^2}{L}. \tag{2.3.23}$$

To estimate the ratio $\frac{\tilde{v}}{v}$ in the free flow, we assume that the eddies know how big they are, and at which rate energy is supplied to them. Moreover as we are in steady state, the rate of energy supplied to any eddy is the same, and balances the rate of energy dissipated by the smallest eddies (no accumulation of energy). Let R_k be the energy dissipated by the fluid viscosity, per unit mass and time. The orbital velocity of eddies of size L scales as

$$v \sim (R_k L)^{1/3}, \tag{2.3.24}$$

and the orbital velocity of eddies of size dx scales as

$$\tilde{v} \sim (R_k dx)^{1/3}. \tag{2.3.25}$$

This allows to estimate the ratio

$$\frac{\tilde{v}}{v} \sim \left(\frac{dx}{L}\right)^{1/3}. \tag{2.3.26}$$

This yields

$$\nabla \cdot \langle \tilde{\mathbf{v}}_\beta \tilde{\mathbf{v}}_\beta \rangle^\beta \sim \left(\frac{dx}{L}\right)^{1/3} \frac{v^2}{L}, \tag{2.3.27}$$

i.e.

$$\nabla \cdot \langle \tilde{\mathbf{v}}_\beta \tilde{\mathbf{v}}_\beta \rangle^\beta \sim \left(\frac{dx}{L} \right)^{1/3} \langle \mathbf{v}_\beta \rangle^\beta \cdot \nabla \langle \mathbf{v}_\beta \rangle^\beta \,, \tag{2.3.28}$$

in the free flow region. Hence in the homogeneous free-flow region it is difficult to neglect the effect of the SGS in the VANS. We could resolve the Navier-Stokes equations with a fine enough mesh to make sure that the SGS are negligible but this would require too many mesh points. In order to keep the mesh size tractable, we can make use of a model [51] for the SGS in the free-flow region. Subgrid-scale modeling aims at representing the effects of unresolved small-scale fluid motions (small eddies and vortices) in the equations governing the large-scale motions that are resolved in a macroscopic model. The formulation of a physically realistic subgrid-scale model requires insight on the physics of the interaction among different scales in turbulent flow. It is still an open research question. However some models exist that at the very least afford to incorporate a physically meaningful impact of the subgrid-scale flow on the large scale flow. For instance intuitively turbulence enhances the mixing rate in a shear flow, and this translates into an increased momentum transfer, often modeled as an increased effective viscosity for the large-scale flow. Such models are available in Open∇FOAM®, such as the Smagorinsky-Lilly model [53].

For now the discussion deals with homogeneous regions, which allows for simplifying assumptions such as the scale-separation assumption. As is discussed in next section, the situation near a wall or an interface requires more care, because

- volume-averaged velocity gradients become large, and
- the length scale separation assumption collapses, and
- porosity gradients are not well-defined, and
- the nature of the SGS lies in-between the homogeneous free-flow view and the homogeneous porous medium view.

A particular approach is needed in order to clearly understand the handling of the interface.

2.4 Free-flow/porous medium interface

The free-flow/porous medium interface is a key region where the flow above the porous medium exchanges with the flow inside the porous medium. For example [54] proposes a study of heat exchange at the interface between a porous medium and a free-flow. This study shows the development of large scale vortices at the interface, which enhance the heat transfer, and have an impact deep inside the porous medium in terms of temperature fluctuations. In our case we are rather concerned with the exchange of mass and momentum but the issue is the same, we need to model how the free-flow exchanges with the flow inside the porous region through the interface. Hence to obtain a good description of the porous medium/free-flow coupling, we should describe this region with great care and have a clear understanding of the assumptions made to develop our macroscopic model at the interface region.

2.4.1 Issues at the interface

From a microscopic point of view at the boundary of a porous medium [55], the fluid in the free flow is expected to see both pores and solid parts. The fluid velocity in the pores and the solid- phase velocity at the interface matches with the fluid velocity in the free flow (no-slip condition). Moreover we have continuity of the stress tensor over the pore- and solid- sections. In the homogeneous porous medium (ω-region, see Fig.2.3), we resolve transport equations (VANS) that are valid under Assumption 2, as well as the LSA assumption. At the boundary between the ω-region and the free-flow (η-region, see Fig.2.3), two main events occur.

- Large gradients in volume averaged quantities occur. The LSA assumption collapses, the remaining term in Eq. 2.2.36 becomes large, and the system of Eqs. 2.3.8 can not be written as such.
- The porous medium geometry encounters significant changes. Therefore, Conditions 2.1.7 and 2.1.13 can not be satisfied as in the homogeneous porous medium.

As the consistency of the VANS falls down at the interface, the macroscopic fields certainly do not match the volume-average fields in the interface region. Our objective however is that the macroscopic fields recover the volume-average fields at least in homogeneous regions. In other words, we must constrain the macroscopic fields inside the interface region (or within an ad-hoc transition region), so that it matches the volume-average fields in homogeneous regions. To achieve this, we start with a short discussion of existing solutions. Then, we propose a mass and momentum balance at the interface, which leads us to think that the interface can be treated by an adequate space varying source term in the VANS.

2.4.2 Short review of existing solutions

Different approaches are available to connect the free flow and the porous medium at a fluid/porous interface. The one-domain approach (ODA) considers the whole domain as a continuum with effective transport coefficients [56]. In this approach, the transition from the free flow to the porous medium is considered as a transition of properties such as permeability and porosity. This change in effective properties can be determined through the resolution of a closure problem. An advantage of the ODA is that it avoids an explicit formulation of matching conditions at the fluid/porous medium inter-region, as well as the imposition of a particular boundary condition at the fluid/porous interface. However the ODA amounts to considering a mesoscopic model (a model for the volume-average fields in the interface region), whose validity at the interface is not clear. Typically, such models often involve porosity gradients, that are not well-defined at the interface, as they directly depend on the size of the AV.

A second type of approach is called the two-domain approach (TDA), that model the porous medium and the fluid separately and connect them via boundary conditions, such that the effective behaviour (*i.e.* the macroscopic fields match the volume-average fields) in homogeneous regions is recovered. This results in particular matching- (or jump-) boundary conditions. The jump conditions are expressed in terms of effective coefficients, which depend on the microscopic nature of the inter-region, as well as the flow regime under study. In [57] for example, Beavers and Joseph impose a slip velocity which grows proportionally to the transverse gradient of longitudinal velocity in the η-region (Navier condition). In this study, experiments with different porous media are conducted to measure the Navier length, which is found to vary by a factor of 40 according to the porous medium. Hence the effective coefficient strongly depends on the structural characteristics of the porous medium, and a better parametrization should be found to determine the jump condition.

A more systematic approach is proposed in [58] to determine the jump condition. Here, a volume averaging approach is implemented to identify boundary conditions as corrections to the ω- and η-macroscopic fields, introducing a jump in stress at the interface expressed by

$$\epsilon_\beta^{-1} \frac{\partial}{\partial y} \langle u \rangle_\omega^\beta - \frac{\partial}{\partial y} \langle u \rangle_\eta^\beta = \frac{\chi}{K^{1/2}} \langle u \rangle_\omega^\beta \,, \tag{2.4.1}$$

where u is the tangential component of the velocity. Let us call v the normal component. Eq. 2.4.1 introduces a dimensionless parameter χ whose value is determined by fitting the data of Beavers and Joseph in [57]. This approach appears to give a more accurate and physically meaningful scaling than the previous one since the fitting parameter χ is less dependent on the tested porous media. Much research effort has been spent thereafter to find a way to compute the fitting parameter afterwards ([59, 60, 61, 62, 63]), including the writing of a closure problem at the interface in order to compute the effective coefficient of the jump condition.

We could say that the TDA is based on the ODA. Indeed, a TDA often uses an ODA to compute or derive the matching conditions. Therefore in both the ODA and the TDA, the main issue is the use of a mesoscopic model at the interface, with the issue that porosity gradients are not intrinsic as

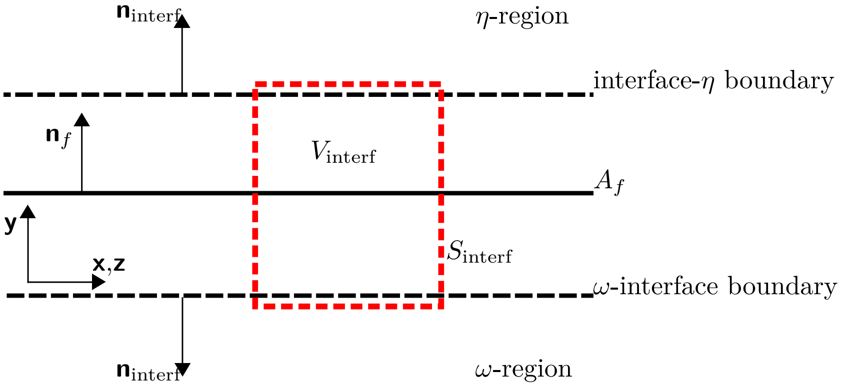

Figure 2.3: Details at the interface. The ω-region and η-region refer to the homogeneous porous- and free-flow region, respectively. V_{interf} is the region of space or control volume delimited by S_{interf}, within which the macroscopic fields do not match the volume-average ones. A_f is a fictitious surface that lies within V_{interf}. V_{interf} and A_f are useful for the purpose of deriving the large-scale balance at the fluid/porous interface.

they depend on the size of the AV, and Assumption 2 and LSA that collapse at the interface. In the following we aim to bring some theoretical clarification to this issue.

2.4.3 Balance at the interface

We follow the idea of a mass and momentum balance at the interface, at a scale larger than the AV. This approach is similar to the development presented in [41], with some conceptual differences that we find interesting to discuss, and that is why we provide a complete development of our ODA interface condition. For example it remains that the size and position of the interface region is to be determined, but we demonstrate what length-scale conditions should be satisfied for that purpose.

2.4.3.1 Theoretical development

To overcome the previously mentioned issues related to the use of a mesoscopic model at the interface, we express the balance of mass and momentum at the interface, relying on partially averaged transport equations that are unconditionally valid. Such equations (Eqs. 2.2.16) were derived in Section 2.2.2.1 without any length-scale assumptions. Let V_{interf} be a control volume on the interface, of dimensions (l_x, l_y, l_z) such that $l_y \gg l_x, l_z$, and delimited by the surface S_{interf}. We introduce $\mathbf{F}_{\beta\sigma}$ defined as

$$\mathbf{F}_{\beta\sigma} = \epsilon_\beta \mathbf{D}_{\beta\sigma} = +\frac{1}{V}\int_{\mathscr{A}_{\beta\sigma}} \mathbf{n}_{\beta\sigma} \cdot \left(-\mathbf{I}p_\beta + \mu_\beta \left[\nabla \mathbf{v}_\beta +^T (\nabla \mathbf{v}_\beta)\right]\right) dA. \tag{2.4.2}$$

In order to obtain the momentum balance over the interface, we take the volume integral of Eq. 2.2.16 over V_{interf}. For the sake of simplicity, we set $\mathbf{s}_\beta = 0$. This yields

$$\int_{V_{\text{interf}}} \mathbf{F}_{\beta\sigma}\, dV = \int_{V_{\text{interf}}} \left(\rho_\beta \left(\frac{\partial \langle \mathbf{v}_\beta \rangle}{\partial t} + \nabla \cdot \langle \mathbf{v}_\beta \mathbf{v}_\beta \rangle \right) - \nabla \cdot \left\langle -\mathbf{I} p_\beta + \mu_\beta \left[\nabla \mathbf{v}_\beta +^T (\nabla \mathbf{v}_\beta) \right] \right\rangle \right) dV, \tag{2.4.3}$$

which we can re-organize as

$$\int_{V_{\text{interf}}} \mathbf{F}_{\beta\sigma}\, dV = \int_{V_{\text{interf}}} \left(\rho_\beta \frac{\partial \langle \mathbf{v}_\beta \rangle}{\partial t} + \nabla \cdot \left(\underbrace{\rho_\beta \langle \mathbf{v}_\beta \mathbf{v}_\beta \rangle - \left\langle \mu_\beta \left[\nabla \mathbf{v}_\beta +^T (\nabla \mathbf{v}_\beta) \right] \right\rangle}_{\mathbf{T}} + \mathbf{I} \langle p_\beta \rangle \right) \right) dV. \tag{2.4.4}$$

We will then apply the Green-Ostrogradski theorem, which states that

$$\int_{V_{\text{interf}}} \nabla \cdot \mathbf{T}\, dV = \int_{S_{\text{interf}}} \mathbf{n}_{\text{interf}} \cdot \mathbf{T}\, dA, \tag{2.4.5}$$

where $\mathbf{n}_{\text{interf}}$ is the normal unit vector pointing outside V_{interf} (Fig. 2.3).

Similarly to Assumption 1, we assume that the porous medium is disordered in the directions tangential to the interface. This allows to simplify the problem by assuming that the $\mathbf{T}$-field and $\nabla \langle p_\beta \rangle$-field are invariant in the x and z directions, the two directions tangential to the interface. This is similar to a *boundary layer* assumption, *i.e.* we assume that normal gradients are much larger than tangential gradients. This leads to

$$\begin{aligned} \int_{V_{\text{interf}}} \nabla \cdot (\mathbf{T} + \mathbf{I} \langle p_\beta \rangle)\, dV =& \int_{l_y} \nabla \cdot (\mathbf{T} + \mathbf{I} \langle p_\beta \rangle)\, dy l_x l_z \\ =& \mathbf{n}_f \cdot \Big((\mathbf{T}_\eta - \mathbf{T}_\omega) + \mathbf{I} \left(\langle p_\beta \rangle_\eta - \langle p_\beta \rangle_\omega \right) \Big) l_x l_z \\ &+ \int_{l_y} (\mathbf{I} - \mathbf{n}_f \mathbf{n}_f) \cdot \nabla \langle p_\beta \rangle\, dy l_x l_z, \end{aligned} \tag{2.4.6}$$

where $\mathbf{n}_f$ is the normal unit vector pointing outside the homogeneous porous region (see Fig. 2.3), and we use the fact that $l_y \gg l_x, l_z$. Moreover we recall that for any C^2 field ψ on R^3

$$\frac{\partial^2 \psi}{\partial y \partial x} = \frac{\partial^2 \psi}{\partial x \partial y}, \text{ and } \frac{\partial^2 \psi}{\partial y \partial z} = \frac{\partial^2 \psi}{\partial z \partial y}, \tag{2.4.7}$$

(Clairaut's theorem). Hence the tangential pressure gradient $(\mathbf{I} - \mathbf{n}_f \mathbf{n}_f) \cdot \nabla \langle p_\beta \rangle$ is constant in the y direction. As a consequence

$$\int_{l_y} (\mathbf{I} - \mathbf{n}_f \mathbf{n}_f) \cdot \nabla \langle p_\beta \rangle\, dy = l_y (\mathbf{I} - \mathbf{n}_f \mathbf{n}_f) \cdot \nabla \langle p_\beta \rangle. \tag{2.4.8}$$

By construction, V_{interf} is such that its top and bottom regions lie in homogeneous regions (see Fig. 2.3).

As shown in Section 2.3, in both homogeneous regions we have

$$\mathbf{T}_{(\eta \text{ or } \omega)} = \rho_\beta \left\langle \mathbf{v}_\beta \right\rangle \left\langle \mathbf{v}_\beta \right\rangle^\beta - \epsilon_\beta \mu_\beta \left(\nabla \left\langle \mathbf{v}_\beta \right\rangle^\beta +^T \left(\nabla \left\langle \mathbf{v}_\beta \right\rangle^\beta \right) \right) + \epsilon_\beta \rho_\beta \left\langle \tilde{\mathbf{v}}_\beta \tilde{\mathbf{v}}_\beta \right\rangle^\beta . \tag{2.4.9}$$

We obtain one equation for the tangential direction and another one for the normal direction:

$$\begin{aligned}
\int_{l_y} \left(\mathbf{I} - \mathbf{n}_f \mathbf{n}_f \right) \cdot \mathbf{F}_{\beta\sigma} \, dy = & \int_{l_y} \epsilon_\beta \rho_\beta \left(\mathbf{I} - \mathbf{n}_f \mathbf{n}_f \right) \cdot \frac{\partial \left\langle \mathbf{v}_\beta \right\rangle^\beta}{\partial t} \, dy \\
& + \underbrace{\mathbf{n}_f \cdot \left[\rho_\beta \left(\left\langle \mathbf{v}_\beta \right\rangle^\beta \left\langle \mathbf{v}_\beta \right\rangle^\beta \right)_\eta - \epsilon_\beta \left(\rho_\beta \left\langle \mathbf{v}_\beta \right\rangle^\beta \left\langle \mathbf{v}_\beta \right\rangle^\beta \right)_\omega \right]}_{\text{advective jump}} \\
& + \underbrace{\mathbf{n}_f \cdot \left[\rho_\beta \left(\left(\left\langle \tilde{\mathbf{v}}_\beta \tilde{\mathbf{v}}_\beta \right\rangle^\beta \right)_\eta - \epsilon_\beta \left(\left\langle \tilde{\mathbf{v}}_\beta \tilde{\mathbf{v}}_\beta \right\rangle^\beta \right)_\omega \right) \right]}_{\text{SGS jump}} \\
& - \underbrace{\mathbf{n}_f \cdot \left[\mu_\beta \left(\nabla \left\langle \mathbf{v}_\beta \right\rangle^\beta +^T \left(\nabla \left\langle \mathbf{v}_\beta \right\rangle^\beta \right) \right)_\eta - \epsilon_\beta \mu_\beta \left(\nabla \left\langle \mathbf{v}_\beta \right\rangle^\beta +^T \left(\nabla \left\langle \mathbf{v}_\beta \right\rangle^\beta \right) \right)_\omega \right]}_{\text{tangential stress jump}} \\
& + \left(\mathbf{I} - \mathbf{n}_f \mathbf{n}_f \right) \cdot \nabla \left\langle p_\beta \right\rangle l_y , \\
\int_{l_y} \mathbf{n}_f \cdot \mathbf{F}_{\beta\sigma} \, dy = & \int_{l_y} \epsilon_\beta \rho_\beta \mathbf{n}_f \cdot \frac{\partial \left\langle \mathbf{v}_\beta \right\rangle^\beta}{\partial t} \, dy + \underbrace{\mathbf{n}_f \left(\left\langle p_\beta \right\rangle_\eta - \left\langle p_\beta \right\rangle_\omega \right)}_{\text{normal stress jump}} .
\end{aligned} \tag{2.4.10}$$

Doing the same development with Eq. 2.2.6 yields

$$\mathbf{n}_f \cdot \left\langle \mathbf{v}_\beta \right\rangle_\eta - \mathbf{n}_f \cdot \left\langle \mathbf{v}_\beta \right\rangle_\omega + \int_{\text{interf}} \frac{\partial \epsilon_\beta}{\partial t} \, dy = 0. \tag{2.4.11}$$

We consider that the interface is a thin layer, that only transfers mass, and either destroys or transfers momentum. In other words, the interface region does not accumulate mass or momentum. Hence we assume steadiness in the following. We decompose the macroscopic velocity into a tangential- and a normal- component

$$\left\langle \mathbf{v}_\beta \right\rangle^\beta = \left\langle \mathbf{u} \right\rangle^\beta + \left\langle v \right\rangle^\beta \mathbf{n}_f , \tag{2.4.12}$$

and this yields

$$
\begin{aligned}
(\mathbf{I}-\mathbf{n}_f\mathbf{n}_f)\cdot\left[\int_{\text{interf}}\mathbf{F}_{\beta\sigma}\,dy-\nabla\left\langle p_\beta\right\rangle l_y\right] &= \underbrace{\rho_\beta\left\langle v\right\rangle_\eta\left(\left\langle\mathbf{u}\right\rangle^\beta_\eta-\left\langle\mathbf{u}\right\rangle^\beta_\omega\right)}_{\text{advective jump}}+\underbrace{\rho_\beta\left(\left\langle\tilde{\mathbf{u}}_\beta\tilde{v}_\beta\right\rangle^\beta_\eta-\epsilon_\beta\left\langle\tilde{\mathbf{u}}_\beta\tilde{v}_\beta\right\rangle^\beta_\omega\right)}_{\text{SGS jump}}\\
&\quad+\underbrace{\mu_\beta\left(\epsilon_\beta\frac{\partial}{\partial y}\left\langle\mathbf{u}\right\rangle^\beta_\omega-\frac{\partial}{\partial y}\left\langle\mathbf{u}\right\rangle^\beta_\eta\right)}_{\text{tangential stress jump}},\\
\mathbf{n}_f\cdot\int_{\text{interf}}\mathbf{F}_{\beta\sigma}\,dy &= \underbrace{\left\langle p_\beta\right\rangle_\eta-\left\langle p_\beta\right\rangle_\omega}_{\text{normal stress jump}},\\
\left\langle v\right\rangle_\eta &= \left\langle v\right\rangle_\omega .
\end{aligned}
\tag{2.4.13}
$$

This gives an interpretation of the stress-jump expressed in Eq. 2.4.1, which was developed for low Reynolds numbers and a rigid porous medium. In particular we identify

$$
\frac{\epsilon_\beta\mu_\beta}{l_y}\frac{\chi}{K^{1/2}}\left\langle\mathbf{u}\right\rangle^\beta_\omega=(\mathbf{I}-\mathbf{n}_f\mathbf{n}_f)\cdot\left[\frac{1}{l_y}\int_{\text{interf}}\mathbf{F}_{\beta\sigma}\,dy-\nabla\left\langle p_\beta\right\rangle\right]. \tag{2.4.14}
$$

This is interesting because our approach provides a way to recover this well-known jump condition.

Regarding the general case expressed by Eqs. 2.4.13, strictly speaking we should choose a volume V_{interf} at the interface, and resolve a closure problem on it. This closure problem would in fact be a direct numerical simulation, that would yield the term $\int_{\text{interf}}\mathbf{F}_{\beta\sigma}\,dy$, as well as the SGS jump term in Eq. 2.4.13, depending on the flow conditions (Reynolds number, shear rate) and the shape of the porous medium at the interface. Boundary conditions for this closure problem would be macroscopic boundary conditions on the two surfaces that lie in the ω- and η- regions, in addition to periodic boundary conditions in the two tangential directions. The obtained $\int_{\text{interf}}\mathbf{F}_{\beta\sigma}\,dy$- and SGS jump-terms would then provide a jump condition to impose to the macroscopic fields $\left\langle\mathbf{v}_\beta\right\rangle^\beta$ and $\left\langle p_\beta\right\rangle^\beta$ at the fluid/porous interface (TDA). This approach is the most satisfying from a physical point of view, but requires a heavy computational effort. Many flow conditions need to be tested depending on the case under study. Instead, we propose an asymptotic approach that allows to handle the fluid/porous interface with a continuous source term (ODA). A simple closure is then proposed to allow the numerical implementation, highlighting the source of errors and where research efforts should be spent to improve the condition at the fluid/porous interface.

2.4.3.2 Asymptotic interface condition

Let ζ be any macroscopic field. We impose continuity of the ζ-field at the $\eta-\omega$ interface, and suppose that the ζ-field matches the corresponding volume-average field in the homogeneous regions. We still consider a volume V_{interf}. Let $y = y_i$ be the center of V_{interf}. Let ζ^+ and ζ^- be the values of ζ on top and bottom of V_{interf}, respectively. We evaluate ζ^+ and ζ^- by Taylor expansions from $y = y_i$ the center of V_{interf}. We set the origin $y = 0$ at the bottom of V_{interf}, and define α such as $y_i = \alpha l_y$. We obtain

$$\begin{aligned} \zeta^- &= \zeta_i - \left(\frac{\partial}{\partial y}\zeta\right)_i \alpha l_y + O\left(\frac{l_y}{l_\zeta}\right)^2, \\ \zeta^+ &= \zeta_i + \left(\frac{\partial}{\partial y}\zeta\right)_i (1-\alpha) l_y + O\left(\frac{l_y}{l_\zeta}\right)^2, \end{aligned} \tag{2.4.15}$$

where the $\bullet_i$ subscript refers to the value of the ζ- field at $y = y_i$, and l_ζ characterizes the variation of the macroscopic ζ-field in the direction normal to the interface. Clearly we need

$$l_y \ll l_\zeta, \tag{2.4.16}$$

for Eq. 2.4.15 to be acceptable. Here we emphasize the fact that the ζ-field is a *macroscopic* field, not a volume-average field. As a macroscopic field, the ζ-field is well-defined at the interface, and is subject to much lower gradients than a volume-average field at the interface. The fact that the ζ-field is a *macroscopic* field makes assumption 2.4.16 acceptable, in addition to the fact that l_y should be chosen as small as possible. Also, l_y should be large enough so that ζ^+ and ζ^- match the volume-average field. This implies that ζ^+ and ζ^- must lie in homogeneous regions, and this requires them to be far enough from the interface region. The severity of the "far enough" condition depends on the rate of convergence of the macroscopic model to the volume-average fields. This is where the order of Eq. 2.2.36 plays a significant role. As we move away from the interface, the $\frac{r_0}{L}$ term goes to zero, making the macroscopic fields converge to the volume-average ones. Hence the larger the order of the remaining term, the smaller the acceptable l_y, so that Eq. 2.4.15 is acceptable.

If the expansions of the macroscopic fields match the volume-average fields in the homogeneous regions, the different terms in Eq. 2.4.13 take the form

$$\begin{gathered}
\underbrace{\rho_\beta \left\langle v \right\rangle_i \left(\left\langle \mathbf{u} \right\rangle_i^\beta + \left(\frac{\partial}{\partial y} \left\langle \mathbf{u} \right\rangle^\beta \right)_i (1-\alpha) l_y - \left(\left\langle \mathbf{u} \right\rangle_i^\beta - \left(\frac{\partial}{\partial y} \left\langle \mathbf{u} \right\rangle^\beta \right)_i \alpha l_y \right) \right)}_{\text{advective jump}}, \\
\underbrace{\rho_\beta \left(\left\langle \tilde{\mathbf{u}}_\beta \tilde{v}_\beta \right\rangle_i^\beta + \left(\frac{\partial}{\partial y} \left\langle \tilde{\mathbf{u}}_\beta \tilde{v}_\beta \right\rangle^\beta \right)_i (1-\alpha) l_y - \left(\left\langle \tilde{\mathbf{u}}_\beta \tilde{v}_\beta \right\rangle_i^\beta - \left(\frac{\partial}{\partial y} \left\langle \tilde{\mathbf{u}}_\beta \tilde{v}_\beta \right\rangle^\beta \right)_i \alpha l_y \right) \right)}_{\text{SGS jump}}, \\
\underbrace{-\mu_\beta \left(\frac{\partial}{\partial y} \left\langle \mathbf{u} \right\rangle_i^\beta + \left(\frac{\partial^2}{\partial y^2} \left\langle \mathbf{u} \right\rangle^\beta \right)_i (1-\alpha) l_y + \epsilon_\beta \left(\frac{\partial}{\partial y} \left\langle \mathbf{u} \right\rangle_i^\beta - \left(\frac{\partial^2}{\partial y^2} \left\langle \mathbf{u} \right\rangle^\beta \right)_i \alpha l_y \right) \right)}_{\text{tangential stress jump}}, \\
\underbrace{\left(\left\langle p_\beta \right\rangle_i + \left(\frac{\partial}{\partial y} \left\langle p_\beta \right\rangle \right)_i (1-\alpha) l y \right) - \left(\left\langle p_\beta \right\rangle_i - \left(\frac{\partial}{\partial y} \left\langle p_\beta \right\rangle \right)_i \alpha l_y \right)}_{\text{normal stress jump}}.
\end{gathered} \tag{2.4.17}$$

Let y_i be a point inside the interface region. Considering a volume V_{interf} centered on y_i, in the context $1 - \epsilon_\beta \ll 1$ we obtain

$$\begin{aligned}
(\mathbf{I} - \mathbf{n}_f \mathbf{n}_f) \cdot \left[\frac{1}{l_y} \int_{\text{interf}} \mathbf{F}_{\beta\sigma} \, dy - \nabla \left\langle p_\beta \right\rangle \right]_{y_i} &= \rho_\beta \left\langle v \right\rangle_i^\beta \left(\frac{\partial}{\partial y} \left\langle \mathbf{u} \right\rangle^\beta \right)_{y_i} - \mu_\beta \left(\frac{\partial^2}{\partial y^2} \left\langle \mathbf{u} \right\rangle^\beta \right)_{y_i} \\
&\quad + \rho_\beta \left(\frac{\partial}{\partial y} \left\langle \tilde{\mathbf{u}}_\beta \tilde{v}_\beta \right\rangle^\beta \right)_{y_i}, \\
\mathbf{n}_f \cdot \left[\frac{1}{l_y} \int_{\text{interf}} \mathbf{F}_{\beta\sigma} \, dy - \nabla \left\langle p_\beta \right\rangle \right]_{y_i} &= 0, \\
\left(\frac{\partial}{\partial y} \left\langle v \right\rangle \right)_{y_i} &= 0.
\end{aligned} \tag{2.4.18}$$

Eq. 2.4.18 is valid for any y_i within the interface. This shows that the interface between the free-flow and the porous medium can be handled via continuity of macroscopic quantities, provided a space variable source term $\mathbf{f}_{\text{interf}}$ in the macroscopic equations (One-Domain-Approach). This space variable source term is explicitly given by

$$\left(\mathbf{f}_{\text{interf}} \right)_{y_i} = \frac{1}{l_y} \int_{\text{interf}} \mathbf{F}_{\beta\sigma} \, dy. \tag{2.4.19}$$

$\mathbf{f}_{\text{interf}}$ results from a *double-averaging* operation. Indeed $\mathbf{F}_{\beta\sigma}$ is obtained by surface-integration of the fluid-stress over $\mathscr{A}_{\beta\sigma}$ within the regular AV (see Eq. 2.2.17), and is then space-averaged at a larger scale over V_{interf} in the direction normal to the fluid/porous interface to obtain $\mathbf{f}_{\text{interf}}$. We recall that V_{interf} should be chosen large enough so that its top- and bottom- part lie in a homogeneous region (whether it is the free-flow or the porous medium), and small enough so that evaluation 2.4.15 remains reasonable. These two conditions should be used in practice to determine V_{interf} on a real case, although it is not an obvious task and remains an ongoing research topic.

Note that we could think that the $\left(\frac{\partial}{\partial y}\left\langle\tilde{\mathbf{u}}_\beta\tilde{v}_\beta\right\rangle^\beta\right)_{y_i}$ term in Eq. 2.4.18 is not closed, as it involves the microscopic flow field at the fluid/porous interface. Actually the $\left(\frac{\partial}{\partial y}\left\langle\tilde{\mathbf{u}}_\beta\tilde{v}_\beta\right\rangle^\beta\right)_{y_i}$ term is closed. Indeed, we should remind that in our macroscopic model, this term was closed with a subgrid-scale (SGS) model, that depends on the macroscopic velocity fields. Therefore in Eq. 2.4.18, the $\left(\frac{\partial}{\partial y}\left\langle\tilde{\mathbf{u}}_\beta\tilde{v}_\beta\right\rangle^\beta\right)_{y_i}$ term should be seen as closed by a SGS model (*e.g.* the Smagorinsky-Lilly model).

2.4.3.3 Closure

We now propose a rough way to evaluate $\mathbf{f}_{\text{interf}}$, that will be eventually implemented in the macroscopic code (see Chapter 3). Let ϵ_β^o be the porosity of the porous medium just under the interface. We approximate $\mathbf{F}_{\beta\sigma}$ within the porous medium part of V_{interf} by

$$\mathbf{F}_{\beta\sigma} = \epsilon_\beta^o \times \mathbf{D}_{\beta\sigma}(\left\langle\mathbf{v}_\beta\right\rangle_{y_i}^\beta, \epsilon_\beta^o), \tag{2.4.20}$$

where $\mathbf{D}_{\beta\sigma}$ corresponds to the fluid-solid force that would be computed in the homogeneous region at corresponding porosity ϵ_β and macroscopic velocity $\left\langle\mathbf{v}_\beta\right\rangle^\beta$. With this approximation of $\mathbf{F}_{\beta\sigma}$ within the porous medium part of V_{interf}, $\mathbf{f}_{\text{interf}}$ at $y = y_i$ becomes

$$\left(\mathbf{f}_{\text{interf}}\right)_{y_i} = \epsilon_\beta^o \mathbf{D}_{\beta\sigma}(\left\langle\mathbf{v}_\beta\right\rangle_{y_i}^\beta, \epsilon_\beta^o) \times (1 - \left(\epsilon_{\text{interf}}\right)_{y_i}), \tag{2.4.21}$$

where ϵ_{interf} is the volume fraction of free-fluid inside V_{interf}, which is composed of a free-fluid region and a porous medium region. Note that ϵ_{interf} increases toward unity as y_i increases. Indeed, as y_i increases, owing to Condition 2.4.16 the bottom side of V_{interf} must move toward the free-flow region as well. Hence as y_i increases, the volume fraction of porous medium within V_{interf} goes to zero.

This procedure to evaluate $\mathbf{f}_{\text{interf}}$ is used as a closure for the One-Domain-Approach in the hybrid model presented in Chapter 3. In practice, we approximate

$$\epsilon_\beta^o \times \mathbf{D}_{\beta\sigma}(\left\langle\mathbf{v}_\beta\right\rangle_{y_i}^\beta, \epsilon_\beta^o) \times (1 - \left(\epsilon_{\text{interf}}\right)_{y_i}) = \left(\epsilon_\beta\right)_{y_i} \mathbf{D}_{\beta\sigma}(\left\langle\mathbf{v}_\beta\right\rangle_{y_i}^\beta, \left(\epsilon_\beta\right)_{y_i}), \tag{2.4.22}$$

where $\left(\epsilon_\beta\right)_{y_i}$ is the porosity obtained by reconstructing the solid-phase-indicator γ_σ, as detailed in Chapter 3.

Obviously, the computation of $\mathbf{f}_{\text{interf}}$ proposed here is rough and could be much improved, by direct computation through experiments (which seems very tough), or more simply (but still with a huge computational effort) with numerical simulations of the flow at a free-flow/porous medium interface. Also it is not clear whether the closure used in the free flow for the SGS remains valid at the interface. In particular, we know that the presence of the porous medium develops large scale coherent structures, but it is likely that it influences the small scale as well, and hence that it impacts the SGS, as shown by direct numerical simulation in [28]. Our theoretical development shows that the development of an SGS model at the fluid/porous is an important research project, as it is directly involved in the condition to impose to the macroscopic fields at the fluid/porous interface.

Chapter 3

Hybrid model

3.1 Momentum transport in the solid phase

As done in [64], volume averaging a poro-elastic system yields local macroscopic equations when we can write transport equations in a Eulerian framework (*i.e.* Eqs. 2.1.2) for both the solid- phase (σ- phase) and the fluid- phase (β- phase). In practice, a Eulerian approach for the σ- phase is not always possible. Here, the σ phase is an ensemble of flexible fibres, fixed to an impermeable rigid wall. These fibres are very weakly coupled among each other, compared to their interaction with the flow. Hence, the mechanics of the σ- phase is non-local in nature, and this prevents the development of local macroscopic equations for the σ- phase. Therefore we need a non-local strategy, and we develop a *hybrid* model, where the equations for the fluid- phase are local (*i.e.* are expressed in a Eulerian frame) and the equations for the solid phase are non-local (*i.e.* are expressed in a Lagrangian framework).

3.1.1 Macroscopic equations for the solid phase

3.1.1.1 Upscaling the solid phase mechanics

We refer the reader to Fig. 3.1 to illustrate the parametrization of the fibre. Let D be the diameter of the fibre, h its height. Let s be the curvilinear coordinate along the axis of the fibre. We consider by convention that forces and moments expressed at $s = s^*$ correspond to the action of the upper part on the lower part of the fibre, *i.e.* $s > s^* \to s < s^*$. Let $\mathbf{t}$ be the unit vector tangential to the axis and pointing to the upper part of the fibre. Let θ be the angle made by $\mathbf{t}$ with the vertical. We define $\mathbf{c}$ as

$$\frac{\partial \mathbf{t}}{\partial s} = \left| \frac{\partial \theta}{\partial s} \right| \mathbf{c}. \tag{3.1.1}$$

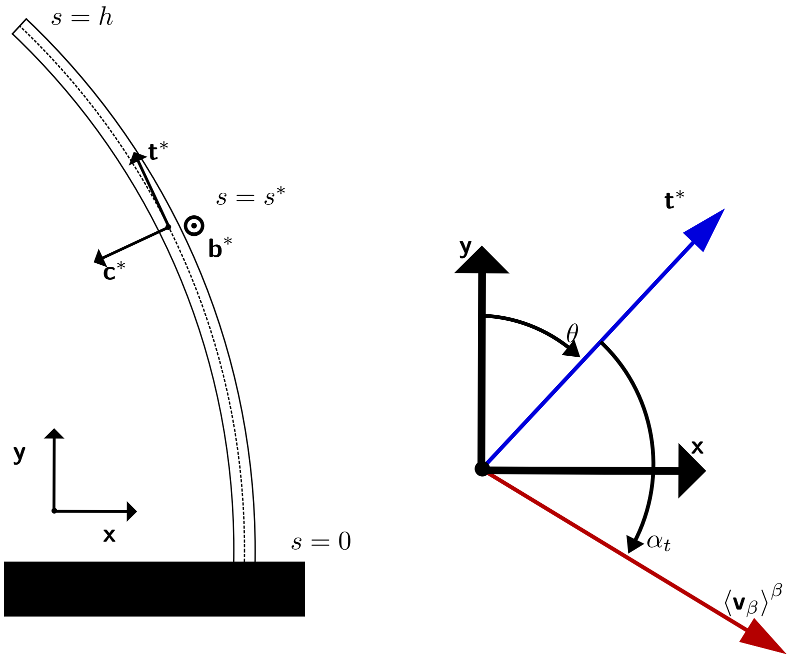

Figure 3.1: Details of a fibre fixed to the impermeable rigid wall.

$\mathbf{c}$ is a unit vector orthogonal to $\mathbf{t}$. We define $\mathbf{b}$ as the unit vector such that $(\mathbf{t}, \mathbf{c}, \mathbf{b})$ is a right-handed coordinate system.

Assumption 7 *The fibres sustain 2D deformations in the $(\boldsymbol{x}, \boldsymbol{y})$ plane.*

We model the bending moment applied by the upper part to the lower part at point s by

$$\mathbf{m}_b = EI \frac{\partial \theta}{\partial s} \mathbf{b}. \tag{3.1.2}$$

This model relies on assuming linear elasticity at the stem scale D. E is Young modulus, I is the second moment of area of the fibre, a purely geometrical parameter. For a fibre with a circular cross section of diameter D we have

$$I = \pi \frac{D^4}{64}. \tag{3.1.3}$$

The dissipation moment applied by the upper part to the lower part at point s is modeled as

$$\mathbf{m}_d = \gamma \frac{\partial \Omega}{\partial s} \mathbf{b}, \tag{3.1.4}$$

where Ω is the local time derivative of θ, and γ is the dissipative constant. Note that $\dfrac{\gamma}{EI}$ is a time scale that characterizes the relaxation of the fibre, *i.e.* it characterizes how rapidly the oscillations of the fibre decay in time. This time scale can be set relative to the natural frequency of the fibre, *i.e.*

$$\frac{\gamma}{EI} \sim h^2 \sqrt{\frac{m_l}{EI}}, \tag{3.1.5}$$

where m_l is the mass per unit length of the fibre. γ could also be used to incorporate the effect of fibre-fibre interactions. Intuitively, fibre-fibre contacts result in an additional dissipation by solid friction during the bending of a bundle of fibres. However this notion of dissipation is vague and should be quantified precisely depending on the case under study. Here we simply use it as a tuning parameter to help convergence of our simulation.

Eqs. 3.1.2 and 3.1.4 are equivalent to a first up-scaling step, because instead of considering the fibre as a continuum with momentum transport and mass conservation equations, we assume a simplified behaviour at the stem scale in order to describe the behaviour of the fibre at a larger scale, say length scale h. The second step of the upscaling process for the σ phase consists in making assumptions on the kinematics of the fibres, and this is further described in Section 3.1.1.2.

Let $\mathbf{v}$ be the shearing force along the fibre. Let $(\mathbf{t}, \mathbf{n}_1, \mathbf{n}_2)$ be an arbitrary right-handed coordinate system. We discretize our fibre in n_h elements of length δs. The force balance on a small element of fibre of length δs gives

$$\mathbf{v} = \underbrace{\left(-\frac{\partial}{\partial s}\left(EI\frac{\partial \theta}{\partial s}\right) + I\rho_\sigma \frac{\partial \Omega}{\partial t} - \gamma \frac{\partial^2 \Omega}{\partial s^2}\right)}_{v} \mathbf{c}, \tag{3.1.6}$$

i.e. the shearing force needs to be collinear to $\mathbf{c}$ for a 2D deformation of the fibre. In our application this is not strictly the case (the hydrodynamic loading is 3D), but the 2D assumption is a reasonable first step. Further developments for 3D cases are discussed in Section 3.2.3, with the issue of code performance in terms of computational time when dealing with a large number of fibres to resolve.

Let $\delta\mathbf{f}_\beta$ be the hydrodynamic force applied to an element δs of the fibre. The force balance on the upper part of the fibre $(s \geqslant s^*)$ gives

$$\mathbf{c}^* \cdot \int_{s^*}^{h} \mathbf{a}_\sigma \, dm = -v^* + \mathbf{c}^* \cdot \int_{s^*}^{h} \delta\mathbf{f}_\beta, \tag{3.1.7}$$

where $\mathbf{a}_\sigma$ is the local acceleration of the solid phase. Connecting with equation (3.1.6)

$$\left[-\frac{\partial}{\partial s}\left(EI\frac{\partial \theta}{\partial s}\right)\right]_{s=s^*} + \left[I\rho_\sigma \frac{\partial^2 \theta}{\partial t^2}\right]_{s=s^*} - \left[\gamma \frac{\partial^2 \Omega}{\partial s^2}\right]_{s=s^*} = \mathbf{c}^* \cdot \int_{s^*}^{h} \delta\mathbf{f}_\beta - \mathbf{c}^* \cdot \int_{s^*}^{h} \mathbf{a}_\sigma \, dm. \tag{3.1.8}$$

In the context of our application, we assume

$$\mathbf{c}^* \cdot \int_{s^*}^{h} \mathbf{a}_\sigma \, dm \ll \mathbf{c}^* \cdot \int_{s^*}^{h} \delta\mathbf{f}_\beta \text{ or } \left[-\frac{\partial}{\partial s}\left(EI\frac{\partial \theta}{\partial s}\right)\right]_{s=s^*}, \tag{3.1.9}$$

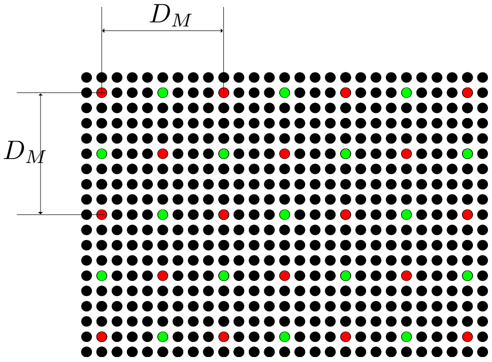

Figure 3.2: Meshing of the canopy. Master fibres are in red, slave fibres are in green, and some of the fibres left are represented in black. Note that the sketched arrangement of fibres is not representative of the actual arrangement of the fibres that constitutes the canopy. This means for example that although the actual arrangement of the fibres in the canopy is disordered, the meshing used to represent the canopy can be ordered (or regular).

i.e. the fibre is *light*, and the flexural rigidity and hydrodynamic loads dominate its dynamics.

Finally, for a light fibre we obtain

$$\left[-\frac{\partial}{\partial s}\left(EI\frac{\partial \theta}{\partial s}\right)\right]_{s=s^*} + \left[I\rho_\sigma \frac{\partial^2 \theta}{\partial t^2}\right]_{s=s^*} - \left[\gamma \frac{\partial^2 \Omega}{\partial s^2}\right]_{s=s^*} = \mathbf{c}^* \cdot \int_{s^*}^{h} \delta \mathbf{f}_\beta. \tag{3.1.10}$$

The latter equation is then numerically resolved (see Section 3.2.1) to give results for the behaviour of a fibre under 2D, pure bending subject to arbitrary hydrodynamic loads. Boundary conditions are imposed at both ends of the fibre. At $s = h$

$$\frac{\partial^2 \theta}{\partial s^2}|_{s=h} = 0, \tag{3.1.11}$$

because the shearing force $\mathbf{v}$ at the free end of the fibre vanishes, hence due to Eq. 3.1.6 the bending moment must vanish too. This translates into a homogeneous Neumann boundary condition

$$\theta|_h = \theta|_{h-\delta s}. \tag{3.1.12}$$

At $s = 0$

$$\theta|_{s=0} = 0, \tag{3.1.13}$$

i.e. the fibre is solidly anchored to the impermeable rigid wall.

3.1.1.2 Masters, slaves and others

A further step in reducing the number of degrees of freedom (DOF) is to reduce the number of fibres' mechanics that we resolve. To do so, we make assumptions on the fibres' kinematics. Fibres are divided

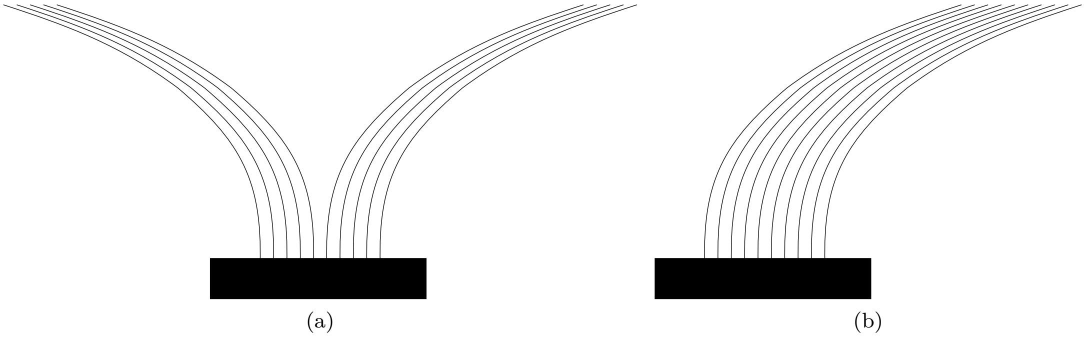

Figure 3.3: A bundle of fibres in different situations. Fig. 3.3a, forbidden case of a bundle of fibre splitting in two halfs. Fig. 3.3b, regular case of a bundle of fibres that illustrates the induced porosity variation (the porosity is lower on top of the bent bundle).

into N_M *master* fibres, N_S *slave* fibres, and the fibres left. The dynamics of the master fibres only is resolved. The kinematics (inclination and velocity) of the slave fibres is then interpolated between the master fibres' kinematics. The kinematics of the other fibres are then taken to be the same as the nearest master or slave fibre.

Let D_M be the spacing between master fibres (Fig. 3.2). Roughly, we simulate bundles of fibres of size D_M. This constrains the porous medium deformation and affects the coupling with the flow. For example, the situation illustrated in Fig. 3.3 is forbidden, *i.e.* a bundle of fibres can not split into two clusters under the hydrodynamic forcing. Hence the smaller D_M, the better the description of the dynamics of the canopy. Let L_σ be the macroscopic solid scale; typically we should ensure that

$$D_M \ll L_\sigma. \tag{3.1.14}$$

Thanks to experiments (*e.g.* [9, 65]), L_σ can be guessed to be of order of the height of the fibres, which gives an idea of how fine the meshing of the canopy should be to reasonably capture the large scale fluid-structure interaction.

3.2 Algorithm of the Hybrid model

3.2.1 Solid mechanics solver

A solver is implemented to compute the porosity- and solid velocity- fields at runtime from Eq. 3.1.10 and under aforementioned kinematics assumptions. The fibres are considered homogeneous, *i.e.* the fibres' properties are independent of the curvilinear coordinate s.

The objective of the structural solver is to obtain the geometry of the fibre $\theta_{n+1}(s)$ at time t_{n+1}, based on the geometry history $\theta_k(s)$, $k \in [0, \cdots, n-1]$. The fibre is divided into n_h elements of size δs.

In order to speed-up the computation, the first step is to determine δt_{max}, the largest acceptable solid time step. δt_{max} depends on the loading conditions and on the characteristics of the fibre. To make the resolution process feasible, we must determine a systematic way to evaluate δt_{max} at runtime. For a fluid- solver, this task is relatively easy, because the advection and the viscous diffusion times can be used to evaluate δt_{max}. Here, the system is subject to an arbitrary external forcing (the hydrodynamic load), and the solid-time step must be adapted consequently. To do so we impose a condition on the difference in curvature of the fibre after one iteration, as further explained here. We proceed by trial and error in order to determine δt_{max}. We advance Eq. 3.1.10 explicitly in time, starting with a guess time step δt_{guess}. This gives a guess solution (denoted by the $\bullet_g$ subscript) defined as

$$\begin{aligned} I\rho_\sigma \frac{\Omega_g - \Omega_n}{\delta t_{guess}} &= \left[\mathbf{c}^* \cdot \int_{s^*}^{h} \delta \mathbf{f}_\beta + EI \frac{\delta^2 \theta}{\delta s^2} + \gamma \frac{\delta^2 \Omega}{\delta s^2} \right]_n , \\ \frac{\theta_g - \theta_n}{\delta t_{guess}} &= \Omega_g . \end{aligned} \tag{3.2.1}$$

The $\bullet_n$ subscript denotes variables at time t_n. Here it is very important that the right hand side be explicit (*i.e.* we use the data from the previous time step), otherwise the search for δt_{max} blows up. Time derivatives are first order explicit, and second order space derivatives are evaluated with a central difference scheme. The local increment in curvature is proportional to

$$\Delta(\delta\theta(s)) = (\theta_g(s+1) - \theta_g(s)) - (\theta_n(s+1) - \theta_n(s)). \tag{3.2.2}$$

In practice, δt_{max} is the largest δt_{guess} such that

$$\Delta(\delta\theta(s)) < \frac{D}{\delta s}, \tag{3.2.3}$$

i.e. the increment in curvature after one iteration is controlled with a geometrical criterion.

Now that we have δt_{max}, we follow an implicit step

$$\begin{aligned} I\rho_\sigma \frac{\Omega_{k+1} - \Omega_n}{\delta t_{max}} &= \left[\mathbf{c}^* \cdot \int_{s^*}^{h} \delta \mathbf{f}_\beta \right]_k + \left(EI \frac{\delta^2 \theta}{\delta s^2} + \gamma \frac{\delta^2 \Omega}{\delta s^2} \right)_k , \\ \frac{\theta_{k+1} - \theta_n}{\delta t_{max}} &= \Omega_{k+1} . \end{aligned} \tag{3.2.4}$$

Convergence of these sub-iterations is obtained when $|\theta_{k+1} - \theta_k|$ is small enough, *i.e.* the stopping criterion for these sub-iterations is

$$|\theta_{k+1} - \theta_k| < err_{implicit}. \tag{3.2.5}$$

After convergence we have

$$\begin{aligned} I\rho_\sigma \frac{\Omega_{n+1}-\Omega_n}{\delta t_{max}} &= \left[\mathbf{c}^* \cdot \int_{s^*}^{h} \delta \mathbf{f}_\beta\right]_{n+1} + \left(EI\frac{\delta^2\theta}{\delta s^2} + \gamma\frac{\delta^2\Omega}{\delta s^2}\right)_{n+1}, \\ \frac{\theta_{n+1}-\theta_n}{\delta t_{max}} &= \Omega_{n+1}, \end{aligned} \tag{3.2.6}$$

i.e. , the structural solver is implicit. This process allows to advance Eq. 3.1.10 in time starting from any initial state, to find the kinematics of the fibre at any time, under an arbitrary loading.

3.2.2 Integration into icoFoam

In order to resolve Eq. 2.3.1, the structure solver is integrated in the flow solver **icoFoam** from the open source CFD software Open∇FOAM® [66]. **icoFoam** solves the incompressible Navier-Stokes equations using the PISO algorithm [67], and we simply add the source term due to the presence of the porous medium, that depends on the local macroscopic velocity $\langle \mathbf{v}_\beta \rangle^\beta$ and the porosity ϵ_β. Implicitly, this amounts to use the asymptotic interface condition developed in Section 2.4.3.2 along with the simple closure proposed in Section 2.4.3.3. This One-Domain-Approach (ODA) allows to handle the deformable fluid/porous interface.

The fluid- and solid- equations are resolved sequentially. The fluid- state is first obtained at time t_{n+1}, based on the geometry at time t_n. Then, the solid phase is advanced in time with the fluid- state at time t_{n+1}. Here we could implement an iterative process to make the algorithm implicit, *i.e.* ensure the fluid- state at time t_{n+1} is obtained with the geometry at time t_{n+1}. For the sake of simplicity we keep it explicit but note that this could have an impact on the honami (see Section 1.1.1). As the dynamics of the fluid- and solid- phases are different, the time stepping must be different. Typically the time step of the fluid- phase is constrained with a CFL condition. The time step δt_{max} for the solid phase is either larger (in which case we simply use the fluid- time step as solid time step), or smaller (in this case we need several time iterations for the solid- phase to catch-up with the fluid- phase).

The coupling term in Eq. 2.3.1 between the fluid- and solid- phases depends on the porosity ϵ_β and the solid velocity $\langle \mathbf{v}_\sigma \rangle^\sigma$. After the position of the master fibres is found, velocity and inclination of slave fibres are interpolated using the values of the neighbouring master fibres. The $\langle \mathbf{v}_\sigma \rangle^\sigma$-field is distributed on the fluid- mesh with a nearest neighbour algorithm. The computation of the porosity is not as straightforward. We recall that the porosity is defined as

$$\epsilon_\beta = 1 - \epsilon_\sigma, \tag{3.2.7}$$

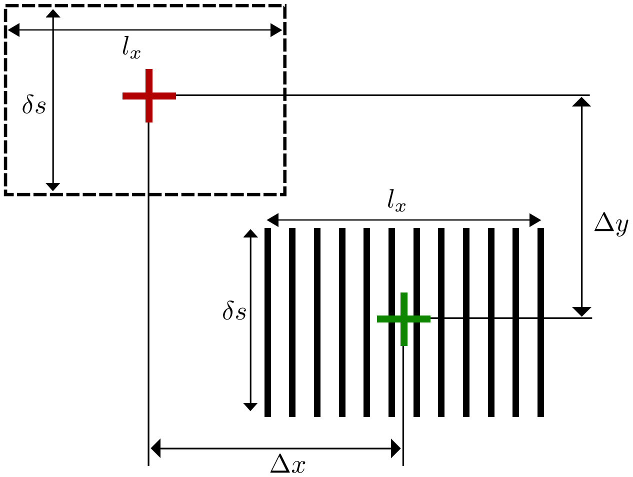

Figure 3.4: Averaging of an element δs of bundle of fibre of width l_x. The averaging volume (AV) is delimited by a dashed line. The centroid of the AV is symbolized with the red cross, and the green cross represents the centroid of the bundle.

where ϵ_σ is the solid fraction, computed by integrating the solid- phase indicator γ_σ as

$$\epsilon_\sigma = \frac{1}{V}\int_{\mathscr{V}} \gamma_\sigma \, dV. \tag{3.2.8}$$

Once the geometry is known, the solid fraction ϵ_σ is distributed on the fluid- mesh along each slave or master fibre. To avoid the need for a discretization at the stem scale, we do not actually average the σ- phase indicator but only mimic the ϵ_σ field obtained by this averaging operation (Eq. 3.2.8) along each element δs of bundles of fibres centered on either a slave- or a master- fibre. We illustrate this process with the help of Fig. 3.4. ϵ_σ takes its maximum value $max(\epsilon_\sigma)$ when it is located on the axis of a slave- or master- fibre, and decreases with the distance to the web as

$$\epsilon_\sigma = \begin{cases} max(\epsilon_\sigma)(1-\frac{\Delta x}{l_x})(1-\frac{\Delta y}{\delta s}) & , \Delta x < l_x \text{ and } \Delta y < \delta s \\ 0 & , \Delta x > l_x \text{ or } \Delta y > \delta s \end{cases} \tag{3.2.9}$$

When the bundle of fibres is unbent ($\theta = 0$), $max(\epsilon_\sigma)$ is simply ϵ_σ^0 the solid fraction of the undeformed canopy. As pictured on Fig. 3.3, the bending of the bundle of fibres induces a porosity variation. We take this into account by making $max(\epsilon_\sigma)$ depend on θ as

$$max(\epsilon_\sigma) = \epsilon_\sigma^0 + (\epsilon_\sigma^{\text{packed}} - \epsilon_0)\frac{1-cos(\theta)}{1-{}^{l_m}/_{l_x^0}}. \tag{3.2.10}$$

l_m is the smallest value of l_x when the fibres are packed, and l_x^0 is the value of l_x when the fibres are unbent ($\theta = 0$). $\epsilon_\sigma^{\text{packed}}$ is the solid fraction obtained when the fibres are packed. ϵ_σ can not be greater than $\epsilon_\sigma^{\text{packed}}$, *i.e.*

$$\epsilon_\sigma < \epsilon_\sigma^{\text{packed}}. \tag{3.2.11}$$

When two bundles overlap, the resulting solid faction is simply the sum of the solid fraction of the two overlapped bundles. The obtained ϵ_σ-field is then smoothed by applying the filter operator from Eq. 3.2.8. This smoothing operation is relatively expensive in terms of computational time. Indeed if the porous medium is deformable, at each time step, for each mesh point, we need to sum the value of ϵ_σ-field corresponding to each cell that lie inside the AV centered at this mesh point. Fortunately this operation can be distributed and the simulation can be run on several Central Processing Units (CPU). This allows to reduce the time spent simulating a case, as is discussed in the following section.

3.2.3 Toward larger, 3D cases

Real canopy flows are 3D [4] and the coherent structures that develop are sensitive to boundary conditions. Hence there is a great interest in a parallel code to make large scale 3D simulations tractable. The fluid- solver **icoFoam** is inherently parallel through a domain decomposition method (DDM), hence the effort to parallelize the code concerns only the solid phase.

As the computation of the structure of the master fibres is expensive, it is interesting that each CPU (or processor) resolves at most one master fibre. The result is then scattered to every CPUs with the following typical code structure. This uses the **Pstream** library that manages parallel communications in Open∇FOAM®.

```
for (each master fibre){
  for (each element of the master fibre){
    if (this master fibre is assigned to this CPU){
      resolve this master fibre
      find its solid velocity "us" and inclination "theta"
      }
    else{
      us = 0;
      theta = 0;
      }
    Foam::sumReduce(us, count, Foam::Pstream::msgType(), Foam::UPstream::worldComm);
    Foam::sumReduce(theta, count, Foam::Pstream::msgType(), Foam::UPstream::worldComm);
    }
  }
```

Then, each CPU has the kinematics of the whole deformable canopy, and is able to compute the porosity field in its own domain.

An issue with the DDM is that as the fluid- domain is decomposed among CPUs, a processor may have to resolve a fibre that lies outside its piece of the domain. The fluid- velocity must therefore be transmitted to the CPU that resolves the fibre. In order to keep this simple, the fluid- velocity along each fibre is scattered to every CPU. The typical code to do this is the following.

```
for (each master fibre){
  for (each element of the master fibre){
    if (the element is inside the domain of this CPU)
      find the nearest fluid- cell
      set "uf" the fluid- velocity at the location of the element
      }
    else{
      set "uf" the fluid- velocity at the location of the element to 0
      }
    }
for (each master fibre){
  for (each element of the master fibre){
    Foam::sumReduce(uf, count, Foam::Pstream::msgType(), Foam::UPstream::worldComm);
    }
  }
```

Surprisingly there is no library available in Open∇FOAM® to compute space correlations. Here we only need to compute a space correlation to smooth the porosity field. Due to the DDM, computing a space correlation requires boundary cells from neighbouring CPUs. This issue is overcome simply by the use of ghost cells, which store data from boundary cells of each neighbouring processor.

Further numerical development are needed to make the structure solver 3D. This would require to take two more angles into account (torsion and an additional bending). However, assuming 2D deformation for the fibres seems a good preliminary step, even if the domain is 3D, because the fibres are mainly forced in the direction of the mean flow.

3.3 Hydrodynamic load

3.3.1 Elementary load

We need to find the expression for the force applied by the flow to the fibres. Due to the boundary condition 2.1.4, the force applied by the flow to an element of fibre is

$$\delta \mathbf{f}_\beta = -\int_{\delta s} \mathbf{n}_{\beta\sigma} \cdot \boldsymbol{\tau}_\beta \, dA. \tag{3.3.1}$$

This can be decomposed as

$$\begin{aligned} \delta \mathbf{f}_\beta = &-\int_{\delta s} \mathbf{n}_{\beta\sigma} \cdot \left(-\mathbf{I}\tilde{p}_\beta + \mu_\beta \left[\nabla \tilde{\mathbf{v}}_\beta +^T (\nabla \tilde{\mathbf{v}}_\beta)\right]\right) dA \\ &- \int_{\delta s} \mathbf{n}_{\beta\sigma} \cdot \left(-\mathbf{I} \langle p_\beta \rangle^\beta + \mu_\beta \left[\nabla \langle \mathbf{v}_\beta \rangle^\beta +^T \left(\nabla \langle \mathbf{v}_\beta \rangle^\beta\right)\right]\right) dA. \end{aligned} \tag{3.3.2}$$

It is interesting to see that there are two contributions to the hydrodynamic load on an element of fibre. The first contribution is due to the spatial deviations. It can be estimated after the modeling of $\mathbf{D}_{\beta\sigma}$ (Section 3.3.2.2 and 4), by assuming that the N fibres inside the REV all sustain the same equal load, *i.e.*

$$\int_{\delta s} \mathbf{n}_{\beta\sigma} \cdot \left(-\mathbf{I}\tilde{p}_\beta + \mu_\beta \left[\nabla \tilde{\mathbf{v}}_\beta +^T (\nabla \tilde{\mathbf{v}}_\beta)\right]\right) dA \simeq \frac{1}{N} \mathbf{D}_{\beta\sigma} \epsilon_\beta V_{\mathrm{REV}} \frac{\delta s}{l_{\mathrm{REV}}} + 0\left(\frac{\delta s}{L}\right), \tag{3.3.3}$$

(l_{REV} is the dimension of the REV). The second term is due to the macroscopic fields. An order of magnitude can be given as

$$\int_{\delta s} \mathbf{n}_{\beta\sigma} \cdot \left(\mu_\beta \left[\nabla \langle \mathbf{v}_\beta \rangle^\beta +^T \left(\nabla \langle \mathbf{v}_\beta \rangle^\beta\right)\right]\right) dA = 0\left(\frac{\delta s}{L}\right), \tag{3.3.4}$$

as this viscous term is proportional to the variation of the velocity gradient over δs, and the velocity gradient actually varies over L. Hence the viscous term is of order of the remaining term in Eq. 3.3.3 and can be neglected. The pressure term can be developed as

$$\begin{aligned} \int_{\delta s} \mathbf{n}_{\beta\sigma} \cdot \left(-\mathbf{I} \langle p_\beta \rangle^\beta\right) dA &= -\int_{\delta s} \mathbf{n}_{\beta\sigma} \mathbf{y}_\sigma \cdot \nabla \langle p_\beta \rangle^\beta |_{\mathbf{x}} \, dA + 0\left(\frac{\delta s}{L}\right) \\ &\sim \frac{1}{N}(1-\epsilon_\beta) V_{\mathrm{REV}} \frac{\delta s}{l_{\mathrm{REV}}} \nabla \langle p_\beta \rangle^\beta . \end{aligned} \tag{3.3.5}$$

This contribution is similar to a buoyancy force. It can be neglected in the expression for $\delta \mathbf{f}_\beta$ if

$$(1-\epsilon_\beta)\nabla \langle p_\beta \rangle^\beta \ll \epsilon_\beta \mathbf{D}_{\beta\sigma}. \tag{3.3.6}$$

Typically, this is not acceptable in underwater canopy flows where buoyancy is the major restoring force [5]. However this is acceptable if the porous medium has a large enough porosity, such that $\mathbf{D}_{\beta\sigma}$ dominates, as is the case here. To conclude, we approximate the force on the fibres by

$$\delta \mathbf{f}_\beta =\simeq \frac{1}{N}\mathbf{D}_{\beta\sigma}\epsilon_\beta V_{\mathrm{REV}}\frac{\delta s}{l_{\mathrm{REV}}}. \tag{3.3.7}$$

3.3.2 DNS on a REV

3.3.2.1 The periodicity assumption

As discussed in Section 2.3.1.1, System 2.3.8 is resolved over an REV in order to evaluate $\mathbf{D}_{\beta\sigma}$. As we consider that the porous medium is homogeneous, the geometry of the REV is periodic.

Assumption 8 *Periodic conditions are imposed on $\mathbf{v}_\beta$ and p_β over the REV to evaluate $\mathbf{D}_{\beta\sigma}$.*

Let us understand the consequence of Assumption 8. As introduced in Section 2.2.3, the velocity field $\mathbf{v}_\beta$ is decomposed as

$$\mathbf{v}_\beta = \tilde{\mathbf{v}}_\beta + \langle \mathbf{v}_\beta \rangle^\beta , \tag{3.3.8}$$

in an attempt to separate scales. However due to boundary condition 2.1.4

$$\tilde{\mathbf{v}}_\beta = -\langle \mathbf{v}_\beta \rangle^\beta \text{ at } \mathscr{A}_{\beta\sigma}, \tag{3.3.9}$$

and the $\tilde{\mathbf{v}}_\beta$ field still contains a macroscopic scale component. We overcome this via the parametrization

$$\tilde{\mathbf{v}}_\beta = \mathbf{M} \cdot \langle \mathbf{v}_\beta \rangle^\beta . \tag{3.3.10}$$

Note that $\mathbf{M}$ is introduced here only for the purpose of separating the scales in $\tilde{\mathbf{v}}_\beta$. We do not intend to compute $\mathbf{M}$, and the derivation of a closure problem in the inertial regime is more widely discussed in Section 4. Such an $\mathbf{M}$- field verifies

$$\mathbf{M} = -\mathbf{I} \text{ at } \mathscr{A}_{\beta\sigma}, \tag{3.3.11}$$

hence if the geometry of the REV is periodic, the source of $\mathbf{M}$ is periodic over the REV and it is legitimate that $\mathbf{M}$ verifies periodic conditions over the REV. We have that

$$\mathbf{v}_\beta = (\mathbf{M} + \mathbf{I}) \cdot \langle \mathbf{v}_\beta \rangle^\beta , \tag{3.3.12}$$

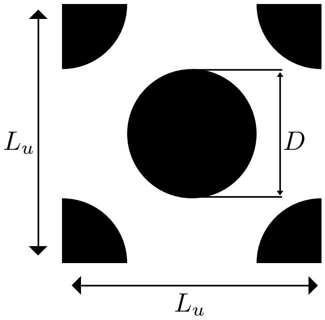

Figure 3.5: REV used in [68] to evaluate $\mathbf{D}_{\beta\sigma}$.

hence Assumption 8 is acceptable only if variations of the macroscopic field $\langle \mathbf{v}_\beta \rangle^\beta$ over the REV can be neglected. To understand the implication on the evaluation of $\mathbf{D}_{\beta\sigma}$, we recall Eq. 2.2.29

$$\mathbf{D}_{\beta\sigma} = \frac{1}{V_\beta} \int_{\mathscr{A}_{\beta\sigma}} \mathbf{n}_{\beta\sigma} \cdot \left(-\mathbf{I}\tilde{p}_\beta + \mu_\beta \left[\nabla \tilde{\mathbf{v}}_\beta +^T (\nabla \tilde{\mathbf{v}}_\beta) \right] \right) dA. \tag{3.3.13}$$

To decouple the scales we parametrize

$$\mathbf{D}_{\beta\sigma} = \frac{\mu_\beta}{V_\beta} \int_{\mathscr{A}_{\beta\sigma}} \mathbf{n}_{\beta\sigma} \cdot \left(-\mathbf{Im} + \left[\nabla \mathbf{M} +^T (\nabla \mathbf{M}) \right] \right) \cdot \langle \mathbf{v}_\beta \rangle^\beta \, dA, \tag{3.3.14}$$

and develop with a Taylor expansion to obtain

$$\begin{aligned} \mathbf{D}_{\beta\sigma} &= \frac{\mu_\beta}{V_\beta} \int_{\mathscr{A}_{\beta\sigma}} \mathbf{n}_{\beta\sigma} \cdot \left(-\mathbf{Im} + \left[\nabla \mathbf{M} +^T (\nabla \mathbf{M}) \right] \right) \cdot \left(\langle \mathbf{v}_\beta \rangle^\beta |_x + \mathbf{y}_\beta \cdot \nabla \langle \mathbf{v}_\beta \rangle^\beta |_x + O\left(\frac{r_0}{L}\right)^2 \right) dA \\ &= \frac{\mu_\beta}{V_\beta} \int_{\mathscr{A}_{\beta\sigma}} \mathbf{n}_{\beta\sigma} \cdot \left(-\mathbf{Im} + \left[\nabla \mathbf{M} +^T (\nabla \mathbf{M}) \right] \right) dA \cdot \langle \mathbf{v}_\beta \rangle^\beta |_x \\ &+ \frac{\mu_\beta}{V_\beta} \int_{\mathscr{A}_{\beta\sigma}} \mathbf{n}_{\beta\sigma} \cdot \left(-\mathbf{Im} + \left[\nabla \mathbf{M} +^T (\nabla \mathbf{M}) \right] \right) \cdot \mathbf{y}_\beta \, dA \cdot \nabla \langle \mathbf{v}_\beta \rangle^\beta |_x + O\left(\frac{r_0}{L}\right)^2 . \end{aligned} \tag{3.3.15}$$

This allows to express explicitly the term that we neglect when we make Assumption 8. Interestingly this term vanishes if the REV verifies certain geometric conditions. Indeed the term

$$\mathbf{n}_{\beta\sigma} \cdot \left(-\mathbf{Im} + \left[\nabla \mathbf{M} +^T (\nabla \mathbf{M}) \right] \right) \cdot \mathbf{y}_\beta \tag{3.3.16}$$

corresponds to the fluid- force applied to the solid at location $\mathbf{y}_\beta$, when $\langle \mathbf{v}_\beta \rangle^\beta$ is parallel to $\mathbf{y}_\beta$. For instance, if the REV has a point of symmetry, the integration of term 3.3.16 on surface $\mathscr{A}_{\beta\sigma}$ gives zero.

3.3.2.2 The metamodel

In [68], Luminari evaluates $\mathbf{D}_{\beta\sigma}$ under Assumption 8 by solving System 2.3.8 on a periodic REV. The REV used is the square unit cell of a staggered array of cylinders (Fig. 3.5), so that

$$L_u = D\sqrt{\frac{\pi}{2}}\frac{1}{\sqrt{1-\epsilon_\beta}}, \tag{3.3.17}$$

where L_u is the side size of the square unit cell. The Reynolds number used to characterize the flow regime in this metamodel is Re_m, defined with D the diameter of the fibre as reference length and v the magnitude of $\langle \mathbf{v}_\beta \rangle^\beta$. Let k be the permeability of the fibrous material. In the frame of the fibre, it is found that a diagonal permeability tensor is suitable to describe the fluid-solid force on the REV. In other words, the fluid-solid force in the tangential- and normal- direction of the fibre is proportional to the fluid- velocity in the tangential- and normal- direction, respectively. The strategy adopted in [68] is to build a metamodel for the permeability based on a number of DNS points. The output of the metamodel summarizes as

$$\epsilon_\beta, Re_m, \alpha_t \rightarrow h_t^*, h_n^*, \tag{3.3.18}$$

where (see Fig 3.1)

- t and n refer to the component of $\langle \mathbf{v}_\beta \rangle^\beta$ in the direction tangential and normal to the fibre respectively,
- α_t is the angle made by $\langle \mathbf{v}_\beta \rangle^\beta$ and $\mathbf{t}$,
- h^* is such that

$$\begin{aligned} {L_u}^2 k_t^{-1} &= h_t^*, \\ {L_u}^2 k_n^{-1} &= h_n^*. \end{aligned} \tag{3.3.19}$$

The metamodel is finely discretized for the α_t dimension. However, ϵ_β is restricted to the range $[0.4, 0.8]$, and Re_m to the range $[0, 100]$.

3.3.2.3 Continuous extension

In order to use efficiently the data collected in [68], we must deal also with the case when ϵ_β or/and Re_m are out of the range of the metamodel. To do so, we assume that there are roughly two regimes (Fig. 3.6b) for the pressure gradient depending on the Reynolds number based on the fibre diameter

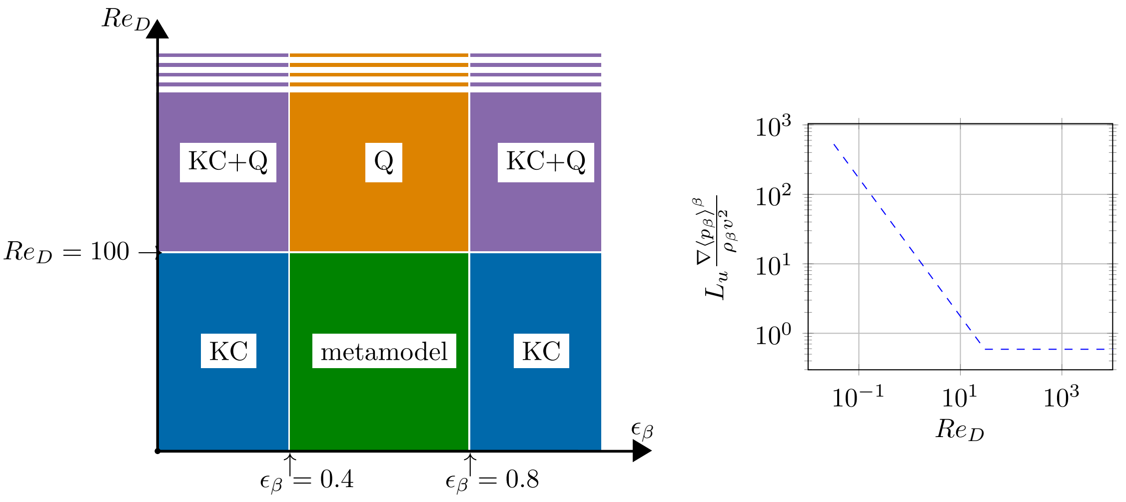

(a) (b)

Figure 3.6: Fig. 3.6a, principle of the continuous expansion. KC refers to the Kozeny-Carman expansion, Q refers to the quadratic expansion. Fig. 3.6b, the two asymptotic regimes of the pressure gradient.

Re_D, mainly

$$\begin{aligned} L_u \frac{\nabla \langle p_\beta \rangle^\beta}{\rho_\beta v^2} &\sim 1/Re_D, Re_D < Re_t, \\ L_u \frac{\nabla \langle p_\beta \rangle^\beta}{\rho_\beta v^2} &\sim 1, Re_D > Re_t, \end{aligned} \tag{3.3.20}$$

with two different values of the transition Reynolds number Re_t for the tangential and normal directions. This model is inspired from experiments and direct numerical simulations [69, 70]. Note that the model is completely determined by the value of h^* at $Re_m = 0$ (which we call H^*), and the constant value of $L_u \frac{\nabla \langle p_\beta \rangle^\beta}{\rho_\beta v^2}$ in the quadratic regime (Q). This constant is determined from the Ergun expression and we ensure that it recovers the asymptotic behaviour when ϵ_β goes to 1. When ϵ_β goes to 1 the effect of confinement vanishes, and the force exerted on each fibre should be the force exerted on an isolated cylinder, *i.e.*

$$L_u \frac{\nabla \langle p_\beta \rangle^\beta}{\rho_\beta v^2} \underset{\epsilon_\beta \to 1}{\sim} C_d \sqrt{\frac{(1-\epsilon_\beta)}{{}^{\pi}/_{2}}}. \tag{3.3.21}$$

where C_d is the drag coefficient for an isolated cylinder. For lower porosities, the Ergun expression gives

$$L_u \frac{\nabla \langle p_\beta \rangle^\beta}{\rho_\beta v^2} = C \frac{\sqrt{(1-\epsilon_\beta)}}{\epsilon_\beta}, \tag{3.3.22}$$

where C is a non-dimensional constant to be determined. By matching Eqs. 3.3.21 and 3.3.22 we obtain

$$C = \frac{C_d}{\sqrt{\pi/2}}. \tag{3.3.23}$$

Taking $C_d = 1.1$ for the value of the drag coefficient for an isolated cylinder in the turbulent regime, we thus have

$$C \simeq 0.88. \tag{3.3.24}$$

By stating that the linear and quadratic regimes match at Re_t

$$\nu_\beta \rho_\beta h^* \epsilon_\beta v = 0.88 \frac{\rho_\beta v^2}{L_u} \frac{\sqrt{(1-\epsilon_\beta)}}{\epsilon_\beta}, \tag{3.3.25}$$

we can express the transition Reynolds number as

$$Re_t = \frac{\epsilon_\beta^2 h^*}{0.88\sqrt{\pi/2}}. \tag{3.3.26}$$

Let ϵ_β,Re_D be an input of the metamodel. There are different cases to consider depending on the values of Re_D and ϵ_β (see Fig. 3.6a).

A $\epsilon_\beta < 0.4$ **or** $\epsilon_\beta > 0.8$ We define ϵ_0 as either 0.4 or 0.8 (we take the nearest value to ϵ_β).

A.1 $Re_D < 100$ The metamodel yields h_0^* corresponding to ϵ_0 at the desired Reynolds number $Re_m = Re_D$, and the output is extrapolated assuming the Kozeny-Carman dependence (KC)

$$h^* \sim \frac{(1-\epsilon_\beta)^2}{\epsilon_\beta^3} \tag{3.3.27}$$

to obtain h^* at the desired porosity ϵ_β. The case $\epsilon_\beta > 0.8$ could be improved by matching the regime of an isolated cylinder in Stokes flow. At the very least the Kozeny-Carman approximation is consistent because

$$h^* \underset{\epsilon_\beta \to 1}{\longrightarrow} 0, \tag{3.3.28}$$

as expected, *i.e.* the pressure gradient vanishes as the solid phase vanishes.

A.2 $Re_D > 100$ We must use Eq. 3.3.20. We determine H_0^* corresponding to h^* at ($\epsilon_\beta = \epsilon_0, Re_m = 0$). We extrapolate with Kozeny-Carman to obtain H^* at the desired porosity ϵ_β. Then, we evaluate in which regime we lie for each direction (linear or quadratic for the tangential and normal directions). Let Re_T and Re_N be the Reynolds numbers in the tangential and normal directions of the fibre, respectively. We determine the transition Reynolds numbers $Re_t(N)$ and $Re_t(T)$ from Eq. 3.3.26

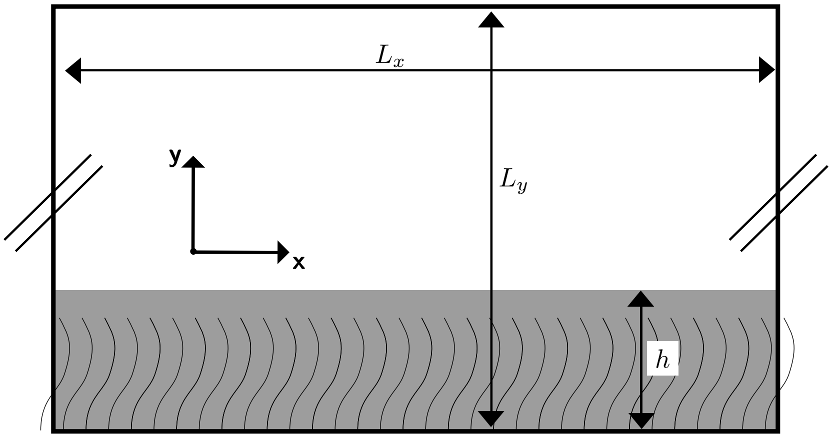

Figure 3.7: Illustrative case for the hybrid model. The double slash symbolizes periodic conditions imposed to the fluid- and the solid- phase. The darker region represents the space occupied by the porous medium at rest.

and compare them to Re_N and Re_T, respectively. For each direction, if the regime is linear, then we already have the desired result since $h^* = H^*$. Otherwise, if the regime is quadratic, we extrapolate with

$$h^* = H^* \frac{Re_D}{Re_t}, \tag{3.3.29}$$

to obtain h^* at the desired Reynolds number.

B $0.4 < \epsilon_\beta < 0.8$

B.1 $Re_D < 100$ We simply use the metamodel, as we are inside its domain of validity.

B.2 $Re_D > 100$ We must use the model depicted in Eq. 3.3.20, so we repeat step A.2, with no need to extrapolate with Kozeny-Carman.

3.4 Application of the hybrid model

3.4.1 Illustrative case

We present here a case that illustrates the capability of the hybrid model to simulate the unsteady interaction between the flow and a carpet of flexible fibres. The case under study is sketched on Fig. 3.7. Periodic conditions are imposed on each end of the domain (right and left), for both the fluid- and the solid- phase. A free-slip condition is imposed on top of the domain for the fluid- phase, *i.e.*

$$v_\beta = 0, \; \frac{\partial p_\beta}{\partial y} = 0, \; \frac{\partial u_\beta}{\partial y} = 0, \text{ on top of the domain.} \tag{3.4.1}$$

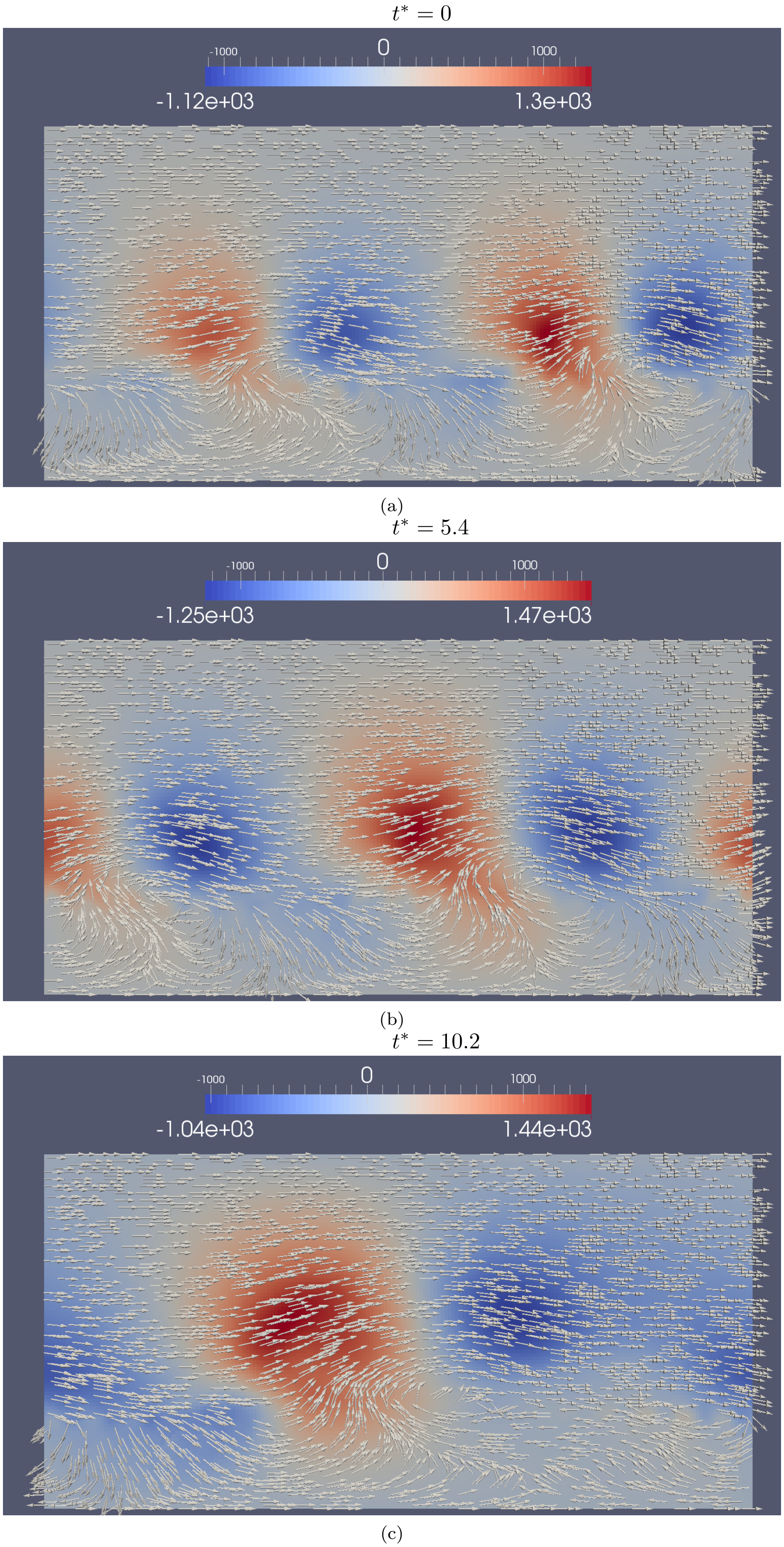

Figure 3.8: Instability developing on top of the rigid porous medium as the flow accelerates. The color field represents the v_β-field. The arrows represent the direction of $\langle \mathbf{v}_\beta \rangle^\beta$.

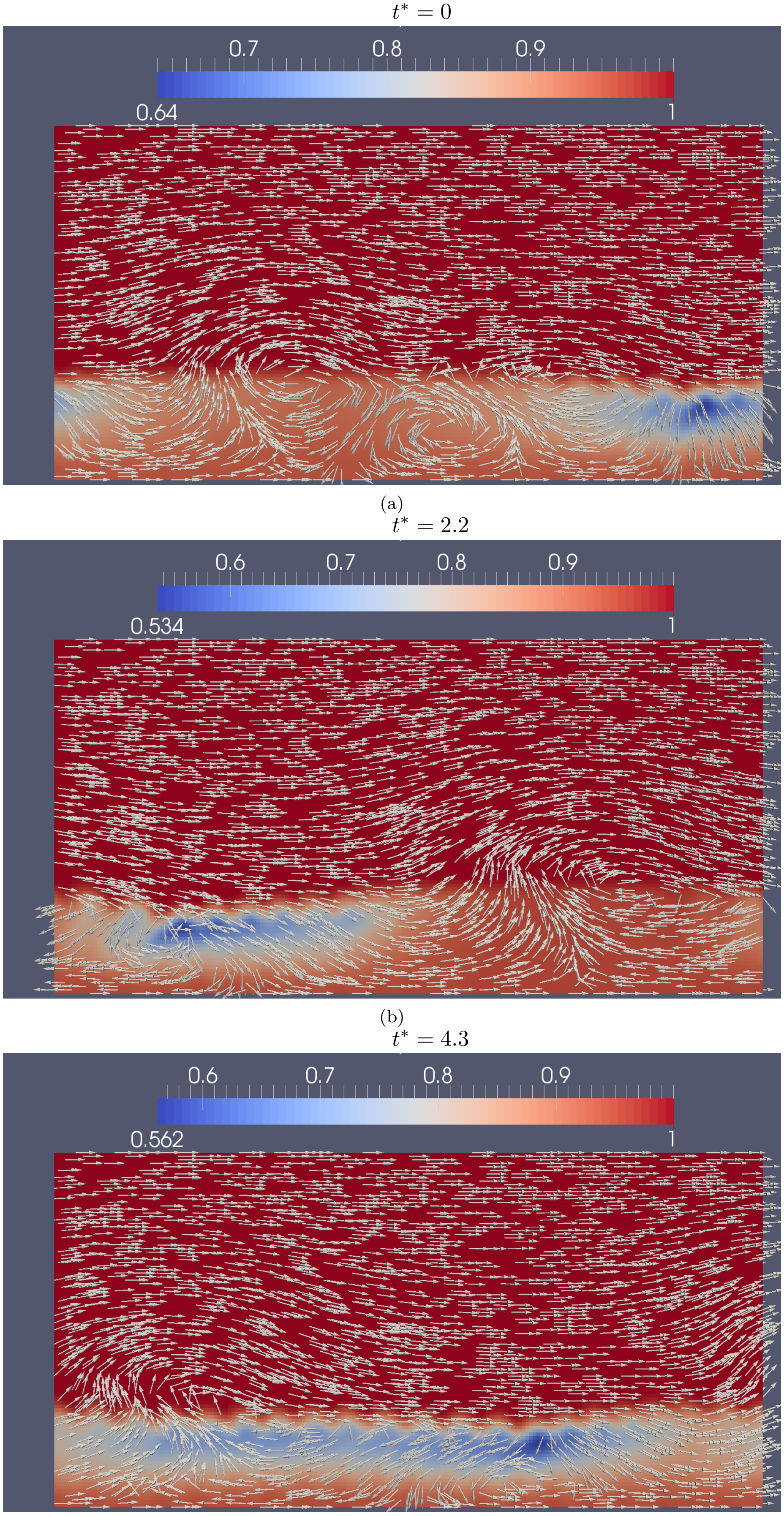

(a)

(b)

(c)

Figure 3.9: Instability developing on top of the deformable porous medium as the flow accelerates. The color field represents the ϵ_β-field. The arrows represent the direction of $\langle \mathbf{v}_\beta \rangle^\beta$.

The fluid is moved forward with a constant source term, represented by $\mathbf{s}_\beta = s_\beta \mathbf{x}$ in Eq. 2.1.2, that mimics a constant pressure gradient or gravity force. Such a flow over a canopy is known to develop a Kelvin-Helmholtz - like instability due to the inflection point in the mean velocity profile [4, 29, 19], and this is an interesting feature here as we wish to display an unsteady interaction between the flow and the elastic porous medium (canopy).

The fluid- domain is 2D and we take L_y the height of the domain as reference length scale. We define the non-dimensional time as

$$t^* = t\frac{\sqrt{L_y s_\beta}}{L_y}. \tag{3.4.2}$$

The width of the domain is taken to be $L_x = 2L_y$. The dimensions of the fibres are $h = 0.3L_y$ (height) and $D = 0.01L_y$ (diameter). The arrangement of the fibres is such that the porosity of the undeformed porous medium is 0.95. The Reynolds number Re_g, defined as

$$Re_g = \frac{L_y\sqrt{L_y s_\beta}}{\nu_\beta}, \tag{3.4.3}$$

is set to 10^3. We use a Geometric Agglomerated Algebraic Multigrid solver (GAMG) for the pressure equation and a Preconditioned Bi-Conjugate Gradient solver (PBiCG) for the velocity solver. Preconditioning is made with Diagonal-based Incomplete LU factorization (DILU). For both the pressure and velocity solvers, the absolute tolerance is set to 10^{-15} and the relative tolerance is set to 10^{-8}. We have made these choices as they give a good convergence rate and we refer to [71] for further details on linear solvers available in Open∇FOAM®. The fluid- mesh is uniform and is composed of 200 × 100 square cells. Parallel computations are carried out on a cluster of Intel® Ivybridge (2.8Ghz) cores. 4 CPUs are used for the computation and it takes approximately 33 minutes to simulate 100 units of time of a fluid- particle through the domain when the porous medium can deform, *i.e.* when the structural solver is activated (this implies additional operations to solve the fibres, hence an additional CPU time). The computation of the porous structure is observed to multiply the computational time by 4, and this shows the interest of distributing the fibres' resolution on 4 CPUs, in order to reduce the amount of time required to obtain the simulation. No subgrid-scale model is used for this illustrative case.

We first run the case with a rigid porous medium. The Reynolds number based on the maximum magnitude of u_β in the domain is observed to be around 10^4. As shown on Fig. 3.8, the KH- instability grows over the rigid porous medium, and ends up developing coherent structures of size equivalent to the height of the fibres. We therefore know that this case is unsteady by nature and is capable of displaying an unsteady coupling between the flow and the deformable porous medium.

We then release the porous medium. The deformation of the porous medium is described with 4 master fibres and 4 slave fibres for each master fibre. Each master fibre is discretized with 12 elements. The dissipative constant γ is set to a very low value of $\frac{\gamma}{EI} = 10^{-3}h^2\sqrt{\frac{m_l}{EI}}$. The fibres' density is set to $\rho_\sigma = 10^2\rho_\beta$ (we have to be careful here, since the model for the fibre was developed for light fibres). We now need to set the bending rigidity EI. This is done by setting the the Cauchy number C_Y ([5, 22, 3]). The Cauchy number evaluates the ratio of the fluid-solid force to the fibre restoring (or elastic) force. This can be expressed as

$$C_Y = \frac{\rho_\beta L_y s_\beta D H^3}{2EI}, \tag{3.4.4}$$

by taking $\sqrt{L_y s_\beta}$ as reference velocity and assuming a quadratic form for the fluid-solid force applied to the fibre. We need

$$C_Y > 1, \tag{3.4.5}$$

to obtain a deformation of the porous medium under the unsteady hydrodynamic load. In our case we have set the bending rigidity EI of the fibres such that the Cauchy number $C_Y \simeq 13.5$. The stopping criterion $err_{implicit}$ of Eq. 3.2.6 is set to 10^{-6}.

The case presented here shows a transient regime, corresponding to the development of a KH-like instability on top of the canopy. As this unsteadiness was previously obtained for a rigid porous medium, it is a pure flow- instability (*i.e.* this instability is not due to the deformation of the canopy). Fig. 3.9 shows the development of a canopy-scale vortex, similar to the one obtained over the rigid medium. The porous medium strongly deforms under the hydrodynamic load, as expected regarding the value of the Cauchy number ($C_Y \simeq 13.5$). The hybrid model is able to capture this deformation of the porous medium, as well as the effect of the displacement of the solid- phase on the flow. The hybrid model allows for the computation of the porosity ϵ_β, and variations of about 40% of the ϵ_β-field are displayed. Qualitatively, this test case shows that it is relatively easy with the hybrid model implemented in Open∇FOAM® to set-up a case where a KH- instability develops, and where a large-scale fluid-structure interaction is observed. However this case is only illustrative, and it would be interesting to compare our hybrid model quantitatively to a real experiment.

3.4.2 Future quantitative comparisons

We have proposed a solution to effectively implement a macroscopic model of a canopy flow. Most of the technical features are provided in order to reproduce this hybrid model, and we have seen that it allows to simulate the coupling between the flow and the canopy in a canopy flow. The next step is to obtain quantitative comparisons with experiments in order to demonstrate the relevance of this hybrid model.

For example, some experiments in [65] are conducted to study the honami phenomenon. An artificial canopy is immersed in a water channel, that can be inclined in order to obtain the desired flow velocity. The reference flow velocity U_m is taken as the space- and time- average velocity parallel to the channel bed. The artificial canopy is made of a uniform arrangement of identical plastic sheets, of height h and width b. The bending rigidity EI of the plastic material is reported as well. The density of the canopy is modified by arranging the plastic sheets in a more or less sparse way. Several canopy flow conditions are tested. The canopy density and the Reynolds number, as well as the relative depth are varied, and the interaction between the flow and the elastic canopy is observed by direct measurement of the flow field and displacement of the plastic sheets constituting the artificial canopy. The development of coherent flow structures, coupling with the canopy deformation on top of the canopy, are reported to exist only under certain condition (*i.e.* for certain sets of parameters). The parameters characterizing the experiment are indicated, allowing to numerically reproduce the real experiment. Based on the hybrid model we developed, we try to set-up a numerical simulation that reproduces the experiment defined by

- the Reynolds number $Re = \dfrac{L_y U_m}{\nu_\beta} = 4.2 \times 10^4$ based on U_m the volume- and time- averaged velocity.
- the stiffness of the fibres (Young modulus). This is done via the Cauchy number, that compares the hydrodynamic load to the stiffness of the canopy. ($C_Y = \dfrac{\rho_\beta U_m^2 b h^3}{2EI} = 0.75$).
- the total surface exposed per canopy unit of volume. In the hybrid model we set a porosity. We simply set the porosity to 0.95, which ensured that the total surface exposed per canopy unit of volume is the same as in the experiment.
- the relative submergence depth $\dfrac{L_y}{h} = 3$.

The fact that $\dfrac{L_y}{h} = 3$ is interesting because it corresponds to a reasonable size of the computational domain and this limits the CPU cost. The knowledge of these key parameters allows to compute the corresponding porosity and Cauchy number in order to set a numerical simulation with the hybrid model that we developed in this section that preserves the similarity numbers. The top of the domain is a free surface (air/water interface), which we model with the boundary condition we set in the previous numerical experiment (symmetry condition).

Unfortunately, we were not able to properly reproduce this experiment here, and the difficulty in reproducing the experiment lies in different issues.

- A first time demanding issue is the finding of the proper source term s_β in the Navier-Stokes equations that yields the goal- Reynolds number on a rigid canopy. We proceed by trial and error in order to find the proper s_β so that the Reynolds number Re reaches the value of the experiment $\simeq 4.2 \times 10^4$. This is time consuming, as we need to wait for each try that the statistically steady regime is reached. This task is mesh dependent as we use coarse meshes to gain computational time. With $L_x = 2L_y$ and for a 200×100 mesh, we found that $Re_g = 8.83 \times 10^2$ yields a Reynolds number Re around 3.9×10^4 for a rigid canopy.

- The Reynolds number defined with the local velocity and the height of the domain is of order of 10^5 on top of the computational domain. Due to the CFL condition, this high value of the local Reynolds number constrains the simulation to use small time steps, increasing the number of iterations required to simulate the canopy flow.
- Once we have reached the objective Reynolds number with a rigid canopy, we release it and ask the CPU to resolve the solid phase. Although an effort was made on parallelization, the solving of the solid phase is still CPU demanding and considerably increases the computational time. This point in particular is purely technical and requires more code development regarding parallelization, and optimization of the algorithm that resolves the solid phase.

The hybrid approach proposed here is a promising way toward the numerical simulation of a canopy flow. Yet, it was not possible to conduct a satisfying comparison with experiments that would validate the hybrid model. This is mainly due to a lack of time. Provided further developments, the attempt we have made here should be a good basis toward the macroscopic simulation of the fluid-structure coupling in a canopy flow.

Part III

Modelling of the small-scale

Chapter 4

Inertial sensitivity of porous microstructures

Fluid flows through porous media are subject to different regimes, ranging from linear creeping flows to unsteady, chaotic turbulence. These different flow regimes at the pore-scale have repercussions at larger scales, with the macroscale drag force experienced by a fluid moving through the medium becoming a non-linear function of the average velocity beyond the creeping flow regime. Accurate prediction of the transition between different flow regimes is an important challenge with repercussions onto many engineering applications. Here, we are interested in the first deviation from Darcy's law, when inertia effects become sizeable. Our goal is to define a Reynolds number, Re_C, so that the inertial deviation occurs when $Re_C \sim 1$ for any microstructure. The difficulty in doing so is to reduce the multiple length scales characterizing the geometry of the porous structure to a single length scale, ℓ. We analyze the problem using the method of volume averaging and identify a length scale in the form $\ell = C_\lambda \sqrt{K_\lambda / \epsilon_\beta}$, with C_λ a parameter that indicates the sensitivity of the microstructure to inertia. The main advantage of this definition is that an explicit formula for C_λ is given; C_λ is computed from a creeping flow simulation in the porous medium and Re_C can be used to predict the transition to a non-Darcian regime more accurately than by using Reynolds numbers based on alternative length scales. The theory is validated numerically with data from flow simulations for a variety of microstructures.

4.1 Introduction

A fluid flowing through a porous medium experiences three main transition phenomena with increasing flow rate [72, 73, 74, 75, 76, 77, 78, 79, 80]. The first one is a transition from the creeping flow regime to the non-Darcian, inertial steady regime. Then, the flow evolves to successive unsteady regimes. The last transition occurs when turbulence appears, characterized by unsteady, chaotic flow features in the porous medium. This latter regime presents several open modeling issues [81, 82, 83, 84, 85, 86, 34, 87]. Since the filtration law in porous media strongly depends on the flow regime, it is of importance to characterize these transitions. This has applications to natural and as well as industrial systems, including modeling the transport of chemical species [88, 89, 90, 91, 92] and heat [93, 94, 95, 96, 97, 98, 99] in, *e.g.* , packed-bed column reactors, soil percolation, microscopic heat exchangers, and the fluid-structure coupling in flexible canopies [29, 12, 14, 24, 22].

Under a macroscopic pressure gradient $\mathbf{g}_\beta$[1], a fluid initially at rest in a porous medium accelerates[2] until the internal viscous dissipation of the flow balances the rate of work of $\mathbf{g}_\beta$. In the steady regime, the flow reaches a state characterized by a spatially averaged velocity $\langle \mathbf{v}_\beta \rangle^\beta$. This velocity can be written as

$$\langle \mathbf{v}_\beta \rangle^\beta = v\boldsymbol{\lambda}, \tag{4.1.1}$$

with $\boldsymbol{\lambda}$ the unit vector defining the mean flow direction and v the amplitude of $\langle \mathbf{v}_\beta \rangle^\beta$. To a given $\mathbf{g}_\beta$ corresponds a unique $\langle \mathbf{v}_\beta \rangle^\beta$, and viceversa. We write this as a filtration law, $\mathbf{g}_\beta = \mathbf{g}_\beta(\boldsymbol{\lambda}, v)$. A priori the nature of $\mathbf{g}_\beta(\boldsymbol{\lambda}, v)$ depends on the topology of the porous medium, the flow regime and the physical properties of the fluid [100, 101, 102, 103, 104, 105, 106].

In Appendix A.1, we show that for a fluid under constant volume force $\mathbf{s}_\beta$, the macroscopic pressure gradient can be related to the gradient of the intrinsic average pressure $\nabla \langle p_\beta \rangle^\beta$ as

$$\mathbf{g}_\beta = \nabla \langle p_\beta \rangle^\beta - \rho_\beta \mathbf{s}_\beta, \tag{4.1.2}$$

where ϵ_β is the porosity of the medium. In the creeping flow regime, $\mathbf{g}_\beta(\boldsymbol{\lambda}, v)$ is Darcy's law [107], which amounts to write

$$\nabla \langle p_\beta \rangle^\beta - \rho_\beta \mathbf{s}_\beta = -\epsilon_\beta \mu_\beta \mathbf{K}_D^{-1} \cdot \boldsymbol{\lambda} v, \tag{4.1.3}$$

where μ_β is the dynamic viscosity of the fluid. The "$\cdot$" symbol in Eq. 5.1.1 refers to the usual inner product. $\mathbf{K}_D$ (a second order tensor) is the permeability of the porous medium. We can further define a scalar characterizing the permeability for a flow in the $\boldsymbol{\lambda}$ direction as

$$K_\lambda^{-1} = ||\mathbf{K}_D^{-1} \cdot \boldsymbol{\lambda}||. \tag{4.1.4}$$

Beyond the creeping flow regime, non-linear effects at the pore scale modify the flow pattern, and the filtration law becomes non-Darcian [108, 109, 110, 111, 112, 113, 114, 115, 116]. We can extend

---

[1] See Section A.1 and Eq. A.1.10 for a detailled derivation of $\mathbf{g}_\beta$ with respect to the microscopic fields.

[2] This initial transient regime is generally neglected in macroscopic models.

Darcy's law as

$$\nabla \langle p_\beta \rangle^\beta - \rho_\beta \mathbf{s}_\beta = -\epsilon_\beta \mu_\beta \left(\mathbf{K}_D^{-1} \cdot \boldsymbol{\lambda} + \mathbf{f} \right) v. \tag{4.1.5}$$

A simple way of characterizing the range of validity of Darcy's law is by considering the Forchheimer number [117, 118, 119, 120, 121]

$$F_\lambda = \frac{||\mathbf{f}||}{K_\lambda^{-1}}, \tag{4.1.6}$$

which is the ratio of the non-linear to the linear part of the filtration law. Darcy's law remains valid as long as $F_\lambda \ll 1$ and the inertial transition occurs when $F_\lambda \sim 1$.

To capture the inertial transition *a priori*, a Reynolds number Re_C is of practical interest. Let ν_β be the kinematic viscosity of the fluid ($\mu_\beta = \nu_\beta \rho_\beta$). In general, Re_C is expressed as a ratio of the advection time to the viscous diffusion time, in terms of v, ν_β, and a length scale ℓ as

$$Re_C = \frac{\ell v}{\nu_\beta}. \tag{4.1.7}$$

The choice of the characteristic length scale to define such a Reynolds number is widely discussed in the literature [119, 116, 79, 122, 123, 124, 125, 126, 121]. For a given porous medium, ℓ should be easy to identify, and such that Re_C past a well defined threshold indicates the inertial transition. A simple choice for ℓ is a characteristic pore size ℓ_β [94, 125, 126, 127, 128, 129]. However such a microscopic length scale may not be well defined for porous media that exhibit non-trivial or complex microstructures, such as, *e.g.* , sandstones.

If we have an explicit filtration law, we can use the Forchheimer number as a Reynolds number [118, 119, 120]. For example, the classical filtration law (Ergun's equation, [103]) takes into account inertia effect on the filtration law via a quadratic form. For a one-dimensional filtration process, this quadratic filtration law is a scalar relation given by

$$g_\beta (\boldsymbol{\lambda}, v) = \epsilon_\beta \mu_\beta K_\lambda^{-1} (1 + bv) v. \tag{4.1.8}$$

Inertia effects are small as long as the quadratic part is small against the linear part. Taking the ratio of the quadratic part to the linear part (*i.e.* $\frac{bv}{1}$), and identifying it with Re_C, *i.e.*

$$\frac{bv}{1} = \frac{\ell v}{\nu_\beta}, \tag{4.1.9}$$

we obtain ℓ as

$$\ell = b \nu_\beta. \tag{4.1.10}$$

This means that if we use this expression for the characteristic length scale ℓ in Eq. 4.1.7, Re_C compares directly the relative influence of the linear and inertial contributions in the macroscopic filtration law. Unfortunately in practice, either experiments or direct numerical simulations (DNS) are needed to determine the parameter b. Moreover, Eq. 4.1.8 assumes a quadratic form, which is questionable when going from the linear to the non-linear regime [109, 110, 112, 113, 128, 130, 131]. In Section 4.3.2.1 we propose an expression for the Forchheimer number.

Yet another possibility is the use of a permeability-based Reynolds number [122, 132, 133, 134, 69, 121] defined as

$$Re_k = v \frac{\sqrt{K_\lambda/\epsilon_\beta}}{\nu_\beta}. \tag{4.1.11}$$

One of the main advantages of this definition is that $\ell = \sqrt{K_\lambda/\epsilon_\beta}$ is not a pure geometrical length scale. ℓ defined as such is associated with Stokes flow in the specific structure of interest, and characterizes the overall viscous dissipation in the porous medium. Therefore $\ell = \sqrt{K_\lambda/\epsilon_\beta}$ should be much better than a geometrical pore length-scale at characterising viscous effects for the purpose of comparing them to inertial effects, which is the point of a Reynolds number. Unfortunately, even Re_k is inaccurate in predicting the inertial deviation, as will be shown later on for a variety of porous structures (Section 4.3.2.2). An obvious example of this is the case of cylindrical pores, for which the non-Darcian, steady regime simply does not exist [113]. This is due to the fact that in cylindrical pores, the streamlines (*i.e.* lines that are parallel to the $\mathbf{v}_\beta-$ field) are locally orthogonal to velocity gradients $\nabla\mathbf{v}_\beta$. Under such circumstances, in the momentum part of the Navier-Stokes equations

$$\underbrace{\mathbf{v}_\beta \cdot \nabla \mathbf{v}_\beta}_{\text{advective term}} = -\frac{1}{\rho_\beta}\nabla p_\beta + \nu_\beta \nabla^2 \mathbf{v}_\beta + \mathbf{s}_\beta, \tag{4.1.12}$$

the advective term vanishes identically, cancelling inertia effects. In this case the Navier-Stokes equations reduce to the linear Stokes equations, until the first transition to a non-Darcian, unsteady turbulent regime, which is due to a flow instability that starts several orders of magnitude beyond the stage $Re_k = 1$ (*e.g.* , [135]).

In this paper, we use the framework of volume averaging to derive a filtration law for weakly inertial flows in periodic porous media. We carefully define the volume averaging operator and apply it to the Navier-Stokes equations in the porous medium. We make a separation of scales assumption to derive the volume-averaged equations, which are closed by a model of the average hydrodynamic force. This requires the modeling of small scale fields and leads to a closure problem (CP) over a representative elementary volume (REV).

We further use the CP to derive the expression for the Reynolds number, Re_C. We proceed by evaluating the order of magnitude of the advective term in the CP, and this allows us to correct Re_k with a new parameter C_λ, thus yielding Re_C. C_λ characterizes the likeliness of the flow in the microstructure to deviate from Darcy's law and is thus the *inertial sensitivity* of the microstructure. The filtration law is evaluated from direct numerical simulations (DNS) on a variety of porous structures and it is shown that Re_C is much better suited than Re_k to predict the non-Darcian transition, and resolves the pathological case of cylindrical pores. We finally use this new scaling to derive a generalized-Forchheimer law in a highly anisotropic porous medium.

4.2 Non-linear effects

In this section, we propose a framework to study the effect of inertia on the filtration law of a porous medium.

4.2.1 Pore scale flow model

We consider a rigid periodic porous medium, saturated with a Newtonian fluid. We call β the fluid-phase and σ the solid- phase within the domain, *cf.* Fig. 2.1. We focus on steady and incompressible flows as a response to a constant source term $\mathbf{s}_\beta$. Hence the fluid- phase is driven by the steady Navier-Stokes equations, *i.e.*

$$\nabla \cdot (\mathbf{v}_\beta \mathbf{v}_\beta) = -\frac{1}{\rho_\beta}\nabla p_\beta + \nu_\beta \nabla^2 \mathbf{v}_\beta + \mathbf{s}_\beta, \tag{4.2.1a}$$

$$\nabla \cdot \mathbf{v}_\beta = 0, \tag{4.2.1b}$$

$$\mathbf{v}_\beta = 0 \text{ at } \mathscr{A}_{\beta\sigma}, \tag{4.2.1c}$$

with ρ_β the density of the fluid. No-slip conditions are imposed on the fluid-solid interface $\mathscr{A}_{\beta\sigma}$.

Upscaling the Navier-Stokes equations through volume averaging has already received much attention in the literature (see, *e.g.* , [116, 136, 137]). Our development is slightly different in terms of the representation of the spatial deviations (the linear mapping in the cited literature is inconsistent with modeling microscopic inertial effects) and the construction of the anisotropic inertial correction to Darcy's law. The complete derivation provided in Appendix A leads to Eq. A.2.10 that we recall here

$$\frac{\ell^2}{\mu_\beta}\mathbf{g}_\beta(\boldsymbol{\lambda}, \delta) = -\mathbf{h}^* v. \tag{4.2.2}$$

Depending on v, the equation above yields the macroscopic pressure drop $\mathbf{g}_\beta$ for a steady inertial flow in the $\boldsymbol{\lambda}$ direction. The issue now is to determine $\mathbf{h}^*$ from Eqs. A.2.9.

We intend to study the effect of inertia on this filtration law. To characterize the evolution of $\mathbf{h}^*$ due to a flow in the $\boldsymbol{\lambda}$ direction, we build a frame of reference with $\boldsymbol{\lambda}$ and two orthogonal unit vectors

$(\mathbf{n}_1, \mathbf{n}_2)$, such that

$$\mathbf{n}_1 \times \mathbf{n}_2 = \boldsymbol{\lambda}, \tag{4.2.3}$$

where × denotes the usual vector product. In this frame, we decompose $\mathbf{f}$ (see Eq. 4.1.5), the correction to Darcy's law, into a drag component, $F_{||}$ and an orthogonal component, $F_{\perp}$, with ω the angle between the orthogonal term of $\mathbf{f}$ and $\mathbf{n}_1$. These quantities may be expressed as

$$\begin{aligned} F_{||} &= \frac{\boldsymbol{\lambda} \cdot \mathbf{f}}{K_{\lambda}^{-1}}, & (4.2.4a)\\ F_{\perp} &= ||\left(\mathbf{I} - \boldsymbol{\lambda}\boldsymbol{\lambda}\right) \cdot \frac{\mathbf{f}}{K_{\lambda}^{-1}}||, & (4.2.4b)\\ \omega &= \left(\left(\mathbf{I} - \boldsymbol{\lambda}\boldsymbol{\lambda}\right) \cdot \frac{\mathbf{g}_{\beta}}{\epsilon_{\beta}\mu_{\beta}K_{\lambda}^{-1}v}, \mathbf{n}_1\right). & (4.2.4c) \end{aligned}$$

The triplet $(F_{||}, F_{\perp}, \omega)$ completely determines $\mathbf{f}$ according to the relation

$$\mathbf{f} = K_{\lambda}^{-1}\left(F_{||}\boldsymbol{\lambda} + F_{\perp}\left(cos\left(\omega\right)\mathbf{n}_1 + sin\left(\omega\right)\mathbf{n}_2\right)\right). \tag{4.2.5}$$

The advantage of the decomposition expressed by Eq. 4.2.4 will become clear in the following.

4.2.2 Asymptotic analysis

In this section, we want to check that the form of our closure problem is compatible with results from the literature [109, 110, 130]. The end result of our analysis here is an asymptotic generalized-Forchheimer law (AGF); the developments starts with the identification of a parameter δ given by

$$\delta = \frac{\ell}{\nu_{\beta}}v, \tag{4.2.6}$$

and with the search of an asymptotic form of Eq. 4.2.2 when $\delta \ll 1$. According to Eq. A.2.9, we assume that the $\mathbf{v}^*$ and p^* fields can be approximated as

$$\begin{aligned} \mathbf{v}^* &= \mathbf{v}_0^* + \delta\mathbf{v}_1^* + \delta^2\mathbf{v}_2^* + O\left(\delta^3\right), & (4.2.7a)\\ p^* &= p_0^* + \delta p_1^* + \delta^2 p_2^* + O\left(\delta^3\right). & (4.2.7b) \end{aligned}$$

This yields

$$\mathbf{f} = \sum_{i\geq 0}^{N}\mathbf{f}^{(i)}\delta^i, \text{ with } \mathbf{f}^{(i)} = \mathbf{K}_D^{-1} \cdot \left\langle \mathbf{v}_{i0}^* \right\rangle^{\beta}, \tag{4.2.8}$$

where $\mathbf{v}_{i0}^{*}$ are solutions of Stokes problems (see Appendix B). This yields the asymptotic form of Eq. 4.2.2

$$\mathbf{g}_\beta = -\epsilon_\beta \mu_\beta \mathbf{K}_D^{-1} \cdot \left(\boldsymbol{\lambda} - \sum_{i \geq 1}^{N} \langle \mathbf{v}_{i0}^{*} \rangle^{\beta} \delta^{i} \right) v, \tag{4.2.9}$$

which is our asymptotic generalized-Forchheimer law. In Section 4.3, the AGF expressed in Eq. 4.2.9 is compared with data from DNS for different microstructures.

Numerical and experimental evidences [112, 113, 128, 131] indicate that $\mathbf{f}^{(1)}$ vanishes, leading to a first cubic correction to Darcy's law. This regime is referred to as the *cubic regime*, or *weak inertia regime*, and was studied by two-scale asymptotics [109, 110, 130], with theoretical results for periodic porous media. In particular, Firdaouss et al. [110], have shown that $\mathbf{f}^{(1)}$ must be zero for periodic porous media which verify the reversibility assumption

$$\mathbf{g}_\beta \left(-\boldsymbol{\lambda}, v \right) = -\mathbf{g}_\beta \left(\boldsymbol{\lambda}, v \right) + O\left(\delta^2 \right). \tag{4.2.10}$$

For example, a square array of cylinders verifies exactly the reversibility assumption, due to symmetry properties. It has further been shown [109, 130] that $F_{\|}^{(1)} = 0$ in periodic porous media, while the orthogonal term $F_{\perp}^{(1)}$ is a priori non-zero. This yields a *partial* cubic regime in the general case, or the cubic regime in the specific case of porous media for which $F_{\perp}$ vanishes due to characteristics of the microstucture. Such media are defined as *isotropic*, but it is likely that a zero $F_{\perp}$ requires a *disordered* microstructure, or a symmetry condition. Indeed ordered porous media may be isotropic with respect to the permeability ($\mathbf{K}_D = K_\lambda \mathbf{I}$), while the $F_{\perp}$ term is non-zero (*e.g.* [138]).

In [109, 110, 130], asymptotic expansions are performed on both the Reynolds number Re_C, and the ratio of microscopic and macroscopic scales

$$\epsilon_l = \frac{\ell_\beta}{L_v}, \tag{4.2.11}$$

where, for *technical* reasons intrinsic to the asymptotic method, the value of Re_C is related to the value of ϵ_l. Although there are cases for which this relation is justified, there is no *physical* reasons for this relation in the general case, as ϵ_l and Re_C are *a priori* independent parameters. In particular, the assumption $\epsilon_l \ll 1$ does not require Re_C to be small. Even for turbulent flows where $Re_C \gg 1$, the length scales separation assumption holds ($\epsilon_l \ll 1$) in homogeneous porous media [34]. Moreover a creeping flow may encounter strong shear, yielding $Re_C \ll 1$ while $\epsilon_l \sim 1$.

Our approach recovers all these theoretical results from the literature. We show that $F_{\|}^{(1)} = 0$ (see Appendix C) for any periodic porous medium. For media that satisfy the reversibility assumption, $F_{\perp}^{(1)} = 0$ is required for our AGF to be consistent. In the framework of volume averaging, we have derived the closure problem before carrying out the perturbation analysis in Re_C, keeping ϵ_l and Re_C independent. The form of our closure problem is further validated by DNS in Section 4.3.2.1.

4.2.3 Inertial sensitivity parameter

We use the closure problem (Eq. A.2.9) to develop a dimensionless number that characterizes the Darcy/non-Darcy transition. To do so, we use Eqs. 4.1.5 and 4.2.2 and rewrite the first equation in System A.2.9 as

$$\underbrace{\frac{\ell v}{\nu_\beta}\mathbf{v}^* \cdot \nabla^* \mathbf{v}^*}_{(I)} = -\nabla^* p^* + \nabla^{*2}\mathbf{v}^* + \underbrace{\epsilon_\beta \ell^2 \left(\mathbf{K}_D^{-1} \cdot \boldsymbol{\lambda} + \mathbf{f}\right)}_{(II)}. \tag{4.2.12}$$

In the creeping flow regime, term (I) in Eq. 4.2.12 is negligible and term (II) is the only source term. As the flow rate increases, $\mathbf{f}$ becomes important via the increasing importance of term (I). We thus consider the ratio of the orders of magnitude of terms (I) and (II). As term (II) is of order $\epsilon_\beta \ell^2 K_\lambda^{-1}$ at the Darcy/non-Darcy transition, we have

$$\frac{(I)}{(II)} \simeq \frac{\ell v}{\nu_\beta} \frac{\zeta\left(\mathbf{v}^* \cdot \nabla^* \mathbf{v}^*\right)}{\epsilon_\beta \ell^2 K_\lambda^{-1}}, \tag{4.2.13}$$

where the symbol ζ defines a norm for the field $\mathbf{v}^* \cdot \nabla^* \mathbf{v}^*$. ζ is essential in the evaluation of the order of magnitude of term (I). Any choice for ζ is acceptable, depending on the goal of the study. A choice of ζ is proposed in Section 4.3, where our goal is to find the proper Reynolds number to assess the validity of Darcy's law for a variety of porous media.

We now wish to eliminate ℓ from Eq. 4.2.12, and start from the consideration that, at steady state, the total rate of work of the pressure gradient balances the total internal viscous dissipation over the REV

$$\int_{\mathscr{V}_\beta} \mathbf{v}_\beta \cdot \left(-\mathbf{g}_\beta\right) dV = \int_{\mathscr{V}_\beta} \mu_\beta \nabla \mathbf{v}_\beta :^T \left(\nabla \mathbf{v}_\beta\right) dV. \tag{4.2.14}$$

We integrate a second time over $\mathscr{V}_\beta$ and recall Eq. A.1.6 to obtain

$$-\left\langle \mathbf{v}_\beta \right\rangle^\beta \cdot \mathbf{g}_\beta = \mu_\beta \left\langle \nabla \mathbf{v}_\beta :^T \left(\nabla \mathbf{v}_\beta\right)\right\rangle^\beta. \tag{4.2.15}$$

Rewriting the left-hand-side with definition 4.1.5 yields

$$\left\langle \nabla \mathbf{v}_\beta :^T \left(\nabla \mathbf{v}_\beta\right)\right\rangle^\beta = \boldsymbol{\lambda} \cdot \epsilon_\beta \left(\mathbf{K}_D^{-1} \cdot \boldsymbol{\lambda} + \mathbf{f}\right) \simeq \boldsymbol{\lambda} \cdot \epsilon_\beta \mathbf{K}_D^{-1} \cdot \boldsymbol{\lambda}, \tag{4.2.16}$$

at the Darcy/non-Darcy transition. Using the change of variables of Eq. A.2.2 we can write

$$\ell^2 \boldsymbol{\lambda} \cdot \epsilon_\beta \mathbf{K}_D^{-1} \cdot \boldsymbol{\lambda} = \left\langle \nabla^* \mathbf{v}^* :^T (\nabla^* \mathbf{v}^*) \right\rangle^\beta . \tag{4.2.17}$$

This gives an expression for ℓ, as

$$\ell = \sqrt{\frac{\left\langle \nabla^* \mathbf{v}^* :^T (\nabla^* \mathbf{v}^*) \right\rangle^\beta}{\boldsymbol{\lambda} \cdot \epsilon_\beta \mathbf{K}_D^{-1} \cdot \boldsymbol{\lambda}}}, \tag{4.2.18}$$

which we use in Eq. 4.2.13

$$\frac{(I)}{(II)} \simeq \frac{v}{\nu_\beta} \sqrt{\frac{K_\lambda}{\epsilon_\beta}} \frac{\zeta \left(\mathbf{v}^* \cdot \nabla^* \mathbf{v}^* \right)}{\sqrt{\left\langle \nabla^* \mathbf{v}^* :^T (\nabla^* \mathbf{v}^*) \right\rangle^\beta}} \sqrt{\frac{\boldsymbol{\lambda} \cdot \mathbf{K}_D^{-1} \cdot \boldsymbol{\lambda}}{K_\lambda^{-1}}}. \tag{4.2.19}$$

We approximate $\mathbf{v}^*$ by $\mathbf{v}_0^*$, a zero order approximation in terms of δ (see Eq. 4.2.7), and obtain

$$\frac{(I)}{(II)} \simeq \frac{v}{\nu_\beta} \sqrt{\frac{K_\lambda}{\epsilon_\beta}} \frac{\zeta \left(\mathbf{v}_0^* \cdot \nabla^* \mathbf{v}_0^* \right)}{\sqrt{\left\langle \nabla^* \mathbf{v}_0^* :^T (\nabla^* \mathbf{v}_0^*) \right\rangle^\beta}} \sqrt{\frac{\boldsymbol{\lambda} \cdot \mathbf{K}_D^{-1} \cdot \boldsymbol{\lambda}}{K_\lambda^{-1}}}. \tag{4.2.20}$$

We now define Re_C as

$$Re_C = \frac{v}{\nu_\beta} \sqrt{\frac{K_\lambda}{\epsilon_\beta}} C_\lambda, \tag{4.2.21}$$

with the inertial sensitivity, C_λ, defined as

$$C_\lambda = \frac{\zeta \left(\mathbf{v}_0^* \cdot \nabla^* \mathbf{v}_0^* \right)}{\sqrt{\left\langle \nabla^* \mathbf{v}_0^* :^T (\nabla^* \mathbf{v}_0^*) \right\rangle^\beta}} \sqrt{\frac{\boldsymbol{\lambda} \cdot \mathbf{K}_D^{-1} \cdot \boldsymbol{\lambda}}{K_\lambda^{-1}}}, \tag{4.2.22}$$

such that by construction

$$Re_C \simeq \frac{(I)}{(II)}. \tag{4.2.23}$$

The length scale ℓ therefore corresponds to

$$\ell = \sqrt{\frac{K_\lambda}{\epsilon_\beta}} C_\lambda. \tag{4.2.24}$$

The distribution pattern of the advective term $\mathbf{v}_0^* \cdot \nabla^* \mathbf{v}_0^*$ is closely related to the microstructure and the flow direction, as shown on Fig. 4.4, Section 4.3.2.2. The effect of inertia on Darcy's law is driven by the shape of the microstructure, and the topological parameter C_λ measures the ability of inertia to affect Darcy's law. The inertial sensitivity C_λ is specific to both the porous medium and the flow direction $\boldsymbol{\lambda}$. We can distinguish among different cases:

- $C_\lambda \simeq 1$: $\sqrt{K_\lambda / \epsilon_\beta}$ is the proper length scale to measure the effects of inertia.

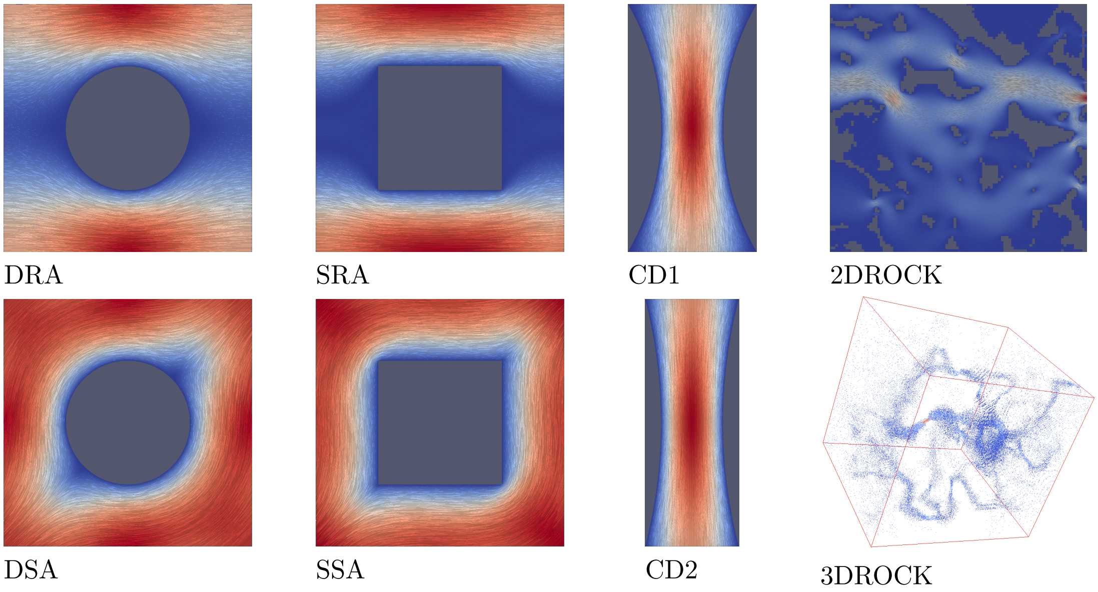

Figure 4.1: Normalized fields of velocity magnitude for Stokes flows through the considered porous media. Small (large) values correspond to blue (red) area. We refer to Table 4.1 for the meaning of the acronyms that we use to refer to each porous medium.

- $C_\lambda \ll 1$: $Re_k = 1$ does not capture the inertial transition, as illustrated by the limit case of cylindrical pores. In this case, C_λ identically vanishes as streamlines are orthogonal to velocity gradients. Therefore Darcy's law is correct for any Re_k in the laminar regime and breaks down only when transition to unsteady flow occurs [113].

- $C_\lambda \gg 1$: This situation is opposite to the previous one. Effects of inertia impact the macroscale Darcy's law early, while $Re_k \ll 1$ still holds. There is no obvious examples of geometry for this case, but it is more likely that tortuous geometries generate large values of C_λ (see later Table 4.1).

This classification resolves the issue encountered with certain porous media for which $Re_k \ll 1$ is not the correct order of magnitude to assess the validity of Darcy's law. The relevance of Re_C is further assessed in Section 4.3.2.2 by the interpretation of numerical experiments over a variety of porous structures.

4.3 Numerical results

We test the AGF and validate the relevance of Re_C in describing the inertial transition on model and realistic porous media with various microstructures (Fig. 4.1). We consider

- two-dimensional arrangements of cylinders,

- two-dimensional convergent-divergent unit cells of equal throat size,

Table 4.1: Computed values of C_λ and $F_\parallel^{(2)}$ for each porous media. The acronym and full name of each porous medium is indicated as well.

short-cut	C_λ	$F_\parallel^{(2)}$	medium
3DROCK	176	$1.07 \times 10^{+03}$	three-dimensional rock
2DROCK	5.77	3.92×10^{-01}	two-dimensional rock
DSA	0.62	2.84×10^{-02}	disks in staggered arrangement
DRA	0.49	8.46×10^{-03}	disks in regular arrangement
SSA	0.77	3.77×10^{-02}	squares in staggered arrangement
SRA	0.36	4.43×10^{-03}	squares in regular arrangement
CD1	0.19	1.08×10^{-03}	convergent-divergent 1
CD2	0.10	3.00×10^{-04}	convergent-divergent 2

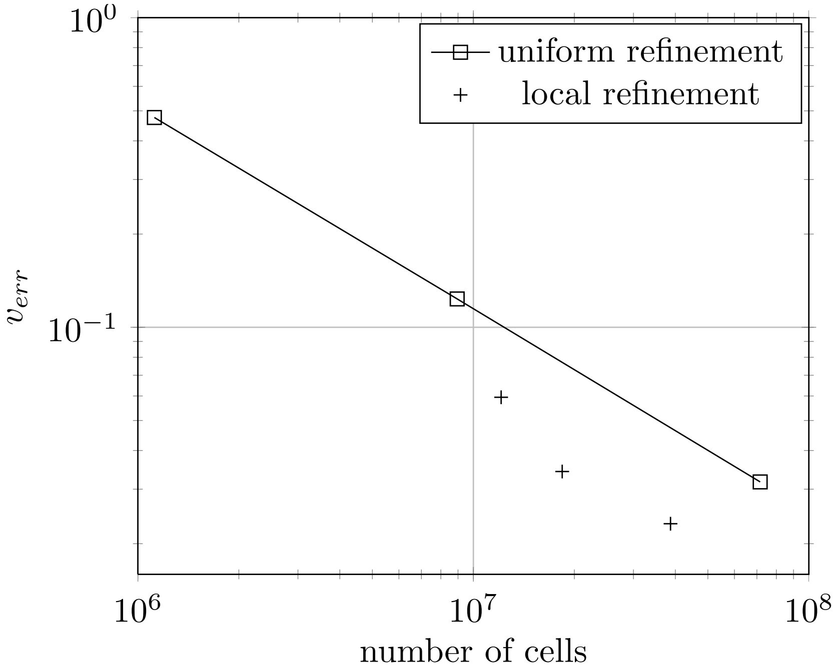

Figure 4.2: Mesh convergence for the 3DROCK geometry. The local refinement strategy accelerates the convergence to mesh independence compared to the uniform refinement strategy.

- two- and three-dimensional geometries exhibiting complex, realistic geometrical features, obtained by x-ray tomography imaging of a sandstone.

The acronyms of all studied geometries are provided in Table 4.1.

4.3.1 Method

Flow simulations are carried out with the C++ toolbox Open∇FOAM®, which allows for the development of numerical solvers, and comes up with pre- and post- processing utilities for computational fluid dynamics (CFD). Open∇FOAM® is released as free and open-source software, and this allows the user to customize the source code in order to implement her/his own problem. This aspect of Open∇FOAM® is crucial, because in order to compute the coefficients of the asymptotic form of $F_\parallel$,

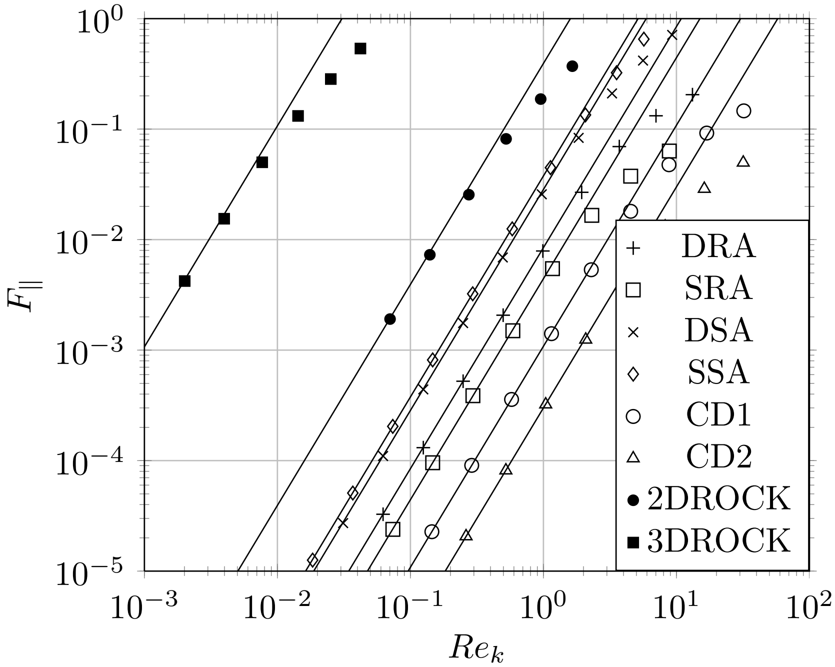

Figure 4.3: Drag Forchheimer term $F_\parallel$ as function of Re_k. Data from DNS (symbols) and AGF (solid lines).

we need to solve Stokes problems obtained in Appendix B with specific source terms. We use a classical finite-volume discretization method. For each cell of the mesh, an integral form of the equations to solve is obtained by integrating the momentum- and mass- conservation law over the volume of the cell. The Gauss theorem is then applied to write the volume integrals as surface integrals, which involve field- and gradient- evaluation on cell faces. The evaluation of different quantities on cell faces are performed by linear interpolation between cell centres, or by use of a finite difference scheme for the gradients.

For periodic geometries, imposition of periodic boundary conditions is trivial. For the 3DROCK case, while periodic conditions are imposed on the inlet and outlet faces by adding a thin layer of fluid, symmetry conditions are imposed on other faces. One should notice that this is equivalent to symmetrizing the geometry and imposing periodic conditions. Symmetry conditions are also imposed on each side of the 2DROCK case. As the order of the discretization method is relatively low, and because we need a relatively high accuracy in our simulations, the number of mesh points to achieve mesh independence can be very large. We must adopt the proper method according to the geometry of interest. Since we are interested in the value of the macroscopic parameter $F_\parallel$, we only use a macroscopic convergence criterion to assess mesh independence. For a given value of the pressure gradient, we compute the relative error on v between two refinement levels to evaluate the accuracy of the simulation. For 2D geometries, we use a simple uniform mesh and uniformly refine until mesh independence is achieved. Hence the fine mesh is a uniform structured hexahedral mesh for these geometries. For the 3DROCK case however, this simple approach would involve a too large computational cost.

Mesh independence with a uniform structured hexahedral mesh for the 3DROCK geometry is achieved with $5.73 \cdot 10^8$ cells. This number of cells is comparable to the number of cells used in other numerical study of the inertial deviation from Darcy's law in sandstones, see *e.g.* [121]. This requires approximately 10^4cores hours to converge on the supercomputer EOS-CALMIP. This large cost in CPU time is due to the fact that the 3DROCK geometry is a 3D, tortuous geometry that contains many more pore throats and sizes than the other simple geometries studied here. Typically, the ratio of the largest pore size to the smallest pore throat is around 10 for the 3DROCK. To reduce the number of mesh points, local refinements are performed for the 3DROCK geometry. We first compute an expensive reference solution with a uniform structured hexahedral mesh. Then, a coarser mesh, that gives low-accuracy results, is locally refined only in regions where the value of the viscous dissipation is above a certain threshold (*i.e.* regions of high velocity gradients $\nabla \mathbf{v}_\beta$). For each level of refinement, the threshold of viscous dissipation above which cells are refined is adjusted to find a compromise between the number of cells and the accuracy of the simulation. This process allows to approximate fairly well the reference solution (within the desired accuracy criterion) with only $1.8 \cdot 10^7$ mesh cells (Fig. 4.2). As a result, the local refinement process reduces the required amount of CPU time by an order of magnitude, making simulations on the 3DROCK medium tractable.

4.3.2 Inertial effects

For each geometry, K_λ is first computed by carrying out Stokes flow simulations. We then solve for the Navier-Stokes equations (Eq. 4.2.1) and compute $F_{\|}$ from Eq. 4.2.4. The drag Forchheimer term $F_{\|}$ is plotted in Fig. 4.3 as a function of the Reynolds numbers Re_k for the porous media represented in Fig. 4.1.

4.3.2.1 Asymptotic form

To validate the developments of Section 4.2.2 and the form of the CP that is the base of our theory, we compute coefficients of the asymptotic form of $F_{\|}$ for the considered porous media. For that purpose, the derivation of the system of equations to resolve for each order i is presented in full details in Appendix B. These developments yield

$$\mathbf{S}_i^* = -\nabla^* p_i^* + {\nabla^*}^2 \mathbf{v}_i^* + \epsilon_\beta \mathbf{h}_i^*, \tag{4.3.1a}$$

$$\nabla^* \cdot \mathbf{v}_i^* = 0, \tag{4.3.1b}$$

$$\mathbf{v}_i^* = 0 \text{ at } \mathscr{A}_{\beta\sigma}, \tag{4.3.1c}$$

The same numerical method as the one described above is adapted to resolve Eqs. B.0.1, with proper source terms $\mathbf{S}_i^*$. These source terms are given explicitely in Appendix B. As explained in Appendix B, the numerical resolution of Eqs. B.0.1 provides $F_{\parallel}^{(i)}$ at any order i. The numerical results for $F_{\parallel}^{(i)}$ are shown in Table 4.1. For each geometry, $F_{\parallel}^{(1)}$ is zero (up to the order of accuracy of the simulation) and $F_{\parallel}^{(2)}$ accurately matches the DNS (see Fig. 4.3, solid lines), therefore validating our form of CP. Furthermore, the scaling $F_{\parallel} \sim Re_C^2$ of the weak inertia regime is universal across the samples tested. A possible expression of the Forchheimer number to capture the limit of Darcy's law is (here, $F_{\perp} \ll F_{\parallel}$)

$$F_{\lambda} = F_{\parallel}^{(2)} Re_k^2, \tag{4.3.2}$$

with the inertial deviation from Darcy's law occuring at $F_{\lambda} = 0.1$. As shown by experiments [100, 103, 139], a quadratic dependence of the pressure drop on the flow rate eventually occurs, but this regime is beyond the velocity range studied here and cannot be captured by our asymptotic development.

4.3.2.2 Validation of Re_C

Fig. 4.3 shows the different behaviours of $F_{\parallel}$ for the various media considered; notably, the 3DROCK geometry has a very early deviation from Darcy's law. This results is in agreement with the results obtained in [121]. In this article, the authors evaluate the deviation from Darcy's law on a few sample of sandstones. They find that the value of the Reynolds numbers at the deviation from Darcy's law varies of several orders of magnitude, depending on the type of sandstone. Such differences cannot be captured only by a pore throat size or even by a permeability-based Reynolds numbers. This is because Reynolds numbers based only on porosity, permeability and pore size cannot differentiate geometries depending on their ability to develop advection dominated areas as the Reynolds number increases. This can be better accounted for by Re_C thanks to the inertial sensitivity C_{λ}. To illustrate this, we evaluate C_{λ} for porous media represented in Fig. 4.1, from Eq. 4.2.21 and 4.2.22, recalling that C_{λ} depends on the advective term $\mathbf{v}_0^* \cdot \nabla^* \mathbf{v}_0^*$ (*cf.* Eq. 4.2.22).

In Fig. 4.4, we can visualize the normalized fields of $||\mathbf{v}_0^* \cdot \nabla^* \mathbf{v}_0^*||$ in the selected ordered porous media. The pattern is very different from a geometry to another. C_{λ}, via ζ, uses this signature to characterize the topology of a porous medium in terms of the distribution of the advective term within it. To do so, we propose to define ζ as a generalized mean of order n

$$\zeta \left(\mathbf{v}_0^* \cdot \nabla^* \mathbf{v}_0^* \right) = \left(\langle ||\mathbf{v}_0^* \cdot \nabla^* \mathbf{v}_0^*||^n \rangle^{\beta} \right)^{1/n}. \tag{4.3.3}$$

We have tested a few values of n in Eq. 4.3.3. Results are plotted on Fig. 4.7. For $n = 1$, whilst the curves collapse well for simple geometries, there is still a gap between $2D$- and $3D$ROCK geometries

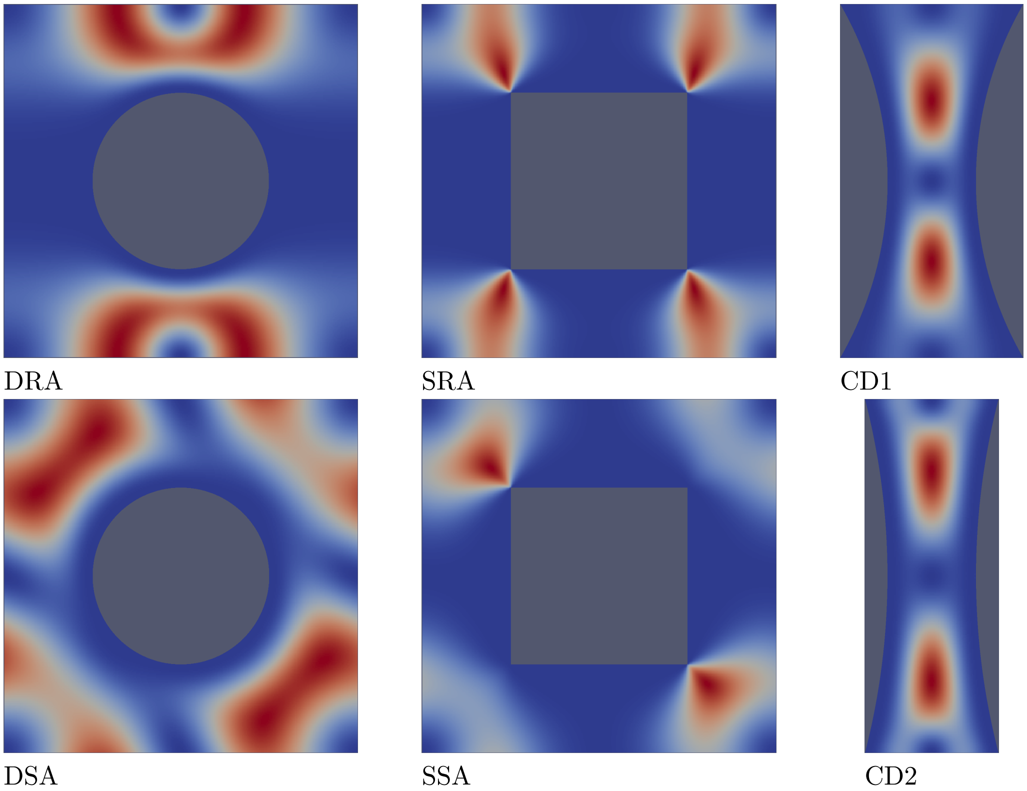

Figure 4.4: Normalized fields of $||\mathbf{v}_0^* \cdot \nabla^* \mathbf{v}_0^*||$ in model porous media. Small (large) values correspond to blue (red) area.

and the other cases. We assume that this is due to the weight given to high values of $||\mathbf{v}_0^* \cdot \nabla^* \mathbf{v}_0^*||$ in the computation of C_λ in Eq. 4.2.22. To verify this assumption, we increase the value of n, thus augmenting the weight of high values of $||\mathbf{v}_0^* \cdot \nabla^* \mathbf{v}_0^*||$ in the computation of C_λ. While the good collapse for simple geometries is conserved, the curves of $2D$- and $3D$ROCK geometries tend to collapse with the others on Fig. 4.7. This suggests that the effect of inertia is more localized in $2D$- and $3D$ROCK geometries than in ordered ones. The best collapse of the curves is found for $n = 4$ and values of C_λ in Table 4.1 refer to this n. Connecting with Fig. 4.3, we observe that for each geometry, the earlier the rise in $F_{||}$, the larger the value of C_λ; this shows that the form of ζ allows C_λ to be a consistent indicator to predict the strength of the effects of inertia on Darcy's law. From a quantitative point of view, Re_C is a much better indicator than Re_k, as the data scatter on the bottom plot of Fig. 4.7 is much reduced compared to Fig. 4.3. This is further emphasized below in the case of anisotropic porous media.

4.3.3 Filtration law for a model anisotropic structure

While in the linear regime the tensorial writing of Darcy's law (Eq. 5.1.1) provides a filtration law for any flow direction, a difficult issue with inertial flows is the derivation of the filtration law in anisotropic

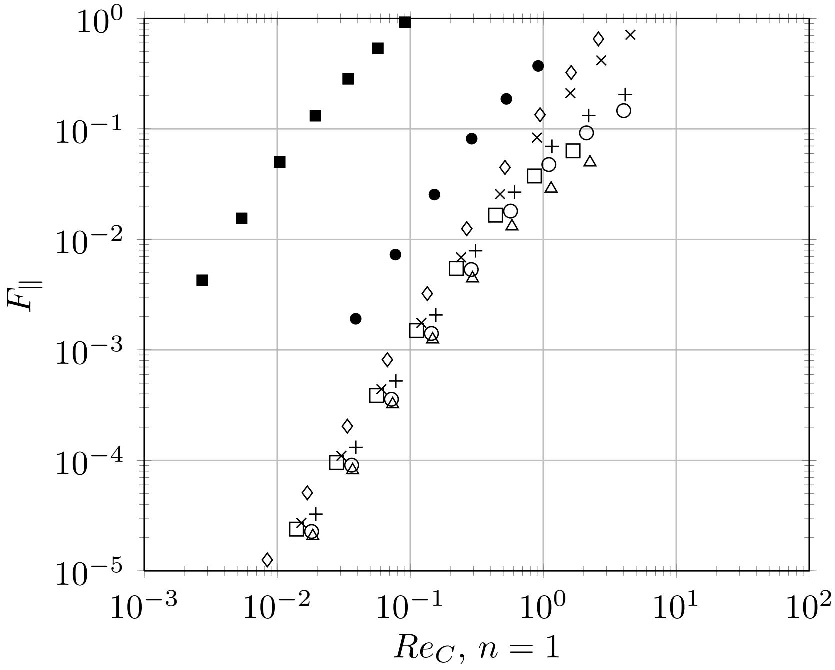

Figure 4.5: *Parallel* component of the inertial correction for different definitions of Re_C (here, $n = 1$).

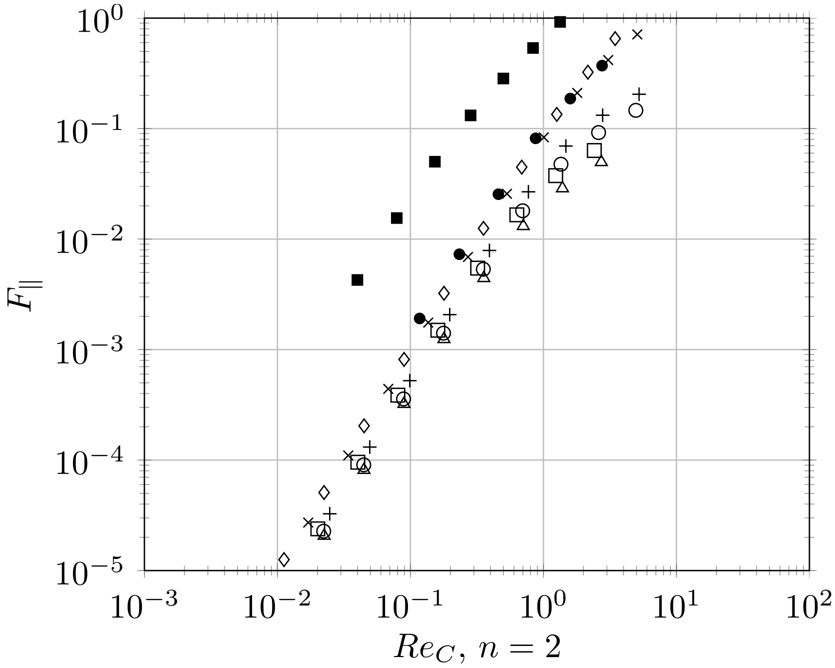

Figure 4.6: *Parallel* component of the inertial correction for different definitions of Re_C (here, $n = 2$).

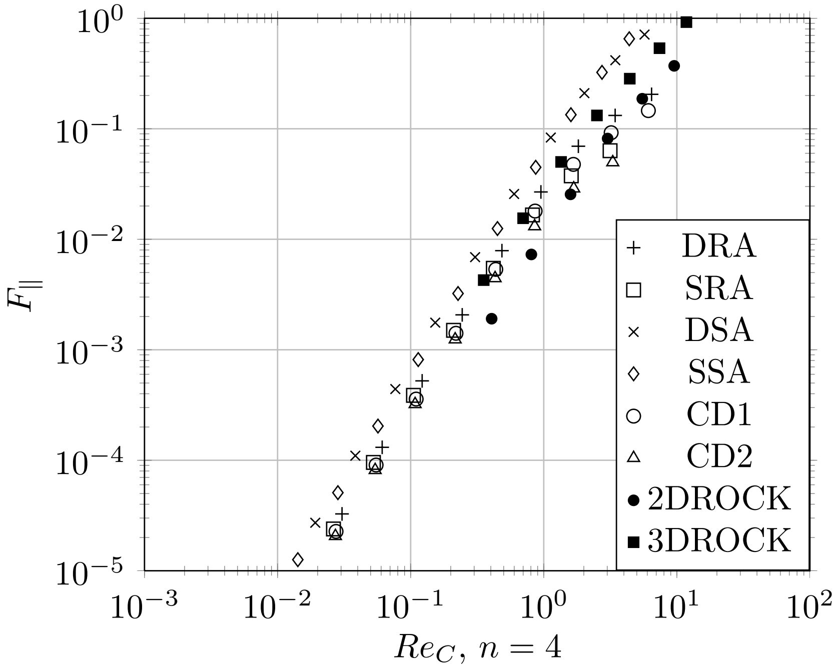

Figure 4.7: *Parallel* component of the inertial correction for different definitions of Re_C (here, $n = 4$). The inertial transition starts at $Re_C \sim 1$ for all model porous media when $n = 4$.

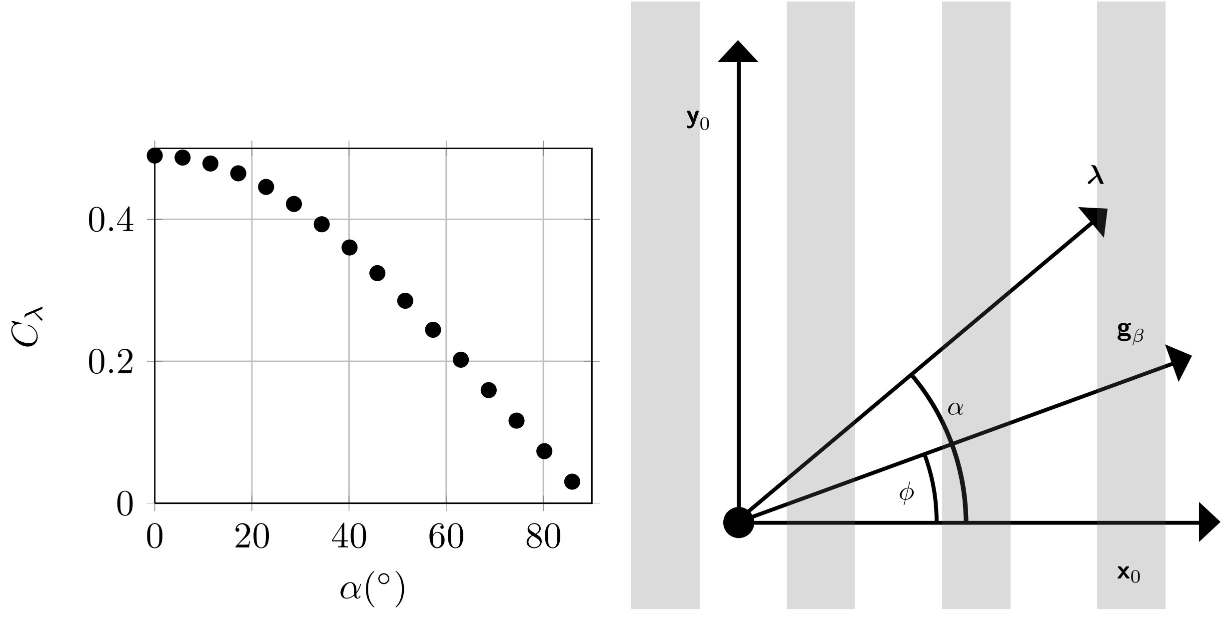

Figure 4.8: C_λ as a function of α for a regular array of cylinders. $\alpha = 0$ corresponds to a flow orthogonal to the cylinders axis, $(\alpha = \pi/2, C_\lambda = 0)$ corresponds to a flow parallel to the cylinders axis. Values of C_λ are computed from Eq. 4.2.22 with $n = 4$.

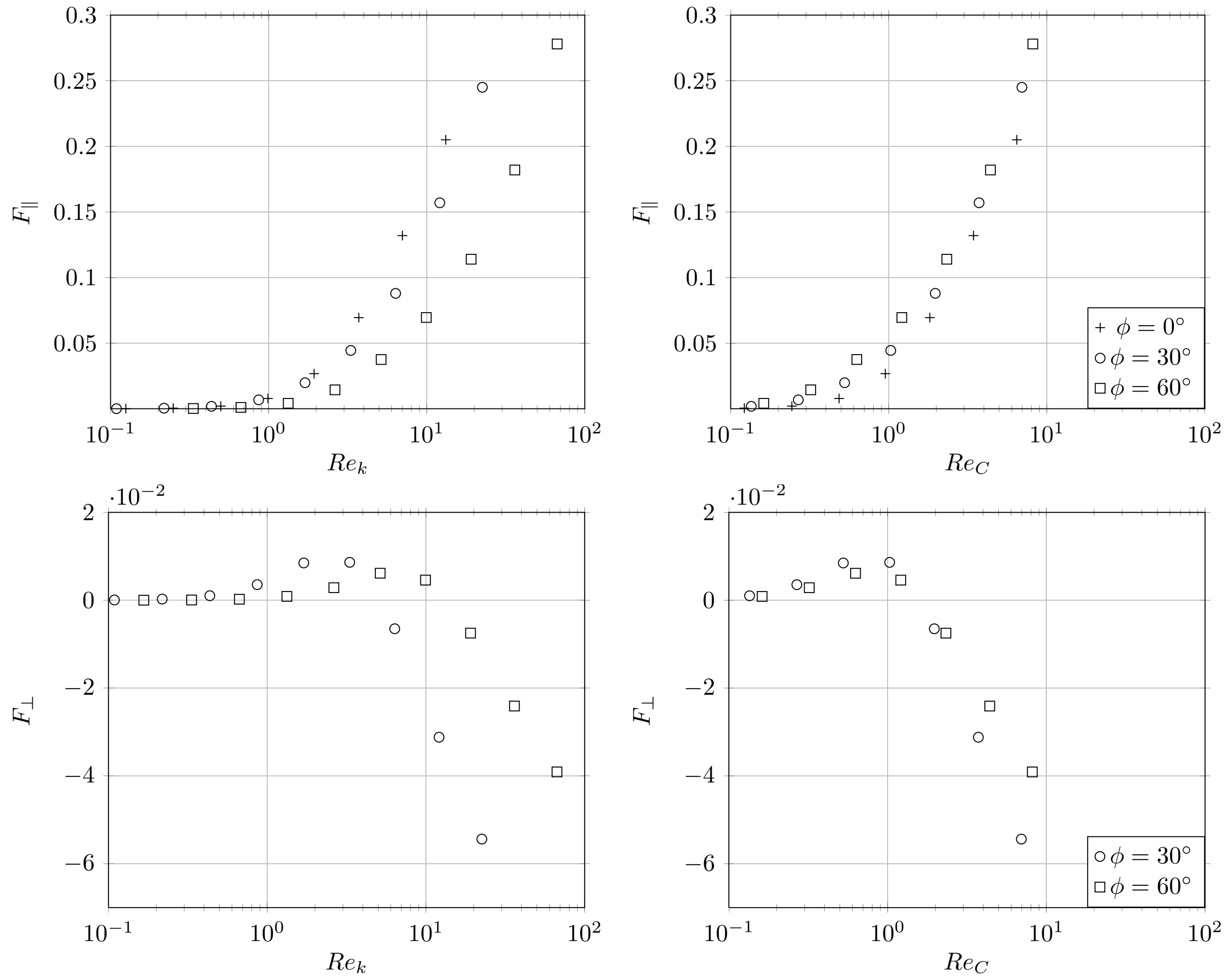

Figure 4.9: $F_{\|}$ and $F_{\perp}$ as function of Re_k and Re_C for a regular array of cylinders. Re_C is computed from Eq. 4.2.21. Values of C_λ are provided on Fig. 4.8.

porous media, since the characteristics of the filtration law must be determined for each direction. An expensive solution consists in building a dataset by numerical simulations or experiments, for each Reynolds number and direction of the flow [140]. Here, we propose a solution for a restricted range of Reynolds number, but at a much more affordable cost than the DNS, as it requires only a few flow simulations to give a filtration law for any direction.

We consider an orthotropic porous medium made of a regular arrangement of cylinders (Fig. 4.8) of porosity $\epsilon_\beta = 0.8036$. Let ϕ be the angle between the pressure gradient and the cylinders' axis. For three values of ϕ, the evolution of $F_{\|}$ as a function of Re_k and Re_C is displayed in Fig. 4.9. For a given ϕ, the flow direction varies with Re_C. Hence, $C_\lambda(\phi)$ is computed for the flow direction corresponding to $F_{\|} = 0.1$

$$C_\lambda(\phi) = C_\lambda\left(\boldsymbol{\lambda}\left(\phi, F_{\|} = 0.1\right)\right). \tag{4.3.4}$$

Fig. 4.9 shows that with this definition, the curves of $F_{\|}$ and $F_{\perp}$ tend to collapse. We now explain how this can be used to derive a filtration law for this range of Re_C.

As $\mathbf{v}_0^*$ arises from a Stokes equation, the $\mathbf{v}_0^*$ field corresponding to a given flow direction $\boldsymbol{\lambda}$ can be obtained as

$$\mathbf{v}_0^* = \mathbf{M}_0^* \cdot \boldsymbol{\lambda}, \tag{4.3.5}$$

where $\mathbf{M}_0^*$ is solution of (see Appendix B)

$$\begin{aligned} 0 &= -\nabla^* \mathbf{m}_0^* + \nabla^{*2} \mathbf{M}_0^* + \epsilon_\beta \ell^2 \mathbf{K}_D^{-1}, && (4.3.6a) \\ \nabla^* \cdot \mathbf{M}_0^* &= 0, && (4.3.6b) \\ \mathbf{M}_0^* &= 0 \text{ at } \mathscr{A}_{\beta\sigma}. && (4.3.6c) \end{aligned}$$

Let ϕ be the angle between the pressure gradient and the cylinders' axis. This allows to determine C_λ for any flow direction $\boldsymbol{\lambda}$ (Fig. 4.8) with only three flow simulations in three independent directions of space, in order to build $\mathbf{M}_0^*$. Then, instead of building an expensive dataset, we can compute the profile of $\left(F_{\|}, F_{\perp}\right)$ for one value of the flow direction $\boldsymbol{\lambda}^0$, to generalize to any values of $\boldsymbol{\lambda}$. Indeed, the collapse of the curves in Fig. 4.9 translates into

$$\left(F_{\|}, F_{\perp}\right)(\boldsymbol{\lambda}, v) = \left(F_{\|}, F_{\perp}\right)\left(\boldsymbol{\lambda} = \boldsymbol{\lambda}^0, Re_C(\boldsymbol{\lambda}, v)\right), \tag{4.3.7}$$

which provides a profile for $F_{\|}(\phi, v)$ and $F_{\perp}(\phi, v)$ with a limited number of simulations. This feature is of importance in applications for which a large number of simulations is prohibited due to the large amount of computational time required.

4.4 Conclusion

The volume averaging method is used to investigate the onset of inertial effects for flows in porous media. The introduction of the new Reynolds number, Re_C, captures well the Darcy/non-Darcy transition. This number contains a parameter, C_λ, which characterizes the sensitivity to inertia of a microstructure for a given flow direction, and is defined as

$$Re_C = \frac{\upsilon\sqrt{K_\lambda/\epsilon_\beta}}{\nu_\beta} C_\lambda. \tag{4.4.1}$$

We show that this definition of Re_C is appropriate to measure the effect of microscopic inertia on the filtration law. Further, we find that a possible application of this new scaling is the derivation of a correction to Darcy's law for weakly inertial flows in highly anisotropic porous media, where the tensorial Darcy's law collapses.

Finally, our study focuses on the evolution of $F_{\|}$, while the examination of the orthogonal component $F_{\perp}$ and of the angle ω (Eq. 4.2.4) is left for future work. Anisotropic, ordered, three-dimensional microstructures are expected to generate varying features of $F_{\perp}$ and ω with increasing Re_C; such features are the object of current research efforts.

Chapter 5

Unsteady flow through elastic porous media

As introduced in Section 1.1.1, turbulent flows over a poro-elastic layer are characterized by a broad range of scales. Toward the development of a macroscopic model, modeling the small-scale flow phenomena inside the porous layer is a required step. This is due to the fact that we do not want to compute the small-scale flow features, but they still affect the behaviour of the large scale flow. The ”small-scale phenomena” term refers here to both solid- and fluid- phase phenomena (vortex shedding and stem scale displacement, the two are related by the no-slip boundary condition at the fluid-solid interface). We expect that these small-scale phenomena have an effect on the large-scale flow only, *i.e.* that the large-scale solid phase is unaffected by the small-scale. In other words while the small-scale flow features are involved in the large-scale flow transport, the small- and large- scales for the solid-phase are not coupled.

5.1 Model elastic porous media

In the porous medium theory, the effect of the small-scale on the large scale can sometimes be modeled by means of effective parameters. These effective parameters should be determined with a good accuracy as they drive the quality of the macroscopic model. A straightforward, well-known example of effective parameter is the Darcy permeability $\mathbf{K}_D$

$$\mathbf{g}_\beta = -\epsilon_\beta \mu_\beta \mathbf{K}_D^{-1} \cdot \langle \mathbf{v}_\beta \rangle^\beta . \tag{5.1.1}$$

Eq. 5.1.1 is a filtration law, *i.e.* it relates the volume average velocity $\langle \mathbf{v}_\beta \rangle^\beta$ to the pressure gradient $\mathbf{g}_\beta$ for a Stokes flow in a porous medium. The Darcy permeability encapsulates the macroscopic viscous dissipation generated by the multiple, complicated small-scale flow structures occurring within the pores. It is well-known however that this filtration law (Darcy's law, Eq. 5.1.1) takes advantage of the fact that the Stokes equation is linear, and is valid only in the range of small inertia effects. When non-linear effects occur, such as inertia or fluid-structure interaction at the pore-scale, the determination of the filtration law requires direct measurements, either through experiments or numerical simulations. In this section, we perform a numerical study of the effect of pore scale fluid-structure interaction on the filtration law. This interaction can be observed when a fluid flows at moderate Reynolds number within an elastic porous medium. Above a certain Reynolds number, the fluid flow within a periodic array of cylinders becomes unsteady [33]. This arises from a flow instability generated by the non-linear term in the Navier-Stokes equations. This flow unsteadiness generates an unsteady hydrodynamic force at the pore-scale that deforms the elastic pores. In turn, these unsteady deformations modify the geometry of the porous medium and impact the flow and viscous dissipation. In other words, the fluid-structure coupling that occurs at the stem scale has an effect on the permeability (or filtration law, Eq.5.1.1) of the porous medium. The knowledge of the filtration law is crucial to the modeling of the large scale in many processes.

Heat exchangers design is a typical application of the study of unsteady flow confined in an elastic matrix. In turbulent regime, the flow across an array of cylinders is strongly unsteady and intermittent and causes the cylinders to vibrate. This phenomenon is called the fluid-elastic instability. This fluid-elastic interaction may generate large displacements and cause deterioration of the heat exchanger if not taken into account in the design of heat exchanger. Due to the significant industrial implications, there have been many efforts in getting insight on this topic in order to provide design constraints so that this instability is damped [141, 142] and deterioration is avoided. Although these studies provide a useful background, our context is a little different with regard to a few aspects. Roughly speaking, our tubes are much softer, and our range of Reynolds number is typically between 10^2 and 10^3. It is much smaller than the Reynolds numbers considered in industrial applications, where often the Reynolds number is beyond 10^4. So currently, there is a lack of data corresponding to our case. Moreover, in heat exchangers, the stiffness and damping of tubes is set according to the operating microscopic flow conditions. In our study it is the opposite, as the poro-elastic medium is designed to manipulate the large scale turbulence over the porous medium, for example so as to maximize the vertical mixing due to coherent structures [29]. Hence the stiffness of the fibres is set with a macroscopic criterion. At the microscopic level the stiffness perceived by our system depends on this macroscopically set stiffness, *i.e.* the stiffness is an input for the microscopic level. We need to know the effect of elasticity of the

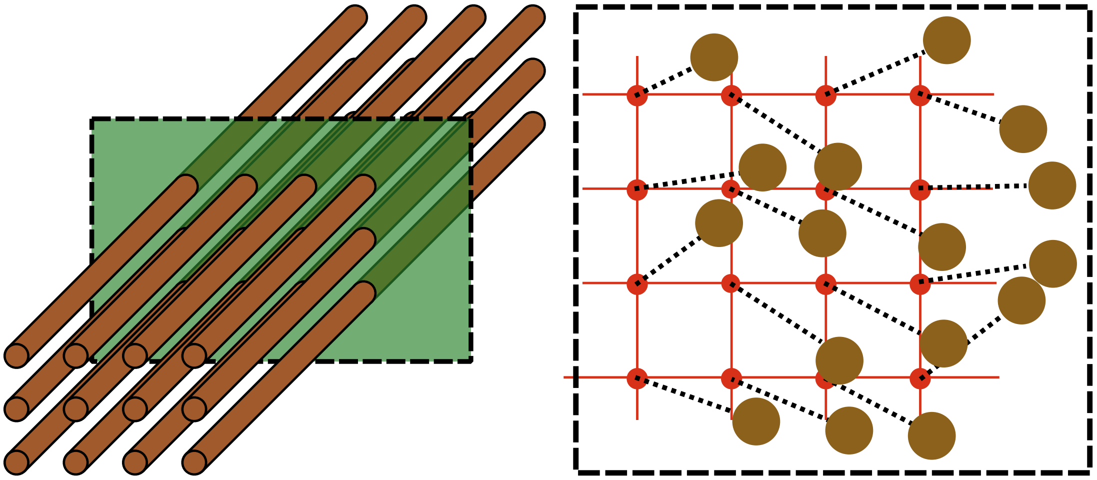
(a) (b)

Figure 5.1: Periodic cell with elastically mounted cylinders corresponds to a cross section (plane delimited with a dashed line) of the bundle of fibres. The cylinders are attached to their rest position by linear springs symbolized by dotted lines.

porous matrix on the filtration law, to be able to describe the macroscopic flow with accuracy. To get insight on this complex scientific issue, we start with a simple case.

The simple model we consider is an array of parallel cylinders of porosity 0.8, *i.e.* the unit cells are twice as large as the diameter of the cylinders. The cylinders are free to move, except that they are attached by a linear spring to a rigid regular matrix. The case is two-dimensional (2D), *i.e.* the flow is 2D and the displacements of the cylinders take place in the plane orthogonal to the fibres. This simple 2D model might seem irrelevant to our 3D bundle of tubes. Actually the 3D case (see Fig. 5.1) resembles a lot the 2D case when the fluid flows at moderate Reynolds number in the direction orthogonal to the fibres, with periodic conditions. Moreover if the fibres' displacement is not too large, we can consider that any cross section of the fibre remains in the same plane. This point is further discussed in the following, where we show that this 2D study should be limited to a high enough stiffness.

As explained in Section 3.3.2.2, a periodic flow is acceptable to evaluate the filtration law in a porous medium. Hence the domain has periodic boundary conditions for both the fluid pressure and velocity (p_β, $\mathbf{v}_\beta$) and the solid velocity and phase indicator ($\mathbf{v}_\sigma$, γ_σ). The objectives here are

- to develop a numerical method that provides data on the filtration law depending on the characteristics (stiffness, density) of the porous medium when the flow is unsteady, and

- to question the limits of the model in terms of geometry, REV size, the 2D assumption and numerical method.

5.1.1 Mechanics

Each cylinder is subjected to the restoring force of its linear spring, and the hydrodynamic force applied by the fluid. The force balance on a cylinder reads

$$m\frac{d^2\mathbf{x}}{dt^2} = k\left(\mathbf{X}_0 - \mathbf{x}\right) + \mathbf{f}_h, \tag{5.1.2}$$

where $\mathbf{x}$ is the position of the center of the cylinder and $\mathbf{f}_h$ is the hydrodynamic force applied to the cylinder. $\mathbf{X}_0$ is the position of the cylinder when the elastic matrix is at rest, symbolized by the grid on Fig. 5.1b. k is the spring stiffness. $\mathbf{f}_h$ reads

$$\mathbf{f}_h = \int_{S_{\text{cylinder}}} \mathbf{n}_S \cdot \left(-\mathbf{I}p_\beta + \mu_\beta\left[\nabla\mathbf{v}_\beta +^T \left(\nabla\mathbf{v}_\beta\right)\right]\right) dS. \tag{5.1.3}$$

In the fluid phase, we have the Navier-Stokes equations

$$\frac{\partial \mathbf{v}_\beta}{\partial t} + \nabla\cdot\left(\mathbf{v}_\beta\mathbf{v}_\beta\right) = -\frac{1}{\rho_\beta}\nabla p_\beta + \frac{\mu_\beta}{\rho_\beta}\nabla^2\mathbf{v}_\beta + \mathbf{s}_\beta, \tag{5.1.4}$$

$$\nabla\cdot\mathbf{v}_\beta = 0. \tag{5.1.5}$$

Using the following dimensionless variables

$$\begin{aligned} x' &= \frac{x}{D} \\ \mathbf{v}'_\beta &= \frac{\mathbf{v}_\beta}{U} \\ t' &= U\frac{t}{D} \\ Re &= \frac{\rho_\beta U D}{\mu_\beta}, \end{aligned} \tag{5.1.6}$$

one may introduce the dimensionless form of the Navier-Stokes equations

$$\begin{aligned} \frac{\partial \mathbf{v}'_\beta}{\partial t'} + \mathbf{v}'_\beta\cdot\nabla'\mathbf{v}'_\beta &= -\nabla' p'_\beta + \mathbf{g}' + \frac{1}{Re}\nabla'^2\mathbf{v}'_\beta, \\ p'_\beta &= \frac{p_\beta}{\rho_\beta U^2}, \\ \mathbf{g}' &= \mathbf{s}_\beta\frac{L}{U^2}, \end{aligned} \tag{5.1.7}$$

and the dimensionless cylinder equation reads

$$\begin{aligned}\left(\frac{U/L}{\omega_0}\right)^2 \frac{d^2\mathbf{x}'}{dt'^2} &= \left(\mathbf{x}'_0 - \mathbf{x}'\right) + \mathbf{f}'_h \frac{\rho_\beta S_{\text{solid}} L}{m} \left(\frac{U/L}{\omega_0}\right)^2, \\ \omega_0 &= \sqrt{\frac{k}{m}}, \\ \mathbf{f}'_h = \frac{\mathbf{f}_h}{\rho_\beta S_{\text{solid}} U^2} &= \frac{1}{S_{\text{solid}}} \int_{S_{\text{solid}}} \mathbf{n}_S \cdot \left(-\mathbf{I}p'_\beta + \frac{1}{Re}\left[\nabla'\mathbf{v}'_\beta +^T \left(\nabla'\mathbf{v}'_\beta\right)\right]\right) dS.\end{aligned} \tag{5.1.8}$$

Hence, three dimensionless numbers appear

$$\begin{aligned} f_s^* &= \frac{\omega_0}{U/L}, \\ m^* &= \frac{m}{\rho_\beta S_{\text{solid}} L}, \\ Re &= \frac{\rho_\beta L U}{\mu_\beta}. \end{aligned} \tag{5.1.9}$$

We choose

- S_{solid} so that $m^* = \frac{\rho_\sigma}{\rho_\beta}$, and
- $L = D$ the diameter of the cylinder.

This leads to

$$m^* \frac{d^2\mathbf{x}'}{dt'^2} = f_s^{*2} m^* \left(\mathbf{x}'_0 - \mathbf{x}'\right) + \mathbf{f}'_h, \tag{5.1.10}$$

for the solid equation. Note that there are several possible choices of Reynolds number. Two of them are

- $U = || \langle \mathbf{v}_\beta \rangle^\beta ||$, which gives Re_D, and
- $U = \frac{L\sqrt{L||\mathbf{s}_\beta||}}{\nu}$, which gives Re_g.

We will discuss the advantages and disadvantages of Re_g versus Re_D in the following.

5.1.2 Interpretation of numerical results

This study aims at observing the effect of the f_s^* and m^* parameters on the pressure drop through a periodic elastic model porous medium. Our medium is such that in time-invariant regimes, each unit-cell is translation-invariant. Hence the elasticity of our model porous medium has no effect in time-invariant regimes. Therefore we focus on unsteady regimes. We should use the Reynolds number Re_D to make sure the flow is unsteady. We use the correlation proposed in [33] to determine the onset of unsteadiness for an in-line array of cylinders of porosity 0.8. This correlation gives the limit of unsteadiness at $Re_D = Re_u \simeq 71$. In order to avoid phenomena related to this transition to unsteady regime, we set $\mathbf{s}_\beta$ so that Re_D is far above Re_u in rigid mode, *i.e.* $Re_D > 100$ when the geometry is rigid. We do not study transient regimes, and wait until a statistically steady regime is achieved. To give a definition of a statistically steady regime, let us define the time average f_A of an arbitrary function of time f as

$$f_A(t) = \int_0^\infty f(u)h(u-t)\, du, \tag{5.1.11}$$

where $h(t)$ is the rectangular function centered in 0. We can say that we are in the statistically steady regime with regard to (I, h), when f_A is independent of $t \in I$. In our case we solve Eq. 5.1.4 with $\mathbf{s}_\beta = g\mathbf{e}_x$ set as a constant parameter during the simulation. The quantity we observe to determine whether we are in statistically steady regime is the component of $\langle \mathbf{v}_\beta \rangle^\beta$ in the $\mathbf{e}_x$ direction

$$v_x = \langle \mathbf{v}_\beta \rangle^\beta \cdot \mathbf{e}_x. \tag{5.1.12}$$

The advantage of setting $\mathbf{s}_\beta$ to a constant value is that it fixes the mean hydrodynamic force applied to the solid- phase in the statistically steady regime. To show this we integrate the Navier-Stokes equations over the periodic domain and obtain

$$\begin{aligned} \frac{\partial \int_{\mathscr{V}_{\text{cell}}} \mathbf{v}_\beta\, dV}{\partial t} + \nabla\cdot\int_{\mathscr{V}_{\text{cell}}} \mathbf{v}_\beta\mathbf{v}_\beta\, dV = &-\frac{1}{\rho_\beta}\nabla\int_{\mathscr{V}_{\text{cell}}} p_\beta\, dV + \frac{1}{\rho_\beta}\nabla\cdot\int_{\mathscr{V}_{\text{cell}}}\mu_\beta\left[\nabla\mathbf{v}_\beta +^T(\nabla\mathbf{v}_\beta)\right] dV \\ &+ \frac{1}{\rho_\beta}\underbrace{\int_{\mathscr{A}_{\beta\sigma}} \mathbf{n}_{\beta\sigma}\cdot\left(-\mathbf{I}p_\beta + \mu_\beta\left[\nabla\mathbf{v}_\beta +^T(\nabla\mathbf{v}_\beta)\right]\right) dA}_{\mathbf{T}_{\beta\sigma}} + \epsilon_\beta V_{\text{cell}}\mathbf{s}_\beta. \end{aligned} \tag{5.1.13}$$

$\mathbf{T}_{\beta\sigma}$ is the total force applied to the fluid by the solid. Let ψ_β a field with periodic conditions over the unit cell. We have

$$\nabla\int_{\mathscr{V}_{\text{cell}}} \psi_\beta\, dV = \underbrace{\frac{1}{V}\int_{\mathscr{A}_{\beta e}} \mathbf{n}_{\beta e}\psi_\beta\, dA}_{\text{vanishes due to periodic BCs}} \quad . \tag{5.1.14}$$

Then we assume that the statistically steady regime is set over a time frame Tp. Averaging over this time frame leads to

$$\left|\frac{1}{T_p}\int_{T_p}\frac{\partial\psi_\beta}{\partial t}\, dt\right| < \frac{\text{amplitude}(\psi_\beta)}{T_p} \underset{T_p\to\infty}{\to} 0, \tag{5.1.15}$$

hence, if T_p is large enough, then the time averaged force applied to the solid by the fluid is set by the source term in the Navier-Stokes equations. We introduce the mean effective surface S_{eff} as a scalling of the drag, *i.e.*

$$(\mathbf{T}_{\beta\sigma}\cdot\mathbf{e}_x)_A = \frac{1}{2}S_{\text{eff}}\rho_\beta\underbrace{\left(\langle\mathbf{v}_\beta\rangle^\beta\cdot\mathbf{e}_x\right)_A}_{v}{}^2, \tag{5.1.16}$$

i.e. for a given value of Re_g, we interpret the displacement of cylinders that depends on the stiffness as a variation in mean effective surface S_{eff}. Let S_r the mean effective surface of the rigid case, and S_d the mean effective surface of a deformable case. For a given value of Re_g, a deformable case compares to the rigid case as

$$S^* = \frac{S_d}{S_r} = \left(\frac{v_r}{v_d}\right)^2. \tag{5.1.17}$$

S^* is interesting because it provides a meaningful way of evaluating the effect of elasticity on the flow rate. It allows to interpret the beating of cylinders as a rigid medium with an increased (or decreased, we will see) solid surface exposed to the flow.

5.2 Numerical methods

5.2.1 Immersed boundary method of Jadim

The cylinders can sustain large displacements, with possible solid-solid contacts involved. To solve our problem, we use a numerical code called **Jadim**. This code implements an Immersed Boundary Method described in detail in [143]. Immersed Boundary Methods (IBM, [144]) allow to overcome mesh issues, as a flow with complex and moving boundaries can be simulated using a simple fixed, regular cartesian mesh. The IBM method in **Jadim** resolves

$$\begin{aligned} \frac{\partial \mathbf{v}}{\partial t} + \nabla \cdot (\mathbf{v}\mathbf{v}) &= -\frac{1}{\rho_\beta}\nabla p + \frac{\mu_\beta}{\rho_\beta}\nabla^2 \mathbf{v} + \mathbf{s}_\beta + \mathbf{f}_\sigma, \\ \nabla \cdot \mathbf{v} &= 0, \end{aligned} \tag{5.2.1}$$

in the fluid- and the solid- phase. The $\mathbf{v}$- and p- fields are continuous on the whole domain. The forcing term $\mathbf{f}_\sigma$ is such that

$$\mathbf{v} = \begin{cases} \mathbf{v}_\beta & \text{the solution of the Navier-Stokes equations in the fluid- phase} \\ \mathbf{v}_\sigma & \text{the rigid body velocity in the solid- phase} \end{cases} \tag{5.2.2}$$

The hydrodynamic force applied to a solid particle is then computed through

$$\mathbf{f}_h = -\rho_\beta \int_{V_p} \mathbf{f}_\sigma \, dV. \tag{5.2.3}$$

In this method the pressure field is resolved in the fluid phase as well as in the solid phase, and the pressure field is advanced by solving a Poisson equation so that mass-conservation is ensured on the whole domain. Hopefully the resulting p- field corresponds to the p_β- field in the $\beta-$ phase, and $\mathbf{f}_h$ computed from $\mathbf{f}_\sigma$ gives good results at the Reynolds number we consider. Although there are some validation cases in [143], these points are discussed in the following, especially in Section 5.2.2 where **Jadim** is challenged with a mixed- cut-cell- direct-forcing method on a case with moving solid boundaries.

As we limit the study to cases where solid-solid contacts are rather rare, we propose to handle collisions in a simple way. We implement elastic, instantaneous, normal solid-solid shocks, so that when two particles collide, each particle conserves its rotational energy, and the overall kinetic energy is conserved. Consider two cylinders i and j close to each other, *i.e.* such that

$$D + \delta_c > d_{ij}, \tag{5.2.4}$$

where d_{ij} is the distance between the centers of cylinder i and j and δ_c is the contact thickness. We define v_{ij} the closure rate of the two particles as

$$v_{ij} = \frac{(\mathbf{x}_i - \mathbf{x}_j)}{d_{ij}} \cdot (\mathbf{v}_i - \mathbf{v}_j)\,, \tag{5.2.5}$$

where $\mathbf{v}_i$ ($\mathbf{v}_j$) is the velocity of the center of cylinder i (cylinder j). Solid-solid collision must be handled only if $v_{ij} < 0$. In this case, the two cylinders exchange their closure rate component, *i.e.*

$$\begin{aligned} \mathbf{v}_i^+ &= \mathbf{v}_i + \frac{(\mathbf{x}_i - \mathbf{x}_j)}{d_{ij}} v_{ij}, \\ \mathbf{v}_j^+ &= \mathbf{v}_j - \frac{(\mathbf{x}_i - \mathbf{x}_j)}{d_{ij}} v_{ij}. \end{aligned} \tag{5.2.6}$$

$\mathbf{v}_i^+$ ($\mathbf{v}_j^+$) is the velocity of cylinder i (cylinder j) after the collision. In the case of multiple shocks, a cylinder might end up penetrating another one if multiple cylinders are close to each other. To avoid this, at each time step collisions are detected and treated until there are no more converging cylinders close to each other. This amounts to the principle of Newton's pendulum, *i.e.* the momentum transfer between cylinders is instantaneous and conservative, as it is between hard spheres.

5.2.2 Mixed cut-cell direct forcing method (MCCDF)

An issue of the immersed boundary method in **Jadim** is that the mass conservation is handled by a *pseudo* Poisson equation. This means that the pressure correction does not have boundary conditions on the impermeable solid boundary. This allows leaks at the solid boundary during the correction step and we can wonder what the consequences are on the results. In the inertial regime where pressure drag is important, the impact on the pressure field and the fluid-structure coupling is concerning. To challenge the method implemented in **Jadim**, we build an IBM code with a different approach to mass-conservation. We then compare the two methods on a 2D unsteady flows ($Re_D \sim 110$) through

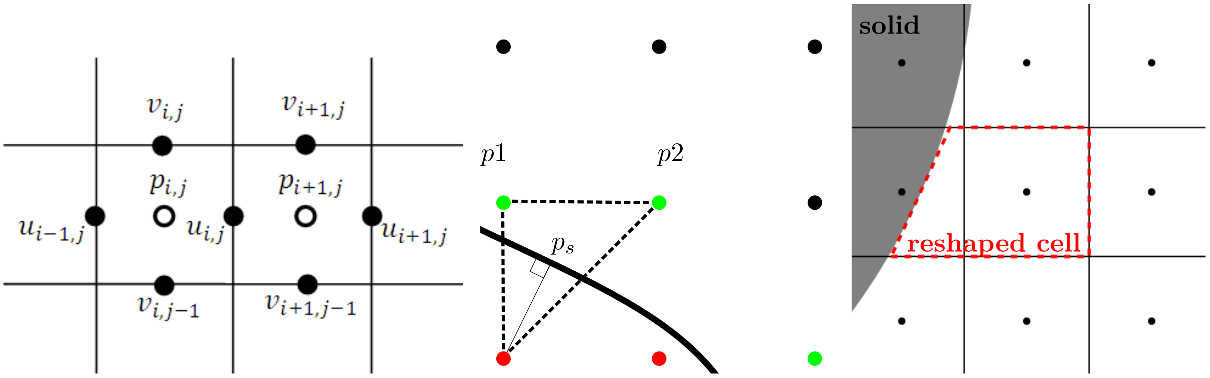

(a) (b) (c)

Figure 5.2: 5.2a arrangement of the staggered grid used in the **MCCDF** code. 5.2b details extrapolation stencil to impose boundary conditions on the solid boundary. Ghost points are in red, with fluid neighbours in green. Regular fluid points are in black. The extrapolation stencil is made of two fluid points p_1 and p_2, and p_s the projection of the ghost point to the immersed boundary, where the no-slip condition applies. 5.2c the cut-cell approach implemented to ensure mass conservation in the **MCCDF** method. The back dots refer to the pressure points, that are also the cell centres. The reshaped cell is delimited with the dashed line.

an array of impermeable cylinders that encounter displacements.

The **MCCDF** method solves Eq. 5.2.1 in the fluid phase only ($\mathbf{v}_\beta$ and p_β are not computed in the solid region). Moving solid boundaries are handled with a direct forcing method. The domain is periodic and a cartesian, staggered grid (Fig. 5.2a) is used. A predictor-corrector approach (PISO algorithm, [67]) is used to advance the pressure in time via the continuity equation, so that at each time step t_{n+1} we have

$$\begin{aligned}\mathbf{v}_\beta^{n+1} = \mathbf{v}_\beta^{n} - dt\left(\frac{3}{2}\nabla\cdot(\mathbf{v}_\beta^{n}\mathbf{v}_\beta^{n}) - \frac{1}{2}\nabla\cdot(\mathbf{v}_\beta^{n-1}\mathbf{v}_\beta^{n-1})\right)\\ + dt\left(-\frac{1}{\rho_\beta}\nabla p_\beta^{n+1} + \frac{\mu_\beta}{\rho_\beta}\frac{1}{2}\left(\nabla^2\mathbf{v}_\beta^{n+1} + \nabla^2\mathbf{v}_\beta^{n}\right)\right),\end{aligned} \tag{5.2.7}$$

$$\nabla\cdot\mathbf{v}_\beta^{n+1} = 0. \tag{5.2.8}$$

In the fluid region, we first obtain a predicted velocity $\mathbf{v}_\beta^*$ at each fluid-point as

$$\begin{aligned}\mathbf{v}_\beta^{*} = \mathbf{v}_\beta^{n} - dt\left(\frac{3}{2}\nabla\cdot(\mathbf{v}_\beta^{n}\mathbf{v}_\beta^{n}) - \frac{1}{2}\nabla\cdot(\mathbf{v}_\beta^{n-1}\mathbf{v}_\beta^{n-1})\right)\\ + dt\left(-\frac{1}{\rho_\beta}\nabla p_\beta^{n} + \frac{\mu_\beta}{\rho_\beta}\frac{1}{2}\left(\nabla^2\mathbf{v}_\beta^{*} + \nabla^2\mathbf{v}_\beta^{n}\right)\right).\end{aligned} \tag{5.2.9}$$

This involves the evaluation of space derivatives, and requires a specific treatment of the immersed solid boundary to impose no-slip condition for the fluid velocity $\mathbf{v}_\beta$. The no slip condition is imposed via ghost-points.

A mesh point has three possible states, either fluid, solid, or ghost. A ghost point is a solid point that has at least one fluid cell. As the solid boundary moves, we must update the state of each point on the mesh. At the beginning of the simulation, each mesh point is set a state, depending on its position with respect to the solid boundary. This task is expensive as it requires to loop over the entire mesh. To avoid this cost at each time iteration, we only keep track of mesh points that have at least one neighbour on the other side of the interface. These points are called the *potential ghost points* (PGP). The PGP list is updated at each time iteration on the basis of the PGP list at the previous time step. Only the states of the points of the PGP list and their neighbours are updated, instead of the states of the points of the whole mesh. This saves precious CPU time. This task, as well as the computation of hydrodynamic forces, are distributed among processors via the message passing interface (MPI). To do so we use the Mpi4py library [145], the Python binding to MPI.

We use a linear extrapolation procedure [146, 147]

$$\mathbf{v}^*_{\beta_{\text{ghost}}} = \alpha_0 + \alpha_x x_{\text{ghost}} + \alpha_y y_{\text{ghost}}, \tag{5.2.10}$$

to determine $\mathbf{v}^*_{\beta_{\text{ghost}}}$ the value of $\mathbf{v}^*_\beta$ at a ghost point. $(x_{\text{ghost}}, y_{\text{ghost}})$ are the coordinates of the ghost point. The computation of α_0, α_x and α_y involves (Fig. 5.2b) two neighbour fluid points p_1 and p_2, and p_s the projection of the ghost point onto the solid boundary. The predicted velocity at a ghost cell takes the semi-implicit form

$$\mathbf{v}^*_{\beta_{\text{ghost}}} = \alpha_1 \mathbf{v}^*_{\beta_1} + \alpha_2 \mathbf{v}^*_{\beta_2} + \alpha_s \mathbf{v}^n_\sigma, \tag{5.2.11}$$

where $\mathbf{v}^n_\sigma$ is the solid velocity at point p_s determined at time t_n, hence $\mathbf{v}^*_\beta$ is implicit but the solid velocity is explicit (implicit treatment of the solid velocity could be achieved via sub-iterations between the solid and the fluid mechanics). Eq. 5.2.11 imposes the no slip condition at the solid boundary with a second order formal accuracy in space [148]. The predicted velocity $\mathbf{v}^*_\beta$ needs to be corrected to satisfy equation (5.1.5). We follow the PISO algorithm and state that $\mathbf{v}^*_\beta$ be corrected by

$$\mathbf{v}^{n+1}_\beta = \mathbf{v}^*_\beta - \frac{dt}{\rho_\beta} \nabla \psi, \tag{5.2.12}$$

where ψ is still to be determined. Taking the divergence of Eq. 5.2.12 and imposing Eq. 5.2.8 yields a Poisson equation for ψ

$$\Delta \psi = \frac{\rho_\beta}{dt} \nabla \cdot \mathbf{v}^*_\beta. \tag{5.2.13}$$

We solve for ψ using an equivalent finite volume formulation, *i.e.* Eq. 5.2.13 is rewritten as

$$\int_{S_{\text{cell}}} \nabla\psi \cdot \mathbf{n} dS = \frac{\rho_\beta}{dt} \int_{S_{\text{cell}}} \mathbf{v}_\beta^* \cdot \mathbf{n} dS, \tag{5.2.14}$$

where S_{cell} delimits the fluid cell, and $\mathbf{n}$ is the outward normal. Whilst this mass balance is trivial on a regular mesh, it is not as obvious if the solid interface is not aligned with the cartesian mesh. The mass conservation requires attention around the solid surface. Indeed if not taken into account during the correction step, cut cells (*i.e.* fluid cells that are cut by the solid interface) lead to some errors between the mass conservation and the imposition of the no-slip condition ([149, 150]) at the solid boundary. To avoid this, fluid cut cells are reshaped by removing their solid part, and solid cut cells are merged with their nearest fluid cell, after their solid part has been removed (see Fig. 5.2c). Then, the mass balance on a reshaped fluid cell reads

$$\int_{S_{\text{cell}}} \mathbf{v}_{\text{rel}} \cdot \mathbf{n} dS = -\frac{dV_{\text{cell}}}{dt}, \tag{5.2.15}$$

where V_{cell} is the volume of the cut cell. V_{cell} is time dependent because the solid boundary moves. $\mathbf{v}_{\text{rel}}$ is the local fluid velocity relative to the moving face of the cell that is cut by the solid boundary. $\mathbf{v}_{\text{rel}}$ explicitly reads

$$\mathbf{v}_{\text{rel}} = \mathbf{v}_\beta - \mathbf{v}_{\text{face}}. \tag{5.2.16}$$

Moreover the time derivative of V_{cell} reads

$$\frac{dV_{\text{cell}}}{dt} = \int_{S_{\text{cell}}} \mathbf{v}_{\text{face}} \cdot \mathbf{n} dS, \tag{5.2.17}$$

therefore Eq. 5.2.15 is equivalent to

$$\int_{S_{\text{cell}}} \mathbf{v}_\beta \cdot \mathbf{n} dS = 0, \tag{5.2.18}$$

which is the same equations as for a rigid cell. So Eq. 5.2.14 is valid for a deforming cell too. The evaluation of fluxes $\nabla\psi \cdot \mathbf{n} dS$ and $\mathbf{v}_\beta^* \cdot \mathbf{n} dS$ is straightforward on an undeformed cell of the staggered grid (Fig. 5.2a). On a reshaped cell however (Fig. 5.2c), this requires to interpolate the $\nabla\psi$- and $\mathbf{v}_\beta^*$- fields at the face center. We use a simple 1D first order scheme to interpolate the flux at a random point. The procedure is illustrated in Fig. 5.3. Depending on the position of the face center, we determine a pair of points that constitutes our interpolation stencil as indicated in Tab. 5.1. This procedure to evaluate a flux at an arbitrary position is very simple and could be improved. This was not explored here. At least, we have a procedure that clarifies mass conservation at the solid boundary.

We need a boundary condition for ψ at the solid surface. Let $\mathbf{n}_{\text{IB}}$ be the unit vector normal to the

position of the face center	zone 1	zone 2	zone 3	zone 4
flux interpolation stencil	(p_a, p_b)	(p_b, p_c)	(p_d, p_e)	(p_e, p_f)

Table 5.1: Table of correspondence between the zone where the face center lies and the stencil used in the interpolation of the flux.

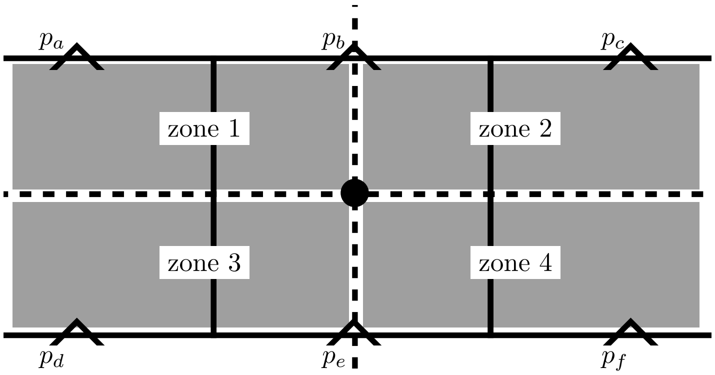

Figure 5.3: Illustration of the interpolation procedure implemented to evaluate a flux at a position that is not on the mesh, as is the case for a reshaped cell. We take the example of the interpolation of the vertical component of a flux. The triangle refer to the mesh points of the vertical velocity on the staggered mesh. The black dot represent the center of the reshaped cell. We interpolate the flux on a face of this reshaped cell. Depending on the position of this face center, a different pair of mesh points is used (see Tab. 5.1).

immersed boundary pointing to the fluid region. From Eq. 5.2.12 we have

$$\left(\mathbf{v}_\beta^{n+1} - \mathbf{v}_\beta^*\right) \cdot \mathbf{n}_{\mathrm{IB}} = -\frac{dt}{\rho_\beta} \nabla\psi \cdot \mathbf{n}_{\mathrm{IB}}. \tag{5.2.19}$$

We recall that the predicted velocity $\mathbf{v}_\beta^*$ at the solid wall already satisfies the no-slip condition, via the linear extrapolation introduced by Eq. 5.2.10. Therefore

$$\mathbf{v}_\beta^* \cdot \mathbf{n}_{\mathrm{IB}} = \mathbf{v}_S \cdot \mathbf{n}_{\mathrm{IB}}; \tag{5.2.20}$$

Since we want to impose

$$\mathbf{v}_\beta^{n+1} \cdot \mathbf{n}_{\mathrm{IB}} = \mathbf{v}_S \cdot \mathbf{n}_{\mathrm{IB}}, \tag{5.2.21}$$

we need

$$\nabla\psi \cdot \mathbf{n}_{\mathrm{IB}} = 0. \tag{5.2.22}$$

Hence we solve Eq. 5.2.13 with a homogeneous Neuman condition for ψ at the solid boundary. We add periodic conditions for ψ at the fluid domain boundaries. This results in a periodic velocity correction and is adapted when a periodic condition is required on the velocity field. The linear system to be solved in order to obtain ψ is singular because ψ is determined up to a constant. We overcome this by using an iterative method available from PETSc (bi-conjugate stabilized gradient method preconditioned with block Jacobi and incomplete LU factorization on each sub-process) which comes with scalability and can handle singular systems. PETSc is an efficient library written in C. As our code is written in Python, we use a Python binding to PETSc (Petsc4py [151]) which allows parallel solving of linear systems.

We still need to compute p_β^{n+1} the pressure- field at time t_{n+1}. Subtracting Eq. 5.2.9 to Eq. 5.2.7 leads to

$$\mathbf{v}_\beta^{n+1} - \mathbf{v}_\beta^{*} = -\frac{dt}{\rho_\beta}\nabla\left(p_\beta^{n+1} - p_\beta^{n}\right) + \frac{\mu_\beta}{\rho_\beta}\frac{dt}{2}\left(\nabla^2\mathbf{v}_\beta^{n+1} - \nabla^2\mathbf{v}_\beta^{*}\right). \tag{5.2.23}$$

Injecting Eq. 5.2.12 yields

$$\nabla\psi = \nabla\left(p_\beta^{n+1} - p_\beta^{n}\right) + \frac{\mu_\beta}{dt}\frac{1}{2}\left(\nabla^2\left(\nabla\psi\right)\right), \tag{5.2.24}$$

wich indicates that the pressure field should be updated as

$$p_\beta^{n+1} = p_\beta^{n} + \psi - \frac{1}{2}dt\frac{\mu_\beta}{\rho_\beta}\nabla^2\psi. \tag{5.2.25}$$

This ensures that Eq. 5.2.23 is satisfied.

We use the stencil depicted in Eq. 5.2.11 in two additional situations. First, $\mathbf{v}_\beta^{n+1}$ obtained from Eq. 5.2.12 is divergence free and verifies the no-penetration condition at the solid boundary, but does not verify the no slip condition. We need to update the value of the ghost points by extrapolating the $\mathbf{v}_\beta^{n+1}$- field, and do this by means of Eq. 5.2.11. Second, when the solid boundary moves, some solid points that were not resolved may become ghost points. These points have no velocity nor pressure value, and are needed to evaluate space derivatives near the solid boundary for the explicit part of Eq. 5.2.9. To overcome this we extrapolate the fluid- fields p_β and $\mathbf{v}_\beta$ to these new ghost points, by means of Eq. 5.2.11. This extrapolation scheme may generate large coefficients α_1 and α_2. This can be easily understood in one dimension, as the extrapolation procedure takes the form

$$\mathbf{v}_{\beta_{\text{ghost}}}^{*} = \mathbf{v}_{\beta_s}^{*} + \underbrace{\frac{x_g - x_s}{x_f - x_s}}_{\alpha_g}\left(\mathbf{v}_{\beta_f}^{*} - \mathbf{v}_{\beta_s}^{*}\right). \tag{5.2.26}$$

Clearly as the fluid point used in the extrapolation gets closer to the solid boundary, x_f tends to x_s while $x_g - x_s$ remains constant, and the α_g coefficient grows indefinitely. A large α_g coefficient makes the computation unstable as it amplifies the error due to successive time iterations. This is relevant for a deformable case as well as for a rigid case. To avoid divergence we constrain the choice of p_1 and

p_2 the two fluid points of the extrapolation stencil with

$$distance(p_i, p_s) > distance(p_{\text{ghost}}, p_s). \tag{5.2.27}$$

The Neuman condition applied to ψ does not generate such an instability. Indeed in one dimension a Neuman condition translates into

$$\psi_{\text{ghost}} = \psi_f + (x_g - x_f)\,\mathbf{n}_{\text{IB}} \cdot \nabla\psi. \tag{5.2.28}$$

Hence no particular condition is imposed on the extrapolation stencil for the Neuman condition. We simply take the closest pressure points.

To save computational time we implement a variable time step, that is set via a target CFL condition. The variations in time step at runtime may generate amplification of numerical errors. To avoid this, we limit the growth rate of the time step from one iteration to another. A predicted CFL number CFL_{pred} is obtained with an explicit step. Then, the time step dt_{n+1} is set as

$$dt_{n+1} = \begin{cases} dt_n \frac{CFL_{\text{pred}}}{CFL_{\text{max}}} & , CFL_{\text{pred}} > CFL_{\text{max}} \\ 1.1 dt_n & , CFL_{\text{pred}} < 0.8 CFL_{\text{max}} \\ dt_n & , \text{otherwise.} \end{cases} \tag{5.2.29}$$

The fluid and solid equations are solved sequentially. At each time step, Eq. 5.1.2 is advanced in time with

$$\dot{\mathbf{x}}^{n+1} = \dot{\mathbf{x}}^n + dt\left(\frac{k}{m}\left(\mathbf{X}_0 - \mathbf{x}^n\right) + \frac{{\mathbf{f}_h}^n + {\mathbf{f}_h}^{n+1}}{2}\right), \tag{5.2.30}$$

and a Crank-Nicolson scheme is used to obtain the new position

$$\mathbf{x}^{n+1} = \mathbf{x}^n + dt\frac{\left(\dot{\mathbf{x}}^{n+1} + \dot{\mathbf{x}}^n\right)}{2}. \tag{5.2.31}$$

5.3 Validation of the numerical approach

5.3.1 Mesh convergence

The cylinders' motion is due to flow unsteadiness. In turn, the motion of the solid boundary acts on the flow via the no-slip condition, and this yields the fluid-solid coupling. As the flow unsteadiness is at the basis of this coupling, it appears crucial here to have an accurate description of the flow unsteadiness if we wish to evaluate the effect of the fluid-solid coupling on the pressure drop. Hence before running

value of $\frac{D}{dx}$	25	50	100
first harmonic magnitude	$65,75\%$	$16,95\%$	$5,56\%$
first harmonic frequency	$6,05\%$	$2,29\%$	$0,75\%$
time average	$4,43\%$	$0,64\%$	$0,18\%$

Table 5.2: Relative error on the fundamental frequency magnitude with the finest mesh ($\frac{D}{dx} = 200$) as reference.

simulations, we wish to determine how fine the mesh should be in order to fairly capture the unsteady characteristics of the flow. We simulate the flow with **Jadim** for $Re_g = 56$ through a 2×2 square rigid array of cylinders (two columns, two rows). We impose periodic periodic flow conditions at the boundaries of the domain. We increase the number of cells so that the ratio $\dfrac{D}{dx}$ ranges from 12 to 200. We lock the maximum value of the CFL number to 1. For each space discretization, we plot on Fig. 5.4 the time averaged Reynolds number, and the power spectrum of the Reynolds number in statistically steady regime. The non-dimensional time t^* is obtained with the advective time at $Re_D = 110$ as reference time, *i.e.*

$$t^* = t \times 110 \frac{\nu_\beta}{D^2}. \tag{5.3.1}$$

ω^* is the non-dimensional frequency obtained with the same characteristic time.

The results show that data are mesh sensitive. The coarsest mesh does not even capture any unsteadiness of the flow, hence a large error on the description of the viscous dissipation, that lead to over-estimating the flow rate. For finer meshes, a periodic signal is obtained for Re_D. On Tab. 5.2, we compare the results to the case with the finest mesh. One can see that the time- frequencies of the flow are rather independent of the space discretization. In terms of magnitude however the situation is quite different. On the one hand, the magnitude of the first harmonic (largest time-scale) tend to decrease with the mesh refinement. The smaller time-scales on the other hand tend to increase their magnitude as the mesh gets finer. This is in accordance with the idea that the mesh refinement allows to improve the description of the small-scale flow structures. We see that the time average of the Reynolds number is well captured with 50 cells per diameter. However we make an error of $\sim 17\%$ on the magnitude of the first harmonic. We should keep in mind that the description of time-scales is only moderately accurate with 50 cells per diameter, and this affects the microscopic fluid-solid coupling. However as we have a limited amount of time, we simulate the flow with 50 cells per diameter in the following. This choice is a compromise between accuracy and CPU time per simulation. Here we see that code parallelization and scalability is crucial, as it conditions the accuracy of the simulations.

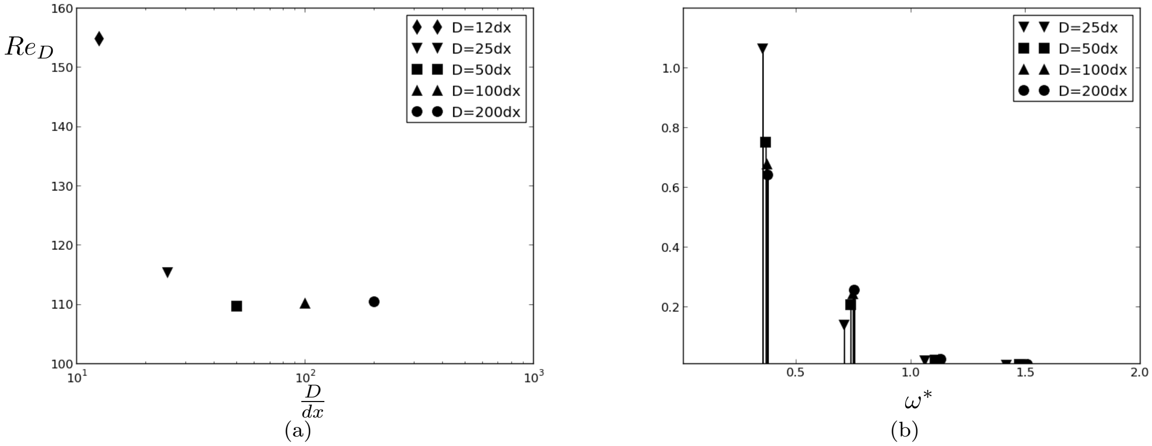

(a) (b)

Figure 5.4: Flow data obtained with **Jadim** for $Re_g = 56$ through a 2×2 square rigid array of cylinders (two columns, two rows). The simulation uses a uniform cartesian mesh. 5.4a, values of the Reynolds number Re_D based on the time-average velocity according to the number of mesh cells per diameter. 5.4b, normalized power spectrum of the instantaneous Reynolds number Re_D obtained with different numbers of cells per cylinder diameter.

5.3.2 Comparisons

5.3.2.1 Solid-solid contacts

The simple approach to solid-solid contacts is validated in the case of two cylinders interacting in a confined shear-flow. The comparison case is taken from [152], where the solid-solid interaction is carefully handled by including an artificial short-distance lubrication force between cylinders. Fig. 5.5b depicts the test case that we validate our approach with. It is made of two cylinders (number 1 and number 2) in a channel. Whilst cylinder 1 is free to move and rotate, cylinder 2 is fixed. The parameters of this numerical experiment are the same as in [152]. The difference lies in the numerical method.

We use a uniform mesh, and the size of a mesh cell dx is such that $D = 30dx$, and our thickness contact δ_c is set to zero ($\delta_c = 0$). Cylinder 1 is released at different position with a zero initial velocity and the flow has zero initial conditions too. The obtained trajectories are compared to data from [152] on Fig 5.5a and show good agreement.

The limit when cylinder 1 goes up cylinder 2 is well captured, and qualitatively the trajectories are the same. There is a little discrepancy on the long term when the trajectory of cylinder 1 reverses (three lower starting positions). This might be due to the difference in numerical method, especially the treatment of the solid-solid interaction. Whereas [152] introduces a short distance interaction, our cylinders interact only when they come in contact. This may induce a difference in rotation speed, hence a difference in trajectories. A finer comparison is required to deal with this more deeply. This comparison is satisfying and shows that our very simple approach to solid-solid contact allows a

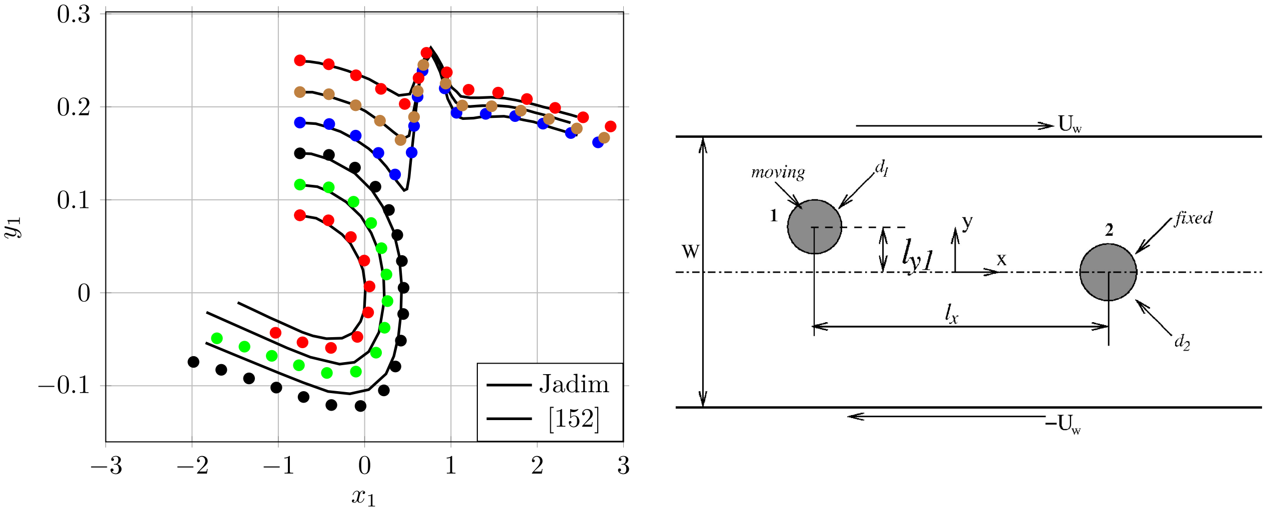

(a) (b)

Figure 5.5: Comparison of the simple solid-solid interaction implemented in **Jadim** with Fig. 10 taken from from [152]. The agreement is rather good when the two particles comes into contact (three upper starting positions). We observe a discrepancy for the three lower starting positions. This shows the effect of modeling the lubrication phenomena (as done in [152]) on the trajectories of the cylinders.

Code	Re_D	gap	C_x	gap
icoFoam	$1,1065 \times 10^2$	/	$3,15$	/
Jadim	$1,1062 \times 10^2$	$0,26\%$	$3,14$	$0,02\%$

Table 5.3: Results of the validation of **Jadim** against OpenFOAM (OF) on the rigid case. The diameter is discretized with 50 cells. C_x refers to the mean drag coefficient of a cylinder. "gap" refers to the difference between the results obtained with the two numerical methods.

rather realistic behaviour. However, simulations should be restricted to cases where solid-solid contacts remain rare.

5.3.2.2 Rigid case

Validation cases of the IBM method of **Jadim** can be found in [143]. Here we verify that it is able to evaluate the flow rate and hydrodynamic forces on a simple rigid case, at $Re_D \simeq 110$. We compare the IBM method of **Jadim** against the **icoFoam** solver from Open∇FOAM®, that solves the incompressible Navier-Stokes equations with a finite-volume formulation, and based on a conforming mesh. The validation case is a 2×2 square array of cylinders. We set $Re_g = 56$. Periodic conditions are imposed to pressure and velocity on the fluid domain. The case is 2D and the geometry is rigid ($\mathbf{v}_\sigma = 0$). The mesh is regular cartesian and such that $D = 50dx$. The instantaneous non-dimensional flow-rate Re^*, drag C_d and lift C_l are plotted on Fig. 5.6 and show a very good agreement of time-dependant signals. Tab. 5.3 compares the time averages and shows that the relative error is less than 0.5%. The agreement between **Jadim** and **icoFoam** is satisfying on this rigid case and suggests that **Jadim** can handle 2D flow within an array of cylinders at $Re_D \simeq 110$.

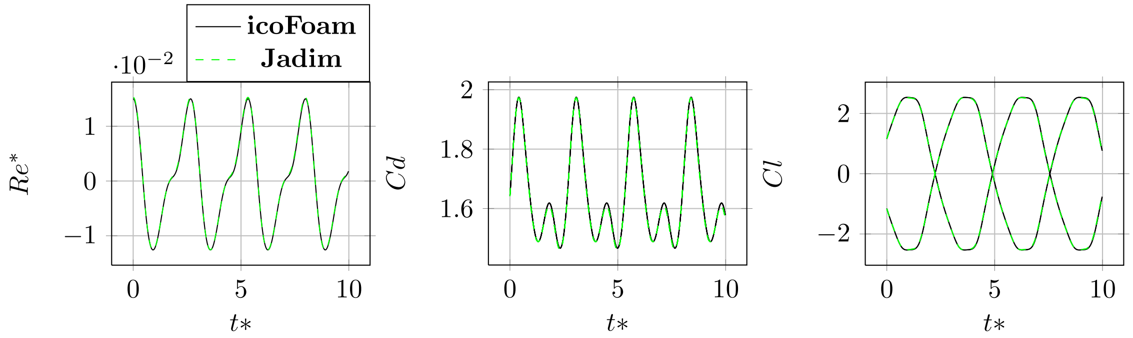

Figure 5.6: Unsteady flow in a periodic elementary cell of an array of cylinders of porosity 0.8. The diameter-based-Reynolds number Re_D is around 110. t^* is the time adimensionalized with the advection time. The flow-rate Re^* is subtracted its time average and scaled with its amplitude.

5.3.2.3 Elastic case

We then compare the **Jadim** code against the **MCCDF** code on deformable cases. We characterize a deformable case by two parameters f^* and m^*. The f^* parameter is defined as

$$f^* = \frac{\sqrt{k/m}}{Re_g \times \nu_\beta/D^2}\frac{56}{110}. \tag{5.3.2}$$

We focus on rather stiff, 2×2 cases ($f^* = 2$, $f^* = 4$ and $m^* = 1$). We compare the instantaneous trajectories of cylinders, and time-average of flow-rate and hydrodynamic coefficients (see Tab. 5.4). Hydrodynamic coefficients are defined as

$$\begin{aligned} C_x &= \frac{f_x}{\frac{1}{2}\rho_\beta L_u g}, \\ C_y &= \frac{f_y}{\frac{1}{2}\rho_\beta L_u g}, \end{aligned} \tag{5.3.3}$$

where L_u is the size of a unit cell. The agreement is rather good in terms of trajectories (Fig. 5.7) and flow rate. These are the most important features in this study, as we wish to evaluate the impact of solid displacement on the flow rate. From this point of view and along with the comparison against Open∇FOAM®, the IBM method of **Jadim** seems a good candidate to start to explore the f^*, m^* space parameters with Re_D around 110.

However we can perform a finer comparison of the two IBM codes. Trajectories of the cylinders are plotted on Fig. 5.7. We observe that the domain occupied by the cylinders obtained with the **MCCDF** method is smaller than the one obtained with the **Jadim** method. This is verified as we look more precisely to the standard deviation of the position of cylinders (Tab. 5.4). The standard deviation is always smaller with the **MCCDF** method than with the **Jadim** method. This gap in

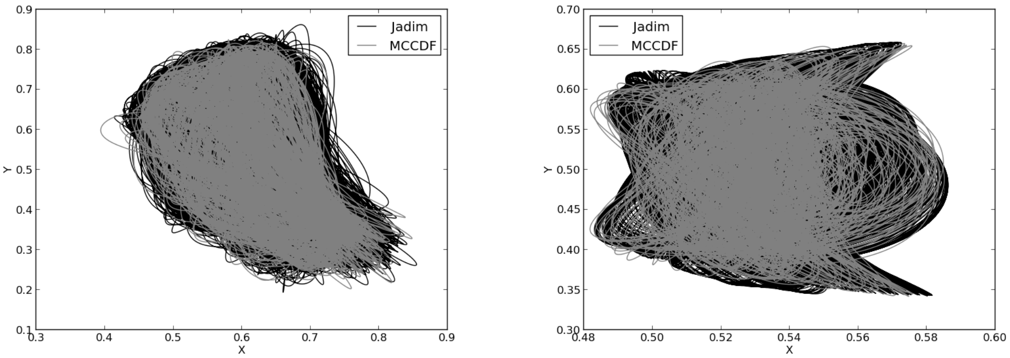

(a) $f^* = 2$ (b) $f^* = 4$

Figure 5.7: Trajectories of the cylinders for ($Re_g = 56$, $m^* = 1$, $f^* \in [1, 4]$) obtained with **Jadim** and the **MCCDF** method. The trajectories obtained with the two different numerical methods compare well.

standard deviation can be explained as we have

$$\mathbf{n}_{\text{IB}} \cdot \frac{D\mathbf{v}_\beta}{Dt} = -\frac{1}{\rho_\beta}\mathbf{n}_{\text{IB}} \cdot \nabla p_\beta, \tag{5.3.4}$$

at the solid boundary. This condition is loosely ensured by **Jadim**, and more carefully applied by the **MCCDF** code. Hence as the cylinder accelerates, the flow opposes a greater pressure drag with the **MCCDF** method and constrains the trajectory of the cylinder inside a smaller domain, compared to the **Jadim** method. This added mass effect should affect the flow rate, as the resulting exposed solid surface is larger with the **Jadim** method. Practically, this is where mass conservation plays a role. Tab. 5.4 reports the Re_D obtained with the two methods at $Re_g = 56$ and show that the **MCCDF** method predicts a slightly greater flow rate than **Jadim**. This is not significant but we expect that the greater the Reynolds number, the greater this effect. The development of a sharp interface IBM method to **Jadim** (*e.g.* the **MCCDF** method) seem relevant to exploring higher values of the Reynolds number.

At the time of this study, **Jadim** affords much better performances than the **MCCDF** method in terms of CPU time. Taking into account the limited amount of CPU time (as well as physical time) available for this project, we chose to perform the numerical campaign with the IBM method of **Jadim**, within the range of validity of this method. However we emphasize the fact that the **MCCDF** method is worth developing in an efficient and maintainable language (*e.g.* C++). Currently it is only a prototype code written in Python language. Moreover the parallelization is only partial and a true distribution approach (*e.g.* following a domain decomposition method) should be implemented to obtain decent scalability performances.

Code	x SD	y SD	Re_D	$(C_x)_A$	$\sqrt{(C_y^2)_A}$
$f^* = 2$ **Jadim**	$9,20 \times 10^{-2}$	$1,60 \times 10^{-1}$	$7,20 \times 10^{1}$	$3,13$	$2,43$
$f^* = 2$ **MCCDF**	$8,47 \times 10^{-2}$	$1,56 \times 10^{-1}$	$7,28 \times 10^{1}$	$3,05$	$2,44$
$f^* = 2$ difference	$8,26\%$	$2,20\%$	$1,09\%$	$2,68\%$	$0,32\%$
$f^* = 4$ **Jadim**	$1,81 \times 10^{-2}$	$7,36 \times 10^{-2}$	$9,06 \times 10^{1}$	$3,14$	$4,27$
$f^* = 4$ **MCCDF**	$1,80 \times 10^{-2}$	$7,23 \times 10^{-2}$	$9,09 \times 10^{1}$	$3,03$	$4,20$
$f^* = 4$ difference	$0,41\%$	$1,86\%$	$0,39\%$	$3,48\%$	$1,62\%$

Table 5.4: Statistics of the displacement of the cylinders. SD refers to the standard deviation of the position of the cylinders. This characterizes how large is the displacement of the cylinder around its time average position. We can appreciate the difference between the two numerical methods and this may be due to the way the no-penetration condition is imposed at the fluid/solid interface.

5.4 Forced flow through an elastic REV

We vary the (f^*, m^*) parameters of an array composed of 2 rows and 2 columns of cylinders (2 × 2 case). During the numerical simulation, the CFL number is maintained to 1. The regular uniform mesh is such that a cylinder diameter is discretized with 50 cells.

5.4.1 Coarse exploration for $m^* \in [1, 2, 4], Reg \in [56, 112], f^* \in [1; 8]$

A Stiff cases We explore the stiff cases space, namely cases for which $f^* \in [1, 2, 4, 8]$ and $m^* \in [1, 2, 4]$ and $Re_g \in [56, 112]$. Fig. 5.8b shows S^* obtained with **Jadim** for these set of parameters (f^*, m^*, Re_g). When cylinders are free to move attached to their rest position (deformable mode), the effective exposed solid surface increases systematically compared to the rigid case ($S^* > 1$ for every deformable media). The stiffer the springs ($f^* \geq 2$), the smaller S^*, which means that the system tends to the rigid case ($S^* = 1$). This is consistent with the idea that a stiff spring constrains the displacement of the cylinders and it is logical that a stiff medium behaves similarly to a rigid medium. A more complicated trend is the evolution of S^* with the reduced mass m^*. For $Re_g = 112$, we see that systematically, the larger m^*, the smaller S^*. The heavier the solid, the harder it is to move and the more it behaves like the rigid medium. However this trend is not so clear for the lower Reynolds number ($Re_g = 56$). The effect of m^* seem stronger as the flow inertia increases.

B Lock-in One last but not least interesting trend is the maximum value of S^* observed on Fig. 5.8b. Strikingly, this maximum value of S^* can be up to 4 times larger than within the rigid medium. This shows that taking into account the elasticity of the medium, and the resulting pore-scale fluid-structure interaction, is relevant to the evaluation of the filtration law in an elastic porous medium, if not crucial. For example the large scale coherent structure observed in canopy flows is sensitive to the solid exposed surface S^* [9, 65]. This maximum value of S^* is reached whatever the value of the Reynolds number or of the reduced mass m^*, around $f^* = 2$. This shows that the fluid-

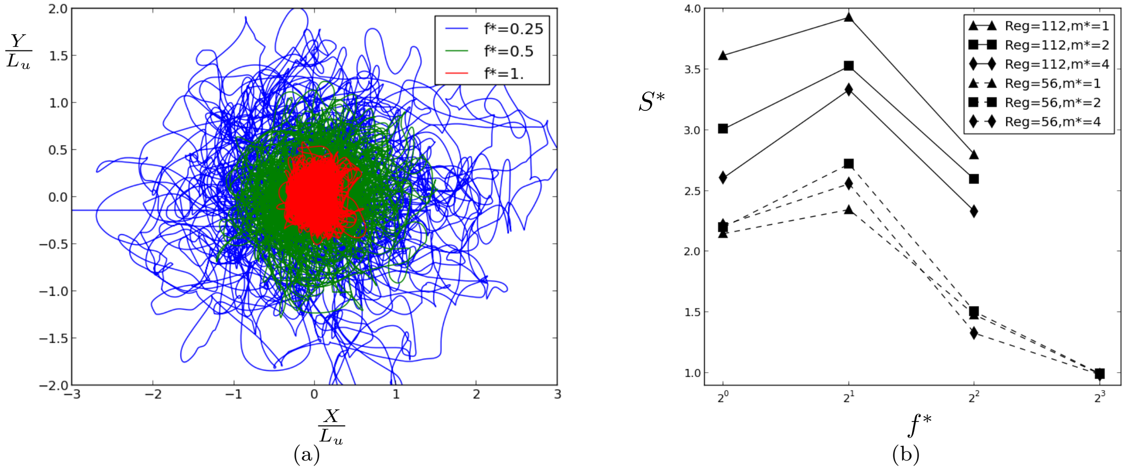

(a) (b)

Figure 5.8: Fig. 5.8a, trajectories for $f^* \leq 1$ at $Reg = 56$, $m^* = 1$. The standard deviation of the position of the cylinder decreases as the stiffness increases. Fig. 5.8b, effective surfaces S^* for a 2×2 cell, $Reg = 56$ and $Reg = 112$. This plot is roughly detailed due to the large number of cases involved. However this plot allows to observe the same trend for each case, *i.e.* there is a region where S^* reaches a maximum.

and solid- time scale have to be comparable in order for the fluid-solid coupling to be strong, and f^* is the relevant parameter to evaluate this. This phenomenon is similar to the *lock-in* phenomenon that was observed in the case of single cylinder under vortex induced vibration in a cross flow (*e.g.* [153]). It is known that when the natural frequency of the mass-spring system is near the flow frequency in rigid mode (*i.e.* $f^* \sim 1$), the elastically mounted cylinder encounters large amplitude oscillations at this natural structural frequency. This effect vanishes when the structural frequency is too different (either larger or smaller) from the flow frequency in rigid mode.

5.4.2 Detailed profile of S^* for $m^* = 1, Reg = 56, f^* \in [1; 8]$

C Soft cases On Fig. 5.8a, we observe the trajectories of three soft cases, *i.e.* cases with the value of the reduced frequency set to $f^* \leq 1$. At these values of f^*, we see that the softness of the spring allows large displacements. A cylinder can travel up to two unit cells away from its rest position. For these stiffnesses, the relevance of the 2D assumption to model our slice of canopy seems to collapse. These soft cases require the third dimension in order to be relevant for our elastic array of tubes. Moreover as the cylinders encounter large displacements, solid-solid contact occur more often. Even if we have proposed in section 5.2.1 a solution to avoid cylinders overlapping, as two cylinders come into contact it is likely that the time-scales involved in the lubrication process that takes place are not well-captured by our simple approach. This issue requires either a finer mesh (at a certain point the cell size is of order of the viscous layer between two cylinders), or the addition of a particular force to account properly for the lubrication time-scales [154]. With our simple method currently implemented in **Jadim**, we should avoid the simulation of cases where cylinders come often into contact and interact a lot with one another. For these reasons, we choose to limit the numerical experiments to rather stiff cases, *i.e.* such that $f^* \geq 1$.

D $f^* \geq 1, m* = 1, Reg = 56$ We plot the results obtained for S^* on Fig. 5.9, corresponding to $f^* \geq 1, m* = 1, Reg = 56$. This profile of S^* is rather well detailed, accounting for the fact that it takes at least 200 CPU hours for each simulation to reach a statistically steady state. The profile of S^* displays different remarkable features. In particular, two distinct maxima are observed (zones B and D, Fig. 5.9). To better understand this behaviour, we can pay attention to the way the cylinders couple between each other depending on the f^* parameter (the stiffness). The vertical positions Y^* (adimensionalized with the size of a unit cell L_u) of the cylinders during time (adimensionalized with the advective time $\frac{L_u^2}{\nu}\frac{1}{Reg}$) are plotted on Fig. 5.10 and Fig. 5.11 and Fig. 5.12. These plots show that the maxima observed on the profile of S^* are due to the fact that the column-to-column cylinders vibrate π rad out-of-phase. The fact that the large values of S^* can be related to the vibration mode of the cylinders means that the viscous dissipation in the pore-flow is the largest when the cylinders vibrate π rad out-of-phase column-to-column. However the nature of the coupling depends on the zone of interest. Indeed the maximum corresponding to zone B (Fig. 5.10) is due to the π rad out-of-phase vibration of column-to-column cylinders, but the amplitude of the signal (*i.e.* the vertical position of the cylinders) is not constant in time, and the signal is not periodic; the maximum corresponding to zone D (Fig. 5.11) corresponds to a π rad out-of-phase vibration of the column-to-column cylinders as well, but this time we clearly observe two superimposed frequencies (a small and a large one), and the signal is periodic. The type of row-to-row coupling alos depends on the zone of interest. Indeed while the row-to-row coupling is in phase for zone B, it is π rad out-of-phase for zone D. From these observations we can conclude that the maxima in S^* are related to the nature of coupling between column-to-column cylinders. In between these maxima, the fluid/solid system lies in-between two vibration modes and goes from one vibration mode to the other in an erratic way. Hence the in-phase vibration deteriorates and the effective surface S^* decreases. For large values of f^* (zone F, Fig. 5.12), the porous medium becomes very stiff and tends to behave like a rigid porous medium. As a consequence S^* tends to 1 when f^* becomes large.

The fact that the type of fibre-to-fibre coupling impacts the effective exposed solid surface S^* is a microscale phenomena. Due to the scale separation assumption, it impacts the large scale behaviour of the fibres only via the modeling of the hydrodynamic force applied to the fibre. In particular, the interpolation process between slave- and master- fibres proposed in Section 3 is used to determine

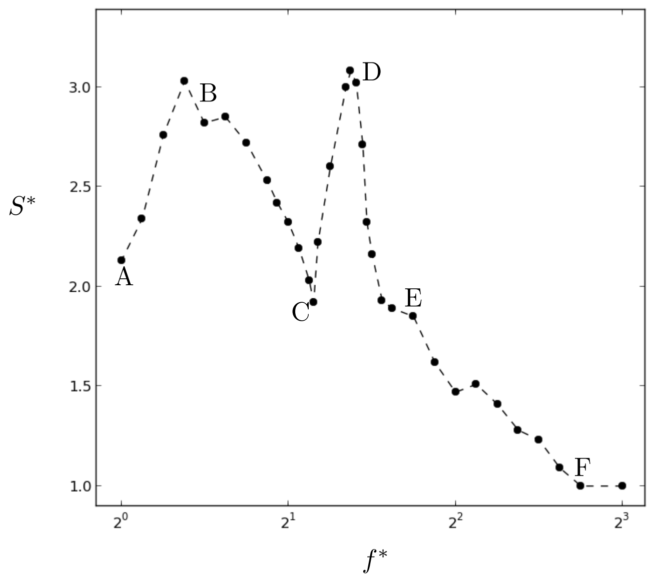

Figure 5.9: Detailed profile of S^* for $m^* = 1, Reg = 56$. This plot reveals a complicated behaviour with two maxima, that can be related to the coupling of the cylinders between each other.

the large scale behaviour of the fibres, which is obtained after filtering the small-scale, fibre-to-fibre coupling. Therefore the interpolation process between slave- and master- fibres at the large-scale is consistent with the fact that at the small-scale (or stem-scale), a fluid-structure fibre-to-fibre coupling occures in many different ways that are not represented in the macroscopic model.

5.4.3 Size of the REV

One last issue studied here is the size of a representative elementary volume (REV). In other words we are willing to determine how many unit-cell (of dimension L_u) the computational domain should contain, so that the small scale fluid-elastic interaction occurring in the real porous medium are representative of the small-scale phenomenon that would occur in an infinitely large domain. Results for a few stiffnesses and REV sizes are reported in Tab. 5.13 and plotted on Fig. 5.13. This shows that the size of the REV impacts the predicted pressure drop. As one can see on Fig.5.13, the size of the REV is crucial in elastic mode, in particular for stiff cases. This is due to the appearance of additional modes as the size of the REV grows, leading to a varying surface exposed to the flow. To explain that, we introduce the space phase shift measurement as

$$\Delta yy_{ij} = \sqrt{\frac{1}{T_p}\int_{T_p} \left(y'_{ij} - y'_{i0}\right)^2 dt}. \tag{5.4.1}$$

This measures the shift in position along the y direction of cylinder of row i and column j compared to the cylinder of column 0 on the same row, *i.e.* the cylinder of column 0 that shares the same Y_0

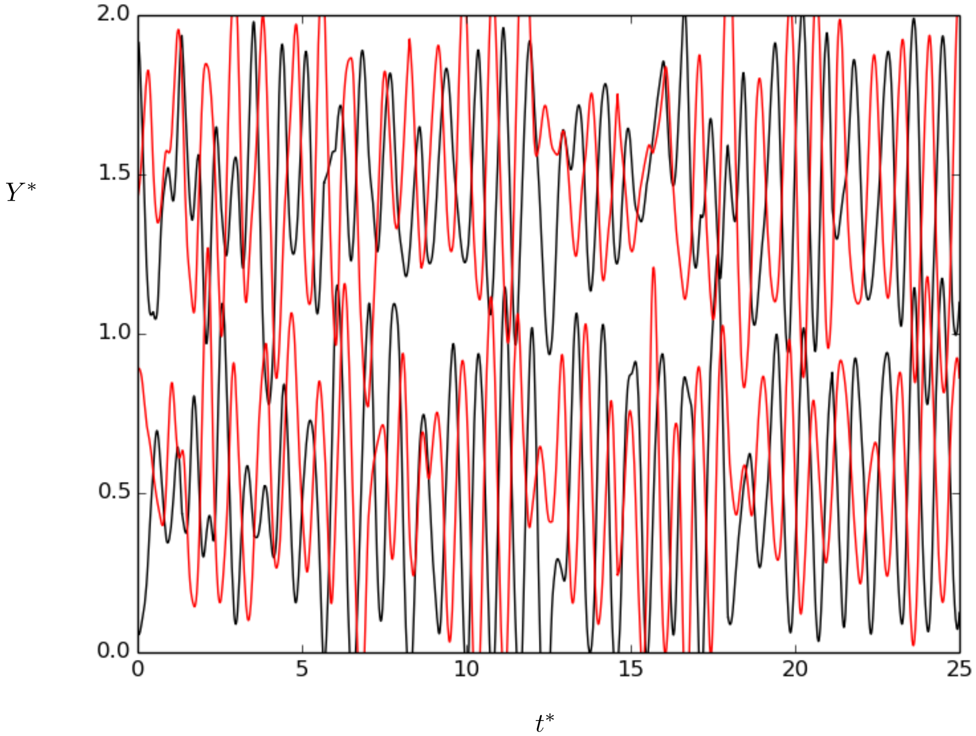

(a) zone A

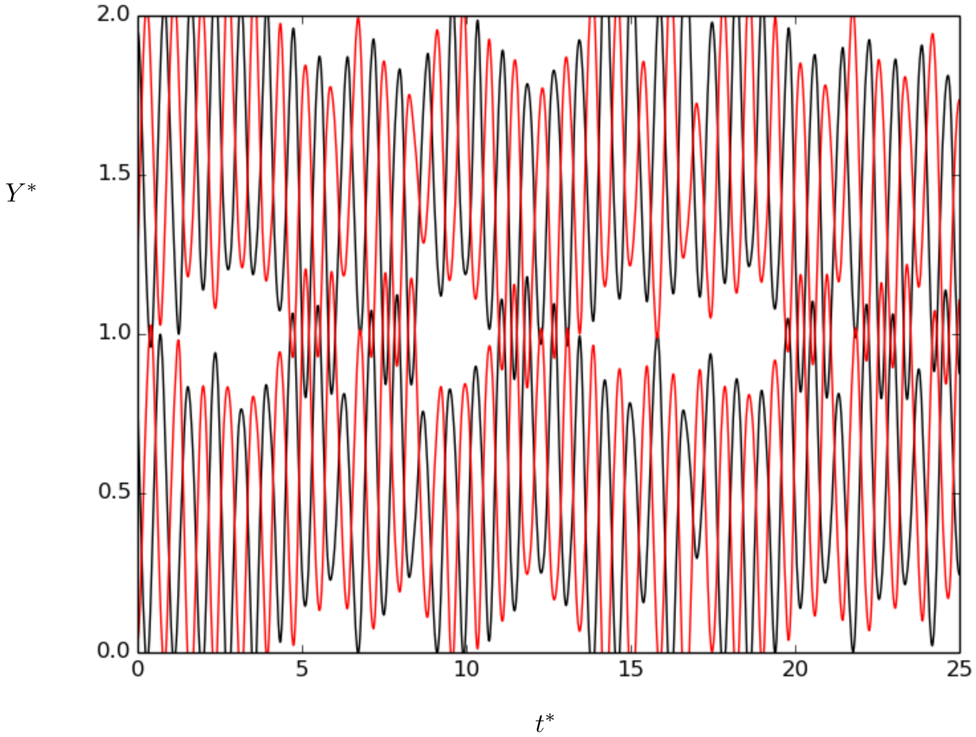

(b) zone B

Figure 5.10: Vertical position of the cylinders during time for different stiffnesses of the porous medium at $Reg = 56$. The zone indicated in caption of each picture gives the corresponding zone of the profile of S^* given on Fig. 5.9. We observe that the maxima in S^* occure when the column-to-column cylinders vibrate π rad out-of-phase (zone B). Note that the row-to-row vibration is in-phase. The color of the curve corresponds to a column of cylinders.

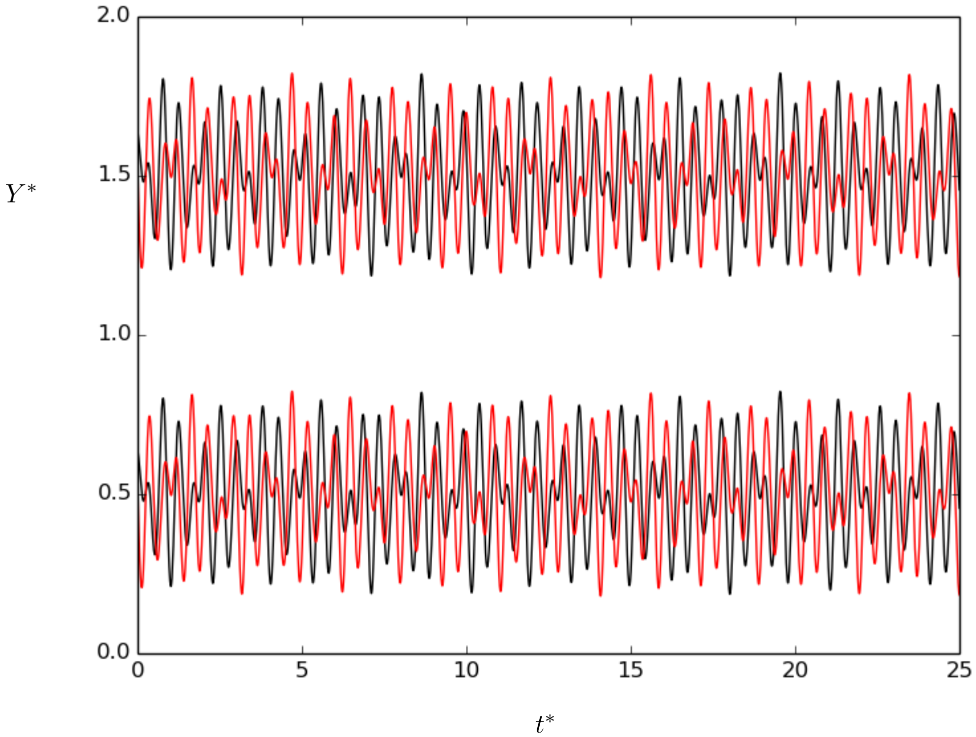

(a) zone C

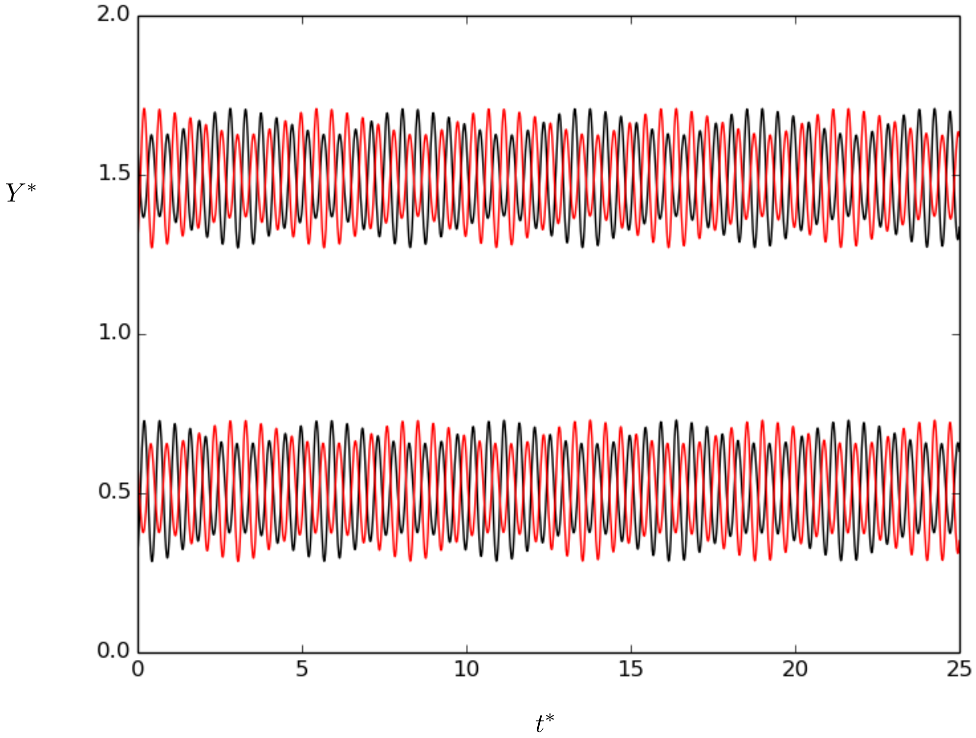

(b) zone D

Figure 5.11: Vertical position of the cylinders during time for different stiffnesses of the porous medium at $Reg = 56$. The zone indicated in caption of each picture gives the corresponding zone of the profile of S^* given on Fig. 5.9. We observe that the maxima in S^* occure when the column-to-column cylinders vibrate π rad out-of-phase (zone D). Note that this time, the row-to-row vibration is π rad out-of-phase. The color of the curve corresponds to a column of cylinders.

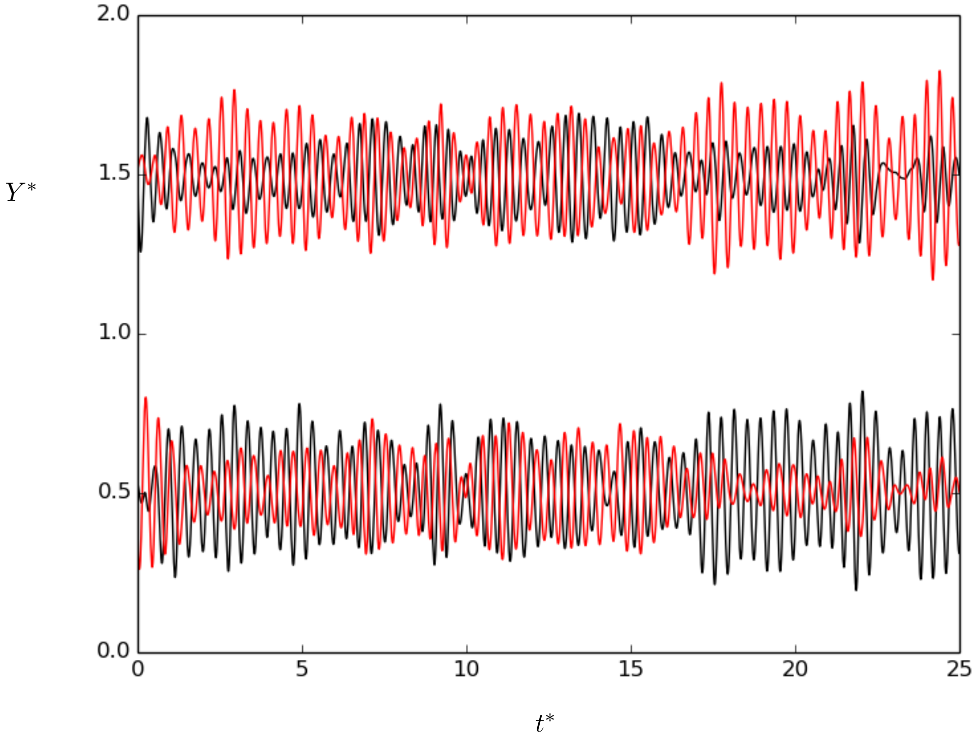

(a) zone E

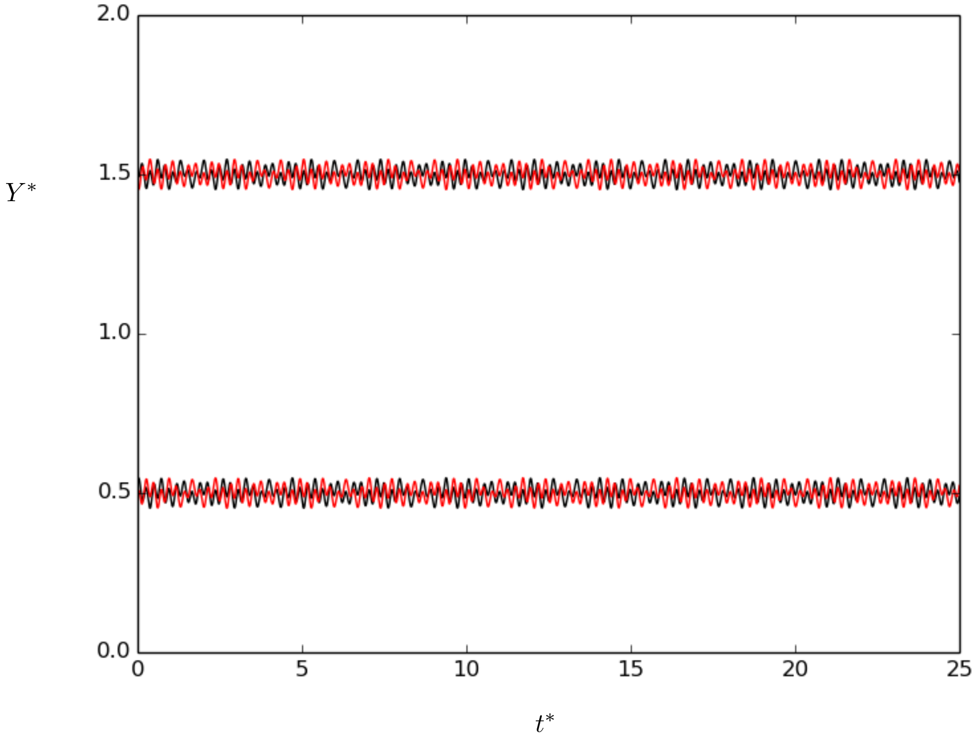

(b) zone F

Figure 5.12: Vertical position of the cylinders during time for different stiffnesses of the porous medium at $Reg = 56$. The zone indicated in caption of each picture gives the corresponding zone of the profile of S^* given on Fig. 5.9. The color of the curve correspond to a column of cylinders.

coordinate for its rest position. We plot the map of this space phase shift on Fig. 5.14 and 5.15. We observe that indeed the size of the REV introduces different vibration modes, and this is correlated to the error on the predicted value of S^*. For case $f^* = 2, m^* = 1$ on a 4×4 REV, it is interesting to see that $Re_D \simeq 62$ is lower than the critical value Re_u for unsteady flow in the rigid porous medium. Here Re_D is not relevant to characterize our cases. Indeed, we can obtain $Re_D \simeq 62$ with or without deformation of the medium, depending on Reg, and the Reynolds number Re_D in rigid case wil be the same in elastic case if the flow is steady. Hence, we rather use Reg to characterize our cases. Re_D is only interesting in terms of physical interpretation, but does not characterize properly our cases.

Another striking result on Fig.5.13 is that the effect of the size of the REV disappears when $f^* \leq 1$. This can be understood as in these soft cases, the cylinders encounter large displacements and are not coupled to their neighbouring column only, but with cylinders from the wider neighbourhood. Thereby the growth in size of the REV does not introduce new vibration modes nor new features, because the cylinder-cylinder interactions are roughly already captured by the smallest REV. It is likely however that for these soft cases, an effect of the size of the REV might appear with macroscopically sheared flow. Indeed we expect that such flows generate large scale effects involving both the elasticity of the medium and the flow inertia. There is the question of the impact on macroscopic transport in terms of momentum diffusion and advective transfer by the subgrid-scale flow. In particular based on our data, we can assume that the fluid-elastic pore-scale interaction enhances the flow mixing at the pore-scale. Therefore there should be more effort spent on macroscopically sheared flow within elastic porous medium, with a specific look at the subgrid-scale stresses.

5.5 Conclusion

This section studies the effect of the fluid-structure interaction on the pressure drop through a periodic box of elastically mounted cylinders. The approach proposes two IBM methods to solve this problem. It appears from this study that the choice of numerical method is indeed important, in particular with large flow inertia effects. However for the Reynolds number considered, the IBM method implemented in **Jadim** [143] is sufficient to explore the trends. A preliminary set of data is obtained for a few values of reduced mass and frequency of the model porous medium. This shows that the impact of elasticity of the solid structure may increase the effective surface exposed to the flow in a significant way (2 to 4 times the exposed surface of the rigid matrix, depending on the Reynolds number and structure parameters). The impact of the size of the computational domain is also evaluated, and a strong influence is found especially when cylinders tend to couple with their neighbours (stiff cases, $f^* \geq 2$). In the future, regimes of stronger inertia should be studied, with larger domains and/or finer

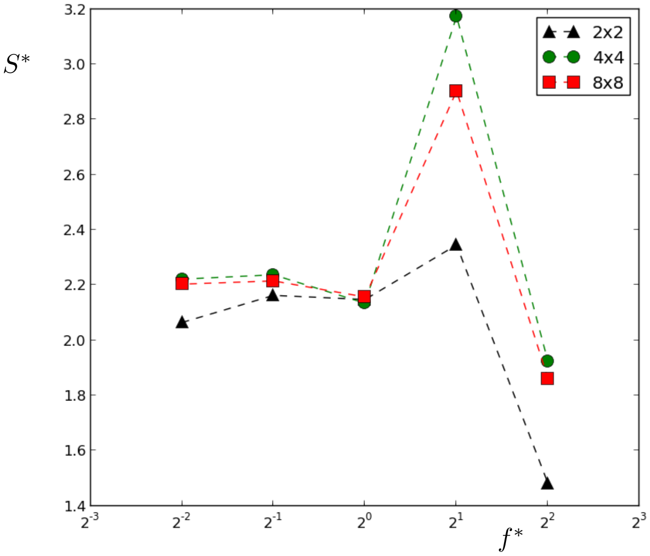

REV	f025m1	f05m1	f1m1	f2m1	f4m1
2×2	76.74	74.97	75.23	71.99	90.61
4×4	73.97	73.71	75.47	61.88	79.53
8×8	74.33	74.14	75.13	64.76	80.91

Figure 5.13: Re_D (table) and S^* for $Reg = 56$ for three REV sizes and different stiffnesses of the elastic medium. The type of coupling between the cylinders depends on the size of the REV for stiff cases, and this impacts the flow rate through the elastic porous medium. This effect is observed mainly for stiff cases ($f^* > 1$). The convergence in REV size is much quicker for soft cases.

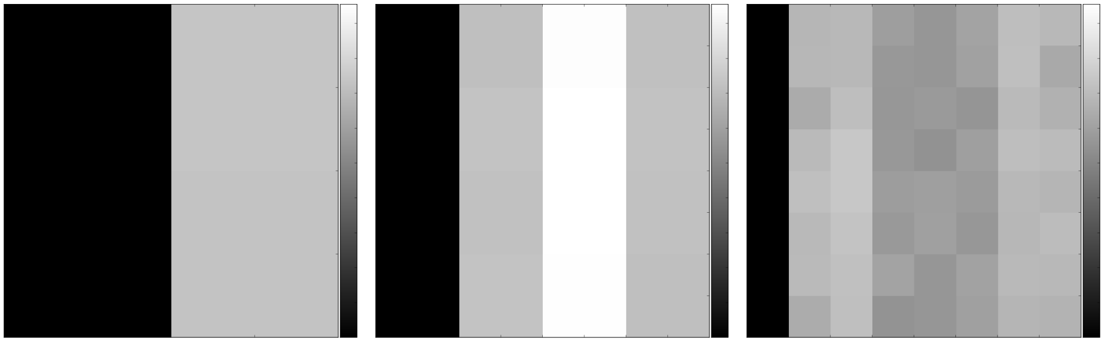
(a) 2×2 (b) 4×4 (c) 8×8

Figure 5.14: Map of Δyy for $f^* = 2, m^* = 1$. The color-scale is the same for each REV size. The clearer the color, the larger the value of Δyy.

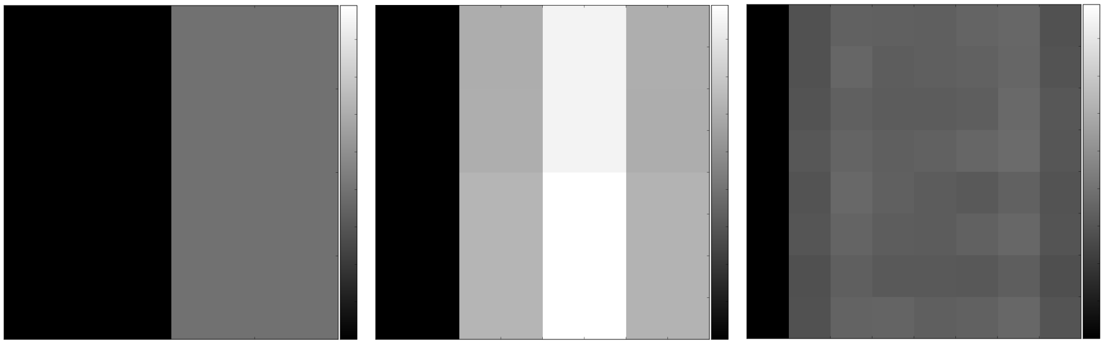

(a) 2×2 (b) 4×4 (c) 8×8

Figure 5.15: Map of Δyy for $f^* = 4, m^* = 1$. The color-scale is the same for each REV size. The clearer the color, the larger the value of Δyy. As in Fig. 5.14, the size of the REV introduces new vibration modes for the cylinders composing the elastic porous medium.

meshes, and different flow conditions (*e.g.* macroscopic shear). The set of data we started to build for the pressure drop through elastic porous media should be completed. A future work should aim at studying non-periodic, unsteady flows in this model porous medium. This would allow to get insight on the impact of elasticity of the solid matrix on the subgrid-scale stresses, under macroscopic shear conditions. The development of an efficient, scalable code, that properly implements the no-penetration condition at the solid boundary, is essential to the study of pore-scale fluid-structure interaction at higher Reynolds number.

Part IV

Conclusion

Chapter 6

Conclusion and future work

In this chapter, we draw a general conclusion, and propose some research perspectives.

6.1 General conclusion

In addition to improving our fundamental understanding of momentum- and mass- transport in honami, the study of canopy flows has plenty other applications like for the modeling of transport of sediments and nutrients in eco-systems, or the development of innovative coatings to manipulate the turbulence on aerodynamic surfaces. For the specific purpose of passive flow control, it would be interesting to estimate the advantages of a hairy coating in terms of net vertical momentum transfer in a turbulent flow. Indeed the issue of vertical momentum transfer is crucial in the context of flow separation postponement at the rear edge of a bluff body. To understand how such a poro-elastic coating can be used to manipulate the flow, we propose a physical modeling and a numerical method that simulates the multi-scale fluid-structure interaction developing over a canopy flow.

Canopy flows are characterised by a wide diversity of scales, making it very difficult if not impossible to simulate due to the large number of degrees of freedom involved. Based on previous observations of canopy flows in nature (*e.g.* wind over forests or over plant fields), the canopy-scale is identified to be the relevant scale to simulate, as it plays a dominant role in the vertical momentum- and mass-transport process within canopy flows. In this study, we propose a physical modeling of the large-scale features of canopy flows (honami), based on a scale separation of the fluid-structure coupling. We focus on the simplest canopy flow, where the hydrodynamic forces and plant elasticity dominate the interaction between the flow and the fibres that constitute the elastic canopy (typically the wind blowing over a wheat field). We take advantage of the volume averaging method to write the macroscopic conservation equations under assumptions that are clearly highlighted and discussed in details. In the context of modeling canopy flows, it appears that the development of a macroscopic model should be adapted to the case under study, *i.e.* there is not such thing as a single model for every types of canopy flow. However the framework of volume averaging allows to separate the different scales and to discuss specific issues that arise. Hence this work can be used in order to

- develop a model adapted to any canopy of interest such as vegetated bed rivers or wheat fields.
- improve different issues, such as the handling of the free-flow/porous medium interface, as well as the effect of the subgrid-scale stresses (SGS) on the large scale.

Among the diversity of scales that are involved in such passive elastic canopy flows, we aim to simulate only the canopy-scale features. Hence, we adopt a porous medium- approach and filter-out the un-desired small scales. To do so, we apply the volume averaging method. It is a flexible method that allows to explicitly and practically filter the small scales of a system. The volume averaging method appears to be a good choice here, although our approach can be improved with a little work on many aspects that were simplified in this study. This leads us to a macroscopic model, that describes only the large-scales of the fluid. Along with a specific approach for the solid-phase, we obtain a macroscopic model (hybrid model) for the fluid-elastic interaction between the flow and the canopy. In this model, although the smaller scales are filtered-out in time and space, they still affect the canopy-scale phenomena via the subgid-scale stresses and the fluid-solid force applied to the canopy. A modeling effort is therefore required in order to close the macroscopic model.

The effect of inertia on the fluid-solid force in porous media are examined in details, focusing on the deviation from Darcy's law. An asymptotic filtration law is derived based on the equations for the fluid obtained from the volume averaging method. This asymptotic law allows to recover theoretical results from the literature, that were obtained by the homogenization method. The framework we propose allows to study the characteristics of the inertial deviation from Darcy's law in terms of magnitude and direction and to help clarify the role of the microstructure. A geometrical parameter, the *inertial sensitivity*, is introduced to quantify the sensitivity to inertia of the microstructure of any porous medium. This leads to the derivation of a new Reynolds number Re_C, that better takes into account inertia effects depending on the microstructure of the porous medium. The asymptotic filtration law, as well as the new Reynolds number Re_C, are tested on a number of ordered and disordered example microstructures, against local direct numerical simulations of the flow within these microstructures. The simulations are CPU demanding and are performed with the efficient, scalable library Open∇FOAM$^{®}$, on the supercomputing facility CalMiP. The *inertial sensitivity* parameter is shown to be essential in the comparison of advection- against diffusion- effects for a flow in a porous medium. This provides insight on the role of the geometry and the length-scales involved in the inertial deviation from Darcy's law. This deviation is mainly due to the ability of the flow within the porous medium to develop advection-dominated area, depending on the shape of the microstructure.

The modeling of the small scales is further improved in the context of the macroscopic modeling of unsteady flow in deformable elastic porous medium. A step toward a better physical understanding of this topic is carried-on here, with the study of the pore-scale fluid-structure interaction (FSI) at moderate Reynolds number occurring in the simplest elastic porous medium, *i.e.* a 2D array of elastically mounted cylinders. This requires an efficient, parallelized code to explore the large panel of geometries, flow regimes, and rigidity of the micro-structure. Two immersed boundary codes are developed and tested. The first method (immersed boundary method (IBM) proposed in **Jadim**) implements a diffuse fluid/solid boundary approach. The second method (mixed cut-cell direct forcing, **MCCDF**) implements a sharp fluid/solid boundary approach. The main difference between the two methods lies in the implementation of the no-slip condition for incompressible flow at the fluid/solid boundary. We focus on a simple model porous medium (array of cylinders) and show that the two methods compare well at the flow regimes ($Re \sim 100$) and rigidity considered. We expect however that the numerical results difference between the two methods becomes greater as the Reynolds number and acceleration of the solid phase increase in magnitude. Based on this cross-validation, the IBM of **Jadim** is used to show that the FSI at the pore scale translates into a dramatic increase in terms of equivalent solid surface exposed to the flow, compared to the same rigid porous medium under the same pressure gradient. This directly impacts the filtration law and should be taken into account in the modeling of pore-scale unsteady flow in elastic porous media. The results are shown to be sensitive to the size of the considered flow domain, in particular for stiff cases. This campaign shows that the effect on S^* is sensitive to the ratio between the flow time scale and the structure time scale, f^*. We observe that depending on the value of f^*, the cylinders display different coupling patterns between each other, leading S^* to reach at least two maxima. This shows that the elasticity plays a complex role in the determination of the pressure drop for unsteady flow in elastic porous media.

In the development of the macroscopic code, a rather simple, Lagrangian modeling of the solid phase dynamics is proposed. A structure solver that resolves the dynamics of the porous medium is integrated into a fluid solver of Open∇FOAM$^{\circledR}$. The coupling between the fluid- and the solid-solver is made sequentially, which means that the fluid- state is resolved first with the last solid- state, then the solid- phase "catches up" with the fluid- phase, then the fluid- state is resolved with the last solid- state, etc. To save CPU-time, only a few fibres' dynamics are resolved, and the porosity- and inclination- fields are re-constructed based on linear interpolation of the kinematics between resolved fibres. The coupling between the fluid and the solid phase is handled via the modeling of the fluid-solid force, that is provided by a metamodel for a given porosity, Reynolds number and inclination of the fibres. The interface between the free-flow and the porous medium is handled by a space varying source term in the transport equations, as proposed in the development of the macroscopic model for the fluid-phase by the volume averaging method. The subgrid-scale stresses (SGS) are taken into account by a SGS model in the free-flow region, but are neglected in the homogeneous porous region. This method appears to be relevant as a first approach because we manage to recover the fluid-structure coupling usually observed in canopy flows (honami) on an illustrative case. However our model, as well as the numerical method, should be further improved in order to be able to conduct deeper comparisons with experiments. This macroscopic code summarizes the work of this thesis, and seems a promising way for simulating canopy flows and see the effect of tuning parameters such as the porosity, the canopy stiffness and dimensions and damping, and the flow characteristics. The framework of Open∇FOAM® is adapted to the simulation of a canopy flow, as it is available and open and it comes up with a message passing interface library that allows for a distribution of the tasks related to the solid deformation among several CPUs. This parallelization feature has appeared to be essential to the simulation of large canopy flows.

6.2 Future work

The development of a macroscopic code is a promising step toward the study of a poro-elastic layer (canopy) under turbulent flow and the resulting large scale fluid-elastic interaction. In the context of turbulent flow control, the numerical simulation of canopy flow could afford precise data measurement at the core of the canopy, as well as valuable parameter studies and design space exploration that could lead to the design of a canopy for a specific set of objectives. However we have seen that there is still a lot of aspects to be developed in this context. Although we proposed some possible solutions, multiple issues remain widely open toward the macroscopic modeling of momentum transport within canopies and the numerical simulation of canopy flows.

In this study, we have written a model adapted to a particular case of canopy. We have made several assumptions on the stiffness, weight and sparsity of the fibres, as well as on the type of macroscopic fluid-solid interaction. Each assumption has been clearly highlighted and this allows the reader to use this work to further develop his own model, adapted to any canopy of interest, whether it is a vegetated river bed or a wheat field under strong wind. Depending on the canopy flow of interest, different assumptions are to be made in order to account for the relevant physical phenomena. For example, buoyancy forces require a particular implementation in the macroscopic model (in this work they are neglected). Another strong assumption of this work is the ”high porosity” assumption, which implies that porosity gradients play a negligible role in the homogeneous porous region.

The database for the fluid-solid force is still incomplete. A wide range of parameters still requires the use of heuristic models. For example the quadratic form of the fluid-solid force is required for high Reynolds number, because direct numerical simulations of the flow a these Reynolds number is too expensive, and there are no reliable experimental data that give the fluid-solid force according to the direction of the mean flow in an array of tubes. Moreover, the determination of the fluid-solid force according to the porosity is still very rough, and we have made use of the Kozeny-Carman correlation in order to extend the metamodel to any porosity. In additions, the effect of elasticity of the porous medium makes it even more complex, potentially involving many 3D, sophisticated fluid-elastic physical phenomena that are still to be discovered.

The question of building macroscopic transport equations for turbulent flows within soft deformable porous media is an exiting challenge. The modeling of the subgrid-scale stresses (SGS) is to be further studied. It was shown that the SGS should be neglected in the homogeneous porous region, but they play an important role in the free-flow region. Here we have used a classical SGS model, but it is not obvious whether this model is acceptable near the top of the canopy. At the fluid/porous interface, strong velocity gradients occur and the fluid interacts with a deformable elastic solid phase. This impacts the vertical mixing and the influence of the fluid-structure coupling on the SGS is a wide open research field. Concerning the study of the small scale, there are still huge challenges remaining. For turbulent flows at the fluid/porous interface of an elastic medium, we have proposed a macroscopic modeling via a continuous source term in the momentum transport equations. This needs to be further investigated and validated on a real case by, *e.g.* , comparison to volume averaged- direct numerical simulations.

One last but not least point is the code development aspect. The coupling between the fluid- and the structure- solver is currently weak. This means that the fluid and the structure are not resolved at the same time but sequentially. This could introduce some numerical artefacts in the prediction of the fluid-structure coupling in canopy flows. This question needs to be investigated thoroughly. More generally, the issue of the choice of numerical method and/or algorithms is challenging. There is the need for efficient, scalable codes, for the study of the microscopic level, as well as for the implementation of the macroscopic model. For example, a decomposition domain (or any other suitable parallelization approach) should be implemented at both the microscopic and the macroscopic levels. An immersed boundary approach adapted to rigid bodies moving at high Reynolds numbers (sharp fluid/solid interface, *e.g.* the **MCCDF** method) is at the core of future perspectives in the study of pore-scale FSI at moderate Reynolds numbers, as well as the study of the interface between a turbulent flow and an elastic porous medium. Along with the writing of the macroscopic model, the development of maintainable, high quality parallelized code is at the core of the numerical modeling of canopy flows.

We believe that the preliminary work we have given here in the development of the macroscopic code is a good start, although much can be done in order to improve it in terms of parallelization strategy, implementation of the fluid-solid coupling and resolution of the solid-phase dynamics.

Appendices

Appendix A

Derivation of the filtration law (periodic porous medium)

In this section, we give some technical details of the derivation of the filtration law by the volume averaging method.

A.1 Upscaling via volume averaging

We volume-average Eq. 4.2.1 in order to obtain a representation at the macroscopic scale. To do so, we first recall a few fundamental steps. Let ψ be a generic field, and γ_β be the β- phase indicator. We define the averaging volume $\mathscr{V}(\mathbf{x})$ of characteristic length ℓ_0, whose centroid is located in $\mathbf{x}$ (which can be in any of the two phases, see Fig. 2.1). The intrinsic average of ψ at point $\mathbf{x}$ is defined in a general way as

$$\langle\psi\rangle^{\beta}|_{\mathbf{x}} = \int_{\mathbb{R}^3} m(\mathbf{r}-\mathbf{x})\,\gamma_\beta(\mathbf{r})\,\psi(\mathbf{r})\;dV(\mathbf{r}), \tag{A.1.1}$$

where $\mathbf{r} = \mathbf{x} + \mathbf{y}_\beta$. This definition of the intrinsic average $\langle\psi\rangle^{\beta}|_{\mathbf{x}}$ allows to choose m so that the resulting intrinsic average is suitable to the porous medium that we volume average [44, 45]. m is a kernel normalized so that

$$\int_{\mathbb{R}^3} m(\mathbf{r})\,\gamma_\beta(\mathbf{r})\;dV(\mathbf{r}) = 1. \tag{A.1.2}$$

In the following we drop the $|_{\mathbf{x}}$ subscript when there is no ambiguity regarding the point where the average is evaluated.

The volume averaging method uses a perturbation decomposition of the fields. Each field ψ is

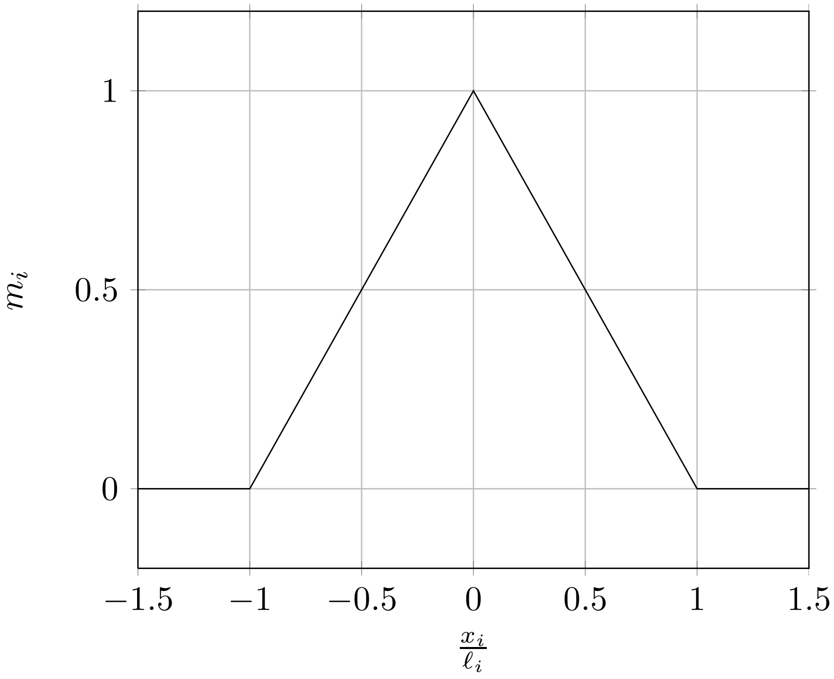

Figure A.1: One dimensional cellular filter, following the concept of *double average* introduced in [44]. ℓ_i is the dimension of the REV in the i^{th} direction. Notice that the support of the cellular filter is twice as large as the dimension of the REV.

decomposed as the sum of an average field, $\langle\psi\rangle^{\beta}$, and a *spatial deviation*, $\tilde{\psi}$, so that

$$\psi = \langle\psi\rangle^{\beta} + \tilde{\psi}, \tag{A.1.3}$$

with the underlying idea that

$$||\nabla \langle\psi\rangle^{\beta}|| \ll ||\nabla\tilde{\psi}||. \tag{A.1.4}$$

The triangular *cellular filter* drawn in Fig. A.1 is a good choice for m (concept of *double average* introduced in [44]). In 3D, $m(\mathbf{x})$ takes the form

$$m(\mathbf{x}) = \prod_{i=1,3} m_i(x_i). \tag{A.1.5}$$

Let $\mathscr{V}_\beta\left(\mathbf{x}\right)$ be the domain filled with the fluid- phase inside the averaging volume $\mathscr{V}\left(\mathbf{x}\right)$ and let V_β be the measure of $\mathscr{V}_\beta\left(\mathbf{x}\right)$. It is useful to note that the cellular filter is such that

$$\int_{\mathbb{R}^n} m\left(\mathbf{r}-\mathbf{x}\right)\psi\left(\mathbf{r}\right)\,dV\left(\mathbf{r}\right) = \frac{1}{V_\beta}\int_{\mathscr{V}_\beta(\mathbf{x})}\left(\frac{1}{V_\beta}\int_{\mathscr{V}_\beta(\mathbf{y})}\psi\left(\mathbf{r}\right)\,dV\left(\mathbf{r}\right)\right)dV\left(\mathbf{y}\right). \tag{A.1.6}$$

In particular the average of a periodic field is such as

$$\int_{\mathbb{R}^n} m\left(\mathbf{r}-\mathbf{x}\right)\psi\left(\mathbf{r}\right)\,dV\left(\mathbf{r}\right)=\frac{1}{V_\beta}\int_{\mathscr{V}_\beta(\mathbf{x})}\psi\left(\mathbf{r}\right)\,dV\left(\mathbf{r}\right). \tag{A.1.7}$$

Since our porous medium is homogeneous and periodic, the kernel m defined by Eq. A.1.5 ensures differentiable average pressure and velocity fields, and volume averaging Eq. 4.2.1 yields a local macroscopic equation. The order upon which the macroscopic equation can be stated depends on the regularity of m. Here m is only C^0, hence average quantities are only C^1 and Taylor expansions of average quantities are truncated with a second order error [44, 45]. We obtain

$$\nabla\left\langle p_\beta\right\rangle^\beta-\rho_\beta\mathbf{s}_\beta=\int_{\mathbb{R}^n} m\left(\mathbf{r}-\mathbf{x}\right)\delta_{\beta\sigma}\left(\mathbf{r}\right)\mathbf{n}_{\beta\sigma}\cdot\left(-\mathbf{I}\tilde{p}_\beta+\mu_\beta\nabla\tilde{\mathbf{v}}_\beta\right)\,dV\left(\mathbf{r}\right)+O\left(\frac{\ell_0}{L_v}\right)^2, \tag{A.1.8}$$

under the assumption that

$$\ell_0\ll L_v, \tag{A.1.9}$$

where L_v is a characteristic macroscopic length.

We can now give a precise definition of the macroscopic pressure drop $\mathbf{g}_\beta$ as

$$\mathbf{g}_\beta=\nabla\left\langle p_\beta\right\rangle^\beta-\rho_\beta\mathbf{s}_\beta. \tag{A.1.10}$$

In Eq. A.1.8, we neglected macroscopic advection and diffusion terms, provided separation of microscopic and macroscopic length scales of the velocity field [136]

$$||\nabla\left\langle\mathbf{v}_\beta\right\rangle^\beta||\ll||\nabla\tilde{\mathbf{v}}_\beta||. \tag{A.1.11}$$

This assumption is reasonable in homogeneous porous media, far from macroscopic boundaries. Thus, for example, the region under study should not lie in a strong shear layer, nor near a wall or a crack.

A.2 The closure problem for spatial deviations

Eq. A.1.8 is a form of the volume averaged Navier-Stokes equations which needs additional equations (*i.e.* a *closure*) for the surface integral term to be evaluated. To derive these equations, we first need to decompose Eq. 4.2.1 applying Eq. A.1.3 to $\mathbf{v}_\beta$ and p_β. By virtue of Eq. A.1.11, we neglect gradients of macroscopic velocities against those of the microscopic velocities in the momentum transport equation and obtain

$$\begin{aligned}
\left(\langle \mathbf{v}_\beta\rangle^\beta + \tilde{\mathbf{v}}_\beta\right)\cdot\nabla\tilde{\mathbf{v}}_\beta &= -\frac{1}{\rho_\beta}\nabla\tilde{p}_\beta + \nu_\beta\nabla^2\tilde{\mathbf{v}}_\beta - \frac{\mathbf{g}_\beta}{\rho_\beta}, && \text{(A.2.1a)}\\
\nabla\cdot\tilde{\mathbf{v}}_\beta &= 0, && \text{(A.2.1b)}\\
\tilde{\mathbf{v}}_\beta &= -\langle \mathbf{v}_\beta\rangle^\beta \text{ on } \mathscr{A}_{\beta\sigma}. && \text{(A.2.1c)}
\end{aligned}$$

At this stage, it is common to introduce a tensorial relation between space deviations and the intrinsic average of the velocity $\langle \mathbf{v}_\beta\rangle^\beta$ [136]. This mapping is adapted to the linear, creeping flow regime, as it expresses the fact that the microscopic flow field is a linear combination of the flow in three independent directions of space. Clearly this is not adapted here due to the non-linear term in Eq. A.2.1. We therefore drop the linear closure relationship of Whitaker [136] and keep working with the deviation fields. We introduce the modified dimensionless perturbations $\mathbf{v}^*$ and p^* defined as

$$\mathbf{v}^* = \frac{\tilde{\mathbf{v}}_\beta}{v} + \boldsymbol{\lambda},\; p^* = \ell\frac{\tilde{p}_\beta}{\mu_\beta v}, \tag{A.2.2}$$

with ℓ as yet undefined. Under such circumstances

$$\nabla\tilde{\mathbf{v}}_\beta = v\left(\nabla\mathbf{v}^* + \frac{\nabla v}{v}\mathbf{v}^* - \frac{\nabla\langle \mathbf{v}_\beta\rangle^\beta}{v}\right),\; \nabla\tilde{p}_\beta = v\frac{\mu_\beta}{\ell}\left(\nabla p^* + p^*\frac{\nabla v}{v}\right). \tag{A.2.3}$$

We inject Eq. A.2.2 and A.2.3 into Eq. A.2.1. Under the assumption given by Eq. A.1.11 we obtain

$$\frac{\ell}{\nu_\beta}v|_{\mathbf{x}+\mathbf{y}_\beta}\left(\mathbf{v}^*\cdot\nabla^*\mathbf{v}^*\right) = -\nabla^* p^* + \nabla^{*2}\mathbf{v}^* + \epsilon_\beta\mathbf{h}^*, \tag{A.2.4}$$

where

$$\begin{aligned}
\mathbf{h}^* &= -\frac{\ell}{\epsilon_\beta \mathsf{V}_\beta}\int_{\mathscr{A}_{\beta\sigma}}\mathbf{n}_{\beta\sigma}\cdot\left(-\mathbf{I}p^* + \nabla^*\mathbf{v}^*\right)dA, && \text{(A.2.5a)}\\
\nabla^* &= \ell\nabla. && \text{(A.2.5b)}
\end{aligned}$$

The weighting function m does not appear in the surface integral, due to the spatially periodic model that we introduce later for the closure variables $\mathbf{v}^*$ and p^* [155]. Compared to the linear case, a non-local term remains in Eq. A.2.4. As we intend to solve for $\mathbf{v}^*$ and p^* on a REV of characteristic size ℓ_0, we linearize

$$v|_{\mathbf{x}+\mathbf{y}_\beta} = v\left[1 + \frac{\mathbf{y}_\beta}{\ell}\cdot\frac{\nabla^* v}{v} + O\left(\frac{\ell_0}{L_v}\right)^2\right]. \tag{A.2.6}$$

We also have that

$$\begin{aligned}\langle \mathbf{v}_\beta \rangle^\beta &= \langle \mathbf{v}^* v \rangle^\beta && \text{(A.2.7a)}\\ &= v \left[\langle \mathbf{v}^* \rangle^\beta + \left\langle \mathbf{v}^* \frac{\mathbf{y}_\beta}{\ell} \right\rangle^\beta \cdot \frac{\nabla^* v}{v} + O\left(\frac{\ell_0}{L_v}\right)^2 \right], && \text{(A.2.7b)}\end{aligned}$$

hence

$$\langle \mathbf{v}^* \rangle^\beta = \boldsymbol{\lambda} - \left\langle \mathbf{v}^* \frac{\mathbf{y}_\beta}{\ell} \right\rangle^\beta \cdot \frac{\nabla^* v}{v} + O\left(\frac{\ell_0}{L_v}\right)^2. \tag{A.2.8}$$

We define the REV as the unit cell of our periodic porous medium. This is consistent with the flow regimes considered. In many systems there may be transport processes with characteristic length scales much larger than the unit cell of the microstructure, as argued in, *e.g.* , [34, 33, 156]. In such cases, one cannot reduce the REV to the unit cell of the porous medium and would need to determine an actual REV size for the flow process to be represented adequately.

We add *periodic conditions* at the boundaries of the REV since source terms of the problem are periodic themselves. By virtue of Eq. A.1.9, $\frac{\nabla^* v}{v}$ terms are negligible. We therefore determine the closure variables $\mathbf{v}^*, p^*$ through the approximate system

$$\begin{aligned}\frac{\ell v}{\nu_\beta}\left(\mathbf{v}^* \cdot \nabla^* \mathbf{v}^*\right) &= -\nabla^* p^* + {\nabla^*}^2 \mathbf{v}^* + \epsilon_\beta \mathbf{h}^*, && \text{(A.2.9a)}\\ \nabla^* \cdot \mathbf{v}^* &= 0, && \text{(A.2.9b)}\\ \mathbf{v}^* &= 0 \text{ at } \mathscr{A}_{\beta\sigma}, && \text{(A.2.9c)}\\ \langle \mathbf{v}^* \rangle^\beta &= \boldsymbol{\lambda}. && \text{(A.2.9d)}\end{aligned}$$

Here, it should be clear that the surface integral in Eq. A.1.8 is well approximated by $\mathbf{h}^* v$ issued from Eq. A.2.9, only if lengthscale assumptions stated by Eq. A.1.9 and Eq. A.1.11 are acceptable. The filtration law is then given from Eq. A.1.8 by

$$\frac{\ell^2}{\mu_\beta} \mathbf{g}_\beta\left(\boldsymbol{\lambda}, \delta\right) = -\mathbf{h}^* v. \tag{A.2.10}$$

Depending on v, the equation above gives the macroscopic pressure drop for a steady inertial flow in the $\boldsymbol{\lambda}$ direction.

Appendix B

The Asymptotic Generalized-Forchheimer equation

We inject the expansion Eq. 4.2.7 into Eqs. A.2.9 to derive the asymptotic generalized-Forchheimer equation (AGF). Order $i \geq 0$ corresponds to

$$\mathbf{S}_i^* = -\nabla^* p_i^* + {\nabla^*}^2 \mathbf{v}_i^* + \epsilon_\beta \mathbf{h}_i^*, \tag{B.0.1a}$$

$$\nabla^* \cdot \mathbf{v}_i^* = 0, \tag{B.0.1b}$$

$$\mathbf{v}_i^* = 0 \text{ at } \mathscr{A}_{\beta\sigma}, \tag{B.0.1c}$$

with

$$\mathbf{S}_0^* = 0, \tag{B.0.2a}$$

$$\mathbf{S}_1^* = \mathbf{v}_0^* \cdot \nabla^* \mathbf{v}_0^*, \tag{B.0.2b}$$

$$\mathbf{S}_i^* = \sum_{k+p=i-1} \left(\mathbf{v}_k^* \cdot \nabla^* \mathbf{v}_p^* + \mathbf{v}_p^* \cdot \nabla^* \mathbf{v}_k^* \right), \forall i \geqslant 2, \tag{B.0.2c}$$

and

$$\mathbf{h}_i^* = -\frac{\ell}{\epsilon_\beta \mathsf{V}_\beta} \int_{\mathscr{A}_{\beta\sigma}} \mathbf{n}_{\beta\sigma} \cdot \left(-\mathbf{I} p_i^* + \nabla^* \mathbf{v}_i^* \right) dA. \tag{B.0.3}$$

To solve System B.0.1 we proceed with this change of variables

$$\mathbf{v}_i^* = \mathbf{v}_{i0}^* + \mathbf{B}_0^* \cdot \mathbf{h}_i^*, \tag{B.0.4a}$$

$$p_i^* = p_{i0}^* + \mathbf{b}_0^* \cdot \mathbf{h}_i^*, \tag{B.0.4b}$$

with

$$
\begin{aligned}
0 &= -\nabla^* \mathbf{b}_0^* + \nabla^{*2} \mathbf{B}_0^* + \epsilon_\beta \mathbf{I}, && \text{(B.0.5a)}\\
\nabla^* \cdot \mathbf{B}_0^* &= 0, && \text{(B.0.5b)}\\
\mathbf{B}_0^* &= 0 \text{ at } \mathscr{A}_{\beta\sigma}, && \text{(B.0.5c)}
\end{aligned}
$$

and

$$
\begin{aligned}
\mathbf{S}_i^* &= -\nabla^* p_{i0}^* + \nabla^{*2} \mathbf{v}_{i0}^*, && \text{(B.0.6a)}\\
\nabla \cdot \mathbf{v}_{i0}^* &= 0, && \text{(B.0.6b)}\\
\mathbf{v}_{i0}^* &= 0 \text{ at } \mathscr{A}_{\beta\sigma}. && \text{(B.0.6c)}
\end{aligned}
$$

From Eq. A.2.8 we have $\langle \mathbf{v}^* \rangle^\beta = \boldsymbol{\lambda}$. Hence, the coefficients of expansion in Eq. 4.2.7 verify

$$
\begin{aligned}
\langle \mathbf{v}_0^* \rangle^\beta &= \boldsymbol{\lambda}, && \text{(B.0.7a)}\\
\langle \mathbf{v}_i^* \rangle^\beta &= 0, \forall i \geq 1. && \text{(B.0.7b)}
\end{aligned}
$$

Taking the average of order 0 in Eq. B.0.4, we obtain

$$\boldsymbol{\lambda} = \langle \mathbf{v}_{00}^* \rangle^\beta + \langle \mathbf{B}_0^* \rangle^\beta \cdot \mathbf{h}_0^*. \tag{B.0.8}$$

Clearly, $\mathbf{v}_{00}^*$ and p_{00}^* are both zero, and Eq. 4.2.2 at order 0 reads

$$\mathbf{g}_\beta = -\frac{\mu_\beta}{\ell^2} \left(\langle \mathbf{B}_0^* \rangle^\beta \right)^{-1} \cdot \boldsymbol{\lambda} v = -\frac{\mu_\beta}{\ell^2} \left(\langle \mathbf{B}_0^* \rangle^\beta \right)^{-1} \cdot \langle \mathbf{v}_\beta \rangle^\beta , \tag{B.0.9}$$

which is the well known [107, 40] Darcy's law (Eq. 5.1.1). The Darcy permeability tensor, $\mathbf{K}_D$, can be identified as

$$\mathbf{K}_D = \epsilon_\beta \ell^2 \langle \mathbf{B}_0^* \rangle^\beta . \tag{B.0.10}$$

Darcy's law is a zero order approximation with regard to our perturbation analysis in δ. As the flow rate increases, inertia effects at the pore scale become increasingly important. The system goes beyond the creeping flow regime and deviates from Darcy's law.

The average of Eq. B.0.4 gives

$$\langle \mathbf{v}_i^* \rangle^\beta = \langle \mathbf{v}_{i0}^* \rangle^\beta + \langle \mathbf{B}_0^* \rangle^\beta \cdot \mathbf{h}_i^*, \forall i \geq 1. \tag{B.0.11}$$

Recalling Eq. B.0.7 and B.0.10 we obtain

$$\mathbf{h}_i^* = -\epsilon_\beta \ell^2 \mathbf{K}_D^{-1} \cdot \langle \mathbf{v}_{i0}^* \rangle^\beta , \forall i \geq 1. \tag{B.0.12}$$

Hence, Eq. 4.2.2 at order $N \geq 1$ is (AGF)

$$\mathbf{g}_\beta = -\epsilon_\beta \mu_\beta \mathbf{K}_D^{-1} \cdot \left(\boldsymbol{\lambda} - \sum_{i \geq 1}^{N} \langle \mathbf{v}_{i0}^* \rangle^\beta \delta^i \right) v. \tag{B.0.13}$$

Appendix C

The cubic regime

Eq. B.0.13 at order one gives ($\mathbf{K}_D$ is symmetric [1])

$$\frac{1}{\mu_\beta}\mathbf{g}_\beta = -\epsilon_\beta v \left(\underbrace{\mathbf{K}_D^{-1} \cdot \boldsymbol{\lambda}}_{\text{Darcy term}} - \underbrace{\langle \mathbf{v}^*_{10} \rangle^\beta \cdot \mathbf{K}_D^{-1} \delta}_{\text{first order correction}} + O\left(\delta^2\right) \right). \tag{C.0.1}$$

We note that $\mathbf{v}^*_0$, $\mathbf{v}^*_{10}$, $\mathbf{B}^*_0$ verify a no-slip condition on $\mathscr{A}_{\beta\sigma}$ and periodic boundary conditions over the REV. $\mathbf{b}^*_0$ verifies periodic boundary conditions over the REV. We start by contracting Eq. B.0.5 with $\mathbf{v}^*_{10}$

$$0 = -\mathbf{v}^*_{10} \cdot \nabla^* \mathbf{b}^*_0 + \mathbf{v}^*_{10} \cdot \nabla^{*2} \mathbf{B}^*_0 + \epsilon_\beta \mathbf{v}^*_{10}. \tag{C.0.2}$$

As $\mathbf{v}^*_{10}$ is divergence-free, we can rewrite the first term as a divergence

$$\mathbf{v}^*_{10} \cdot \nabla^* \mathbf{b}^*_0 = \nabla^* \cdot \left(\mathbf{v}^*_{10} \mathbf{b}^*_0 \right). \tag{C.0.3}$$

Also

$$\mathbf{v}^*_{10} \cdot \left(\nabla^{*2} \mathbf{B}^*_0 \right) = \mathbf{v}^*_{10j} \partial^*_i \left(\partial^*_i \mathbf{B}^*_{0jm} \right) \tag{C.0.4a}$$

$$= \partial^*_i \left(\mathbf{v}^*_{10j} \partial^*_i \mathbf{B}^*_{0jm} \right) - \partial^*_i \mathbf{v}^*_{10j} \partial^*_i \mathbf{B}^*_{0jm}, \tag{C.0.4b}$$

hence, taking the average of Eq. C.0.2, applying Gauss theorem and using boundary conditions for $\mathbf{v}^*_0$ and $\mathbf{v}^*_{10}$ we obtain

$$\epsilon_\beta \langle \mathbf{v}^*_{10} \rangle^\beta = \left\langle {}^T \left(\nabla^* \mathbf{v}^*_{10} \right) : \nabla^* \mathbf{B}^*_0 \right\rangle^\beta. \tag{C.0.5}$$

---

[1] One can show using Eq. B.0.5 that $\mathbf{K}_D$ is symmetric (see proof in [40]).

We contract the order 1 of Eq. B.0.6 with $\mathbf{B}_0^*$

$$\left(\mathbf{v}_0^* \cdot \nabla^* \mathbf{v}_0^*\right) \cdot \mathbf{B}_0^* = -\left(\nabla^* p_{10}^*\right) \cdot \mathbf{B}_0^* + \left(\nabla^{*2} \mathbf{v}_{10}^*\right) \cdot \mathbf{B}_0^*, \tag{C.0.6}$$

rewrite

$$\begin{aligned} \left(\nabla^* p_{10}^*\right) \cdot \mathbf{B}_0^* &= \nabla^* \cdot \left(\mathbf{B}_0^* p_{10}^*\right), && \text{(C.0.7a)} \\ \left(\nabla^{*2} \mathbf{v}_{10}^*\right) \cdot \mathbf{B}_0^* &= \nabla^* \cdot \left(\nabla^* \mathbf{v}_{10}^* \cdot \mathbf{B}_0^*\right) -{}^T \left(\nabla^* \mathbf{v}_{10}^*\right) : \nabla^* \mathbf{B}_0^*, && \text{(C.0.7b)} \end{aligned}$$

and take the average of Eq. C.0.6. Applying Gauss theorem and recalling the boundary conditions for $\mathbf{v}_0^*$ and $\mathbf{v}_{10}^*$ we have

$$\left\langle \mathbf{v}_0^* \cdot \nabla^* \mathbf{v}_0^* \cdot \mathbf{B}_0^* \right\rangle^\beta = -\left\langle {}^T \left(\nabla^* \mathbf{v}_{10}^*\right) : \nabla^* \mathbf{B}_0^* \right\rangle^\beta . \tag{C.0.8}$$

With Eq. C.0.5 we obtain

$$\epsilon_\beta \left\langle \mathbf{v}_{10}^* \right\rangle^\beta = -\left\langle \mathbf{v}_0^* \cdot \nabla^* \mathbf{v}_0^* \cdot \mathbf{B}_0^* \right\rangle^\beta . \tag{C.0.9}$$

Let $\mathbf{v}_d$ such as

$$\mathbf{v}_d = \ell^2 \mathbf{B}_0^* \cdot \mathbf{K}_D^{-1} \cdot \mathbf{d}, \tag{C.0.10}$$

with $\mathbf{d}$ a unit vector along a generic direction. The component along $\mathbf{d}$ of the first order correction to Darcy's law reads

$$\epsilon_\beta \ell^2 \mathbf{f}^{(1)} \cdot \mathbf{d} = \epsilon_\beta \ell^2 \left\langle \mathbf{v}_{10}^* \right\rangle^\beta \cdot \mathbf{K}_D^{-1} \cdot \mathbf{d} = -\left\langle \mathbf{v}_0^* \cdot \nabla^* \mathbf{v}_0^* \cdot \mathbf{v}_d \right\rangle^\beta . \tag{C.0.11}$$

Let us rewrite the $\left\langle \mathbf{v}_0^* \cdot \nabla^* \mathbf{v}_0^* \cdot \mathbf{v}_d \right\rangle^\beta$ term using

$$\begin{aligned} \mathbf{v}_0^* \cdot \nabla^* \mathbf{v}_0^* \cdot \mathbf{v}_d &= \mathbf{v}_0^* \cdot \nabla^* \left(\mathbf{v}_0^* \cdot \mathbf{v}_d\right) - \mathbf{v}_0^* \cdot \nabla^* \mathbf{v}_d \cdot \mathbf{v}_0^* && \text{(C.0.12a)} \\ &= \nabla^* \cdot \left(\mathbf{v}_0^* \mathbf{v}_0^* \cdot \mathbf{v}_d\right) - \mathbf{v}_0^* \cdot \nabla^* \mathbf{v}_d \cdot \mathbf{v}_0^*, && \text{(C.0.12b)} \end{aligned}$$

so that

$$\epsilon_\beta \ell^2 \mathbf{f}^{(1)} \cdot \mathbf{d} = -\left\langle \mathbf{v}_0^* \cdot \nabla^* \mathbf{v}_0^* \cdot \mathbf{v}_d \right\rangle^\beta = \left\langle \mathbf{v}_0^* \cdot \nabla^* \mathbf{v}_d \cdot \mathbf{v}_0^* \right\rangle^\beta . \tag{C.0.13}$$

This is a general equation that gives information on the component in the $\mathbf{d}$ direction of the first correction to Darcy's law.

C.1 Drag component $F_\parallel$

The direction $\mathbf{d} = \boldsymbol{\lambda}$ corresponds to

$$\epsilon_\beta \mathbf{v}_d = \mathbf{v}_0^* . \tag{C.1.1}$$

With Eq. C.0.13 we clearly have that

$$\epsilon_\beta \mathbf{v}_d = \mathbf{v}_0^* \quad \text{implies} \quad \left\langle \mathbf{v}_0^* \cdot \nabla^* \mathbf{v}_0^* \cdot \mathbf{v}_d \right\rangle^\beta = 0, \tag{C.1.2}$$

which is equivalent to $F_\parallel^{(1)} = 0$ due to Eq. C.0.11, so that in a periodic porous medium

$$\frac{1}{\mu_\beta} \boldsymbol{\lambda} \cdot \mathbf{g}_\beta \left(\boldsymbol{\lambda}, v\right) = -\epsilon_\beta v \left[\boldsymbol{\lambda} \cdot \mathbf{K}_D^{-1} \cdot \boldsymbol{\lambda} + O\left(\delta^2\right)\right], \tag{C.1.3}$$

i.e. the first drag inertial correction to Darcy's law of our AGF is cubic in terms of the average velocity.

C.2 Orthogonal component $F_\perp$

Let $\boldsymbol{\lambda}^\perp$ be a unit vector orthogonal to the flow direction $\boldsymbol{\lambda}$. Unfortunately, Eq. C.0.13 does not help to prove that $F_\perp^{(1)} = 0$. We can however show that $F_\perp^{(1)}$ must be zero under specific assumptions on the microstructure of the porous medium.

Eq. C.0.13 gives the information that $\ell^2 \mathbf{f}^{(1)} \cdot \mathbf{d}$ is quadratic in $\boldsymbol{\lambda}$, hence

$$\mathbf{f}^{(1)}(+\boldsymbol{\lambda}) = \mathbf{f}^{(1)}(-\boldsymbol{\lambda}) \tag{C.2.1}$$

If we consider a porous medium that verifies the reversibility assumption (Eq. 4.2.10), as in [110], we have at order 1

$$\underbrace{-\epsilon_\beta v \left[\mathbf{K}_{\boldsymbol{D}}^{\mathbf{-1}} \boldsymbol{\cdot} (\boldsymbol{-\lambda}) + \mathbf{f}^{(1)}(-\boldsymbol{\lambda})\delta + O\left(\delta^2\right)\right]}_{\mathbf{g}_\beta(-\boldsymbol{\lambda},v)} = \underbrace{-\left(-\epsilon_\beta v \left[\mathbf{K}_{\boldsymbol{D}}^{\mathbf{-1}} \boldsymbol{\cdot} (\boldsymbol{+\lambda}) + \mathbf{f}^{(1)}(+\boldsymbol{\lambda})\delta + O\left(\delta^2\right)\right]\right)}_{-\mathbf{g}_\beta(+\boldsymbol{\lambda},v)}, \tag{C.2.2}$$

so that if our AGF equation is correct, we must have

$$\mathbf{f}^{(1)}\left(-\lambda\right) = -\mathbf{f}^{(1)}\left(+\lambda\right), \tag{C.2.3}$$

which implies that $\mathbf{f}^{(1)} = 0$, or equivalently

$$F_\parallel^{(1)} = F_\perp^{(1)} = 0. \tag{C.2.4}$$

We have already shown that our asymptotic development yields $F_\parallel^{(1)} = 0$ for any periodic porous media. Hence the new information in Eq. C.2.4 is that $F_\perp^{(1)}$ must be zero for our AGF expression to be valid in porous media where the reversibility assumption is verified. Interestingly, Eq. C.0.13 does not allow to conclude (to our knowledge) that $F_\perp^{(1)} = 0$ when $d = \boldsymbol{\lambda}^\perp$ a direction orthogonal to the flow direction $\boldsymbol{\lambda}$, and yet, this has to be the case under the reversibility assumption.

Bibliography

[1] S. Dupont, F. Gosselin, C. Py, E. De Langre, P. Hemon, and Y. Brunet, "Modelling waving crops using large-eddy simulation: comparison with experiments and a linear stability analysis," *Journal of Fluid Mechanics*, vol. 652, pp. 5–44, 2010.

[2] J. J. Finnigan, R. H. Shaw, and E. G. Patton, "Turbulence structure above a vegetation canopy," *Journal of Fluid Mechanics*, vol. 637, pp. 387–424, 2009.

[3] T. I. Marjoribanks, R. J. Hardy, S. N. Lane, and D. R. Parsons, "High-resolution numerical modelling of flow-vegetation interactions," *Journal of Hydraulic Research*, vol. 52, no. 6, pp. 775–793, 2014.

[4] T. I. Marjoribanks, R. J. Hardy, S. N. Lane, and D. R. Parsons, "Does the canopy mixing layer model apply to highly flexible aquatic vegetation? Insights from numerical modelling," *Environmental Fluid Mechanics*, vol. 17, no. 2, pp. 277–301, 2017.

[5] M. Luhar and H. M. Nepf, "Flow-induced reconfiguration of buoyant and flexible aquatic vegetation," *Limnology and Oceanography*, vol. 56, no. 6, pp. 2003–2017, 2011.

[6] S. E. Belcher, I. N. Harman, and J. J. Finnigan, "The wind in the willows: Flows in forest canopies in complex terrain," *Annual Review of Fluid Mechanics*, vol. 44, pp. 479–504, 2012.

[7] M. R. Raupach, J. J. Finnigan, and Y. Brunet, "Coherent eddies and turbulence in vegetation canopies: the mixing-layer analogy," in *Boundary-Layer Meteorology 25th Anniversary Volume, 1970–1995*, pp. 351–382, Springer, 1996.

[8] J. Finnigan, "Turbulence in plant canopies," *Annual review of fluid mechanics*, vol. 32, no. 1, pp. 519–571, 2000.

[9] H. M. Nepf, "Flow and transport in regions with aquatic vegetation," *Annual Review of Fluid Mechanics*, vol. 44, pp. 123–142, 2012.

[10] W. Chao, S.-s. ZHENG, P.-f. WANG, and H. Jun, “Interactions between vegetation, water flow and sediment transport: A review,” *Journal of Hydrodynamics*, vol. 27, no. 1, pp. 24–37, 2015.

[11] M. R. Foster-Martinez and E. A. Variano, “Air-water gas exchange by waving vegetation stems,” *Journal of Geophysical Research: Biogeosciences*, vol. 121, no. 7, pp. 1916–1923, 2016.

[12] M. Ghisalberti and H. Nepf, “Mass transport in vegetated shear flows,” *Environmental Fluid Mechanics*, vol. 5, no. 6, pp. 527–551, 2005.

[13] C. Gromke and B. Ruck, “On wind forces in the forest-edge region during extreme-gust passages and their implications for damage patterns,” *Boundary-Layer Meteorology*, pp. 1–20, 2018.

[14] F. Gosselin, *Mécanismes d’interactions fluide-structure entre écoulements et végétation.* PhD thesis, École Polytechnique, 2009.

[15] J. Hussong, W. P. Breugem, and J. Westerweel, “A continuum model for flow induced by metachronal coordination between beating cilia,” *Journal of Fluid Mechanics*, vol. 684, pp. 137–162, 2011.

[16] E. Inoue, “Studies of the phenomena of waving plants (”HONAMI”) caused by wind,” *Journal of Agricultural Meteorology*, vol. 11, no. 3, pp. 87–90, 1955.

[17] J. Huang, M. Cassiani, and J. Albertson, “The effects of vegetation density on coherent turbulent structures within the canopy sublayer: a large-eddy simulation study,” *Boundary-layer meteorology*, vol. 133, no. 2, pp. 253–275, 2009.

[18] S. Dupont and Y. Brunet, “Coherent structures in canopy edge flow: a large-eddy simulation study,” *Journal of Fluid Mechanics*, vol. 630, pp. 93–128, 2009.

[19] N. Luminari, C. Airiau, and A. Bottaro, “Drag-model sensitivity of Kelvin-Helmholtz waves in canopy flows,” *Physics of Fluids*, vol. 28, no. 12, p. 124103, 2016.

[20] C. Py, E. De Langre, and B. Moulia, “A frequency lock-in mechanism in the interaction between wind and crop canopies,” *Journal of Fluid Mechanics*, vol. 568, pp. 425–449, 2006.

[21] C. Py, E. De Langre, and B. Moulia, “Instabilite de couche de melange dans le vent sur un couvert vegetal souple,” *Journal of Fluid Mechanics*, vol. 332, pp. 613–618, 2004.

[22] F. P. Gosselin and E. de Langre, “Drag reduction by reconfiguration of a poroelastic system,” *Journal of Fluids and Structures*, vol. 27, no. 7, pp. 1111–1123, 2011.

[23] F. P. Gosselin, E. de Langre, and B. A. Machado-Almeida, “Drag reduction of flexible plates by reconfiguration,” *Journal of Fluid Mechanics*, vol. 650, pp. –, 2010.

[24] J. Favier, A. Dauptain, D. Basso, and A. Bottaro, “Passive separation control using a self-adaptive hairy coating,” *Journal of Fluid Mechanics*, vol. 627, pp. 451–483, 2009.

[25] D. Venkataraman, A. Bottaro, and R. Govindarajan, “A minimal model for flow control on an aerofoil using a poro-elastic coating,” *Journal of Fluids and Structures*, vol. 47, pp. 150–164, 2014.

[26] M. Gad-el Hak, R. F. Blackwelder, and J. J. Riley, “On the interaction of compliant coatings with boundary layer flows,” *Journal of Fluid Mechanics*, vol. 140, pp. 257–280, 1984.

[27] M. Gad-el Hak and D. M. Bushnell, “Separation control: Review,” *Journal of Fluids Engineering*, vol. 113, 1991.

[28] W. P. Breugem, B. J. Boersma, and R. E. Uittenbogaard, “The influence of wall permeability on turbulent channel flow,” *Journal of Fluid Mechanics*, vol. 562, pp. 35–72, 2006.

[29] M. Ghisalberti and H. Nepf, “Mixing layers and coherent structures in vegetated aquatic flows,” *Journal of Geophysical Research*, vol. 107, no. C2, 2002.

[30] F. Gosselin and E. de Langre, “Destabilising effects of plant flexibility in air and aquatic vegetation canopy flows,” *European Journal of Mechanics B/Fluids*, vol. 28, pp. 271–282, 2009.

[31] Y. Liu, X. Chen, and J. H. Xin, “Hydrophobic duck feathers and their simulation on textile substrates for water repellent treatment,” *Bioinspiration & Biomimetics*, vol. 3, no. 4, p. 046007, 2008.

[32] J. Mizushima and T. Akinaga, “Vortex shedding from a row of square bars,” *Fluid Dynamics Research*, vol. 32, no. 4, pp. 179–191, 2003.

[33] M. Agnaou, D. Lasseux, and A. Ahmadi, “From steady to unsteady laminar flow in model porous structures: An Investigation of the first Hopf bifurcation,” *Computers & Fluids*, vol. 136, pp. 67–82, 2016.

[34] Y. Jin, M. Uth, A. Kuznetsov, and H. Herwig, “Numerical investigation of the possibility of macroscopic turbulence in porous media: A Direct numerical simulation study,” *Journal of Fluid Mechanics*, vol. 766, pp. 76–103, 2015.

[35] T. Zhu, C. Waluga, B. Wohlmuth, and M. Manhart, “A study of the time constant in unsteady porous media flow using direct numerical simulation,” *Transport in Porous Media*, vol. 104, no. 1, pp. 161–179, 2014.

[36] C. Py, E. De Langre, B. Moulia, and P. Hémon, "Measurement of wind-induced motion of crop canopies from digital video images," *Agricultural and Forest Meteorology*, vol. 130, no. 3-4, pp. 223–236, 2005.

[37] F. Schlegel, J. Stiller, A. Bienert, H.-G. Maas, R. Queck, and C. Bernhofer, "Large-eddy simulation of inhomogeneous canopy flows using high resolution terrestrial laser scanning data," *Boundary-layer Meteorology*, vol. 142, no. 2, pp. 223–243, 2012.

[38] G. Bohrer, G. G. Katul, R. L. Walko, and R. Avissar, "Exploring the effects of microscale structural heterogeneity of forest canopies using large-eddy simulations," *Boundary-layer Meteorology*, vol. 132, no. 3, pp. 351–382, 2009.

[39] C. Py, E. De Langre, and B. Moulia, "The mixing layer instability of wind over a flexible crop canopy," *Comptes Rendus Mécanique*, vol. 332, no. 8, pp. 613–618, 2004.

[40] S. Whitaker, *The Method of Volume Averaging*. Kluwer Academic, Dordrecht, The Netherlands, 1999.

[41] P. Angot, B. Goyeau, and J. A. Ochoa-Tapia, "Asymptotic modeling of transport phenomena at the interface between a fluid and a porous layer: Jump conditions," *Physical Review E*, vol. 95, no. 6, p. 063302, 2017.

[42] Y. Bachmat and J. Bear, "Macroscopic modelling of transport phenomena in porous media. 1: The Continuum approach," *Transport in Porous Media*, vol. 1, no. 3, pp. 213–240, 1986.

[43] J. Bear and Y. Bachmat, "Macroscopic modelling of transport phenomena in porous media. 2: Applications to mass, momentum and energy transport," *Transport in Porous Media*, vol. 1, no. 3, pp. 241–269, 1986.

[44] M. Quintard and S. Whitaker, "Transport in ordered and disordered porous media II: Generalized volume averaging," *Chemical Engineering Science*, vol. 14, pp. 179–206, 1994.

[45] Y. Davit and M. Quintard, "Technical notes on volume averaging in porous media I: How to choose a spatial averaging operator for periodic and quasiperiodic structures," *Transport in Porous Media*, pp. 1–30, 2017.

[46] C. Soulaine and M. Quintard, "On the use of a Darcy-Forchheimer like model for a macro-scale description of turbulence in porous media and its application to structured packings," *International Journal of Heat and Mass Transfer*, vol. 74, pp. 88–100, 2014.

[47] R. G. Carbonell and S. Whitaker, "Heat and Mass Transfer in Porous Media," in *Fundamentals of Transport Phenomena in Porous Media*, pp. 121–198, Springer, 1984.

[48] H. M. Nepf, "Drag, turbulence, and diffusion in flow through emergent vegetation," *Water Resources Research*, vol. 35, no. 2, pp. 479–489, 1999.

[49] A. Nicolle and E. I., "Numerical study of a flow through and around a circular array of cylinders," *Journal of Fluid Mechanics*, vol. 679, pp. 1–31, 2011.

[50] U. Fey, M. König, and H. Eckelmann, "A new Strouhal–Reynolds-number relationship for the circular cylinder in the range $47 < re < 2 \times 10^5$," *Physics of Fluids*, vol. 10, no. 7, pp. 1547–1549, 1998.

[51] Y. Li and Z. J. Wang, "A priori and a posteriori evaluations of subgrid stress models with the Burgers' equation," in *53rd AIAA Aerospace Sciences Meeting*, p. 1283, 2015.

[52] L. F. Richardson, *Weather Prediction by Numerical Process.* Cambridge University Press, 1922.

[53] O. Penttinen, E. Yasari, and H. Nilsson, "A pimplefoam tutorial for channel flow, with respect to different LES models," *Peer reviewed tutorial, CFD with OpenSource Software*, 2011.

[54] M. Chandesris, A. d'Hueppe, B. Mathieu, D. Jamet, and B. Goyeau, "Direct numerical simulation of turbulent heat transfer in a fluid-porous domain," *Physics of Fluids*, vol. 25, no. 12, p. 125110, 2013.

[55] D. A. Nield, "The limitations of the Brinkman-Forchheimer equation in modeling flow in a saturated porous medium and at an interface," *International Journal of Heat and Fluid Flow*, vol. 12, no. 3, pp. 269–272, 1991.

[56] F. J. Valdés-Paradas, J. A. Ochoa-Tapia, and J. Alvarez-Ramirez, "Diffusive mass transport in the fluid-porous medium inter region: Closure problem solution for the one-domain approach," *Chemical Engineering Science*, vol. 62, no. 21, pp. 6054–6068, 2007.

[57] G. S. Beavers and D. D. Joseph, "Boundary conditions at a naturally permeable wall," *Journal of Fluid Mechanics*, vol. 30, no. 1, pp. 197–207, 1967.

[58] J. A. Ochoa-Tapia and S. Whitaker, "Momentum transfer at a boundary between a porous medium and a homogeneous fluid. I, Theoretical development," *International Journal of Heat and Mass Transfer*, vol. 38, no. 14, pp. 2635–2646, 1995.

[59] F. J. Valdés-Paradas, B. Goyeau, and J. A. Ochoa-Tapia, "Jump momentum boundary condition at a fluid-porous dividing surface: Derivation of the closure problem," *Chemical Engineering Science*, vol. 62, no. 15, pp. 4025–4039, 2007.

[60] F. J. Valdés-Paradas, J. Alvarez-Ramirez, B. Goyeau, and J. A. Ochoa-Tapia, “Computation of jump coefficients for momentum transfer between a porous medium and a fluid using a closed generalized transfer equation,” *Transport in Porous Media*, vol. 78, no. 3, pp. 439–457, 2009.

[61] M. Chandesris and D. Jamet, “Derivation of jump conditions for the turbulence $k-\epsilon$ model at a fluid/porous interface,” *International Journal of Heat and Fluid Flow*, vol. 30, no. 2, pp. 306–318, 2009.

[62] B. Goyeau, D. Lhuillier, D. Gobin, and M. G. Velarde, “Momentum transport at a fluid-porous interface,” *International Journal of Heat and Mass Transfer*, vol. 46, no. 21, pp. 4071–4081, 2003.

[63] M. Chandesris and D. Jamet, “Boundary conditions at a planar fluid-porous interface for a Poiseuille flow,” *International Journal of Heat and Mass Transfer*, vol. 49, no. 13-14, pp. 2137–2150, 2006.

[64] A. H. D. Cheng, *Poroelasticity*, vol. 27. Springer, 2016.

[65] I. Nezu and T.-a. Okamoto, “The effect of coherent waving motion on turbulence structure in flexible vegetated open channel flows,” in *River Flow*, pp. 429–436, 2010.

[66] H. Jasak, *Error analysis and estimation for finite volume method with applications to fluid flow.* PhD thesis, Imperial College of Science, Technology and Medicine,London,UK, 1996.

[67] R. I. Issa, “Solution of the implicitly discretised fluid flow equations by operator-splitting,” *Journal of Computational Physics*, vol. 62, no. 1, pp. 40–65, 1986.

[68] N. Luminari, C. Airiau, and A. Bottaro, “Effects of porosity and inertia on the apparent permeability tensor in fibrous media,” *International Journal of Multiphase Flow*, vol. 106, pp. 60–74, 2018.

[69] N. Dukhan, Ö. Bağcı, and M. Özdemir, “Experimental flow in various porous media and reconciliation of Forchheimer and Ergun relations,” *Experimental Thermal and Fluid Science*, vol. 57, pp. 425–433, 2014.

[70] W. P. Breugem and B. J. Boersma, “Direct numerical simulations of turbulent flow over a permeable wall using a direct and a continuum approach,” *Physics of Fluids*, vol. 17, no. 2, p. 025103, 2005.

[71] T. Behrens, “Openfoam’s basic solvers for linear systems of equations,” *Chalmers, Department of Applied Mechanics*, vol. 18, no. 02, 2009.

[72] G. Schneebeli, “Expériences sur la limite de validité de la loi de Darcy et l’apparition de la turbulence dans un écoulement de filtration,” *La Houille Blanche*, no. 2, pp. 141–149, 1955.

[73] G. Chauveteau and C. Thirriot, “Régimes d’écoulement en milieu poreux et limite de la loi de Darcy,” *La Houille Blanche*, no. 2, pp. 141–148, 1967.

[74] A. Dybbs and R. Edwards, “A new look at porous media fluid mechanics-Darcy to turbulent,” in *Fundamentals of Transport Phenomena in Porous Media*, pp. 199–256, Springer, 1984.

[75] R. Fand, B. Kim, A. Lam, and R. Phan, “Resistance to the flow of fluids through simple and complex porous media whose matrices are composed of randomly packed spheres,” *Journal of Fluids Engineering*, vol. 109, no. 3, pp. 268–274, 1987.

[76] D. Seguin, A. Montillet, and J. Comiti, “Experimental characterisation of flow regimes in various porous media. I: Limit of laminar flow regime,” *Chemical engineering science*, vol. 53, no. 21, pp. 3751–3761, 1998.

[77] D. Seguin, A. Montillet, J. Comiti, and F. Huet, “Experimental characterization of flow regimes in various porous media. II: Transition to turbulent regime,” *Chemical Engineering Science*, vol. 53, no. 22, pp. 3897–3909, 1998.

[78] J. L. Lage, “The fundamental theory of flow through permeable media from Darcy to turbulence,” in *Transport Phenomena in Porous Media* (D. B. Ingham and I. Pop, eds.), pp. 1–30, Oxford, United Kingdom: Elsevier, 1998.

[79] P. Venkataraman and P. R. M. Rao, “Darcian, transitional, and turbulent flow through porous media,” *Journal of Hydraulic Engineering*, vol. 124, no. 8, pp. 840–846, 1998.

[80] D. Hlushkou and U. Tallarek, “Transition from creeping via viscous-inertial to turbulent flow in fixed beds,” *Journal of Chromatography A*, vol. 1126, no. 1, pp. 70–85, 2006.

[81] T. Masuoka and Y. Takatsu, “Turbulence model for flow through porous media,” *International Journal of Heat and Mass Transfer*, vol. 39, no. 13, pp. 2803–2809, 1996.

[82] B. V. Antohe and J. L. Lage, “A general two-equation macroscopic turbulence model for incompressible flow in porous media,” *International Journal of Heat and Mass Transfer*, vol. 40, no. 13, pp. 3013–3024, 1997.

[83] F. Kuwahara, Y. Kameyama, S. Yamashita, and A. Nakayama, “Numerical modeling of turbulent flow in porous media using a spatially periodic array,” *Journal of Porous Media*, vol. 1, no. 1, 1998.

[84] A. Nakayama and F. Kuwahara, “A macroscopic turbulence model for flow in a porous medium,” *Journal of Fluids Engineering*, vol. 121, pp. 427–433, 1999.

[85] M. Chandesris, G. Serre, and P. Sagaut, “A macroscopic turbulence model for flow in porous media suited for channel, pipe and rod bundle flows,” *International Journal of Heat and Mass Transfer*, vol. 49, no. 15, pp. 2739–2750, 2006.

[86] M. J. De Lemos, *Turbulence in porous media: Modeling and applications.* Elsevier, 2012.

[87] Y. Jin and A. V. Kuznetsov, “Turbulence modeling for flows in wall bounded porous media: An analysis based on direct numerical simulations,” *Physics of Fluids*, vol. 29, no. 4, p. 045102, 2017.

[88] S. Whitaker, “Diffusion and dispersion in porous media,” *American Institute of Chemical Engineers*, vol. 13, no. 3, pp. 420–427, 1967.

[89] K. Vafai and C. Tien, “Boundary and inertia effects on convective mass transfer in porous media,” *International Journal of Heat and Mass Transfer*, vol. 25, no. 8, pp. 1183–1190, 1982.

[90] J. Hoffmann, R. Echigo, H. Yoshida, and S. Tada, “Experimental study on combustion in porous media with a reciprocating flow system,” *Combustion and flame*, vol. 111, no. 1-2, pp. 32–46, 1997.

[91] H. P. A. Souto and C. Moyne, “Dispersion in two-dimensional periodic porous media. Part I: Hydrodynamics,” *Physics of Fluids*, vol. 9, no. 8, pp. 2243–2252, 1997.

[92] B. D. Wood, “Inertial effects in dispersion in porous media,” *Water Resources Research*, vol. 43, no. 12, 2007.

[93] J. Hong, Y. Yamada, and C. Tien, “Effects of non-darcian and nonuniform porosity on vertical-plate natural convection in porous media,” *Journal of Heat Transfer*, vol. 109, no. 2, pp. 356–362, 1987.

[94] A. Amiri and K. Vafai, “Analysis of dispersion effects and non-thermal equilibrium, non-Darcian, variable porosity incompressible flow through porous media,” *International Journal of Heat and Mass Transfer*, vol. 37, no. 6, pp. 939–954, 1994.

[95] B. Goyeau, J.-P. Songbe, and D. Gobin, “Numerical study of double-diffusive natural convection in a porous cavity using the Darcy-Brinkman formulation,” *International Journal of Heat and Mass Transfer*, vol. 39, no. 7, pp. 1363–1378, 1996.

[96] M. Quintard, M. Kaviany, and S. Whitaker, "Two-medium treatment of heat transfer in porous media: Numerical results for effective properties," *Advances in Water Resources*, vol. 20, no. 2, pp. 77–94, 1997.

[97] S. Y. Kim, J. W. Paek, and B. H. Kang, "Flow and heat transfer correlations for porous fin in a plate-fin heat exchanger," *Journal of Heat Transfer*, vol. 122, no. 3, pp. 572–578, 2000.

[98] O. Aydın and A. Kaya, "Non-Darcian forced convection flow of viscous dissipating fluid over a flat plate embedded in a porous medium," *Transport in Porous Media*, vol. 73, no. 2, pp. 173–186, 2008.

[99] N. Chikhi, R. Clavier, J.-P. Laurent, F. Fichot, and M. Quintard, "Pressure drop and average void fraction measurements for two-phase flow through highly permeable porous media," *Annals of Nuclear Energy*, vol. 94, pp. 422–432, 2016.

[100] P. H. Forchheimer, "Wasserbewegung durch boden," *Zeitschrift des Vereines Deutscher Ingenieure*, vol. 45, pp. 1782–1788, 1901.

[101] P. C. Carman, "Fluid flow through granular beds," *Chemical Engineering Research and Design*, vol. 15, pp. 150–166, 1937.

[102] L. J. Klinkenberg, "The permeability of porous media to liquids and gases," in *Drilling and Production Practice*, American Petroleum Institute, 1941.

[103] S. Ergun, "Fluid flow through packed columns," *Chemical Engineering Progress*, vol. 48, pp. 89–94, 1952.

[104] W. F. Brace, J. B. Walsh, and W. T. Frangos, "Permeability of granite under high pressure," *Journal of Geophysical Research*, vol. 73, no. 6, pp. 2225–2236, 1968.

[105] G. W. Jackson and D. F. James, "The permeability of fibrous porous media," *The Canadian Journal of Chemical Engineering*, vol. 64, no. 3, pp. 364–374, 1986.

[106] T.-f. Wong, C. David, and W. Zhu, "The transition from brittle faulting to cataclastic flow in porous sandstones: Mechanical deformation," *Journal of Geophysical Research: Solid Earth*, vol. 102, no. B2, pp. 3009–3025, 1997.

[107] H. Darcy, *Les fontaines publiques de la ville de Dijon.* Victor Dalmont, 1856.

[108] S. M. Hassanizadeh and W. G. Gray, "High velocity flow in porous media," *Transport in porous media*, vol. 2, no. 6, pp. 521–531, 1987.

[109] C. C. Mei and J. L. Auriault, “The effect of weak inertia on flow through a porous medium,” *Journal of Fluid Mechanics*, vol. 222, pp. 647–663, 1991.

[110] M. Firdaouss, J.-L. Guermond, and P. Le Quéré, “Nonlinear corrections to Darcy’s law at low Reynolds numbers,” *Journal of Fluid Mechanics*, vol. 343, pp. 331–350, 1997.

[111] H. Ma and D. Ruth, “Physical explanations of non-Darcy effects for fluid flow in porous media,” *SPE Formation Evaluation*, vol. 12, no. 01, pp. 13–18, 1997.

[112] S. Rojas and J. Koplik, “Nonlinear flow in porous media,” *Physical Review E*, vol. 58, pp. 4776–4782, 1998.

[113] E. Skjetne and J. L. Auriault, “New insights on steady, nonlinear flow in porous media,” *European Journal of Mechanics-B/Fluids*, vol. 18, no. 1, pp. 131–145, 1999.

[114] M. Panfilov, C. Oltean, I. Panfilova, and M. Buès, “Singular nature of nonlinear macroscale effects in high-rate flow through porous media,” *Comptes Rendus Mécanique*, vol. 331, no. 1, pp. 41–48, 2003.

[115] R. W. Zimmerman, A. Al-Yaarubi, C. C. Pain, and C. A. Grattoni, “Nonlinear regimes of fluid flow in rock fractures,” *International Journal of Rock Mechanics and Mining Sciences*, vol. 41, pp. 163–169, 2004.

[116] D. Lasseux, A. A. Abbasian Arani, and A. Ahmadi, “On the stationary macroscopic inertial effects for one phase flow in ordered and disordered porous media,” *Physics of Fluids*, vol. 23, no. 7, p. 073103, 2011.

[117] D. Ruth and H. Ma, “On the derivation of the Forchheimer equation by means of the averaging theorem,” *Transport in Porous Media*, vol. 7, no. 3, pp. 255–264, 1992.

[118] J. S. Andrade Jr, U. M. S. Costa, M. P. Almeida, H. A. Makse, and H. E. Stanley, “Inertial effects on fluid flow through disordered porous media,” *Physical Review Letters*, vol. 82, no. 26, p. 5249, 1999.

[119] J. L. Lage and B. V. Antohe, “Darcy’s experiments and the deviation to nonlinear flow regime,” *Journal of Fluids Engineering*, vol. 122, no. 3, pp. 619–625, 2000.

[120] Z. Zeng and R. Grigg, “A criterion for non-Darcy flow in porous media,” *Transport in Porous Media*, vol. 63, no. 1, pp. 57–69, 2006.

[121] B. P. Muljadi, M. J. Blunt, A. Q. Raeini, and B. Bijeljic, “The impact of porous media heterogeneity on non-Darcy flow behaviour from pore-scale simulation,” *Advances in Water Resources*, vol. 95, pp. 329–340, 2016.

[122] G. S. Beavers and E. M. Sparrow, “Non-Darcy flow through fibrous porous media,” pp. –, American Society of Mechanical Engineers, 1969.

[123] I. F. Mcdonald, M. S. El-Sayed, K. Mow, and F. A. L. Dullien, “Flow through porous media-the Ergun equation revisited,” *Industrial & Engineering Chemistry Fundamentals*, vol. 18, no. 3, pp. 199–208, 1979.

[124] A. P. Philipse and H. L. Schram, “Non-Darcian airflow through ceramic foams,” *Journal of the American Ceramic Society*, vol. 74, no. 4, pp. 728–732, 1991.

[125] L. Li and W. Ma, “Experimental study on the effective particle diameter of a packed bed with non-spherical particles,” *Transport in Porous Media*, vol. 89, no. 1, pp. 35–48, 2011.

[126] L. Li and W. Ma, “Experimental characterization of the effective particle diameter of a particulate bed packed with multi-diameter spheres,” *Nuclear Engineering and Design*, vol. 241, no. 5, pp. 1736–1745, 2011.

[127] J. S. Andrade Jr, D. A. Street, T. Shinohara, Y. Shibusa, and Y. Arai, “Percolation disorder in viscous and nonviscous flow through porous media,” *Physical Review E*, vol. 51, no. 6, p. 5725, 1995.

[128] R. Clavier, N. Chikhi, F. Fichot, and M. Quintard, “Experimental investigation on single-phase pressure losses in nuclear debris beds: Identification of flow regimes and effective diameter,” *Nuclear Engineering and Design*, vol. 292, pp. 222–236, 2015.

[129] R. Clavier, N. Chikhi, F. Fichot, and M. Quintard, “Experimental study of single-phase pressure drops in coarse particle beds,” *Nuclear Engineering and Design*, vol. 312, pp. 184–190, 2017.

[130] J.-C. Wodie and T. Levy, “Correction non linéaire de la loi de Darcy,” *Comptes Rendus de l’Académie des Sciences. Série 2, Mécanique, Physique, Chimie, Sciences de l’Univers, Sciences de la Terre*, vol. 312, no. 3, pp. 157–161, 1991.

[131] Y. Lucas, M. Panfilov, and M. Buès, “High velocity flow through fractured and porous media: The Role of flow non-periodicity,” *European Journal of Mechanics-B/Fluids*, vol. 26, no. 2, pp. 295–303, 2007.

[132] K. Vafai and C. L. Tien, “Boundary and inertia effects on flow and heat transfer in porous media,” *International Journal of Heat and Mass Transfer*, vol. 24, no. 2, pp. 195–203, 1981.

[133] D. A. Nield and A. Bejan, *Convection in Porous Media.* New York: Springer-Verlag, 1999.

[134] T. D. Papathanasiou, B. Markicevic, and E. D. Dendy, "A computational evaluation of the Ergun and Forchheimer equations for fibrous porous media," *Physics of Fluids*, vol. 13, no. 10, pp. 2795–2804, 2001.

[135] K. V. Sharp and R. J. Adrian, "Transition from laminar to turbulent flow in liquid filled microtubes," *Experiments in Fluids*, vol. 36, no. 5, pp. 741–747, 2004.

[136] S. Whitaker, "The Forchheimer equation: A Theoretical development," *Transport in Porous Media*, vol. 25, no. 1, pp. 27–61, 1996.

[137] D. Lasseux and F. J. Valdés-Parada, "On the developments of Darcy's law to include inertial and slip effects," *Comptes Rendus Mécanique*, vol. 345, no. 9, pp. 660–669, 2017.

[138] D. L. Koch and A. J. C. Ladd, "Moderate Reynolds number flows through periodic and random arrays of aligned cylinders," *Journal of Fluid Mechanics*, vol. 349, pp. 31–66, 1997.

[139] R. Clavier, *Étude expérimentale et modélisation des pertes de pression lors du renoyage d'un lit de débris.* PhD thesis, Institut National Polytechnique de Toulouse, France, 2015.

[140] N. Luminari, C. Airiau, and A. Bottaro, "Effects of porosity and inertia on the apparent permeability tensor in fibrous media," *International Journal of Multiphase Flow*, vol. 106, pp. 60–74, 2018.

[141] D. S. Weaver and L. K. Grover, "Cross-flow induced vibrations in a tube bank - turbulent buffeting and fluid elastic instability," *Journal of Sound and Vibration*, vol. 59, no. 2, pp. 277–294, 1978.

[142] J. H. Lever and D. S. Weaver, "A theoretical model for fluid-elastic instability in heat exchanger tube bundles," *Journal of Pressure Vessel Technology*, vol. 104, no. 3, pp. 147–158, 1982.

[143] B. Bigot, T. Bonometti, L. Lacaze, and O. Thual, "A simple immersed-boundary method for solid-fluid interaction in constant-and stratified-density flows," *Computers & Fluids*, vol. 97, pp. 126–142, 2014.

[144] C. S. Peskin, "The immersed boundary method," *Acta Numerica*, vol. 11, pp. 479–517, 2002.

[145] "MPI for Python." https://bitbucket.org/mpi4py/mpi4py. Accessed: 2017-01-24.

[146] J. Yang, S. Preidikman, and E. Balaras, "A strongly coupled, embedded-boundary method for fluid-structure interactions of elastically mounted rigid bodies," *Journal of Fluids and Structures*, vol. 24, no. 2, pp. 167–182, 2008.

[147] J. Yang and E. Balaras, “An embedded-boundary formulation for large-eddy simulation of turbulent flows interacting with moving boundaries,” *Journal of Computational Physics*, vol. 215, pp. 12–40, 2006.

[148] D. Pan, “A comparison of fluid-cell and ghost-cell direct forcing immersed boundary method for incompressible flows with heat transfer,” *Numerical Heat Transfer. Part B: Fundamentals*, vol. 68, no. 1, pp. 30–52, 2015.

[149] J. H. Seo and R. Mittal, “A sharp-interface immersed boundary method with improved mass conservation and reduced spurious oscillations,” *Journal of Computational Physics*, vol. 230, no. 19, pp. 7347–7363, 2011.

[150] T. Ye, R. Mittal, H. S. Udaykumar, and W. Shyy, “A accurate cartesian grid method for viscous incompressible flows with complex boundaries,” *Journal of Computational Physics*, vol. 156, pp. 209–240, 1999.

[151] “PETSc for Python.” https://bitbucket.org/petsc/petsc4py. Accessed: 2017-01-24.

[152] Y. Yan, J. F. Morris, and J. Koplik, “Hydrodynamic interaction of two particles in confined linear shear flow at finite Reynolds number,” *Physics of Fluids*, vol. 19, no. 11, p. 113305, 2007.

[153] S. Mittal and V. Kumar, “Finite element study of vortex-induced cross-flow and in-line oscillations of a circular cylinder at low Reynolds numbers,” *International Journal for Numerical Methods in Fluids*, vol. 31, no. 7, pp. 1087–1120, 1999.

[154] J. C. Brändle de Motta, W. P. Breugem, B. Gazanion, J. L. Estivalezes, S. Vincent, and E. Climent, “Numerical modelling of finite-size particle collisions in a viscous fluid,” *Physics of Fluids*, vol. 25, no. 8, p. 083302, 2013.

[155] M. Quintard and S. Whitaker, “Transport in ordered and disordered porous media III: Closure and comparison between theory and experiment,” *Chemical Engineering Science*, vol. 15, pp. 31–49, 1994.

[156] T. P. de Carvalho, H. P. Morvan, D. M. Hargreaves, H. Oun, and A. Kennedy, “Pore-scale numerical investigation of pressure drop behaviour across open-cell metal foams,” *Transport in Porous Media*, pp. 1–26, 2017.